Improving Na-beta”-alumina interface and grain boundary as solid-state electrolyte for large scale Room Temperature applications

Effect of particle size and liquid addition on capacity, conductivity and cyclability

By Loïc Leclercq

Supervised by:

Dr. Niek de Klerk
Eveline van der Maas

Thesis Committee:

Prof. Dr. Ir. Marnix Wagemaker
Dr. Erik Kelder
Dr. Lambert van Eijck

Acknowledgement

This thesis could not have been possible without the opportunity offered to me by Marnix Wagemaker. It was his class on Energy Storage that made me want to invest more time into this subject. The fascinating, yet challenging subject attracted me enormously, but it was not until I was faced with the myriad of experimental issues that I realized how challenging this Thesis would actually be. That is where my girlfriend Megan Solomon and my parents came into play. Without their support, I might not have found the strength to finish this work. Finally, I would like to thank my friend Eveline van der Maas for providing me with valuable feedback and critical thinking, which was of very valuable assistance.

Contents

List of Figures, Equations and Tables

Abbreviations:

LIB	Lithium Ion Battery
SIB	Sodium Ion Battery
BASE	Na-beta”-alumina or Na- β''-Al_2O_3 or NBA
NNM	P2-$Na_{1/3}[Ni_{1/3}Mn_{2/3}]O_2$
RT	Room Temperature
SEI	Solid Electrolyte Interphase
PVDF	Polyvinylidene fluoride
NMP	N-methylpyrrolidone
IL	ionic liquid
TES-TFSI	Triethylsulfonium (cation) bis(trifluoromethylsulfonyl)imide (anion)
Pyr14-FSI	1-Butyl-1-methylpyrrolidinium (cation) bis(fluorosulfonyl)imide (anion)

Abstract

The aim of my project at the Storage of Electrochemical Energy section of the TU Delft is to improve the performance and uncover the electrolytic hurdles of the widely used Na-beta”-alumina solid electrolyte within Sodium semi solid-state batteries at Room Temperature.
Na-beta”-alumina could be an interesting candidate to replace volatile and flammable organic electrolytes, seeing as it is not flammable and made of abundant elements. It would be a safer, with potential for mass-production due to the abundancy and low costs of the required materials.
However, to make working electrolyte pellets, high sintering temperatures are needed for a high density. The material would be a lot more interesting if it could be used without such high sintering temperatures and reasonable conductivity at room temperature.

The aim of this thesis is to investigate whether the point-contact problem is solid-state electrolytes can be circumvented by varying the solid electrolyte particle size in combination with liquid addition and various potential concepts.

Regarding our conclusions, we can affirm that the mechanically pressed BASE electrolyte pellet concept performs worse than the slurry electrolyte concept. This is related to the improved slurry contact, as well as the increased point contacts for the pellet in combination with a suspected lower ionic liquid coverage.
We can also conclude that the electrolyte resistance is lowered with organic electrolyte or ionic liquid addition.
The evidence space-charge of has yet to be demonstrated for our components, as smaller particles resulted in lower conductivity and capacitance, regardless of the various series and concepts experimented with.
Finally, the Na^+ diffusion was better for bigger particles for all three liquid additions.

1. Introduction

In order to understand the subject of this thesis, the macroeconomic challenges with respect to energy consumption are put into perspective. This will illustrate how battery research is important and needs to be pursued in order to facilitate a sustainable energy transition. At the end of this introductory chapter, I will summarise the aims of my project.

1.1 Energy Demand

Three centuries ago, the western world experienced the first evolution towards an industrialized world, known as the 1st industrial revolution. This marked a transition towards machinery production instead of manual labour, accompanied by technological breakthroughs such as steam powered transportation. The second industrial transition 150 years ago sparked the global use of fossil fuels such as coal and oil, contributing to the fast development of textile, automotive and chemical industry. A neglected consequence of fossil fuels was the accompanying environmental and health issues. Even in recent years, lung damage was attributed to the usage of coal in Chinese power plants, resulting in Beijing air being so polluted. A frightening estimation of the damage to lungs was made. The pollution in the Chinese capital is as damaging to lungs as smoking 40 cigarettes a day, resulting in pollution killing 4000 people daily in China [1].

One would think that such a health and environmental hazard would be regulated. The Kyoto protocol followed by the Paris Agreement were meant to decrease greenhouse gasses such as CO_2, but is proving to be challenging to enforce.

Industrial developments have transformed the world, but also call for an ever-increasing demand in cheap and convenient energy source, a role that has been filled by coal, oil and natural gas for two centuries.

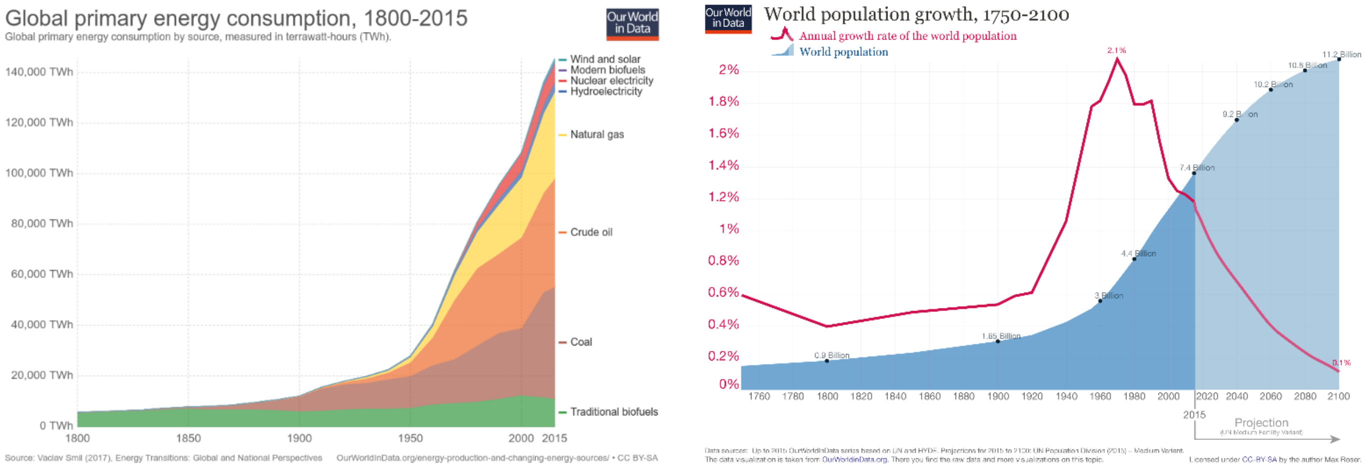

Source: Vaclav Smil (2017), Energy Transitions: Global and National Perspectives OurWorldInData.org/energy-production-and-changing-energy-sources/ • CC BY-SA

Data sources: Up to 2015 OurWorldInData series based on UN and HYDE. Projections for 2015 to 2100: UN Population Division (2015) – Medium Variant. The data visualization is taken from OurWorldinData.org. There you find the raw data and more visualizations on this topic. Licensed under CC-BY-SA by the author Max Roser.

Figure 1. Global primary energy consumption (left) and world population growth (right), including future projections [2]

Besides industrial and technological advances, the energy demand is also fuelled by population growth, estimated to reach 10billion before 2080. The relation between energy demand and population growth is shown in Figure 1. Based on all these facts, the world is compelled to look towards more sustainable solutions to alleviate the increasing energy demand and growing world population. [3].

1.2 Sustainable Energy

The increasing energy consumption paired with population growth and dependence on fossil fuels have forced the inevitable depletion of the Earth's fossil fuel reserves. In order to curb the greenhouse gas emissions from fuel combustion that are projected to affect our daily lives (increasing temperatures, rising sea-levels, extreme weather), [4] and the eventual depletion of fossil fuels with increasing fossil fuel price and demand [5], an alternative to a fossil fuel economy must be put in place to guarantee a continuous energy supply.

Fortunately, there are plenty of options for harnessing energy in a sustainable manner. Environmentally responsible alternative sources such as solar power, wind power, hydro power, biofuels and nuclear (controversial due to inherent risk) are necessary, combined with grid stabilisation to compensate for fluctuations. Countries are already starting to implement new sustainable policies [6], where the E.U are making progress concerning this transition. Complementary to these policies is the rapidly decreasing price of renewable energies, even with prices competing with electricity produced from fossil fuels [7]. The remaining drawback of these renewable technologies, is the intermittence of power generation. Energy storage will play a key role in saving and distributing the produced energy. Large scale energy storage needs to be integrated into the grid, providing balance for production and consumer loads in the grid, and will be essential in applications for transportation methods.

1.3 Energy Storage

Seeing as fossil fuels are depleting and renewable energy technologies are increasing, research towards electricity storage becomes more necessary. Even though the storage method depends on the application, an emphasis has been made on secondary batteries due to the increasing number of laptops, mobile phones, but also the emergence of affordable electric cars [8].

The transportation sector is almost entirely dominated by fossil fuel, thus highly dependent on the fluctuating market price. Nevertheless, electric cars have recently begun making their mark, being competitive especially for short distance applications. Battery electric vehicles and hydrogen powered fuel cell electric vehicles are the prominent options. These cars do not consume fossil fuels, but the efficiency and performance of the energy storage method is a limiting factor. Battery electric vehicles are gaining in popularity due to problems finding adequate hydrogen storage [9]. And even for trucks doing long distance transport, the electrical option is becoming more viable [10].

In the long run, both of these types of electric vehicles are likely to play a big role in ending the dependence of land transportation on fossil fuels [11].

Needless to say, that with the increase in electric devices in our daily lives, the necessity for large-scale, cheap and abundant energy storage materials and technology becomes paramount.

A widely studied solid electrolyte in the past is Na-beta”-alumina, Na- β"-Al_2O_3. This ceramic material has many advantages including being solid and is non-flammable compared to conventional organic electrolytes. It is also multifunctional, as batteries with a solid electrolyte would not need an additional separator. Na- β"-Al_2O_3 has been successfully implemented in a Na-sulphur battery, but functioning around 350 °C. This made it a decent candidate for grid-scale applications, but harder to implement in daily electronic devices. Being a ceramic material, Na- β"-Al_2O_3 solid electrolyte also presents risks concerning transportation applications, as shocks could result in fractures of the ceramic electrolyte pellet and provoke cell failure. Alternatives for commercialization have been Na-MH, metallic hydrides that operate at a slightly lower temperature (280°C), safer and a higher output voltage.

It was found that lowering the operating temperature of batteries prolonged their life-cycle and stability, retaining their capacity by slowing down material degradation, typical of high temperature energy storage. Lowering the temperature also allows for other sealing materials that do not have to be subjected to such high temperatures, reducing manufacturing costs. By aiming towards a Room temperature solution with solid-state materials for energy storage, we can strive towards a potentially better solution for large scale energy storage.

1.4 Objective of the thesis

The approach of this research is to gain understanding of the performances and hurdles of a solid-state electrolyte for large scale and cheap sodium-based energy storage, focussing on Room Temperature applications. The subject of this research is the widely used Na-beta”-alumina solid electrolyte, focussing on applications in Sodium semi solid-state batteries. Na-beta”-alumina could be an interesting candidate due to the abundancy and low costs of the required materials. However, to make working electrolyte pellets, high sintering temperatures are needed. When sintering for 4h at 1600 °C, dense pellet with a conductivity of the 10^{-4} S/cm order can be achieved at room temperature.

The material would be a lot more interesting if it could be used without such high sintering temperatures and reasonable conductivity at room temperature. Common strategies of improving room temperature conductivity are stabilizing a higher conductivity phase or doping the material. However, the main problem in the conductivity of Na-beta”-alumina arises from bad contact between the grains, hence the importance of the thermal treatment and the densification of the pellet. The same problem can arise at the solid-solid interface of the electrolyte and the electrode.

The aim of this thesis is to investigate whether the point-contact problem can be circumvented by varying the solid electrolyte particle size in combination with liquid addition, while keeping the main conduction path through the solid electrolyte. The idea is to use a liquid with a different chemical potential for sodium, so that a space charge layer may form at the interface between the solid and the liquid. This can lead to seemingly larger contact area and therewith lower grain boundary resistance.

If this is the case, one would expect an improvement in the electrochemical properties of the system, which can be measured with impedance spectroscopy. By modelling the electrochemical interactions based on their various time constants, the electrical properties can be derived based on this model. This would provide valuable information concerning the interactions in the system.

By studying the variation in particle size combined with various liquid additions, conclusions can be drawn regarding contact issues, interfacial and grain boundary issues for the different hybrid liquid/solid electrolyte concepts.

After an introduction illustrating the reason for this research in Chapter 1, Chapter 2 gives knowledge regarding electrochemical energy storage and the specific choices made for materials. Chapter 3 introduces the tools necessary for our electrochemical characterization, defining the crystal structures as well as electrochemical properties. Chapter 4 refers to the preparation methods used before assembling the components of the battery and Chapter 5 is a synthesis of the results, highlighting the challenges during this project as well as shedding light upon the electrochemical hurdles in our batteries, which leads us to the outcome of this study.

2. Battery Theory

The Battery theory chapter introduces all the concepts relating to batteries, ranging from the general concepts relating to electrochemical storage, the various components comprising batteries, but also a comparative of the Lithium vs Sodium batteries, as they are both highly relevant and present various interesting aspects

2.1 General concepts of electrochemistry

Batteries are electrochemical systems able to store electrical energy in chemical compounds, reversibly converting chemical energy into electrical. Battery theory is based on harnessing redox reactions to shift the thermodynamic equilibrium within the system driven by a difference in the Gibbs free energy, thus storing energy. Reduction-oxidation reactions are the building block of electrochemistry, where oxidation essentially means increasing the oxidation state of a species (losing one or more electrons), while reduction decreases the oxidation state (gaining electrons). This reaction is reversible, giving electrochemical cells (commonly known as batteries) the ability to be rechargeable.

Electrochemical cells are composed of two electrodes and an electrolyte separating them. One advantage of using a solid-state electrolyte is that an additional separator membrane necessary for conventional batteries (using liquid electrolytes) is no longer required. The electrodes serve as the positive and negative pole of the battery, providing electrons to power external devices; while the electrolyte separating them needs to vehicle only the ions, resisting electron transport since conducting electrons as well would result in a short-circuited, depleted battery. The electrodes are composed of an active material on a current collector, allowing ions to be inserted or extracted. The large variety of electrodes will be covered more in depth later in the chapter. Commonly, the electrolyte is liquid, requiring a porous membrane to avoid direct contact between the two electrodes, which would result in short-circuit. But common organic liquid electrolytes present problems relating to practical and safety issues. Inversely, solid electrolytes such as ceramic or polymer electrolytes, do not require additional separation [**12**]**.**

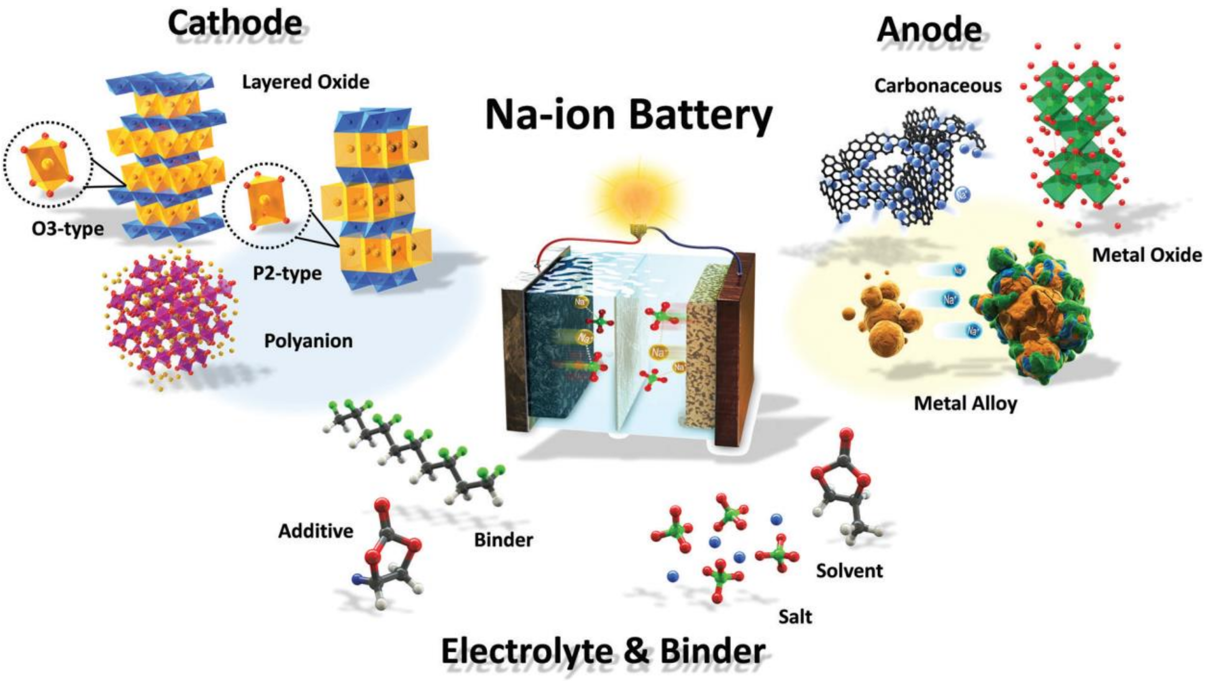

Figure 2. Overview of the components relating to Sodium batteries [**13**]

The positive and negative electrode, respectively cathode and anode, are usually composed of an active material (allowing active particle insertion and extraction), a conductive agent (conducting electrons to the current collectors) and binder (adhering the particles together as a thin film) [**14**], a composite which needs to be electrochemically performant and mechanically resistant to prevent deterioration during battery cycling. These are all summarized in Figure 2.

During discharge, the cathode is where the electrons reduce the material (accepting electrons), while the anode is where the oxidation takes place (providing electrons). Interestingly, in a charging battery (absorbing energy of charge), the cathode side is considered negative, as electrons flow out to receive charge.

The difference in potential between the two electrodes (cathode and anode) determines the driving force within the battery. Thus, the cell has a potential $E_{cell} = E_{cathode}-E_{anode}$ which, when connected through an external circuit, makes electrons flows from the more negative to the more positive potential, allowing to power external electric devices. The electron flow outside the cell is compensated by an ionic flow through the electrolyte inside the cell, which maintains the charge balance of the system.
This driving force translates into the release of Gibbs free energy (Eq.1) [**14**], allowing the system to move to a more thermodynamically stable state.

$$\Delta G = -nFE_{cell} \qquad \textbf{(Eq. 1)}$$

With ΔG as the difference in Gibbs free energy, n the number of electrons transferred, F being Faraday's constant, and E_{cell} the electrochemical potential covered earlier.

By combining the amount of released energy and the number of charged ions released per mass, the specific capacity can be derived from this equation. This is the amount of charge that can be extracted (per unit of volume or mass of active material) from the battery at a specific rate of charge, named C-rate. A C-rate of C/10 means the insertion of 1 mole of ions per 10 hours. The energy extracted from the battery also depends on the C-rate. This capacity depends on the kinetics (insertion/extraction) taking place within the active material, therefore discharging the battery at a higher rate will yield a lower specific capacity. The kinetics of an active material can thus be characterized, which is especially interesting when researching solutions for fast-charging (electric vehicles for example).

2.1.1 Electrochemical stability

The electrochemical stability of a battery determines in which voltage window the components of the cell can be cycled without deterioration of the components. A greater potential window allows for more energy to be transferred. A larger electrode capacity can also store more energy, but it can also influence the volume expansion within the battery, like a sponge absorbing water. Inserting particles in a host material gives rise to volume expansion, which is a reoccurring problem in electrochemical storage. Since cyclability is an important parameter for an increased lifetime, the composition of various materials within cells have to present decent mechanical strength and flexibility, as volume expansion can lead to fissures followed by cell failure. Going outside of the electrochemical window can result in decomposition or side-reactions that could be a safety hazard, or simply destroy a material.

2.1.2 Coulombic efficiency

The Coulombic efficiency is one of the important characteristics when evaluating the performance of an electrochemical cell. This efficiency can be derived from the charge and discharge capacity of the battery (Eq. 2). It describes the number of electrons transferred in a system, and should ideally be close to 100%.

$$\eta C = \frac{Qdischarge}{Qcharge} \tag{Eq.2}$$

In a cell with no side-reactions or decomposition, the coulombic efficiency could be defining for battery performance. Yet this parameter can be misleading, as electrodes undergoing side-reactions or decomposition can show a decreasing capacity, while coulombic efficiency remains high due to these side products providing the additional electrons as a result of continuous oxidation or reduction.

2.2 Lithium vs Sodium for batteries

Sodium and lithium are two largely used elements for ionic transport within batteries. Sodium-based batteries were intensely studied in the 80's, but research was refocussed

towards lithium-based batteries with the commercialization of Sony's Lithium ion batteries (LIB) in the 90's [**15**]. With the upcoming challenges regarding large scale energy storage, the attributes of both elements should be considered.
The most common rechargeable battery is the Lithium-ion battery, found in the majority of mobile electronic devices. A notable attribute of Lithium is that it is the lightest metallic element, with a low redox potential (E_0 Li^+ / Li = -3.04 V versus standard hydrogen electrode). For electrochemical process, this opens the door to high energy density and high voltage batteries. Due to its small ionic radius, diffusion through solids is also facilitated, and allows easier intercalation processes leading to longer cycle life and rate capabilities. Yet a drawback of Lithium metal is the uneven deposition during cycling resulted in dangerous dendrite growth [**16**]**.** But an alternative for Lithium metal was found, a safer insertion material: graphite [**17**]. This was the "rocking chair" concept, as lithium was now getting transferred between to intercalation electrodes. This concept is still used nowadays, attractive due to light weight resulting in a high energy density.

These qualities have made LIB's the dominant energy storage in portable devices and becoming the prime candidate for electric vehicles. Yet a major drawback of using lithium metal, is its availability. As if victim of its success, the demand of Lithium is leading to a steep increase in prices. This is enforced by lithium utilization in the automotive sector, further pushing the price. Being non-uniformly distributed across the Earth's crust and located in geopolitically strained regions [**18**]**,** the availability of this element will decrease in the future. An estimate of Lithium consumption shows that the resource can be sustained for another 65 years before depletion at an average growth rate of 5% [**19**][**20**], making long-term large-scale applications for Lithium challenging.

The most prominent alternative to Lithium, is Sodium. Being the 4th most abundant metal on Earth and its broad distribution [**21**], sodium derivatives are widely used for various applications such as household products, basic chemicals, glass containers or cosmetics. Sodium presents a redox potential only 0.3V higher than for lithium (E_0 Na^+ / Na = -2.71 V versus standard hydrogen electrode). On the periodic table, Na is located right under Li in the s block, indicating that similar approaches towards material synthesis, intercalation or conversion chemistry are possible. Novel Sodium ion batteries (SIB's) can be more efficiently developed using the same characterization tools as for LIB's.[**22**].
A property that has not been addressed yet, is the ionic radius of the two ions. The Na+ ion size (coordination number 6: 1.02 Å) is relatively larger than that of Li^+. (coordination number 6: 0.76 Å). Having a larger size, thermodynamic and kinetic processes differ for Na^+ compared to Li^+. This results in different reaction mechanisms and electrochemical performances relative to LIB's. A larger ion requires a greater intercalation space or more energy input than a smaller one to integrate a host structure.
An overview of the commercial and electrochemical characteristics of the two elements is given, highlighting the differences of the materials for large scale applications. Lithium's raw compound present in the Earth's crust is Li_2CO_3, while Sodium is mostly extracted from soda ash Na_2CO_3.

Table 1. Comparative overview of the available resources for Lithium vs Sodium [23]

Property	**Lithium (Li2CO3)**	**Sodium (Na2CO3)**
World Production (thousands of metric tons)	37 [23]	52,000 [23]
World reserves (thousands of metric tons)	13,000 [23]	24,000,000 [23]
World resources (thousands of metric tons)	39,500 [23]	>50,000,000 [23]
Price ($ton-1)	4500 [23]	155 [23]
Theoretical capacity (Metal) ($mAhg_{-1}$)	3829 [24]	1165 [25]
Electrochemical Potential E_0 (V *vs.* Li+/Li°)	0	0.3 [25]
Ionic Radius	0.76 Å	1.02 Å
Weight	6.9 g/mol	23 g/mol

Aside from the element abundance, the electrochemical properties from Sodium do not appear competitive, where SIB's will always have a lower energy density than their LIB counterparts. Na ions are 30% bigger and roughly three times heavier. Despite this, the mass of Li and Na cycling the battery is negligible compared to the host structures of the electrodes, resulting in a less consequential impact than originally anticipated. [26]. SIB's are also more stable even though Na metal are more reactive than Li [27]
Lastly, ionic diffusion was thought to be an issue considering the larger size of Na^+, yet Ceder et al reported both experimental and computational studies showing that extraction/insertion of Na^+ into Na-containing materials was faster than its Li counterpart [13]. This is declared by the lower Lewis acidity and interaction enthalpy of Na^+. Interactions of the Na^+ ions are weaker than for Li^+. Inversely, inserting Na^+ in a material not containing sodium will be harder than for Li^+.

After analysing the different properties of LIB's and SIB's, Ong et al. [28] drew interesting conclusions concerning the materials used to operate both cells. Aluminium can be used as current collector against Na metal for the sodium batteries, unlike their lithium counterpart which would corrode. Below a potential of 0.1 V vs. Li/Li^+, aluminium undergoes an alloying reaction with lithium, so it cannot be used as current collector in LIB's. This is not the case for sodium, so using aluminium as current collector is cost effective and beneficial for SIB's, as opposed to having to use copper in LIB's. Yet when assembling batteries, the issues remain very similar, such as cathode, anode, electrolyte and interface challenges. To conclude, SIB's represent the more viable option for large scale, low cost, efficient energy storage to support the sustainable energy transition.

2.3 Sodium Ion Battery Electrodes

2.3.1 Anode

Since the development advances of LIBs have been more advanced the last few years, parallels have been drawn, matching the sodium counterparts. Similarly to using lithium metal as anode for LIBs, safety issues have been observed when using sodium metal as anode. This is of concern for large scale production and operation of SIBs due to a rather low melting point of 98 °C of sodium metal [**29**]**.** As previously stated, the main characteristic that electrode active materials should have, is the ability to insert or extract alkali ions through intercalation or conversion reactions. For metal anodes, the process is plating and not intercalation or conversion. Advances in LIB technology inspired Sodium anode research, starting with graphite. With a high capacity of 372 mAhg-1, high stability and a low potential (<0.1 V *vs.* Li^+/Li°), [**30**], graphite seemed like a good alternative. At the time, organic electrolytes were widely used and Ethylene Carbonate (EC) decomposes on the carbon-based anode, forming a solid electrolyte interphase (SEI) [**31**] [**32**] Yet Sodium insertion in graphite is not efficient due to thermodynamic differences [**33**], largely explained by the larger ionic size of Na ions. Organic liquid electrolytes in combination with Hard Carbon were successfully reported by Prof. Dahn's group [**34**][**35**], also showing good reversibility**.** Hard carbon differs with graphite in its structure. Randomly stacked graphene sheets with nanopores allowed Na ions to intercalate from all angles. A theoretical capacity of 300mAhg-1 [**36**] was reported using pyrolysis as synthesis method with sugar. With a low insertion potential (*ca.* 0.005 V *vs.* Na^+/Na°) [**37**] [**38**] [**39**], Hard Carbon or nanoporous carbon present a viable option for high energy density SIB cells using a high potential cathode material. The main drawback of this anode material is that using a high current in such a cell would force Na plating, possibly making the cell unstable and unsuitable for fast charging applications.

Different alloying metals can be considered as anode materials, such as Silicon, Antimony or Tin. The main issues related to these alloying materials, is due to volume change. Upon full alkali ion insertion, the active material expands greatly [**40**] , resulting in mechanical strain and loss of mechanical integrity, thus reduced cyclability. The binder compound plays an important role here. Compensating the volume variations during cycling using an appropriate binder can alleviate the mechanical strains and improve cycling efficiency for the electrode. Typically, Polyvinylidene fluoride (PVDF) has been used as electrode binder, but recently Carboxyl methyl cellulose (CMC) has shown better performance retention [**41**] [**42**], and cheaper. On top of this, CMC is also better for the environment since it does not need NMP (N-methylpyrrolidone) solution to dissolve. Yet CMC dissolves in water, and water is not a welcome component is our batteries, as it reacts with the other compounds present.

2.3.2 Cathode

Aside from anode research for SIBs, cathode materials have been studied extensively **[43][44][45]**

The cathode is composed of the active material which is going to allow ions to reversibly insert into the active material framework of the cathode, a conductive material for improved electronic conductivity allowing electrons to travel inside the cathode to/from the current collector for electro-neutrality, and finally a binder is usually required to maintain the active material and conductive material in place, coping with the volume change upon cycling, providing additional mechanical strength to preserve the electrode intactness and contact. The additional conductive material is necessary since the active materials used are usually semiconductors or insulators, where carbon black or acetylene black are often used. Binder materials are usually polymers such as polytetrafluoroethylene (PTFE) or polyvinylidene fluoride (PVDF), while Carboxyl methyl cellulose (CMC) was reported to show increased cyclability compared to the standard PVDF through improved mechanical integrity during cycling and better capacity retention.[**46**]

The cathode side of the battery serves to take in the Na ions from the anode during battery discharge, through insertion mechanisms such as conversion or intercalation. The active material needs to be able to accept and release an alkali ion in order to have optimal performance, meaning high cyclability and energy transport efficiency. Otherwise, energy is lost in the process. Evidently, the material requires high capacity and mechanical and chemical endurance in order to repeat the charge/discharge process with numerous ion insertions. The cathode material usually has Na in its composition, providing the electrochemical cell with Na^+ charge carriers. This implies that the cell is usually assembled in a discharged state (cathode being “full” of intercalated Na ions), which are then extracted from the cathode at a potential above the resting potential, which translates to charging the battery. An important characteristic of sodiated transition metals (cathode full of intercalated sodium ions for example) can be extremely hygroscopic. This means assembly of the battery needs to be done meticulously and moisture-free, especially when surface contacts are so important. Dry conditions are often required when synthesizing, handling and assembling sodiated compounds, as hydration of the sodiated surface can lead to NaOH formation, a compound with insulating properties when used as a solid, impeding the electrode conductivity and performance.

The active materials used need to show minimal structural change during insertion to provide increased reversibility for cycle life. But change in the volume, structure and bond-strength of the material is bound to happen, especially since Na^+ has a relatively larger size than Li^+ (1.02 A for Na^+ ion against 0.76 A for Li^+ ion), while both have a Coordination Number of 6. Evidently, the larger ionic size also implies a larger insertion energy, slower diffusion kinetics and higher charge transfer resistance for Na^+ against Li^+, which can be verified through Density Functional Theory calculations. [**47**]

These cathode materials can be categorized into 2D and 3D intercalation materials, divided between various sodium oxides NaTMO2, polyanions such as fluorosulfates or phosphates, NASICON and organic compounds. Organic compounds generally receive less attention due to the success of their inorganic counterparts. An overview of the various components and advances in these materials can be seen in Figure 3.

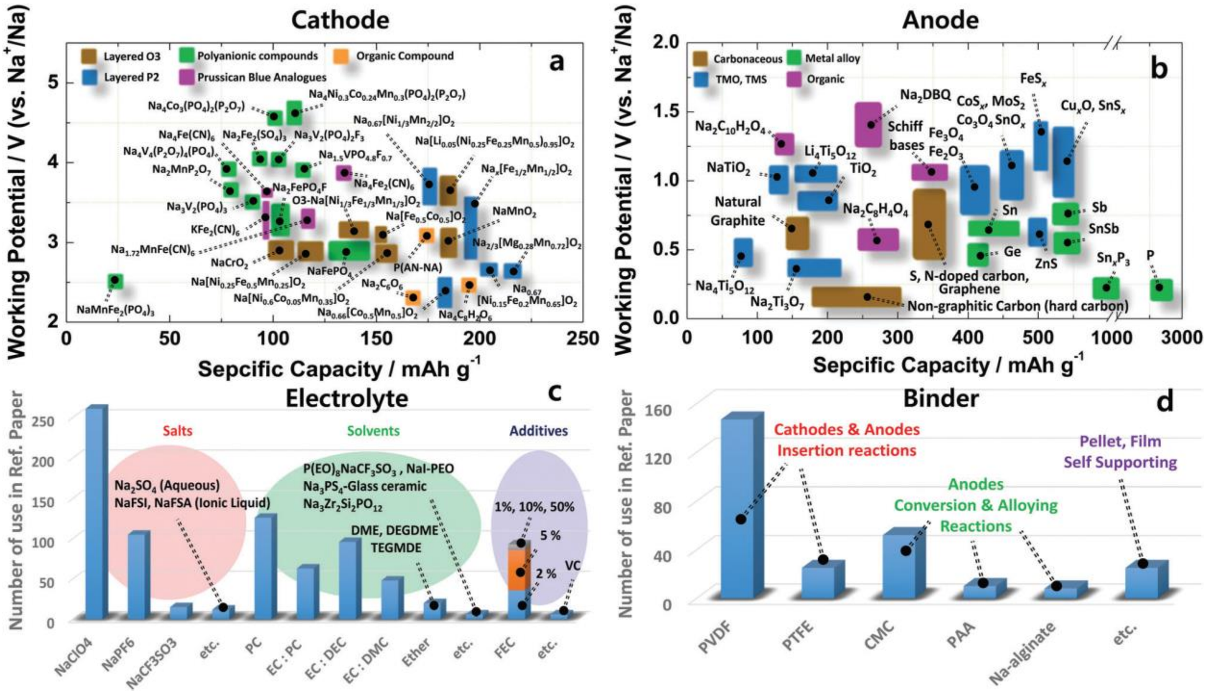

Figure 3. Overview of the advances in prominent cathode, anode, electrolyte and binder materials [13]

2.3.2.1 Layered oxides

Concerning cathode active materials, many similarities can be found concerning layered oxides as active materials for electrochemical cells. With interchangeable transition metals, NaxTMO2 share many properties and synthesis methods with their Lithium counterparts. With growing interest in Sodium materials recently, this facilitates further research into the Sodium layered oxides. Looking at the diffusion barrier and mechanical strength for Na and Li ions in cobalt oxides, Ceder et.al. showed that Sodium ions are actually favourable to Lithium due to weaker bonds formed between Sodium and oxygen compared to Lithium with oxygen, as well as formation energy for Li_2O being higher than for Na_2O, despite the same crystal [48]

These two-dimensional materials are composed of stacks of octahedral MO6 crystal structures with Na that can be inserted into the interlayers. Two main types of structure can be distinguished based on coordination with inserted ion, as per the notation of Delmas et.al. [49]. The prismatic and octahedral coordination, and particularly P2 and O3, have shown promising electrochemical properties for Na insertion materials. Despite showing relatively high capacity of 200mAh/g [50], P2-type crystal structure does not remain stable above a 2/3 Na insertion, limiting the capacity. [51]

2.3.2.2 Moisture-free layered oxide

Since Sodium and sodiated transition metals are often hygroscopic, side reactions are not easily prevented. But substituting transition metals in layered sodium oxides reveals remarkable properties. Lu and Dahn et.al. reported P2-$Na_{2/3}[Ni_{1/3}Mn_{2/3}]O_2$, a compound stable in moist air, where hydration does not occur **[52]**,**[53]** All similar compounds containing Na and Mn are relatively cost-effective due to their abundance, and their stability in air makes them candidates for large scale applications. P2-$Na_{2/3}[Ni_{1/3}Mn_{2/3}]O_2$, shows an average potential of 3.5V with a theoretical capacity of 173 mAh/g, provided by the $Ni^{2+/4+}$ redox reaction in the voltage range of 2-4.5V. In situ XRD revealed that the P2-O2 phase transition at the 4.2V plateau results from the oxygen shift in the crystal layers **[54]**, a transition which is not observed in similar Manganese-based oxides such as P2-$Na_{0.67}MnO_2$, where the Jahn-Teller distortion Mn^{3+} prevents the P2-O2 transition. This also indicates that substituting transition metals allows fine tuning of the desired properties for battery active materials. The transition from P2 to O2 phase at 4.2V is accompanied by a large volume change, therefore diminishing the cyclability. This phase transition is not desirable and is ideally prevented from occurring. The different phases P2 and O2 can be observed in Figure 4.

Besides the large volume change, the octahedral and prismatic phases have different conductivities, related to their diffusion energies. For the octahedral phase O2, Na^+ ions have to cross the tetrahedron between two octahedral sites using a vacancy mechanism **[55]**, requiring an energy of 290meV. For the prismatic phase P2, the Na^+ ions can diffuse through the shared faces of Na prismatic sites, requiring only 170meV. Naturally, the mechanism requiring lowest diffusion energy shows faster Na^+ mobility. This is validated by a larger diffusion path in P2 phase compared to O2, leading to lower activation barrier. Cycling this cathode material in a voltage window preventing phase transformation to O2 above 4.2V (2.3V-4.1V) indicates excellent cycling behaviour, even though capacity is lower.

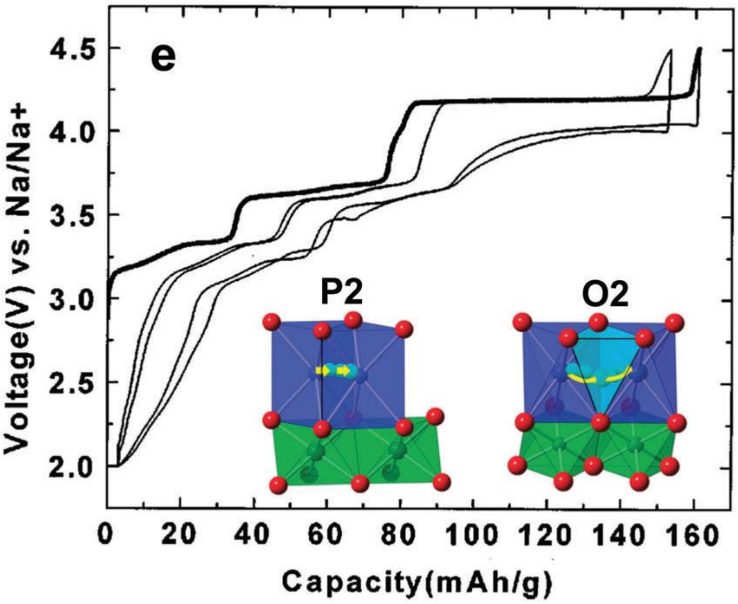

Figure 4. Charge and discharge curves of P2-$Na_{2/3}[Ni_{1/3}Mn_{2/3}]O_2$ **[52]**, in which the inset represents the ionic diffusion paths in P2 crystal structure (left) and O2 (right), illustrating why P2 diffusion path is favourable **[54]**

As mentioned before, substituting transition metals can change crystal properties, such as preventing phase transformation or diminish side-reactions. Using Mg^{2+} and Zn^{2+} instead of Ni is effective for diluting the effect of the above-mentioned P2–O2 phase transition.[**56**][**57**][**58**]
Capacity drop after the first cycle can often be declared through electro-active species (in this case Ni^{2+}) being reduced to compensate for Na^+ extraction. Substituting Ni by Mg in $Na_{2/3}[Ni_{1/3}Mn_{2/3}]O_2$ results in a reduction in capacity drop in $Na_{0.67}[Ni_{0.2}Mg_{0.1}Mn_{0.7}]O_2$ of only 6mAh/g after 50 cycles. [**56**]

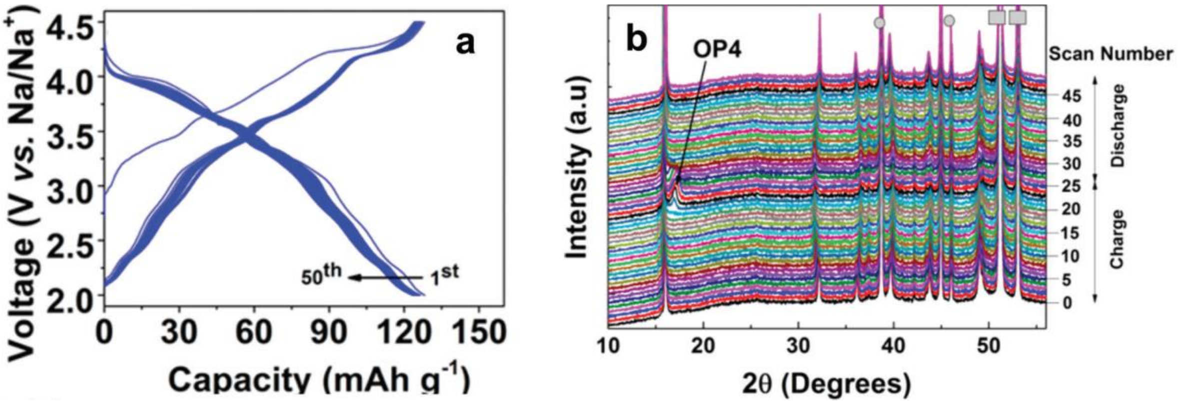

Figure 5. (a) Charge and discharge curves of P2-$Na_{0.67}[Mg_{0.1}Ni_{0.2}Mn_{0.7}]O_2$
(b) in situ powder X-ray diffraction of P2-$Na_{0.67}[Mg_{0.1}Ni_{0.2}Mn_{0.7}]O_2$ showing the reversible evolution of P2–OP4 phase transition at the end of the charge and beginning of the discharge. [**56**]

In trying to uncover the reason for this, in situ XRD identified OP4, a new phase above 4.2V (instead of transitioning directly to O2). This is illustrated in Figure 5. Using Mg^{2+} in the transition metal layers (Mg being electrochemically inactive) provides stabilization of the overall charge balance in the crystal. Extraction of Na+ from the host structure in the prismatic sites is then less straining for the structure, as the ions are not taken from the host structure but assisted by the introduced Mg^{2+} in transition layers. This substitution suppresses the $Na^{+/}$vacancy ordering and P2-O2 transition, leaving P2 as major phase and generating the highly reversible OP4 as minor phase at high voltage when the material is deeply desodiated. [52]

2.3.2.3 3D polyanionic structure

Aside from layered 2D structures, 3D polyanionic structures are also investigated, as their framework is well suited for particle insertion [**59**]. Having an open framework facilitates insertion and extraction of Na+ ions in the crystal structure. Diffusing in x,y and z directions allows fast migration of ions within the crystal, especially relative to two-dimensional compounds such as layered oxides. Considering that Na+ has a larger ionic size than Li+, it is also required for the 3D structures to be sufficiently rigid or be designed with larger pathways. Polyanion compounds are also favourable to oxides when addressing thermal stability, attributed to the presence of the covalent Phosphate-Oxygen bonds in the crystal

structure [**60**]. The same covalent bond suppresses oxygen evolution when batteries are operated above 200 °C [**61**]
Similarly to many layered oxide compounds, polyanionic systems suffer from moisture absorption resulting in NaOH formation. As explained previously, this compound impedes conductivity, unfavourable for battery usage. In order to prevent caustic soda formation, great care in moisture free synthesis and assembly needs to be taken.

2.3.2.4 NASICON (vanadium based)

Finally, NASICON (Na Super Ionic CONductor) structure NaxV2(PO4)3 is a vanadium based material exhibiting high electrochemical performance. Originally synthesised by Delmas et.al. [**62**], this compound can fulfil the roles of both cathode and electrolyte material. The 3D framework was originally thought to be of use as a solid electrolyte due to it high Na+ ionic conductivity [**63**] [**64**]**,** yet incorporating transition metals in the structure allows the compound to be used as electrode. Modifying the surface of $Na_3V_2(PO_4)_3$ with carbons resulted in improved capacity at both sides of the electrochemical window.
NASICON shows two plateaus at 1.6V and 3.4V vs $Na^+/Na°$, respectively reflecting the V^{3+}/V^{2+} and V^{4+}/V^{3+} redox reactions.

Prolonged cyclability and a capacity of 117 mAh/g have been reported [**65**]

Concerning moisture sensitivity, NASICON itself is not sensitive to moisture, but its precursors need to be carefully dried before synthesis in order not to interfere with the reactions [**66**]

2.4 Electrolytes

Whether concerning LIBs or SIBs, the electrolyte inside a battery has an essential role. The electrolyte facilitates cationic transport between the two electrodes during cycling of the battery. Important features inherent to satisfactory electrolytes are chemical and electrochemical stability, thermal stability, a high ionic conductivity (above 1 mS/cm for ionic transport and satisfactory rate capability) combined with electronic insulation and low production costs and toxicity.[**67**] [**68**] High performance batteries require a suitable electrolyte, as this compound also needs to protect both anode and cathode, possibly forming a solid electrolyte interface (SEI).
An appropriate electrolyte also shows minimal interface reaction as well as high performance and inherent safety. This is rather central in today's society seeing as battery combustion has been in the news recently. Compared to electrodes and LIBs in general, research concerning SIB electrolytes is rather scarce**.** [**69.**] This makes research towards performant SIB electrolytes important seeing as large-scale SIB production is predicted to take over LIBs due to sodium cost-effectiveness and geographical distribution. [**70**]

Various electrolytes have been developed over the years, varying from liquid organic electrolyte solutions, polymer electrolytes, inorganic or ceramic electrolytes and ionic liquids with salt additives. **[71]**

The conduction mechanism can be described by different equations, depending on the substance and measured parameter. Since the activation energy is relevant for ionic transfer in battery systems **[72] [73]**, the Arrhenius equation (Eq. 3) describes conductivity as:

$$\sigma = \sigma_0 \exp\left(-\frac{E_a}{k_B * \mathrm{T}}\right) \qquad \textbf{(Eq. 3)}$$

Where σ_0 is the ideal conductivity for infinite T (also called pre-exponential factor), E_a is the activation energy, k_B the Boltzmann constant, and T the temperature.

Keeping in mind that this study has been done for Room Temperature applications, the Arrhenius equation also illustrates that conductivity is lower at Room Temperature than for more performant batteries operating at higher temperatures, making high conductivity electrolytes more challenging.

Experimentally, the electrochemical cell does not only take into account the various chemical compounds and interactions, but also morphology (contact points showing high resistivity vs smooth contacts where ionic and electronic flow is facilitated) and distance between the electrodes (longer distance to travel is more energy costly than a shorter distance). To this end, the conductivity in batteries can also be described on a macroscopic scale. The resistance (Eq. 4) in inversely proportional to the conductivity, and can be written as:

$$\mathrm{R} = \frac{\mathrm{l} * \rho}{\mathrm{A}} \qquad \textbf{(Eq. 4)}$$

Where the resistance R is expressed as the distance between the two electrodes l, the resistivity ρ and the cross-sectional area of the sample A. It is interesting to note that the first hurdle of solid-state batteries is illustrated in this formula. Using solid ceramic particles for example, contact between particles is minimal (unless further processed by sintering at high temperatures or mechanical pressing for example). Point contacts result in conductivity much worse than initially reported for bulk conductivities.

The conductivity, σ is the reciprocal of the resistivity (Eq. 5).

$$\sigma = 1/\rho = \mathrm{C}/\mathrm{R} \qquad \textbf{(Eq.5)}$$

2.4.1 Organic Solvent based Electrolytes

For organic liquid electrolytes in SIBs, the idea is to dissolve a sodium salt in one or a mixture of organic solvents. Organic solvents are used due to their large dielectric constant (ε) allowing easy dissolution of Na salt and larger Na^+ ion concentration in the solution **[74].** An overview of the most popular organic solvents is shown in Illustration 1.

In order to optimize the conductivity of the solution, the dissolution of the sodium salt (the degree of ionic dissociation), and thus the interaction strength between cation and anion must be carefully studied. Simply put, the interaction between the ions is inversely proportional to the dielectric constant. A higher ε solvent leads to a higher dissociation and conductivity. This has been proven experimentally by Barthel et.al. [**75**], who showed that decreasing the ion-ion interaction by 14% increased the conductivity by 440%.

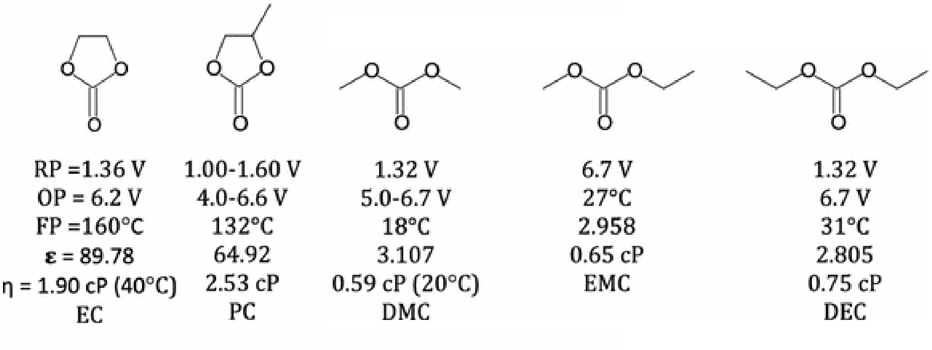

Illustration 1. Overview of the popular organic electrolytes and relevant properties relating to dissolution of additional salts and overall battery operation. RP being the reduction potential, OP the oxidation potentials, FP the flash point, ε the dielectric constant at 25°C, and finally η the viscosity at 25°C [**76**]

The various issues that aprotic (compounds that cannot donate protons) organic solvents present have been extensively researched and documented, flammability being one of them. [**77**],[**78**], [**79**]

Ironically, the high permittivity necessary for organic electrolyte solvents combined with the high salt concentration to provide satisfactory ionic conductivity results in a large potential gradient near the electrode-electrolyte. This large potential difference can give rise to a continuous electrolyte degradation after assembly with either electrode. [**80**] Yet batteries are often engineered to form a good passivation layer.

For SIBs, propylene carbonate (PC) and Ethylene carbonate (EC) are popular solvents. PC has a high dielectric constant and thermal stability but interacts with electrodes such as graphene [**81**] creating undesired structure modifications in the electrodes. PC also continuously corrode Na metal anodes, which pushed research towards new compromises. EC on the other hand assists in creating a protective passivating surface layer, a solid electrolyte interphase (SEI), but cannot be used as a single electrolyte solvent due to its melting point at 36°C. This also brings a high viscosity, which also lowers the conductivity. All this has led to a large variety of solvent mixtures with various dielectric constants, melting points and structural differences to dissolve specific salts: cyclic structures such as EC and PC having high dielectric constants versus linear structures such as Dimethyl Carbonate (DMC) or diethyl carbonate (DEC) with inherently lower dielectric constants, but also lower melting points.

Popular SIB salts used to dissolve in solvents are $NaClO4$, NaTFSI or $NaPF_6$ [**82**] [**83**], due to their thermal stability, viscosities and electrochemical stability. 1 M of $NaClO4$ in EC:DEC or

EC:PC showed excellent performances compared to other combinations of solvents in terms of conductivity **[84]**

As previously mentioned, the high reactivity with organic solvents as well as high volatility and potential leakage present safety issues and possible dendrite formation at the electrode-electrolyte interface during sodium deposition while cycling. This is also relevant for Room Temperature (RT) batteries due to the unstable formation of passivation layer using organic electrolytes.

2.4.2 Solid State Electrolytes

Liquid electrolyte issues triggered further investigation into solid state electrolytes due to their inherent safety (not flammable and suppressing dendrite) as well as not needing an additional separator (necessary for liquid electrolytes) and packaging **[85].** Conductive ceramics, polymers and polymer composites have all been considered as potential solid-state electrolytes **[86][87].** Solid state electrolytes also show promising applications for micro-electronics, as solid-state batteries can be modulated in different shapes to fit specific needs, as well as higher efficiencies and energy density. Wider electrochemical stability window can also be achieved with solid state electrolytes for increased energy density **[88]** **[89]** as well as thinner SEI passivation layers for longer cycle-life.

One of the earliest and most researched solid-state electrolytes is Na-β”-Al_2O_3, Na-Beta”-alumina (NBA). This highly conducting sodium electrolyte was found based on the Na-β-Al_2O_3 and the NASICON structures **[90]** **[91].** This compound is composed of layers of Al_2O_3 with intercalated Na_2O, (Na2O)1+*x* · 11Al_2O_3, where *x* ranges from 0.25 to 0.55. These layers serve as tunnels for sodium ions to hop through, conducting Na^+ ions from one electrode to the other. The micro-technology applications, high thermal stability, wide electrochemical window (>5 V), high bulk ionic conductivity ($>10^{-4}$ S cm^{-1}), low risk of leakage and a cation transference number close to unity makes Na-beta”-alumina a great Na solid electrolyte candidate**.** **[92]** **[93]** **[94].**

When synthesized, two versions of this crystalline structure are present, Na-β-alumina and Na-β″-alumina. The difference between the two resides in different layer stacking, as shown in Illustration 2**.** The two variations also have different chemical compositions, namely β-$Na_2O{\cdot}11Al_2O_3$ ($NaAl_{11}O_{17}$) and β″-$Na_2O{\cdot}5Al_2O_3$. ($NaAl_5O_8$).**[95][96][97]**
Na-β-alumina has a hexagonal structure with space group *P*63/*mmc*, while Na-β″-alumina has a rhombohedral with a space group *R*-3*m*. They are both stacked up by spinel blocks consisting of [AlO_4] tetrahedrals and [AlO_6] octahedrals. All the neighbouring alumina spinel blocks are bonded by an oxygen ion with surrounding mobile Na+, forming the conduction planes capable of transporting Na^+ ions.
Intuitively, the chemical formula also shows why the Na-β″-alumina phase if favoured for conductivity purposes. For every two sodium positions, the β phase has 11 alumina while the β″ only requires 5. Effectively, Na-β″-alumina phase has two mobile Na+ ions in its conduction phase while Na-β-alumina phase has only one. On top of that, the connecting

oxygen ion should also be considered. The weaker electrostatic force between the oxygen ion with surrounding Na+ ions relative to the β phase facilitates Na+ movement, resulting in a higher ionic conductivity in the β″ crystal.
Compounds such as Li_2O, MgO, TiO_2, ZrO_2 and Y_2O_3 promote Na-β"-alumina formation during synthesis, suppressing the Na-β'-alumina phase. [98] [99]

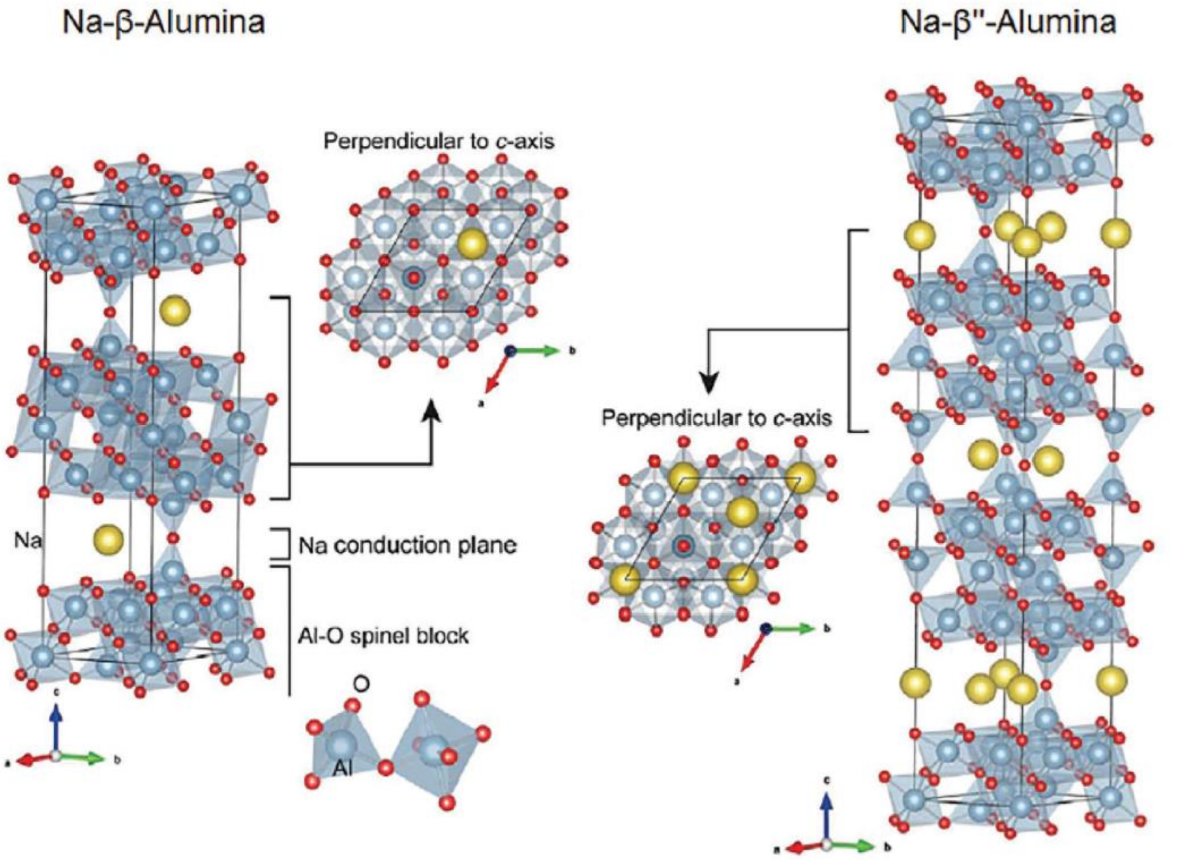

Illustration 2. Crystal structure illustrating the difference between the unit cell of Na-β-Al_2O_3 and Na-β"-Al_2O_3

The main drawback of Na-beta"-alumina is its high interfacial resistance. Even though bulk (single crystal) conductivity is very high, the practical assembly of a cell using NBA means using small solid electrolyte particles with additional treatment to make a dense pellet (mechanical pressing or sintering at 1600degrees). Without satisfactory pellet density, assembly leads to point contacts in the battery instead of a dense pellet, as well as poor contact between the solid electrodes and solid electrolyte [**100**]. Ultimately, this would result in a battery with poor electrolyte conductivity and poor interfacial contacts. Promising attempts to reduce the interfacial impedance have been made, avoiding the high energy cost of sintering at high temperature. [**101**]

NBA has been applied in the Na-S battery for 300 °C applications with compounds liquid at that temperature to insure good contact. This battery contains molten sulphur, molten sodium and highly corrosive polysulfides, potentially forming toxic H_2S gas. Naturally, a resistant container is needed for such an electrochemical system. Even though this concept was a reliable candidate for automotive applications for a long time [102], the inherent cracking possibility leading to cell failure as well as propagation of the corrosive materials cannot be permitted in automotive vehicles prone to shocks. [103]

2.4.3 Ionic Liquid based electrolytes

Ionic liquids (ILs) containing a fraction of salt have been proposed as a viable alternative to organic solvents for LIBs and SIBs, as they do not share their flammable and volatile properties, presenting an improvement concerning the safety factor [104] [105][106]. Room temperature ILs need to be highlighted, as they have been extensively studied for ambient temperature applications. [106] [107] [108]
Aside from being non-flammable, ILS also show high thermal and electrochemical stability. Even though these compounds are a promising alternative to flammable organic solvents, research is still in an early stage [109][110] and ILs present other drawbacks such as a high energy consumption and cost of synthesis, and often have synthesis waste that are not environmentally friendly. For example, BMImBF4 requires 30 steps to be synthesized as well as hydrogen fluoride waste [111]. Depending on the application, ILs need to be either highly conductive or electrochemically stable. For batteries, both are needed. A good example is Triethylsulphonium bis(trifluoromethylsulfonyl)imide with a reported conductivity of 8.2mS/cm and an electrochemical stability window of 5.5V [112]

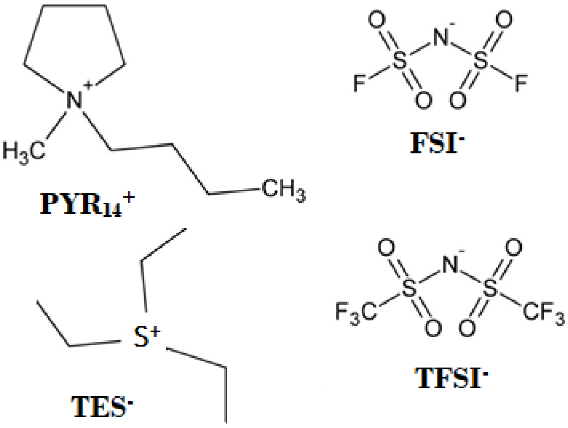

Illustration 3. Ionic liquids used in our project, without salt previously dissolved.

Ionic liquids can be used to dissolve salts in order to increase the conductivity and facilitate ionic transport. For RT applications, pyrrolidinium and imidazolium are used to dissolve NaFSI or TFSI [113], reporting conductivities up to 3.2mS/cm at 298K, with an anodic electrochemical stability window of 5.2V vs Na^+/Na^0. Further research showed the anion FSI having a higher oxidation potential limit [114] [115] Reports have even shown that ionic liquids with dissolved salts can even outperform organic electrolyte solutions due to a stable SEI formation. [116] [117]

2.5 Electrolyte/Electrode Interfaces

Whether for Na^+ or Li^+, ions have to travel through the interface between the electrodes and electrolyte. The electrode-electrolyte interface for solid-state batteries can present issues for high-rate performance **[85]** **[118]** **[119][120].** This can be a bottleneck and has to be optimized in order not to limit ionic diffusion. Concerning solid state electrolytes, the poor ionic diffusion through the electrode-electrolyte interface was suggested to be caused by small contact area for charge transfer **[121]** **[122]**, decomposition products at the interface with low conductivity and possible space-charge layer effects due to layers causing charge redistribution at the interface varying from the nanometre to micrometre order. **[123]**

2.5.1 The Solid Electrolyte Interphase (SEI)

Aside from improving the electrode material structures and electrolyte conductivity, the interfaces need to be studied for high performing SIBs and LIBs. Side reactions at these interfaces are quite common and can cause deficient battery function, low capacities and coulombic efficiencies. On the other hand, these side reactions can be harnessed to extend the theoretical limits of the electrochemical windows (ESW) by creating passivating layers at the interfaces. The thermodynamic limits of the ESW are usually characterized by the LUMO (Lowest Unoccupied Molecular Orbital) and HOMO (Highest Occupied Molecular Orbital) of the electrolyte. In order to avoid electrolyte decomposition by reducing the electrolyte on the anode side or oxidize the electrolyte on the cathode side, care must be taken to find materials with fitting chemical potentials μ_{Anode} and $\mu_{Cathode}$ as shown in Illustration 4**.** A passivating interphase can extend these limits in order to increase the electrochemical operation window of the electrolyte. This can manifest itself as a solid electrolyte interface (SEI).

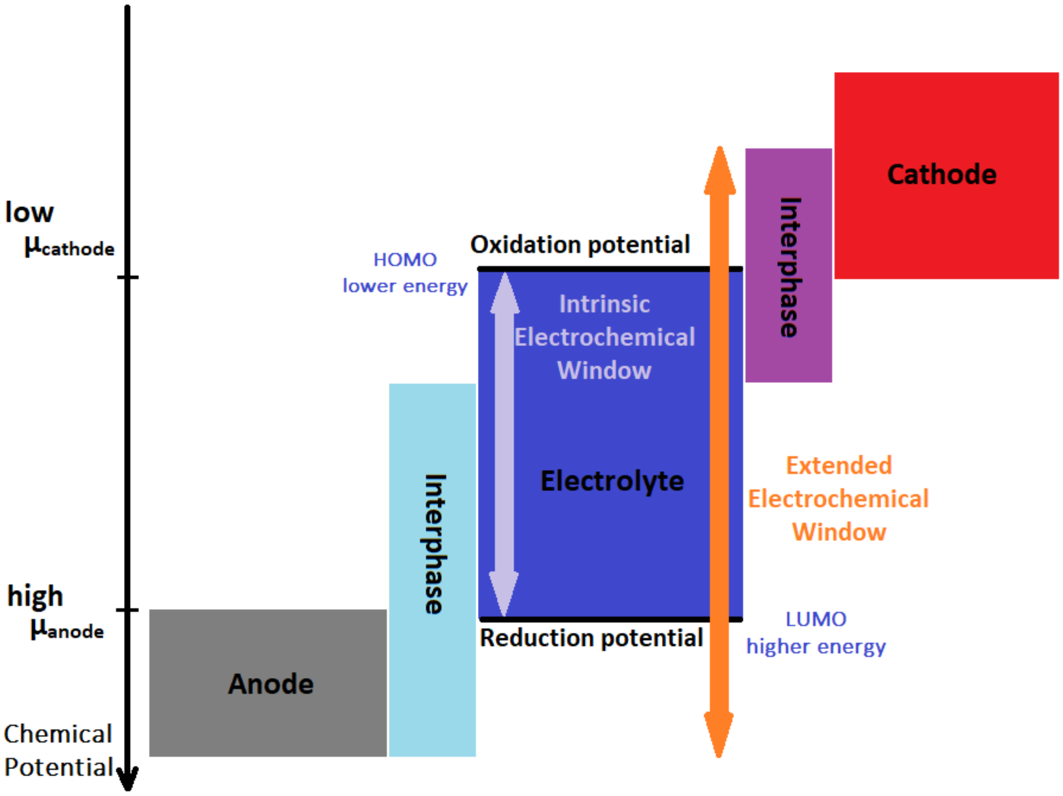

Illustration 4. Electrochemical system illustrating the relationship between electrochemical potentials of electrodes and the HOMO or LUMO of the electrolyte, as well as the possibility of forming passivating interphases to extend the electrochemical window.

The solid electrolyte interphase is a protective passivation layer resulting from the electrolyte decomposition (or dissolved salt decomposition) at the anode during the first cycles of the battery. This can have insulating effects negating charge transport but can also be harnessed for positive results. For an ideal SEI formation, the anode surface in contact with the electrolyte reacts during anode reduction to form a permeable layer for charge carriers to move through, while simultaneously preventing further electrolyte reduction and conserve electrolyte qualities such as electronic insulation [124]. The SEI usually takes several cycles to stabilize, which is noticeable from the charge/discharge patterns and capacity when cycling batteries.

Naturally, understanding the layer formation is essential to a high performing battery, especially since forming a good SEI is dependent on various factors, explaining why a lot of studies have been conducted on the matter [125] [85].
Relatively little study has been reported for SEI formation for SIBs, but with increasing interest in Sodium based batteries, trends concerning SEI are starting to be unravelled. [126] [127] [128]

Unlike for cathode materials, parallels between SIBs and LIBs are harder to draw for SEI formation. Similar compounds can be found at the interphase for SIBs and LIBs, but in different proportions. Using Hard Carbon as anode insertion material against $NaNi_{0.5}Mn_{0.5}O_2$, studies of $NaClO_4$ salt dissolved in PC versus $LiClO_4$ have been conducted for comparison in morphology [**129**]. The interest here, is to observe the different behaviour at the interphase using the same system, but with two different intercalant alkali elements. SEM revealed a more uneven distribution of SEI particle formation for $NaClO_4$ salt than for $LiClO_4$, while XPS and mass spectroscopy showed that the passivation layer had a different composition and thickness. For the XPS analysis, the sp2 peak became better defined and more intense in the C 1s spectra, which points towards a thinner surface layer in the Na cell than the Li cell. Mass spectroscopy also indicated that the Li cell presented a mostly organic layer formation, while the Na cell had an SEI composed of inorganic compounds. It can also be pointed out that $LiClO_4$ in PC presents a higher stability than for $NaClO_4$ [**130**]**.** This may be related to the variation in ionic size, cationic solvation, reactivity, solubility and so on.

In an electrochemical cell, the cathode material requires a high insertion potential in order to store the most energy possible. Yet this demands an electrolyte with a suitable oxidation potential. Using an electrolyte with a lower oxidation potential than the cathode insertion potential can lead to electrolyte decomposition. Thus, developing methods to negate or minimize the decomposition or to stabilize EISs is crucial towards high performance SIBs and LIBs.

2.5.2 Space charges in solid-state batteries

Another interesting material interaction to be considered at the interphase is the space charge effect. It relates to the chemical potential difference of the compounds and affects the electric properties of the battery materials.

This phenomenon can be illustrated as followed. Two materials with atoms in a set space (such as crystal structures in solid state batteries) and different chemical potentials come in contact. With different potentials (in open circuit conditions), the particles in the material with lowest potential will experience a drive towards the higher potential material to seek equilibrium. Yet if only ions can move, an energy gap occurs at the interphase, called space charge. The space charge layer forms at the two-phase boundary to keep the thermodynamic equilibrium. This leads to absorption of ions from one compound to the other, creating additional defects until the repulsive electric field from charge accumulation balances out the higher chemical potential, making the system reach equilibrium.

When describing the process, thickness is the first factor that comes to mind. The depth of ion extraction from one material for the other, as well as the ionic concentration that ensues are central to space-charge description and modelling. Space charge layers have a thickness varying from the nanometre to micrometre order, depending on the material properties such as potential difference, ionic concentrations, interfacial contacts, surface area, but also electric permittivity [**131**].
The thickness of this layer is highly relevant, since compounds with higher permittivity lead to thinner space-charge layers at the interphase, resulting in a lower interfacial resistance.

The thickness also depends on the concentration of free charge carriers and the potential difference between the two materials.

Reports have shown the beneficial effect of space charge on ionic diffusion in solid electrolytes [**132**] as well as in SEI layers [**133**]**.**
Since the intrinsic property of space-charge describes a charge carrier redistribution between two phases, it can naturally also have a negative effect on conductivity and overall performance of the batteries by increasing the resistance [**134**] [**135**]

The root of the phenomenon is based in the mechanism of ionic diffusion, whether with vacancies or interstitial defects. When two materials with large potential difference are in contact, this results in a greater attraction for the alkali ions, subsequently generating more vacancies and making a thicker space-charge layer of the solid electrolyte (where ions are drawn from). If the major carrier of the solid electrolyte is vacancy defects, the ionic conductivity will increase as a result of the ionic migration. But if the major carrier is interstitial defects, the high potential electrode will attract ions from the solid electrolyte, ions are depleted at the interface, decreasing the conductivity. [**136**]

Electrons from the electrode mixture can eliminate the interstitial ions near the boundary, increasing the space charge layer near the oxide boundary side. Since the interface ionic transport properties are determined by the interstitial ions, this carrier redistribution can increase the interfacial resistance, thus increasing the polarization and decrease the rate capabilities of the overall system. This phenomenon was verified experimentally [**137**]

In order to reduce the polarization, the potential difference between the materials must be eliminated by introducing an ionically conductive compound with limited electron concentration. This prevents ion transfer in the intermediate layer, limits the depletion layer and consequently decreases the interfacial resistance. Reports have shown that by coating a non-sintered highly conducting solid oxide with a poorly conducing solid oxide could suppress the grain boundary resistance. [**138**]
Thus, depending on the potentials at the boundary, ionic transport can occur. For highly conducting solid electrolytes, the ionic transfer at the interphase is greater, resulting in a more severe effect since the main charge carriers are not vacancies but interstitials [**139**][**140**][**141**] This interstitial transport mechanism is also dominant in our solid electrolyte Na-beta-alumina, a compound not affected by oxygen partial pressure [**142**]. The ionic transfer between such solid oxide electrolytes and high potential electrode leads to charge carrier depletion in the electrolyte at the interphase, increasing the interfacial resistance. This is why research into space charge layers is relevant, as it can lead to a decrease in the grain boundary resistance, thus increasing the interfacial conductivity.

Space charge behaviour research for solid oxide electrolyte and solid oxide active material is still in its infancy, especially due to the difficulty to measure and model the phenomenon (simulating varying Coulombic interactions between the created defects in and around the space charge layer) and may be one of the key issues for all-solid-state batteries.

3. Characterization techniques and methods

In order to identify and characterize the chemical compounds and battery behaviour, characterization techniques are required. The tools and methods used are described in this chapter. The structural information regarding crystals as well as atomic displacements present in the electrochemical cells are unravelled using powder X-Ray diffraction (XRD). The electrochemical behaviour of assembled batteries is also investigated by cycling the batteries, as well as using Electrochemical Impedance Spectroscopy (EIS) to probe kinetics and electric properties.

3. 1 Powder X-Ray diffraction

Powder X-Ray diffraction (XRD) has been a useful tool to investigate the various atomic positions and crystalline structures encountered during this research on solid-state batteries. The X-Ray electromagnetic waves have a wavelength the order of magnitude of an Angstrom (10^{-10} m or 1 Å), a property that both atomic sizes and interplanar distances share. With the X-rays scattering off the crystalline periodic structure, this provides an explanation on why XRD is used for crystalline structure unravelling. Secondly, X-rays scatter off electrons, with each atom possessing its own electron density. From this, the chemical composition of the crystalline material can be distinguished.

When using powder X-Ray Diffraction (with solid compounds), the (nearly monochromatic) X-Rays aimed at the material scatter in direction distinctive to a specific crystalline structure and atomic composition, received by a detector indicating the intensity of the scattered wave. The resulting diffraction pattern can be solved using an expected structure (initial guess), and the structural parameters are refined to match the measured data using the iterative Rietveld refinement method to find the three-dimensional structure.

When testing air-sensitive compounds, the samples are sealed in a specially designed Kapton covered air-tight sample holder, allowing the electromagnetic waves to go through the Kapton cover and still uncover the powder composition.

3.1.1 Bragg's law for X-Ray Diffraction

Powders are often composed of one or more crystalline compounds. The different structures are called crystalline phases. Phases are divided into seven different lattice systems (Illustration 5) indicating the symmetry of the crystal cell (the shape of the crystal unit cell, simplest being the cubic system with most symmetry axes), sub-divided into 14 Bravais lattices due to variations considering base-centred, face-centred and body-centred lattice points, further categorized into 230 space groups (dependent on atomic placement within the crystal lattices) to index every structure present in a sample.

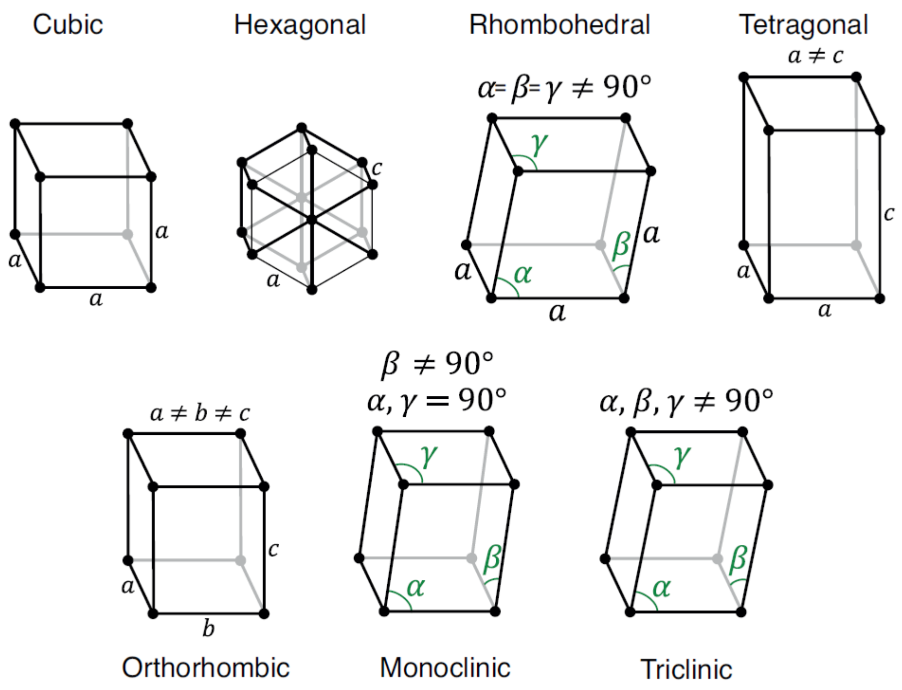

Illustration 5. The seven crystal lattice systems. These are the primitive lattices (lattice points on the corners of the cell), while the 14 Bravais lattices result from additionally characterizing body-centred, face-centred and base-centred lattice points

Since crystals are composed of repetitive structures with defined symmetries, different planes within the unit cells arise. These planes are described by Miller indices (*hkl*), illustrating all the different directions scattering planes can take. Naturally, all planes with identical Miller indices are parallel to one another with a distance d_{hkl}. As such, X-Ray scattering off of parallel planes results in constructive interference at a certain angle, yielding a specific diffraction peak. This is defined as Bragg's law, shown in Illustration 6.

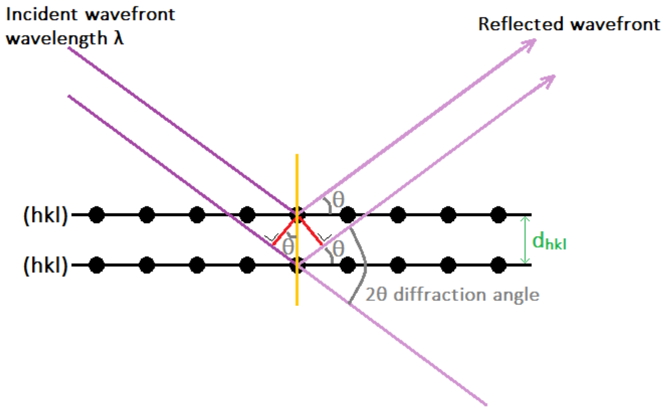

Illustration 6. Illustration of Bragg's law showing wavefront behaviour against a crystal structure. Incident X-Ray beams are hitting atoms on two separate crystal planes, consequently scattered and received by a detector. The distance d_{hkl} indicates the distance between lattice planes, θ the X-Ray scattering angle and λ the wavelength of the incident X-rays.

Constructive interference occurs only when the conditions for Bragg's law are met. θ is the incident scattering angle. Bragg's law shows the following: the path length difference of two incident waves scattering off two parallel planes is equal to an integer of the original wavelength [**143**], according to:

$$2d_{hkl} \cdot \sin(\theta_{hkl}) = n\,\lambda \qquad \textbf{(Eq. 6)}$$

As opposed to constructive wave interference, destructive interference cancels out the scattered wave. This yields high detector counts for the constructively scattered angle, resulting in a diffraction peak corresponding to a specific plane. Every peak is related to a set of parallel planes, corresponding to a set of Miller indices. Gathering the peaks gives information about the crystalline structure (sets of parallel planes) and chemical composition.

When collecting the XRD measurements, peak broadening can be observed. This is a result of Bragg's law being based on an ideal case, while experimental factors also interfere. First of all, the incident XRD wave is not truly monochromatic resulting in a statistical distribution of the peak values instead of an ideal delta-shaped peak. Background interference in the XRD measurement can also arise due to detector noise or amorphous materials, unable to produce sharp XRD peaks. Finally, the most interesting broadening effect present in XRD is sample broadening, the result of the physical qualities of the sample. The size variation of the crystalline powder particles results in a size (symmetric) broadening effect, while crystal lattice strain shows strain (asymmetric) broadening.

3.1.2 Size and Strain Broadening from Rietveld Refinement

Peak broadening is a symptom of size and strain broadening. Bragg's law holds for an ideal case, considering a material with a practically infinite number of lattice planes. This would result in peaks appearing at the true Bragg angle. But when reducing particle size, the number of scattering planes is also smaller, meaning that reflections at angles slightly off the true scattering angle are not cancelled out. This in turn yields a distribution of angles around the true Bragg angle resulting in peak broadening. Based on the observed peak broadening, particle size can be determined.

After refining the XRD spectrum to fit the experimental data to the known database, grain size (Eq.7) can be determined using:

$$D = \frac{18000 * K * \lambda}{\pi\,(Lx - 3.168)} \qquad \textbf{(Eq. 7)}$$

And the integration of this formula yields the error bar (Eq. 8), indicating the window of error:

$$\Delta D = \frac{18000 * K * \lambda}{\pi} * \frac{\Delta \mathrm{Lx}}{(Lx - 3.168)^2} \qquad \textbf{(Eq. 8)}$$

Using the isotropic $\mathbf{L_X}$ (Lorentzian isotropic crystallite size broadening) profile term;

where K = Scherrer constant (typically ~ 1), π = 3.1416 and size units are in Angstroms (Å), same units as wavelength (λ).

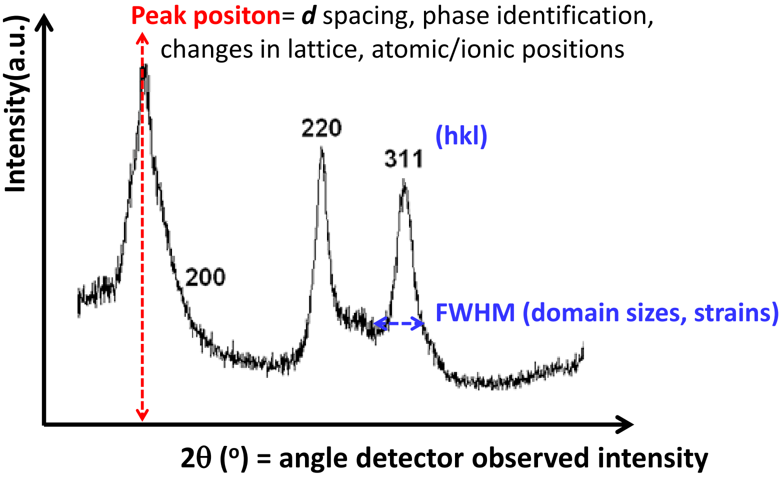

Figure 6. X-Ray diffractogram illustrating the information that XRD can reveal

A wealth of information about the crystalline structure can be unravelled using the X-Ray diffraction pattern (Figure 6). This is done using an iterative refinement named Rietveld refinement. This process allows us to compare and adjust the measured sample with existing data about the crystalline structures present in the sample, where the difference with existing data allows us to extract valuable information. This information is specifically derived from the peak positions and broadness from the sample measurements compared with existing data. Three main parameters should be considered. The peak positions provide insight into the d-spacing and lattice parameters of the crystals (also comprising atomic occupancy and positions). The width and shape of the peaks are equally important, as this parameter translates into the grain size and sample defect. Finally, the peak areas can be derived into quantitative phase distribution, relative amounts of each crystalline compound in the powder sample.

Software such as FullProf or GSAS (General Structure Analysis System) can be applied to XRD refinement. In this thesis, the Rietveld refinement has been performed using GSAS. Extensive information concerning the usage of GSAS has been published by Larson et al.[**144**].

3.2 Impedance Spectroscopy

In order to investigate the frequency dependent impedances within an electrochemical cell, electrochemical impedance spectroscopy (EIS) is used. This perturbative tool can probe the kinetic processes within batteries, for liquid as well as solid electrolytes. By polarizing the electrochemical system at a fixed voltage followed by a small voltage perturbation, a response is incited. The additional voltage is added at a specific frequency, oscillating to create an Alternative Current (AC), applied in our case to the battery. The electrochemical cell produces an oscillating response, which traduces to an alternating current with specific frequency and amplitude. This response can be interpreted as a form of complex resistance to the electrical flow going through the system. When using direct current (DC) in a circuit, the resistance R is the relation of Voltage over direct current; while the impedance Z is a ratio of voltage over alternating current. If no alternating current is used, impedance becomes a regular resistance. Impedance describes not only the resistance, but also the phase shift of the responding signal. These are differentiated with a real and imaginary component.

Naturally, each phenomenon present in an electrochemical cell can be described by an electrical component in a circuit. The most common ones are:

the resistance, with impedance:

$$\mathbf{Z = R} \qquad \textbf{(Eq. 9)}$$

the inductance, where:

$$\mathbf{Z = i\omega L} \qquad \textbf{(Eq. 10)}$$

and the capacitor, described as the inverse of the inductance:

$$\mathbf{Z = 1/i\omega C} \qquad \textbf{(Eq. 11)}$$

We can see that the impedance of the resistance is only correlated to the real component relating to active power, while the impedance of the inductance and capacitance vary with frequency relating to reactive power, as follows:

$$\mathbf{Z_{eq} = R_{eq} + jX_{eq}} \qquad \textbf{(Eq. 12)}$$

The behaviour of a capacitance shows that its impedance decreases with increasing frequency, and it only has an imaginary component, relating to the reactive power.

By applying the impedance measurement process to a large range of frequencies of alternating currents, the various interfaces comprising the battery can be distinguished. The resulting impedance data can be plotted as an impedance spectrum or Nyquist plot, graphing out the real and imaginary part that constitute the impedance. Further information on electrochemical tools and impedance spectroscopy has been published by Barsoukov et al. [**145**] and is widely used for electrochemical processes [**146**]**.** The impedance spectrum can be fitted to investigate the electrical performances of the battery. This will be discussed in detail under heading 3.2.2.

3.2.1 EIS in batteries

Unfortunately, some challenges arise when applying EIS to a fully assembled battery. Since batteries are composed of two electrodes and an electrolyte, the influence of each individual material can be hard to separate.

Concerning solid state batteries, electrolyte ionic conductivity can be an issue. Particles are required to be in close contact in order to efficiently conduct ions. This can be challenging, and EIS can shed light on which part of the particles impedes transportation.
Solid state electrolyte particles have three contributing factors, inherent to any solid conducting material. The bulk conductivity is the highest, as it is synonym to the single crystal conductivity of the material. The grain boundary can be problematic, as the conductivity is related to the contact area. A greater contact area between particles provides higher conductivity, and inversely so for small area. Lastly, the interface between electrolyte and electrode is a factor. This contribution can vary over time, especially when observing the behaviour before and after cycling. Interface formation can severely impact the conductivity of an electrochemical system.

The myriad of contributions in the system are uncovered due to their reaction to the change in polarity. When two processes react to the same disturbance, the time constant is also different. This changes the frequency of their contribution and appears in a different region of the Nyquist plot, allowing us to differentiate the internal processes. In order to quantify the electrochemical parameters in the cell, the impedance spectrum is fitted using a model based on electrical circuits.

The resistances depict conductive pathways for ions and electron transfer in bulk (at high frequency) and charge transfer resistance at the electrode surface at medium frequency. Inductors and capacitors on the other hand, depict space-charge polarization regions. The induction element refers to adsorption and desorption at the electrode surface, while capacitance describes the electrochemical double layer.

3.2.2. Fitting EIS - Equivalent Circuit Elements

The potential of EIS lies in the characterization of various contributions. By fitting the electrochemical impedance response to a model, the different factors influencing the electrochemical system can be highlighted and studied, allowing us to gain further insight into the kinetics and interactions within the battery, as well as potential bottlenecks impeding ionic transport.

In order to fit an impedance spectrum accurately, the electrical circuit components need to have matching frequencies with the impedance response of the studied electrochemical cells. Using the impedance of resistors, inductors, capacitors, constant-phase elements (CPE) and a Warburg element, all the electrochemical processes comprised in the batteries can be simulated and fitted to match the electrochemical impedance spectrum.

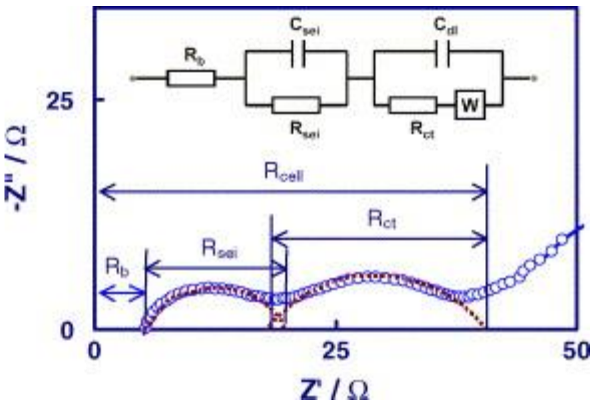

Figure 7. Impedance spectrum of a solid-state battery, as well as the equivalent electrical circuit matching the impedance response. [**147**]

In Figure 7, the Nyquist plot is shown, illustrating the various fitted electrical components simulating the electrochemical effects in the battery. The impedance spectrum reflects the impedance values for a range of frequencies, in our case from 10^{-2}Hz to 1MHz. The far left of Figure 7 indicates the bulk resistance of the cell R_b, the electric conductivity of the electrolyte and electrodes. It is the intersection with the origin of the Real axis (Z'), indicating the total ohmic resistance of the electrolyte and electronic contacts.

The high frequency part of the plot (first semi-circle) can be seen at the left part of Figure 7, relating to the solid state interface resistance R_{sei} and capacitance C_{sei} [**148**]**.**

The second semi-circle (in the middle of Figure 7) relates to medium frequency impedance values, associated with the impedance of faradic charge transfer R_{ct} and double layer capacitance C_{dl}. The second semi-circle relates to the charge transfer kinetics (concerning both ions and electrons). It influences the Sodium-intercalation process and the exchange current density. The charge transfer kinetics are the speed at which the ion and electron transfer from one species to another. When relating to batteries, it is the process of changing an Na^+ ion in the electrolyte into a stored Na in the electrode, by combining with an electron. This speed depends on temperature, concentration of the products, and the potential difference between both compounds.

It can be noted that experimentally, capacitance is more accurately modelled by a CPE. This depicts the behaviour of an imperfect capacitor.

The far-right part of Figure 7 usually reflects the Warburg impedance W. The measured impedance effect is attributed to ionic diffusion [**148**]**,** a line indicating the ionic diffusion through all the interfaces.

Typically, the total cell resistance R_{cell} is composed of the bulk resistance, the solid-state interface resistance and the charge transfer resistance. Relating impedance to temperature puts into perspective that R_b and R_{sei} do not react to temperature variation, while R_{ct} is strongly affected. Since the charge transfer resistance is associated with reaction kinetics in the cell, this impedance factor contributes the most to slow kinetics and low performance of the cell at Room Temperature [**147**]

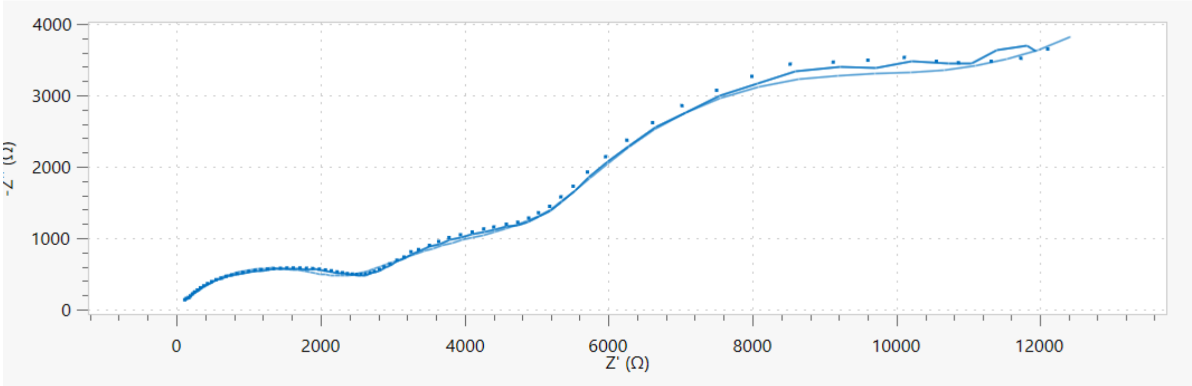

Figure 8. Measured EIS spectrum of an assembled battery with modelled fit, comprising a cathode thin film, tape casted Na-beta"-alumina electrolyte with liquid addition of organic electrolyte, and Sodium metal anode. Three overlapping semi-circles are visible

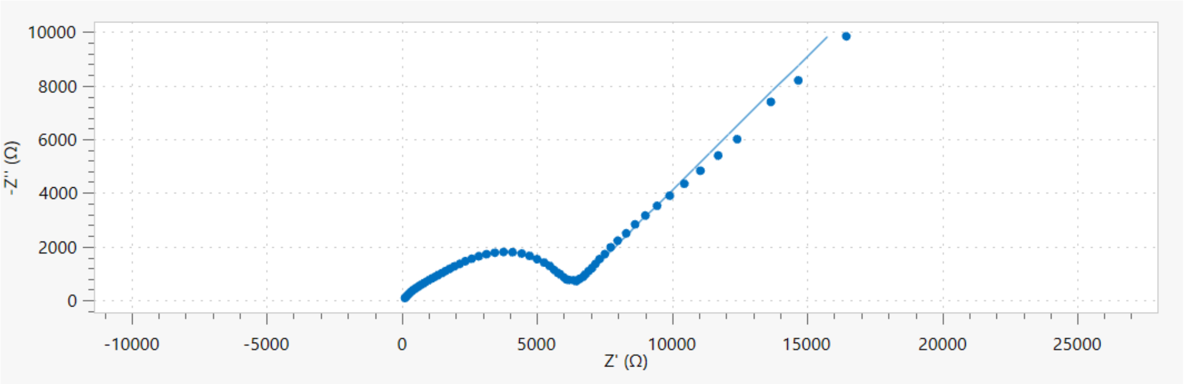

Figure 9. Measured EIS spectrum of an assembled battery with modelled fit, except the electrolyte is a slurry of Na-beta"-alumina particles with ionic liquid. The first and second semi-circle are overlapping, while the third semi-circle overlaps with the tail of the spectrum (far right).

Since our measurements present three semi-circles, the resulting equivalent circuit modelling of the impedance response is introduced as:

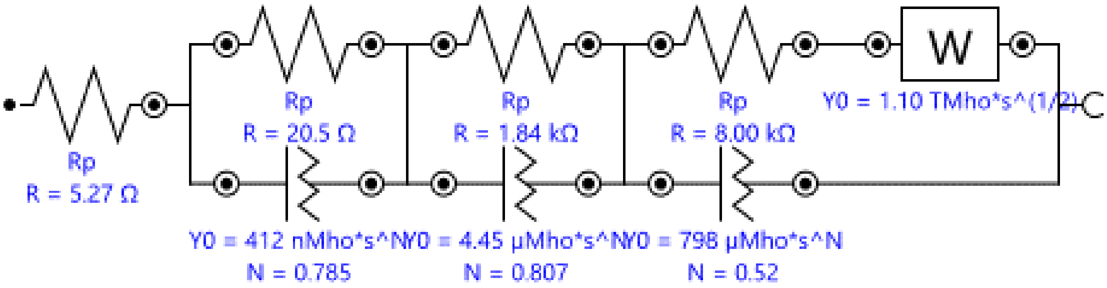

Illustration 7. Equivalent circuit modelling relating to the measured EIS.

In Illustration 7, each semi-circle is described by a an equivalent RC part of this circuit. For three distinct semi-circles, three resistances and capacitances in parrallel have to be introduced, RC parralel circuits. Additionally, the circuit also comprises the bulk resistance (far left) and a Warburg diffusion element (far right).

The resistances are described in Ohm (Ω) and Capacitances in Farads (F). Mho is the same as Siemens unit, electrical conductivity unit. It can be described as the the inverse of resistance, $S = \Omega^{-1}$

In our model, capacitances are replaced by a more accurate experimental fit, CPE. The CPE can be seen as an imperfect capacitance, with N the degree of imperfection. Y_o is the magnitude of the admittance (= 1/Z) at ω=1 rad/s. This relates to the capacitance as well as the Warburg element.

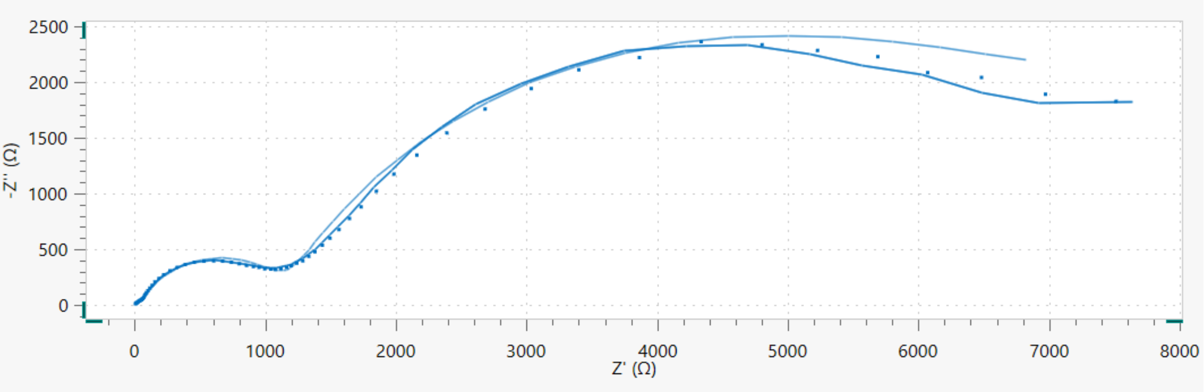

Figure 10. Nyquist plot of a cell with slurry Na-beta"-alumina : Pyr14FSI ionic liquid as electrolyte.

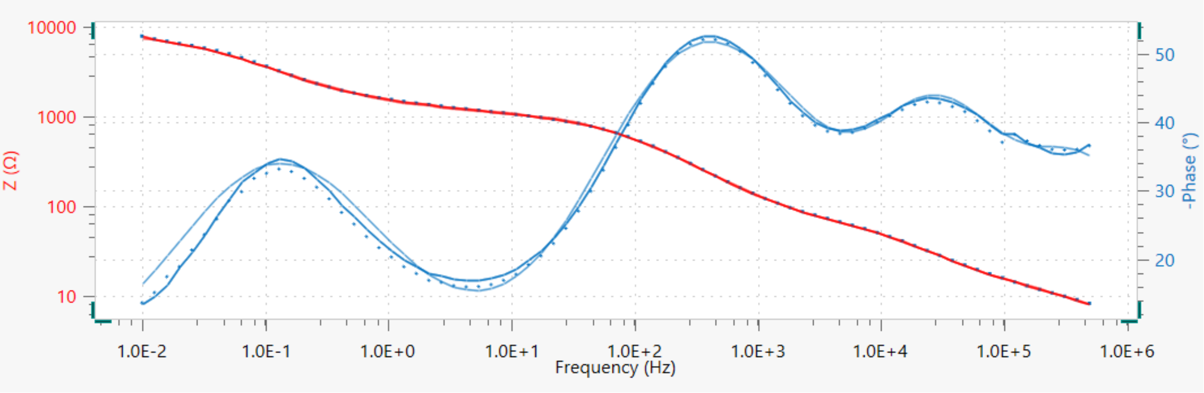

Figure 11. Corresponding Bode plot of the slurry electrolyte cell shown above. The same information is shown, but decomposed in different parameters. Instead of an imaginary and real component of the impedance, the Bode plot shows the overall impedance and the phase angle at each measured frequency.

The Nyquist plot shown in Figure 10 illustrates the challenge relating to fitting EIS measurements. In this case, the low frequency values are challenging to fit, which results in an inaccurate translation to electrical data. This is confirmed by the Bode plot in Figure 11, which indicates the same mismatch at low frequency.

3.2.2.1 CPE vs Capacitance

A true capacitance is indicated by a perfect semi-circle in an EIS measurement. When properties of the system are not homogeneous, the spectrum shows depressed semi-circles. This is explained in Illustration 8.

In our impedance spectra, n describes the degree of "depression" of a semi-circle. A perfect half-circle shape would result in an indice $n=1$, while the same arc with an indice of $n=0.5$ is half the high, but still as broad.

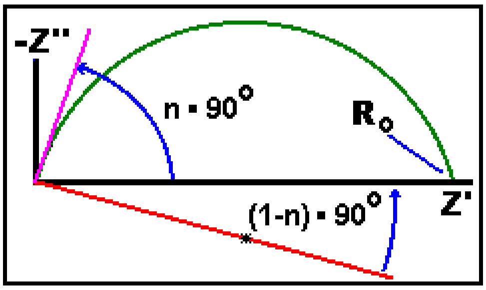

Illustration 8. Schematic explanation of the translation from measured depressed semi-circle to capacitance. Taken from [149]

Capacitance can be derived from the CPE using the following formulas. The first formula (Eq. 13) relates to the parallel resistance (in the depressed semi-circle), while the second one (Eq. 14) relies on the angle (rad/s or frequency in Hz) at the top of the concerned semi-circle. For information, one Radian per second is comparative to $1/2\pi$ Hertz.

$$\mathbf{C = (Qo * R)^{(1/n)} / R} \qquad \textbf{(Eq. 13)}$$

$$\mathbf{C = Qo * (omega_{max})^{(n1)}} \qquad \textbf{(Eq. 14)}$$

Using CPE as elements instead of Capacitance results in better fitted results. Deviations from ideal capacitance has been extensively studied [150] and attributed to electrode inhomogeneity, porosity and surface roughness, variable coating thickness, as well as slow adsorption process. Uneven potential and current distribution and grain boundary of the particles also influence the degree of perfection of the capacitance.

Since a dynamic system is analysed with many electrochemical processes involved, it often occurs that phenomena are overlapping. Impedance responses can have a similar magnitude, but occurring at slightly different time constants, overlapping semi-circles can be observed. This is due to either an electrode having higher kinetics than its counter-electrode (lower charge transfer resistance), which appears as a long flat arc; or electrodes have similar kinetic time constants, appearing as one semi-circle. This makes pinpointing the capacitance using the second Capacitance formula rather challenging, as the peak of overlapping semi-circles is not always visible.

The low frequency element also includes various phenomena, features all put under the denomination of mass transport, but also include thermodynamic phenomena.

4. Experimental procedure

This chapter describes the experimental methods used in this thesis. The various electrolyte concepts and preparation methods for the batteries are being reviewed in the first part, followed by the battery assembly. The various analysing methods comprised of cycling XRD and EIS are then discussed

4.1 Experimental methodology

On the positive electrode side of our electrochemical cells is the catholyte, a mixture of cathode active material P2-$Na_{1/3}[Ni_{1/3}Mn_{2/3}]O_2$, conducting agent Carbon, binder PVDF and various electrolyte compounds.

For the tape casting concept, the catholyte consists of the active material, Na-beta”-alumina solid electrolyte, conducting agent, binder and organic electrolyte. The Na-beta”-alumina was purchased from Ionotec. The solid electrolyte BASE is introduced in the catholyte due to the varying of $NaClO_4$: ECPC and the exclusion of dissolved salt $NaClO_4$ to examine the BASE contribution.
The electrolyte slurry concept contains active material, conducting agent, binder PVDF and ionic liquids Pyr_{14}-FSI and TES-TFSI.

On the negative electrode side of our electrochemical cells is Sodium paste, providing Sodium ions to the discharged P2-$Na_{1/3}[Ni_{1/3}Mn_{2/3}]O_2$, effectively loading the crystalline framework with Na^+ ions until P2-$Na_{2/3}[Ni_{1/3}Mn_{2/3}]O_2$. This process can also be reversed. But not without an electrolyte, highly conductive for ions, but not allowing electrons through.

Various pasting thicknesses and particle sizes of electrolyte were employed to determine the liquid to solid correlation, and effective_contribution of the electrolyte.

This experimental section explains the various attempts to study the effects of liquid additives on the dynamics within solid state batteries, and the solid electrolyte Na-beta”-alumina in particular.

Table 2. Overview of the various concepts tested throughout this project.

	Tape casting concept		**Slurry concept**		**Pellet concept**	
Cathode	5 NNM 5 BASE 1 PVDF 1 Carbon Black	5 NNM 5 BASE 1 PVDF 1 Carbon Black	8 NNM 1 PVDF 1 Carbon Black	8 NNM 1 PVDF 1 Carbon Black	8 NNM 1 PVDF 1 Carbon Black	8 NNM 1 PVDF 1 Carbon Black
Electrolyte	4 BASE 1 PVDF NaClO4 : ECPC	4 BASE 1 PVDF ECPC	7.5 BASE 2.5 Pyr14FSI	7.5 BASE 2.5 TES-TFSI	BASE pellet Pyr14FSI	BASE pellet TES-TFSI
Anode	Na metal	Na metal	Na metal	Na metal	Na metal	Na metal

4.1.1 Tapecasted cathode

The tape casting concept is likely to be used for large scale production, as it is cheap and time effective, it could also be automated in order to improve the casting process. It is essentially a process where a wet slurry is pasted upon a metal foil (serving as current collector), followed by a drying process

* The $\text{P2-Na}_{1/3}[\text{Ni}_{1/3}\text{Mn}_{2/3}]\text{O}_2$ powder is mixed with PVDF and Carbon Black, then dissolved in NMP at the weight ratio of 8:1:1 to form slurry.

* Ball-mill the cathode slurry for 4 hours at 350 rpm for homogeneous paste.

* Tape casting procedure using a 50 μm tape-casting tool.

* Drying at room temperature for 1 hour.

* Drying in oven at 70 °C for 1 hour.

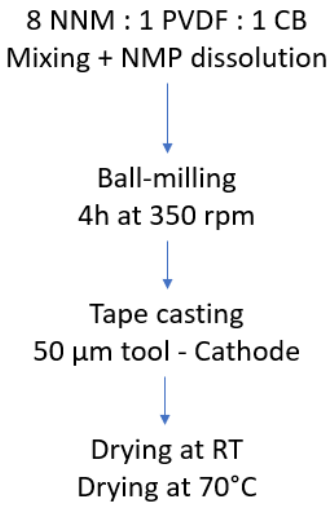

4.1.2 Tape casted electrolyte

* Na-beta” alumina powder is mixed with PDVF at the weight ratio 4:1 with dissolved NMP to form slurry

* Ball-milling Na-beta-alumina solid state electrolyte slurry at 350rpm 2-4 hours to change the solid electrolyte particle size

* Tape casting electrolyte slurry on dry cathode thin film.

* Drying at room temperature for 1 hour.

* Drying in oven at 70 °C for 1 hour.

* Cutting thin films in small circles (1,25cm) for battery assembly.

* Heating ante-chamber of glovebox at 80°C to extract additional water.

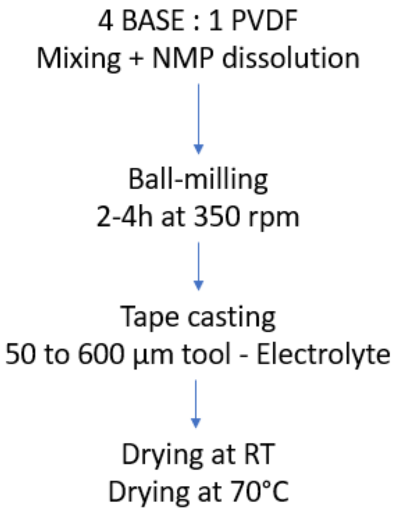

4.1.3 Pellet electrolyte

The Na-beta”-alumina electrolyte powder (ball-milled for different particle sizes) was pressed into pellets with a diameter of 13 mm and a thickness of approx. 1 mm. In order to form a self-standing electrolyte pellet, the press had to exert a pressure of 4.5 tons with steps of 0.5 tons with release. The slow release proved to be defining factor in keeping the integrity of the pellet. Since annealing at 1600 °C was not achievable with our facilities, a pellet electrolyte was attempted using pressed powder. This would imply many point contacts between the particles, which would be vastly improved using an ionic liquid.

4.1.4 Slurry electrolyte

The slurry electrolyte concept is a mixture of BASE particles and ionic liquid without dissolved salt. The idea behind it, is to measure the interaction between these two, while still allowing BASE to provide the ionic conduction paths. The ionic liquids used in this project are abbreviated TES-TFSI and Pyr_{14}FSI for Triethylsulfonium (cation) bis(trifluoromethylsulfonyl)imide (anion) and 1-Butyl-1-methylpyrrolidinium (cation) bis(fluorosulfonyl)imide (anion) respectively.

Ball-milling Na-beta”-alumina solid state electrolyte slurry at 350rpm 0-2-4 hours to change the solid electrolyte particle size

Heat treatment at 600 °C to avoid moisture contamination

Drying Ionic liquids in antechamber of glovebox at 8 0 °C

Mixing solid-state electrolyte with ionic liquid for 2 hours using a stirrer to form a uniform composite slurry

Pasting Ionic Liquid-BASE mixture on Na anode, ideal ratio 7.5:2.5 (not too liquid to prevent short-circuit upon assembly, not too solid to allow correct application and negate point contacts (which would prevent efficient ionic conductivity))

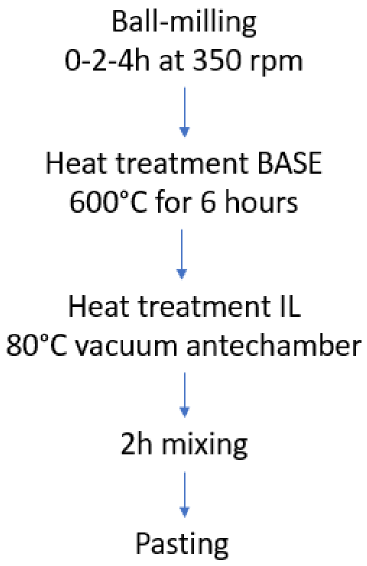

The advantage of the slurry electrolyte is the improved contact at the interfaces, as well as the contact between the particles in the electrolyte. The viscous ionic liquid acts as a binder and permits the conduction of ions over the solid-liquid interface.

4.2 Battery Assembly

The batteries are assembled in the Argon Glovebox. All the elements pertaining to the composition of the electrochemical cells had to be thoroughly dried in order to be used, as many components were reactive to water like Sodium; would lose their conductive properties such as Na-beta"-alumina or are hydrophobic such as the ionic liquids TES-TFSI and $Pyr_{14}FSI$.

Using tape-casted cathode mixture on a thin film and Sodium as anode, various concepts to optimize the electrolyte were experimented with.

- For the tape casted concept, only a drop of organic electrolyte additive has to be added on the film using a pipette, before adding Sodium and encapsulating the system in a Swagelok cell.
- For the mechanically pressed pellet, Sodium paste was pressed onto one face of the pellet, while thin film tape casted cathode material was placed on the other, before encapsulating it in a Swagelok cell.
- The slurry electrolyte (with ionic liquid) was pasted on the Sodium in the glovebox using a clean spatula, before adding the cathode thin film on the other side (shown in Picture 1) and encapsulating the system in a Swagelok cell.

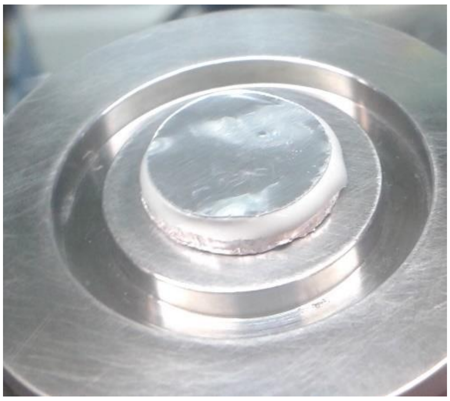

Picture 1. Clear view of the Sodium metal with BASE:IL slurry on top, followed by the cathode thin film pasted on aluminium foil.

A schemtic visualisation can be seen in Illustration 9.

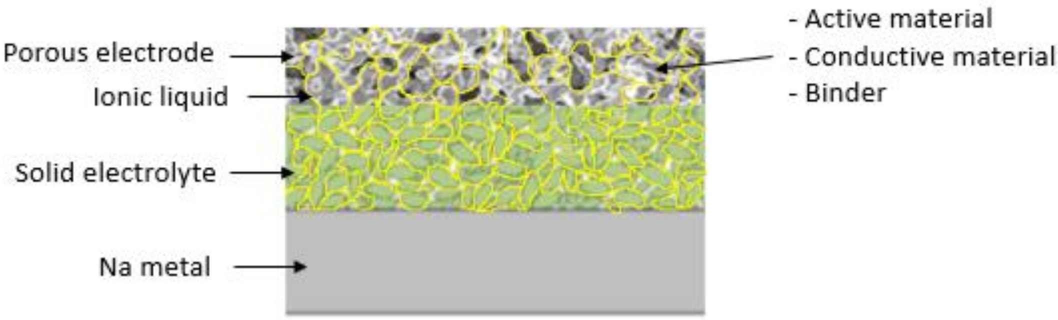

Illustration 9. Schematic illustration of the slurry battery, comprised of a porous tape casted cathode, a slurry electrolyte and a metal Na anode.

4.3 Battery Analysis – Computational methodology

After assembly of the battery inside the glovebox, it is taken out to analyse the electrochemical properties. In particular the electrochemical dynamics between the components. This is done using Electrochemical Impedance Spectroscopy (EIS), connected to Nova Autolab. All impedance measurements were carried out between 10^{-2}Hz and 1MHz with applied voltage of 0.01V using automatic sweep from high to low frequencies, at room temperature. Using a built-in function of Nova Autolab, an electrical circuit can simulate the dynamics of the batteries, as well as a Kronig-Kramers (KK) test to determine the error of the analysis. Electrical parameters can be derived from that, producing quantifiable data. Combining this with the fitting error of the designed electrical circuit, the validity of the measurement can be supported.

The battery is then ready for a series of charge-discharge cycles in the MACCOR, determining if the assembled cell is a viable battery option or not. By studying the voltage curves (indicative of phase transformations within the cathode material) during the cycles, the efficacy of the assembled cell can be assessed.

Post-cycling, the battery is analysed through the EIS once more, which allows us to draw conclusions, correlating the battery cycles with the electrochemical dynamics inside the system, as well as the evolution caused by the charge-discharge process.

For the slurry, after the impedance testing, the battery is disassembled and the thickness of the slurry is measured with a thickness gauge meter.

4.4 X-Ray Diffraction

In order to determine the size of the particles in our cells, XRD measurements were carried out. An air-tight holder with Kapton cover was used for Na-beta”-alumina, as air and water exposure were proven to change the electrochemical properties of the solid electrolyte.

The wavelength was 0.69386 Å. Data processing was operating at 45 kV and 40 mA.

The scanning was done continuously, with an exposure time of 45,0850 s/step and a step size [°2θ] of 0.0080. All XRD measurements were performed at room temperature.

For all diffraction patterns, Rietveld refinement was carried out using the GSAS software. The phase factors, the unit cell parameters as well as the strain and the size broadening parameters were refined for all phases.

Pseudo-Voigt profiles were used for modelling the shapes of the diffraction peaks. The background signal was modelled using a polynomial expression, and the zero point was refined. The weighted profile agreement factor Rwp at the end of the refinements was under 5% for every measurement and the data were refined for convergence. After refinement, the particle size was derived using L_x and Equation 7.

4.5 Electrochemical Impedance spectroscopy (EIS)

Nyquist Plots have one major shortcoming. When you look at any data point on the plot, you cannot tell what frequency was used to record that point.

The Nyquist plot results from the electrical circuit of Figure 4. The semicircle in a Nyquist plot is characteristic of a phenomenon with a "time constant". Electrochemical impedance plots often contain several semicircles. These semi-circles are simulated using a resistance and a Constant phase element, an imperfect capacitance.

The measurements were performed under near-equilibrium conditions, i.e. after resting the cell in open circuit mode for at least 20 minutes prior to the EIS measurements. Near equilibrium was deduced from the Open circuit voltage stabilizing, as well as the EIS measurement drastically gaining in accuracy. The frequency range of the impedance measurements was set from 0.01 Hz to 1MHz.

The temperature during the impedance spectroscopy measurements was the same as during the charge-discharge measurements for each cell, room temperature.

Kronig-Kramer values resulting from the EIS measurements were all below 10^{-4} and Chi^2 fitting values indicating the fitting error were below 5%, validating the accuracy of the measurements.

Note: For future work regarding deriving electrical values from EIS measurements, one should be aware that making an accurate correlation between electrochemical data and a modelled circuit takes a large amount of time. For each EIS measurement, a refinement of under 5% inaccuracy takes 2-3 days, especially for an inexperienced user. When doing a series of battery measurements, this can easily take up to a month to fit the model to the data.

5. Results

In order to study the effects of adding a small fraction of liquid in a solid-state electrochemical cell, EIS was done on a large variety of cells. The idea is to use a liquid with a different chemical potential for sodium, so that a space charge layer forms at the interface between the solid and the liquid. This can lead to seemingly larger contact area and therewith lower grain boundary resistance.

If this is the case, and the contact area is artificially enhanced, one would expect a different response of the corresponding R-C parallel circuit. A circuit corresponding to the interactions in the battery should be modelled. If such a change is large, and the RC-time constant is different from others within the circuit, this phenomenon can be measured with impedance spectroscopy.

Relating these results to cycling capabilities and post-cycling EIS measurements, conclusions can be drawn regarding the electrochemical dynamics and efficiency in these batteries.

The first battery concept was based on thin film solid-state batteries, as they possess qualities regarding ease for mass-production, as well as being able to effectively reduce cell resistance for solid electrolytes. Unfortunately, pasting thin films can also lead to film defects such as pin holes, porosity or agglomerates if the deposition process is not optimized.

Mechanically pressing the solid electrolyte was the second option. Since sintering at 1600 °C is necessary for Na-beta”-alumina to form a dense pellet, mechanically pressing the solid electrolyte was a viable alternative. It would increase the amount of point contacts, therefore developing a better ionically conducting network. Yet making the pellet thin enough, with limited point contacts, while preventing pellet breakage, was highly challenging.

Finally, favourable contact was made by using an electrolyte slurry, combining Na-beta”-alumina with ionic liquids to enhance contact while allowing the solid-state electrolyte to take part in the ionic conduction. By using ionic liquid without dissolved Sodium salt, improved point contacts could be a result of space-charge formation around the solid electrolyte particles.

5.1 Electrochemical Impedance Spectra analysis

By using a standardized equivalent electrical circuit (Illustration 7) to translate the Electrochemical impedance spectroscopy into electrical components, one can quantify the behaviour and interactions in the cell. This can be done using resistances, capacitors and inductors. Drawing a relation between these electrical parameters and the electrochemical characteristic within the batteries is essential for credible conclusions.

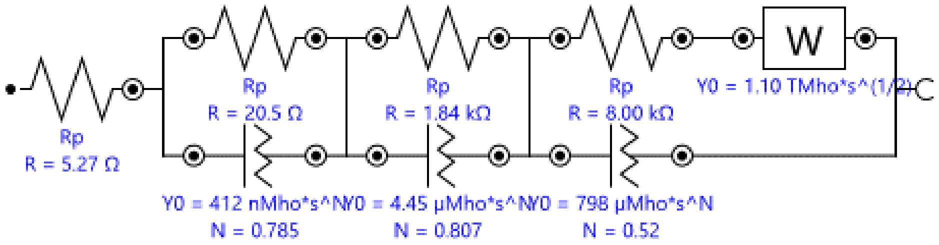

Illustration 7. Equivalent circuit modelling the various interactions in the batteries using parallel RC elements, as shown in 3.2.2.

EIS data is analysed using NOVA. For some of our measurements, invalid data points impede a consistent fit. This can be caused by a number of interferences or disturbances. Since the invalid data point cannot be deleted or changed in NOVA, the Windower can be added to the original data. This allows us to exclude one or two points in the measurement (containing 78 data points all related to a specific frequency response).

5.1.1 Organic electrolyte ECPC with 1M dissolved $NaClO_4$ salt series

The first concept we have studied is a battery concept with a tape casted cathode, followed by a tape casted Na-beta”-alumina coating. By tape casting over the first thin film, we suppose this promotes the contact interface between electrode and electrolyte. By varying the thickness of the coated electrolyte and the amount of added Sodium salt, our first correlations regarding the effect of liquid addition on the Na-beta”-alumina particles can be made. Finally, Sodium metal was added as anode.

Two series of batteries have been made, differentiated only by the Na-beta”-alumina particle size. In order to compare all the reported data, we need to first analyse the contributions for same size Na-beta”-alumina particles with various liquid additions to see if these behave according to expectations. After doing this for both series, we can compare the behaviour of the batteries with different electrolyte particle size and correlate these with the ratio of liquid volume/mass of solid electrolyte to extract information regarding the liquid contribution to the solid electrolyte. A correlation with the surface area would have been an attractive choice because improving surface contacts is relevant, yet it would mean assuming a shape for the Na-beta”-alumina particles, which would have been a rough approximation. By correlating it simply to the mass, the contribution is more accurate.

5.1.1.1 Smaller BASE particles (63.30 nm) in tape casted electrolyte

In our first series, the electrolyte particles have been ball-milled with a binder material and NMP for 4 hours. Analysis with the XRD showed a particle size for our solid electrolyte of 63.30 nm.

Table 3. Overview of the studied electrochemical cells related to organic electrolyte for 4h ball-milling, as well as physical properties of the cells.

	liquid additive	solid electrolyte	thickness after pasting		particle size		additive/BASE	
	cm^3	**mg**	µm	µm	nm	nm	cm^3/mg	
1drop=0.05mL=0.05cm3			NNM	BASE	NNM	beta		
4h milling - 63.3 nm BASE								
140 µm	0.05	9.90	15	140	**91.94**	**63.30**	**5.05E-03**	**1**
55 µm	0.05	3.89	20	55	**91.94**	**63.30**	**1.29E-02**	**2**
87 µm-2 drops	0.1	6.15	20	87	**91.94**	**63.30**	**1.30E-02**	**3**
30 µm	0.05	2.12	20	30	**91.94**	**63.30**	**2.36E-02**	**4**
87 µm-3drops	0.15	6.15	20	87	**91.94**	**63.30**	**2.44E-02**	**5**

This table summarises the parameters with immediate relevance to the case at hand, leading to the correlation between liquid additive volume $NaClO_4$: ECPC and the mass of solid-state electrolyte. It shows the amount of liquid added to the electrolyte, as well as the various thicknesses of the electrolyte paste, particle sizes for both active cathode material P2-$Na_{1/3}[Ni_{1/3}Mn_{2/3}]O_2$ (NNM) and Na-beta"-alumina (BASE). By assuming the cells have a cylindrical shape, the volume of the cell was determined. Finally, the amount of liquid in contact with solid electrolyte was determined. The ranking in red at the far right indicates which cell has the highest volume of liquid per mass of BASE particle.

The following figures are the results of the EIS equivalent circuit fits, resistances and capacitances related to electrochemical properties of the batteries. Not all fitted values from the equivalent circuit are shown here. Factors unrelated to solid electrolyte interactions are therefore reported in the Appendix.

5.1.1.2 Bigger BASE particles (67.37 nm) in tape casted electrolyte with lower volume of liquid additives

For this second series, the Na-beta"-alumina particles are roughly 4nm bigger. These batteries have also been analysed after cycling 100 times at a rate of C/10 (10 hours charging and discharging), which will be discussed in a later chapter.

Table 4. Overview of the studied electrochemical cells related to organic electrolyte for 2h ball-milling, as well as physical properties of the cells

	liquid additive	solid electrolyte	thickness after pasting		particle size		additive/BASE	
	cm^3	**mg**	µm	µm	nm	nm	cm^3/mg	
1drop=0.05mL=0.05cm3			NNM	BASE	NNM	beta		
2h milling - 67.37 nm BASE								
200 µm	0.05	14.14	12.5	200	**91.94**	**67.37**	**3.54E-03**	**1**
24 µm-170 µm	0.05	12.02	24	170	**91.94**	**67.37**	**4.16E-03**	**2**
100 µm	0.05	7.07	12.5	100	**91.94**	**67.37**	**7.07E-03**	**3**
75 µm	0.05	5.30	12.5	75	**91.94**	**67.37**	**9.43E-03**	**4**

With the same setup as previous sub-chapter, this series has been reported and plotted as a function of the liquid contribution to the solid electrolyte. The left side indicates the thickness of pasted electrolyte slurry, as well as a cell with a tape casted cathode twice the regular thickness.

According to this table, liquid contributes the most to the bottom row, a cell with 75µm thick pasted BASE electrolyte. It should therefore also present the lowest resistance, as conductivity is enhanced the most.

5.1.1.3 Series with only ECPC organic solvent – no added $NaClO_4$ salt

In order to study the effect of Sodium salt on the cells, a similar series has been analysed, this time excluding the additional salt. This will allow us to derive the $NaClO_4$ salt contribution.

Table 5. Overview of the studied electrochemical cells related to organic electrolyte ECPC, as well as physical properties of the cells.

			liquid additive	solid electrolyte	thickness after pasting		particle size		additive/BASE	
			cm^3	**mg**	µm	µm	nm	nm	cm^3/mg	
1drop=0.05mL=0.05cm3					NNM	BASE	NNM	beta		
ECPC										
24-170 µm			0.05	12.02	24	170	**91.94**	**67.37**	**4.16E-03**	**1**
12.5-100 µm			0.05	7.07	12.5	100	**91.94**	**67.37**	**7.07E-03**	**2**
7.5-100 µm			0.05	7.07	7.5	100	**91.94**	**63.30**	**7.07E-03**	**3**
12.5-75 µm			0.05	5.30	12.5	75	**91.94**	**67.37**	**9.43E-03**	**4**

Overview $NaClO_4$: ECPC series

The issue with discussing individual results such as these, is the lack of a more general overview. In order to compare the various series, we have plotted the electrical values of each battery in the organic electrolyte series as a function of a contribution ratio (liquid addition/mass of Na-beta”-alumina). The ratio is an indication of how much liquid per solid particle is added, and can be seen as how much “help” is given to the solid particles to improve battery interactions. Therefore, plotting the electrical values as a function of the “contribution per particle” provides clearer insight on the enhancing effect of the liquid on the Na-beta”-alumina particle.

$R_{electrolyte}$ is the modelled resistance value for the current collectors, connectors and electrolyte. Theoretically, with equal particle sizes for the bulk electrolyte in a solid-state battery, the electrolyte resistance measured through EIS should be the same for solid-state batteries (assuming equal thickness and defects). Using additives clearly influences the resistance and therefore the conductivity of the electrolyte. It is interesting to note that the “liquid-solid” ratio from Table 3 somewhat coincides with the modelled values. An increase in $R_{electrolyte}$ is directly related to a decrease in conductivity [**151**].

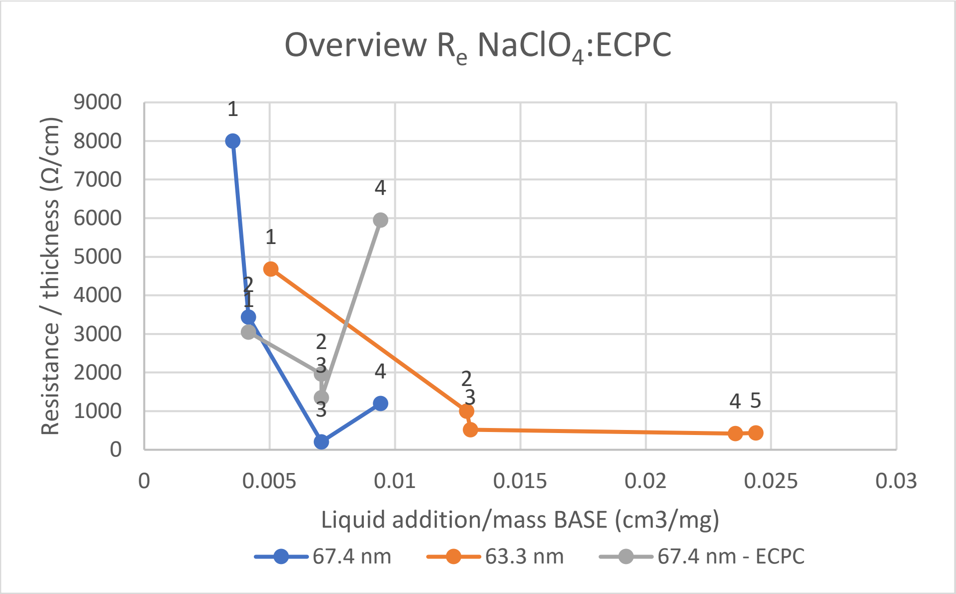

Figure 12. Overview of the electrolyte resistance R_e for the three series done for $NaClO_4$ salt with ECPC organic electrolyte. The numbers indicate the ranking in liquid addition per mass of solid electrolyte. A higher number means a larger liquid addition.

For two series with the same particle size, we would expect a higher liquid addition to show a lower resistance. This is indeed the case (except for the last data point of each series). Yet when comparing both series, the series with added $NaClO_4$ should show lower resistance due to the salt acting as an additional conducting agent. Surprisingly, both series are relatively close to one another in regard to resistance per thickness.

We would also expect smaller particles to produce a higher resistance because these cells would have more point contacts. Yet resistance remained low for all the cells in the 63.3 nm series. This series had the lowest average thickness, which could explain this phenomenon. It was also ball-milled twice as long, which could have resulted in a lower concentration of defects in the coatings. Finally smaller particles could benefit more from the same amount of liquid addition, enhancing the effective liquid contribution.

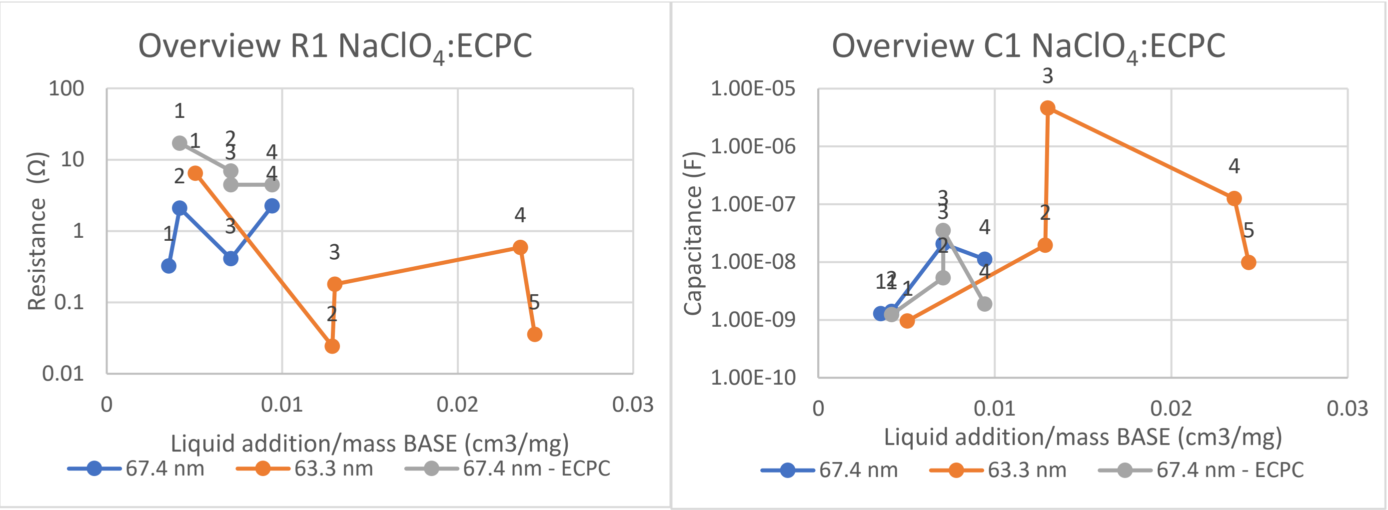

Figure 13. Overview of the Resistance R1 and capacitance C1 for the three series done for $NaClO_4$ salt with ECPC organic electrolyte. The numbers indicate the ranking in liquid addition per mass of solid electrolyte. A higher number means a larger liquid addition.

At high frequency, the EIS response usually pertains to the Solid Electrolyte Interphase (SEI). These results would indicate that adding liquid reduces the SEI (lower R1 and higher C1), yet SEI formation results from irreversible electrochemical decomposition of the electrolyte. More electrolyte would then result in a larger SEI formation. This leads us to believe these figures are the result of overlapping phenomena.

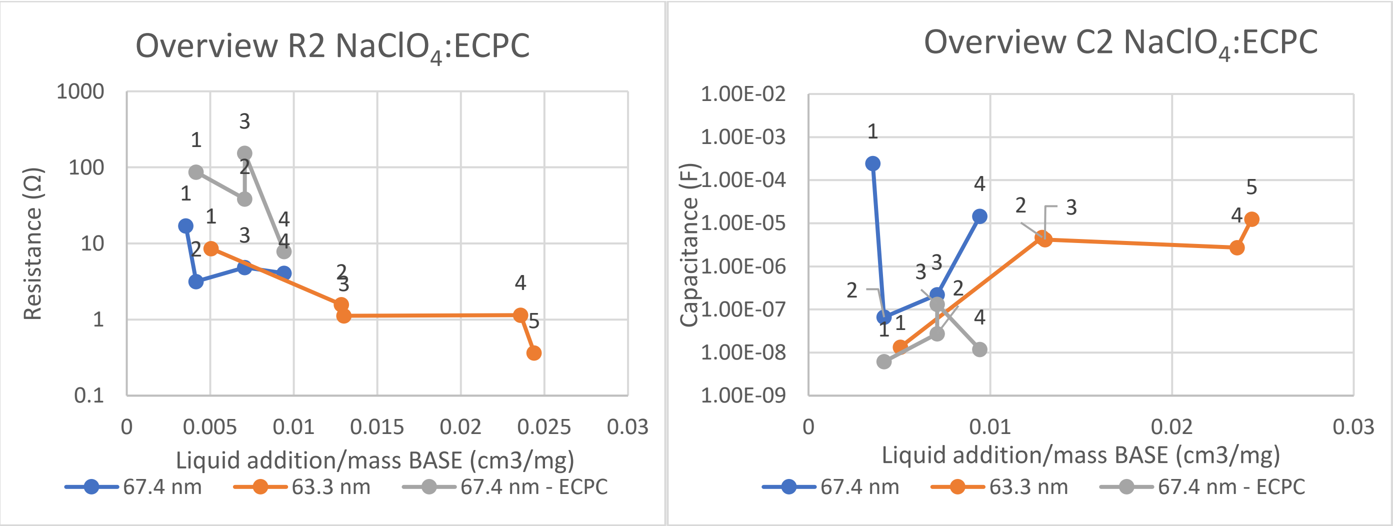

Figure 14. Overview of the Resistance R2 and capacitance C2 for the three series done for $NaClO_4$ salt with ECPC organic electrolyte. The numbers indicate the ranking in liquid addition per mass of solid electrolyte

For the medium frequency characteristics, the resistance plot R2 is generally attributed to the charge transfer resistance. This resistance should only pertain to the ability of the electrodes to transfer their electron charges to the current collectors. Smaller cathode particles would result in a larger surface area, so more effective transfer. The orange curve indicates a lower resistance for all the cells, substantiating this hypothesis.

For a larger concentration of organic electrolyte ECPC with $NaClO_4$ salt, the resistance decreases, indicating the contribution of the organic electrolyte. The Figure indicates that capacitance is highest for the thickest and thinnest batteries with 67.3nm BASE particles (and little liquid addition), while the series with smaller particles presents similar capacitance even though the amount of added liquid is much higher. This indicates that the charged layer around the small particles is saturated. Increasing the concentration for bigger particles could result in a larger double layer capacitance. The capacitance values indicate not only a relation with the liquid addition, but also with the amount of BASE. Increasing the amount of BASE generally increases the capacitance. A large amount of BASE and added liquid naturally results in a high capacitance and low resistance (far right of **Figure**). These results indicate that charge transfer improves with our liquid to solid ratio, and double layer capacitance also increases with addition of ECPC with $NaClO_4$ salt.

Diffusion is often characterized by the Warburg element at low frequency, yet transport phenomena could not be simulated accurately for the EIS measurements using only the Warburg element. Thus, low frequency phenomena had to be modelled using a resistance, capacitance and a Warburg element, which is a form of admittance.

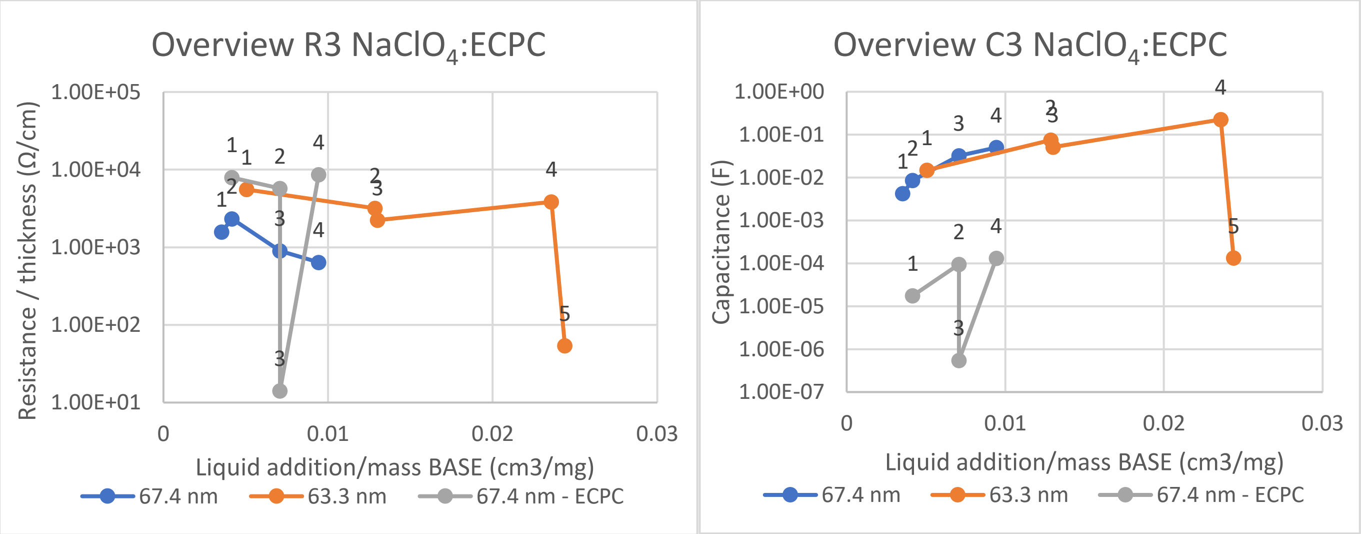

Figure 15. Overview of the Resistance R3 and capacitance C3 for the three series done for $NaClO_4$ salt with ECPC organic electrolyte. The numbers indicate the ranking in liquid addition per mass of solid electrolyte.

Mass transport should be directly related to the thickness it needs to go through. The diffusion resistance relates to the path length L and the diffusion coefficient D of BASE, according to the diffusion path length (L^2/D). For a thicker battery, it is harder to move to the other side than for a thinner one (in the same amount of time).

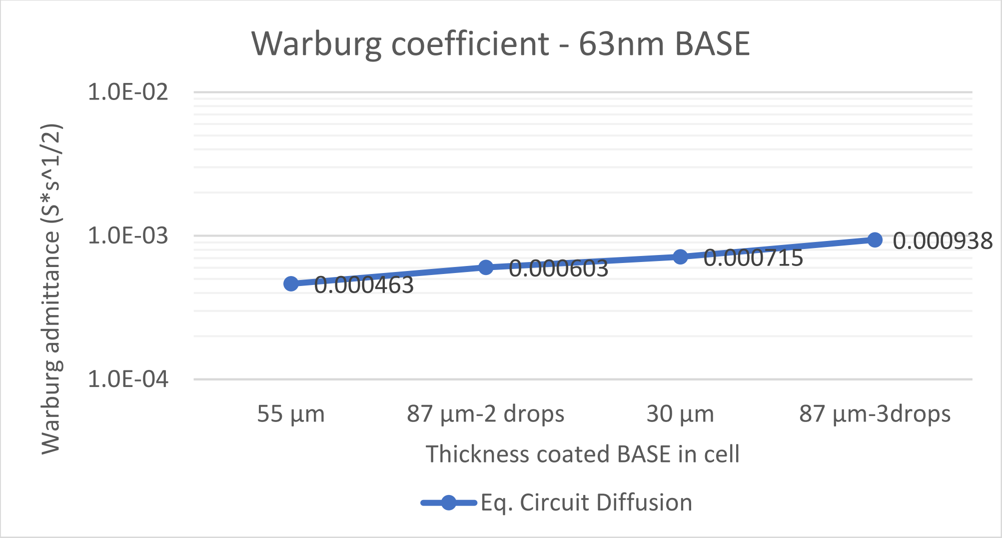

Figure 16. Warburg coefficient for Na^+ ion through the batteries for the 63.3 nm series.

The diffusion of the low frequency third semi-circle for the 63nm BASE series indicates that the equivalent circuit parameter relating to diffusion is related to the organic electrolyte addition, and not the cell thickness.

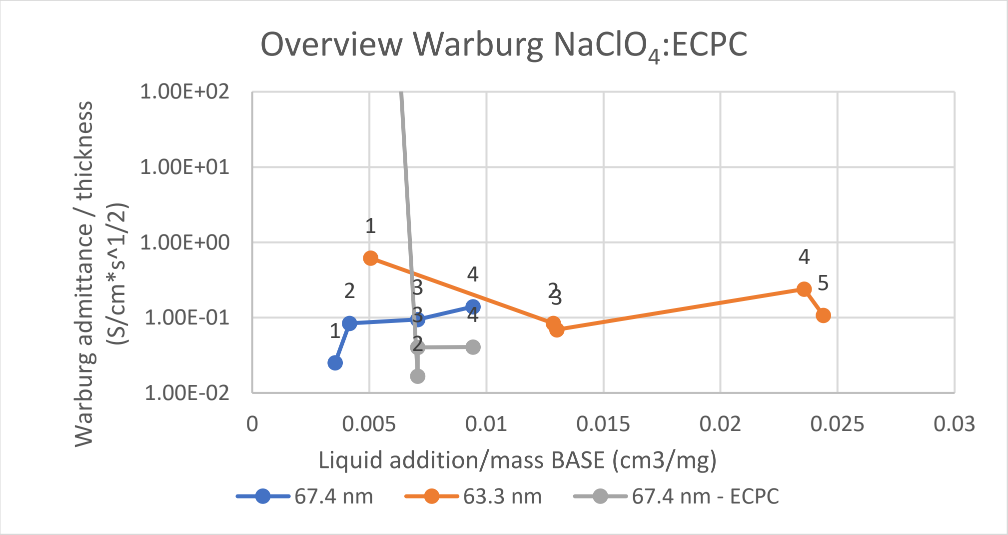

Figure 17. Warburg coefficient pertaining to ionic diffusion through the cells.

The three plots in **Figure 15,16 and 17** are highly relevant to our subject, as they give a direct indication of the ease of ionic transport though the system. Particle size and liquid addition directly influence this phenomenon. The resistance R3 indicates that the $NaClO_4$:ECPC series with 67.4 nm BASE particles is indeed more conducting than without $NaClO_4$ added salt, while decreasing the particle size increases the relative resistance and increasing the liquid addition showed a marginal effect. Only reducing the electrolyte thickness resulted in distinct resistance improvement. This can be explained by the diffusion length (L^2/D) discussed earlier. The third cell of ECPC series had in fact 63.3 nm BASE particles, showing a distinctly lower resistance than the others.

The reported capacitance for C3 indicates a clear correlation between liquid addition and increase in capacitance for the 67.4 nm series. The 63 nm BASE particle series highlights an interesting phenomenon when looking at the difference between cell 4 and 5. While both cells have similar added volumes relative to the BASE mass, cell 5 has a distinctly lower resistance and capacitance. This leads us to believe the sheer amount of added $NaClO_4$ salt is solely responsible for the decrease in resistance and capacitance.

Finally the Warburg element presents a higher ionic diffusion for the $NaClO_4$:ECPC series with 67.4 nm BASE particles than without salt, indicating that $NaClO_4$ facilitates ionic transport as predicted. This indicates that Diffusion is dictated by the amount of organic electrolyte ECPC with $NaClO_4$ salt. Yet, a clear statement cannot be made about the relation between electrolyte particle size and Na^+ transport, as the 63.3 nm series does not present a clearly higher impedance, as would be expected due to more point contacts.

5.1.2 Series with TES-TFSI ionic liquid

After analysing the concept with tape casted Na-beta”-alumina pasted on top of the cathode thin film, the actual contribution of the Na-beta”-alumina particles should be examined. This can be done by using only BASE particles as electrolyte by mechanically pressing the powder into a pellet. The point contacts with dominate the impedance, which is why an addition of a few drops of ionic liquid without Sodium salt can facilitate transport.

The idea behind this concept, is to use the Na^+ ions present in the Na-beta”-alumina by “drawing them out” of the particle. The ionic liquid has a different chemical potential compared to Na-beta”-alumina, which results in the Na^+ ions being drawn out of the solid particles. The ions have a higher affinity with the ionic liquid due to a lower energetical state. It is conceptualized that these ions would form a charged layer on the surface of the particles, facilitating ionic transport and enhancing contact between the particles, without the need for sintering at high temperature. A slurry concept with a form of pasted ionic liquid: BASE slurry is also experimented with to attempt a better interphase contact.

Table 5. Values for the TES-TFSI series, relating volume of ionic liquid TES-TFSI addition to the mass of the solid electrolyte BASE.

			liquid a	solid electrol	thickness after pasting		particle size		additive/BASE	
			cm^3	**mg**	µm	µm	nm	nm	cm^3/mg	
1drop=0.05mL=0.05cm3					NNM	BASE	NNM	beta		
TES-TFSI	slurry/pellets									
Ilslurry	slurry		0.15	450	30	530	**101.95**	**67.37**	**3.18E-13**	**1**
TFSInormal	slurry		0.15	450	30	530	**101.95**	**67.37**	**3.18E-13**	**1**
3,5IL	beta pellet		0.175	430	25	1000	**101.95**	**67.37**	**3.89E-13**	**2**
4IL	beta pellet		0.2	430	30	1000	**101.95**	**67.37**	**4.44E-13**	**3**
TFSIslurry	slurry		0.515	719.95	8	750	**101.95**	**67.37**	**6.83E-13**	**4**
6IL	beta pellet		0.3	400	30	1000	**101.95**	**67.37**	**7.16E-13**	**5**
TFSIsmall	slurry		0.15	450	30	530	**101.95**	**35.56**	**1.14E-12**	**6**
3IL-Small	beta pellet		0.15	430	30	1000	**101.95**	**35.56**	**1.19E-12**	**7**
3IL-Big	beta pellet		0.15	430	30	1000	**101.95**	**32.30**	**1.45E-12**	**8**

The measured elements from the modelled equivalent circuit are plotted hereafter. Values have been derived for both pre and post-cycling in order to assess the evolution of the system after cycling.

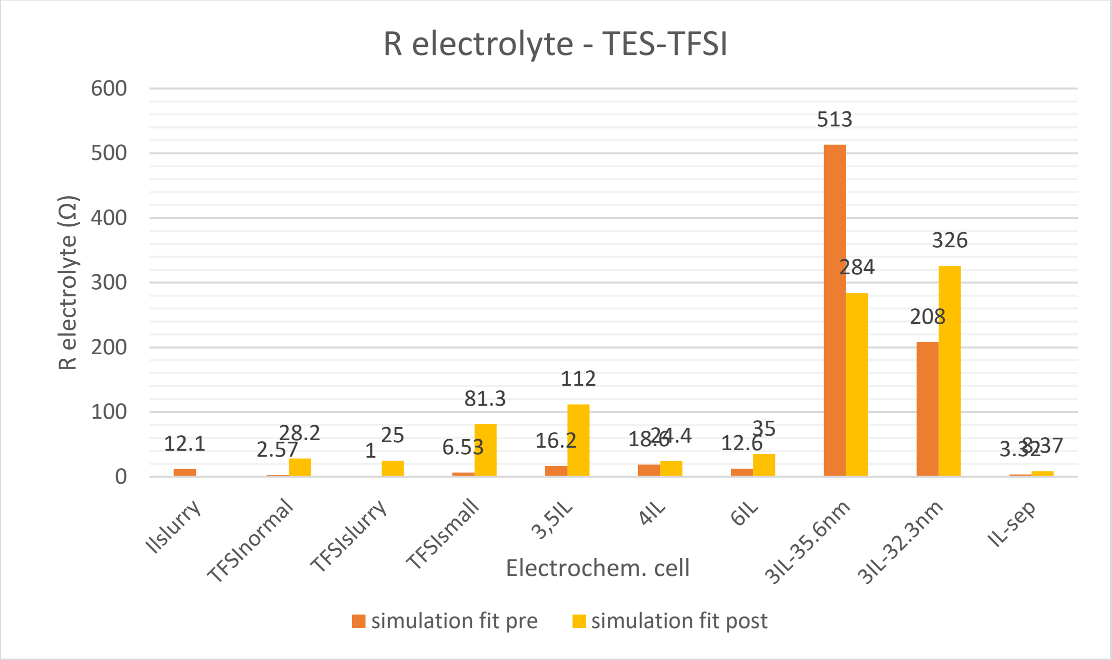

Figure 18. Resistance relating to the first resistance element of the equivalent circuit modelling, R_e, for the TES-TFSI series. This resistance is attributed to the electrolyte resistance, directly related to conductivity.

The $R_{electrolyte}$ plot in Figure 18 indicates that the resistance increases more post cycling when less ionic liquid TES-TFSI was added, pointing towards a form of passivation for higher IL addition. The cells with smaller particle size (far right) also stand out due to a resistance that is far superior to the others. This can be attributed to the higher surface area and amount of point contacts that is far superior for these batteries. Nevertheless, the cell with 32.3nm BASE particles shows a lower resistance than for 35.6nm. This could be a result of the ionic liquid addition. Yet all the other batteries in the series possess an electrolyte particle size almost twice as large (67.4nm), which contradicts the previous reasoning.

In order to compare the effect of additives on the particle size of the electrolyte, each electric value of the batteries has been correlated to the ratio volume of liquid addition/mass of Na-beta”-alumina

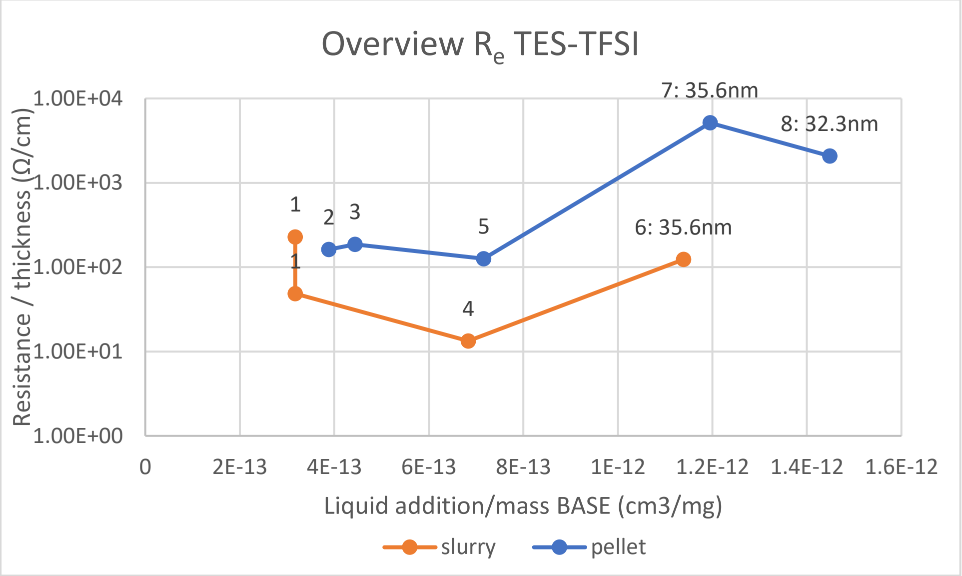

Figure 19. Overview of the electrolyte resistance R_e for pellet and slurry series done with the ionic liquid TES-TFSI without added salt. The numbers indicate the ranking in liquid addition per mass of solid electrolyte. A higher number means a larger liquid addition.

By normalizing all the $R_{electrolyte}$ values by dividing them by the thickness of the electrolyte in the cell, the electrolyte can be analysed without the impeding thickness factor.

According to the $R_{electrolyte}$ overview for TES-TFSI in Figure 19, it is clear that the slurry concept reports lower resistance values for the electrolyte compared to the pellet. Take #4 slurry and #5 pellet, for the same amount of ionic liquid addition, the resistance is tenfold. With mechanically pressed pellets, the ionic liquid would seep between the pressed particles to form a similar layer around the BASE particles as for the slurry. This would indicate that the conductivity through the electrolyte is improved solely by the conceptual difference between slurry and pellet, probably relating to the ionic liquid coverage in the electrolyte.

For the high frequency and medium frequency, the time constants are attributed to SEI, charge transfer resistance and double layer capacitance. These parameters are not dependent on the thickness of the electrolyte. Therefore, they shall only be plotted versus the measured data (R and C).

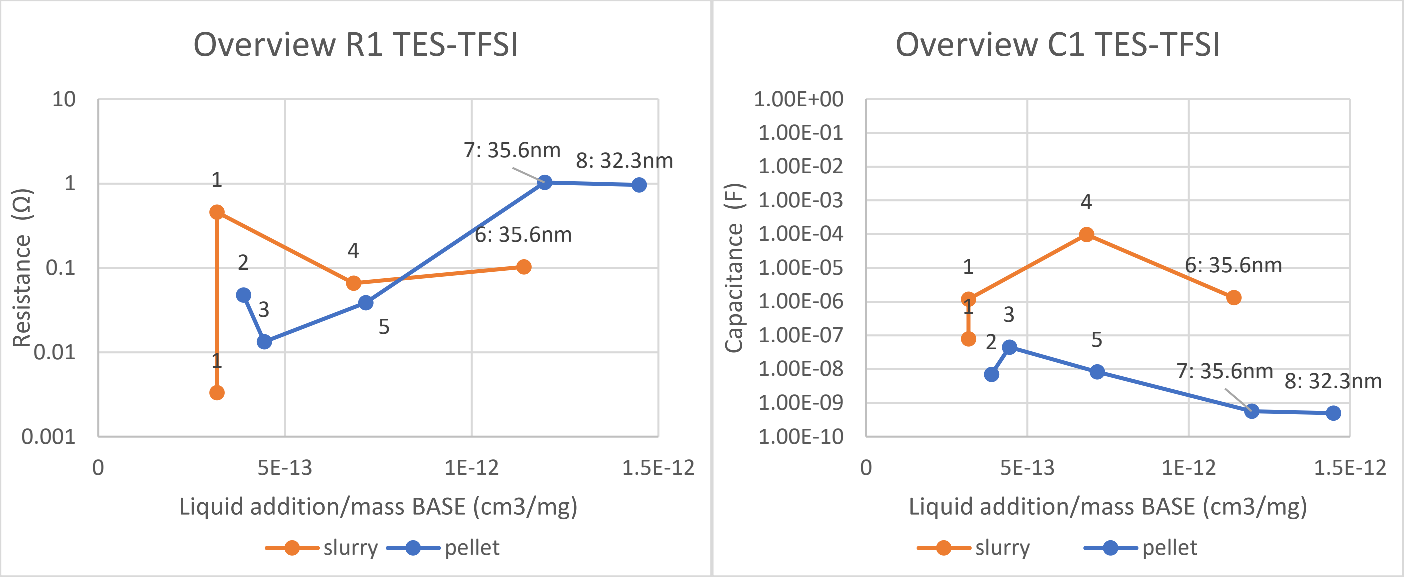

Figure 20. Overview of the Resistance R1 and Capacitance C1 for the pellet and slurry series done with the ionic liquid TES-TFSI without added salt. The numbers indicate the ranking in liquid addition per mass of solid electrolyte. A higher number means a larger liquid addition.

The high frequency values measured here (R1 and C1) are generally attributed to SEI. Ionic liquid addition or electrolyte particle size should not influence this factor. The resistance plot in Figure 20 shows that for the slurry concept, liquid addition barely influences the resistance for this time constant, while resistance increases for the pellet concept.

The capacitance plot in Figure 20 clearly distinguishes both concepts. The slurry presents a steady higher capacitance compared to the pellet concept. This can be due to the interface difference between both concepts. When using a pellet, the electrode-electrolyte interface contact is much worse than when using a slurry. This should also show for the resistance plot R1, but is not quite clear.

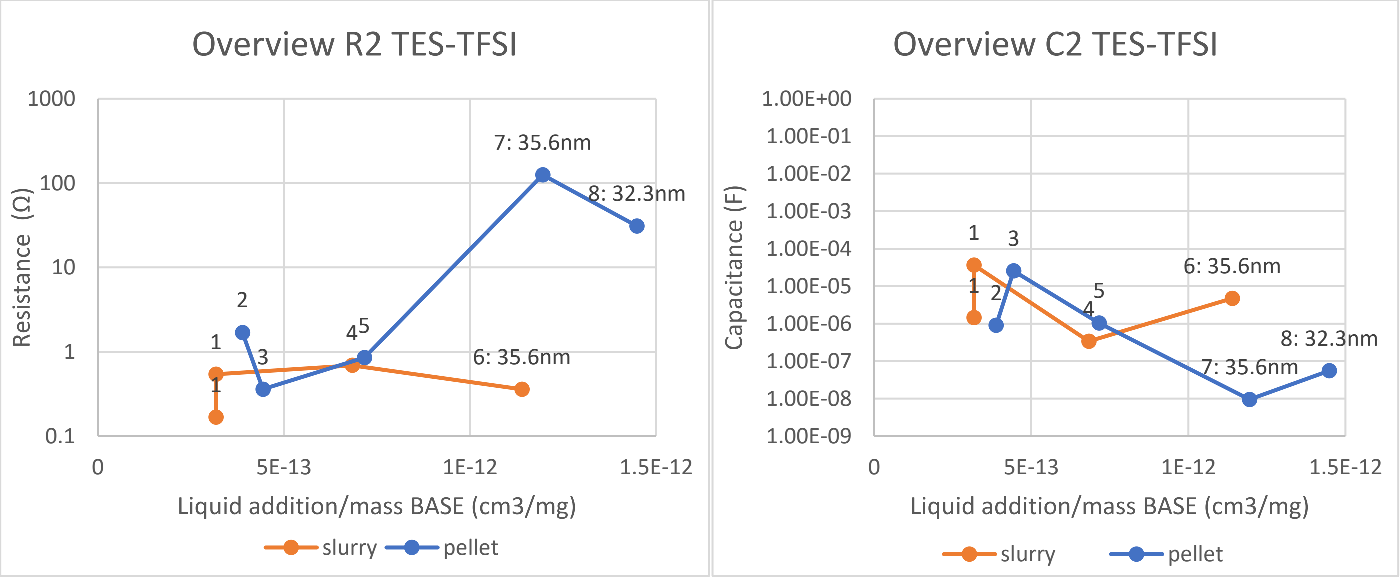

Figure 21. Overview of the Resistance R2 and Capacitance C2 for the pellet and slurry series done with the ionic liquid TES-TFSI without added salt.

The mid-frequency range resistance R2 in Figure 21 indicates that increasing liquid addition barely influences the resistance. This coincides with the attribution of this time constant to charge transfer capabilities. The charge transfer resistance should be influenced solely by particle size of the electrode material, which relates to electron transfer from the electrode to the current collector.

Capacitance plot C2 indicates that a similar capacitance is reached for the pellet compared to the slurry, by adding slightly more ionic liquid. Yet for a same BASE particle size, the slurry once again proves to be more performant.

When comparing particle sizes and a potential correlation with a space-charge layer, a smaller particle size should have a higher ionic liquid effect, so potentially more space charge effect than a bigger particle. In our case, it is hard to say definitively, as the increased capacitance for the smaller particle cells could also be related to the additional ionic liquid present in that system. A concept should be formulated, where all cells have the same liquid to solid ratio. A clear conclusion could be derived from such a concept.

It is possible that the different concepts have influenced the electrochemical interactions between the particles. Indeed, the slurry concept shows much lower resistance compared with the pellet concept, with a somewhat higher capacitance. This could be an indication that the point contacts in the pellet are still dominant, and the ionic liquid provides insufficient support to alleviate this.

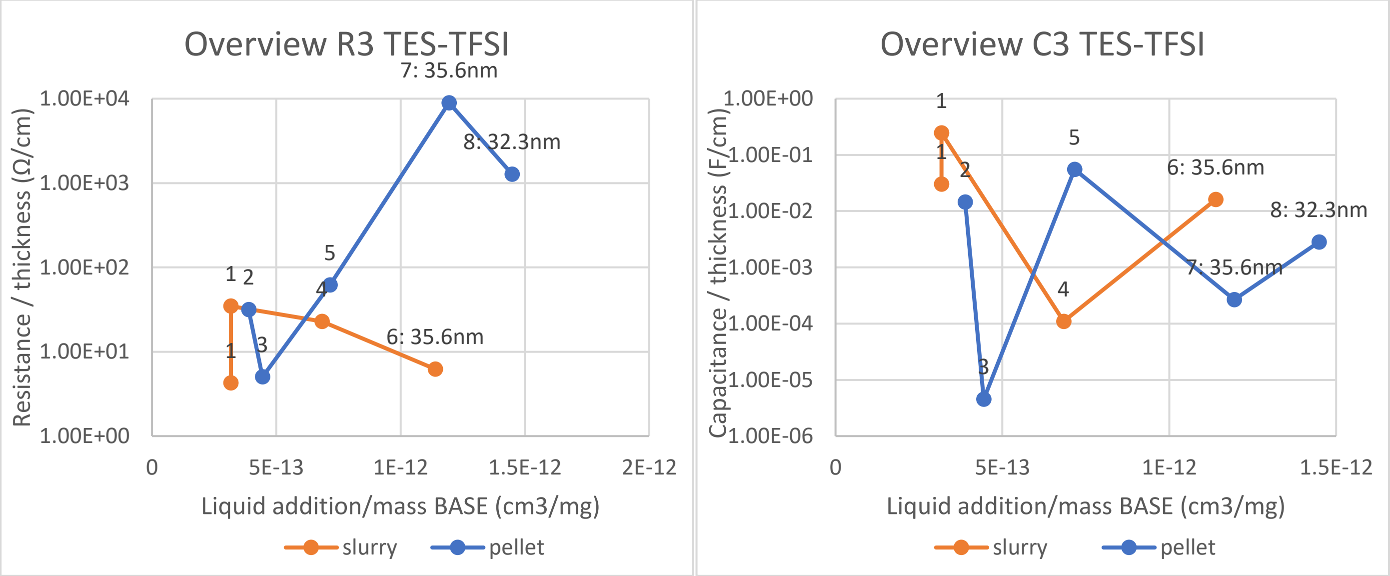

Figure 22. Overview of the Resistance R3 and capacitance C3 for the series done with ionic liquid TES-TFSI without added salt. The numbers indicate the ranking in liquid addition per mass of solid electrolyte.

A general pattern for the resistances in Figure 22 concurs with the rest of the resistance measurements, showing that the pellet series has a higher resistance than the slurry resistance. This is to be expected. The Capacitance C3 may indicate that the capacitance is similar for low addition of ionic liquid, while a high addition of liquid results in a capacitance

100-fold higher for the slurry concept. The particle size difference and relating electrochemical effects cannot be attributed either to the difference in surface area or the liquid addition. Again, a specific design relating to the surface area of the particle should be developed, only after unravelling the shape of the BASE particles.

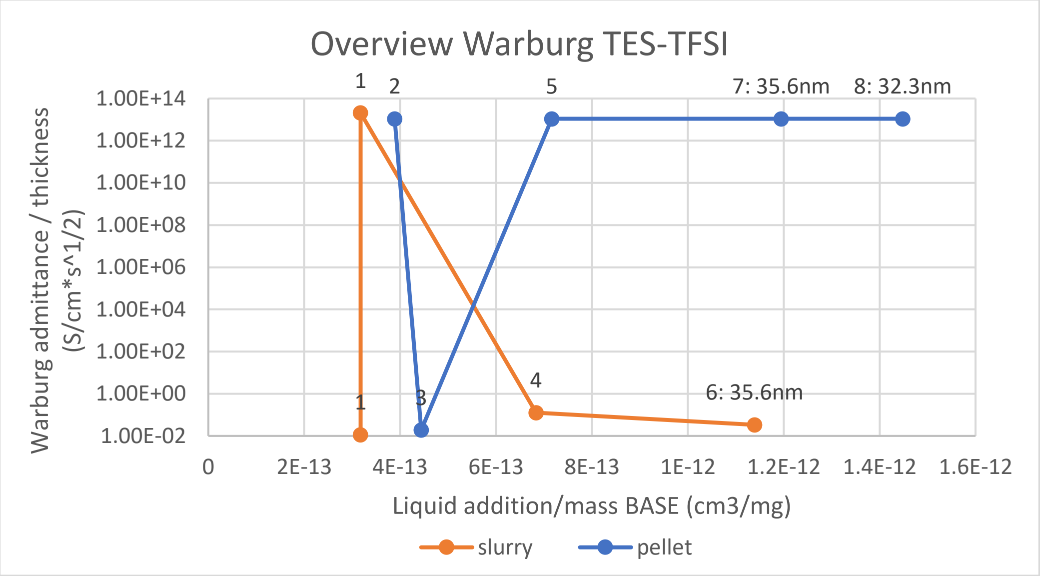

Figure 23. Low frequency equivalent element Warburg for the TES-TFSI ionic liquid series; pertaining to ionic diffusion through the cells.

In Figure 23, the slurry with smaller particles shows a lower diffusion compared to the regular slurries. This could be an indication that the conduction path is still through the BASE particles, and that smaller particles impede ionic diffusion due to the increase in point contacts. It could be in relation to point defects in the solid electrolyte, or the promotion of side-reactions for particles with a higher surface area. In smaller particles, one defect could have a much larger impact than for bigger particles, where the ions can still diffuse through side-channels. The effect of a side-reaction has an equally large impact, as a similar impeding reaction would impede the smaller particle more.

The resistance plot R3 confirms this theory, as the pellet concepts also show a high resistance for the cells with smaller BASE particle compared to the regular pellets.
The Warburg element shows extremes on both sides, which is related to the modelling accuracy. Since the low frequency impedance measurement has overlapping transport phenomena, it is challenging to extract a clear Na^+ diffusion value. Further study should be done based on a concept solely focussing on deriving the impact of ionic liquid on the diffusion.

5.1.4 Series with Pyr$_{14}$FSI ionic liquid

A second series with a different ionic liquid, Pyr$_{14}$FSI, has been done. Since the pellet clearly performs worse than the slurry, the latter was pursued further. By using a different ionic liquid (still without added Sodium salt), the degree of "enhancement" can be compared. Pyr$_{14}$FSI was reported to be the "magic" ionic liquid **[152]**, reporting positive results and the formation of a protective SEI layer. It also showed great promise when used in combination with Na-beta"-alumina pellet, reporting high cyclability at 70 °C [**101**]. Therefore, it was chosen as the ionic liquid for our second attempt at testing the interactions between ionic liquid and Na-beta"-alumina particles in Sodium electrochemical cells.

With a different chemical potential vs Na$^+$ than TES-TFSI, Pyr$_{14}$FSI may shed some light on the difference in interaction with the solid-state Na-beta"-alumina electrolyte particles, and the potential space-charge effect in particular. It is conceptualized that these ions would form a charged layer on the surface of the particles, facilitating ionic transport and enhancing contact between the particles, without the need for sintering at high temperature. With a higher affinity towards Na$^+$ ions, a larger space charge effect may be observed and potentially measured using EIS.

Table 6. Overview of the physical data related to the Pyr$_{14}$FSI series. The ranking at the far right indicate the degree of additive added per solid state electrolyte surface area. This ranking will be used to differentiate the various cells.

		liquid additive	solid electrolyte	thickness after pasting		particle size		additive/BASE	
1drop=0.05mL=0.05cm3		**cm^3**	**mg**	µm	µm	nm	nm	cm^3/mg	
EIS-pyr2.5-base7.5-ocp2.67V	slurry	0.13	510	30	580	**101.95**	67.37	2.54E-04	**1a**
EIS-pyr14-betadry(7.5-2.5)(	slurry	0.13	510	30	580	**101.95**	67.37	2.54E-04	**1b**
EIS slurry pyr14-base	slurry	0.13	510	30	580	**101.95**	67.37	2.54E-04	**1c**
pyr14slurry++(2.56VOCP)	slurry	0.22	633	8	710	**101.95**	67.37	3.48E-04	**2**
slurryPyr14-beta(2.84VOCP)	slurry	0.21	578	10	650	**101.95**	67.37	3.59E-04	**3**
EIS-PyrnormalSlurry-2.56V	slurry	0.14	383	30	440	**101.95**	67.37	3.73E-04	**4**
EIS-PyrsmallSlurry-2.6V	slurry	0.14	383	30	440	**101.95**	**35.56**	3.73E-04	**5: 35.6nm**
pyr14slurryTHICK(2.59VOCP)	slurry	0.24	598	40	680	**101.95**	67.37	3.96E-04	**6**
EIS-NNM-Pyr14FSIslurryBASE	slurry	0.15	320	30	441	**101.95**	67.37	4.72E-04	**7**
betapellet-NNMslurry(2.82V	pellet	0.15	250	100	500	**101.95**	67.37	6.00E-04	**8**
BASEpellet0.5mm(2.5VOCP)	pellet	0.15	250	100	500	**101.95**	67.37	6.11E-04	**9**

In order to present a well performing battery using the concepts initially thought of, the various impeding factors are once more investigated.

Cells 1.c and 3 have not been able to be measured post-cycling, as they short circuited before. A short-circuited battery does not render an impedance spectrum (impedance is then 0). This short-circuit was most likely due to the assembly process. Making a battery comprising an electrolyte slurry implies that the slurry is not fully solid. Upon pressing the cell together when assembling the components, potential contact between cathode and anode could have happened. This contact could also have occurred overtime, as both sides of the Swagelok cell press the contents together for maximal contact strength.

The reason a few of these cells (1a,b,c) have the same "recipe" is due to the fact that a reproducible result and working battery was hard to achieve for this series. This was found to be related to the fact that the Na-beta"-alumina had absorbed water (1a and 1c). BASE is a strong desiccant, and overtime the Na$^+$ ions had been replaced by H$^+$ from the water in the environment. This led to side-reactions during the assembly of the battery, which would only be remedied by a drying process at 600°C for a prolonged period of time.

This water absorption was hard to detect, and did not show on the impedance measurement or in the X-Ray Diffractometer. This is logical, because protons are not a crystal.
The water absorption should have shown in the EIS however, as moisture absorption severely reduces the ionic conduction of the material. Indeed, the Na^+ ions that should be able to hop through the layers of beta”-alumina, were impeded due to their positions being occupied by the hydrogen.

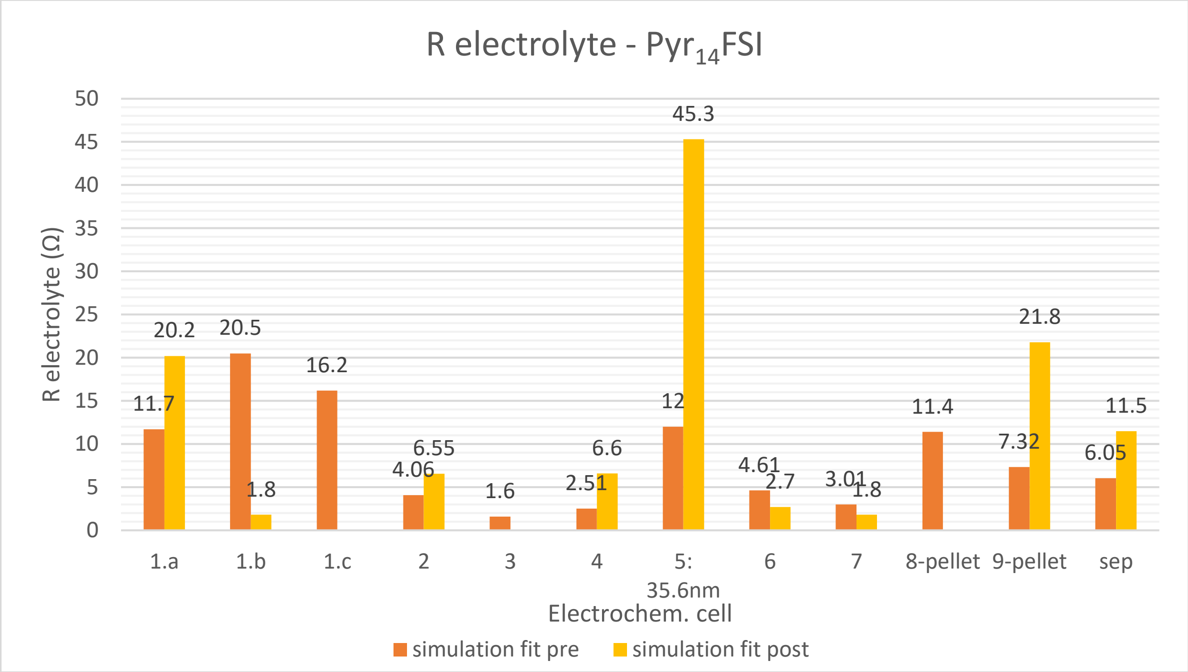

Figure 24. Resistance relating to the first resistance element of the equivalent circuit modelling, R_e, for the $Pyr_{14}FSI$ series. This resistance is attributed to the electrolyte resistance, directly related to conductivity.

The addition of ionic liquid on the system lightly affected the electrolyte resistance, as observed in Figure 24. Yet the improvement between cell 2 and cell 7 is only visible post-cycling. The resistance post-cycling is lower for the cells on the right than the ones on the left. This can be attributed to the liquid addition, as the other parameters remained unchanged. Cell 5 had a BASE particle size almost twice as small as the rest, yet the resistance pre-cycling was still low, relatable to Cell 1a (the cell with wetted solid electrolyte). The resistance post-cycling however, indicated a strong evolution during the cycling. This can be caused by the relative higher surface area of smaller particles, promoting side-reactions, or contaminants in the ball-mill (used to reduce the particle size). Cell 1b, as well as cells 6 and 7, reported a lower resistance post-cycling compared to pre-cycling. This would indicate an improvement in the conductivity, caused by passivation layer forming or a favourable ionic conduction path.
It can be noted that cells 4-5 have the same liquid/mass ratio, yet the resistance for the smaller particle is 4 times greater. This indicates that the bigger particle should work better, implying that the solid electrolyte bulk provides the dominating conductivity.

The pellet concepts were once more tested, resulting in acceptable electrolyte resistances for pre and post-cycling.
A cell with a separator and no Na-beta”-alumina was also tested with an addition of ionic liquid. With no added Sodium salt, it is surprising that this cell still shows a potentially high conductivity.

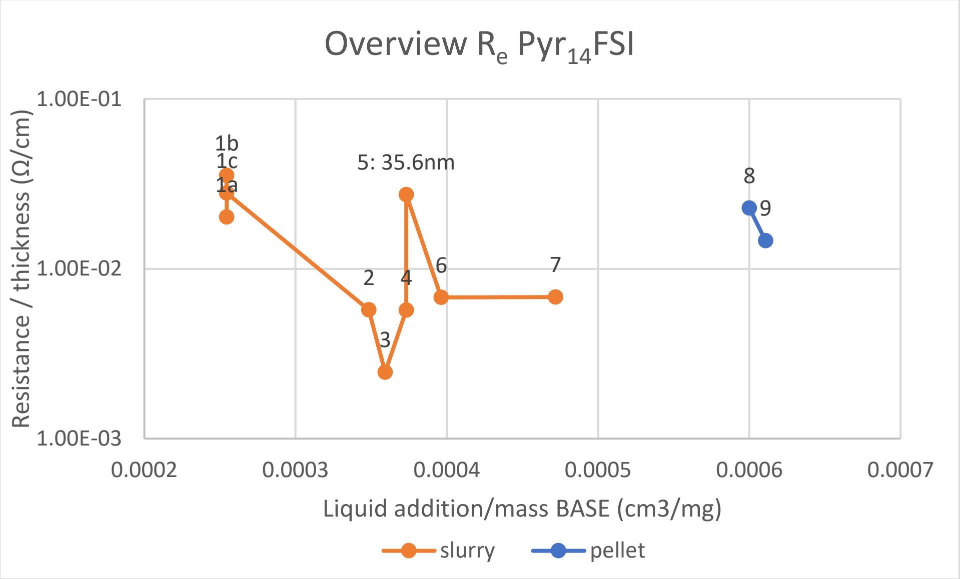

Figure 25. Overview of the electrolyte resistance R_e for pellet and slurry series done with the ionic liquid $Pyr_{14}FSI$ without added salt. The numbers indicate the ranking in liquid addition per mass of solid electrolyte. A higher number means a larger liquid addition.

By normalizing all the $R_{electrolyte}$ values by dividing them by the thickness of the electrolyte in the cell, the electrolyte can be analysed without the impeding thickness factor, in Figure 25.

According to the $R_{electrolyte}$ overview for $Pyr_{14}FSI$, we can observe that an increase in liquid addition per mass of BASE decreases the resistance $R_{electrolyte}$. This trend is visible for the slurry series, and to some extent for the pellet series. The decrease in $R_{electrolyte}$ with liquid addition indicates that the ionic liquid contributes to the electrolyte conductivity, even though it does not have a dissolved Sodium salt at the moment of assembly.

A decent reproducibility is shown with the three cells 1a,b and c. It is also interesting to note that for those three cells, only 1b has thoroughly dried components. This leads us to believe that EIS does not show evidence of decrease in conductivity when BASE is in contact with water, contrary to what was expected. Cycling shown in a later part of the Thesis will show evidence of corrosion for the cells 1a and 1c, while 1b showed acceptable cyclability as well as no evidence of corrosion. In-situ analysis could unravel the mechanisms linked to this corrosion, but we can ascertain that it is related to moisture contamination.

A trend also appears when looking at cells 2 through 7, as they appear to have related $R_{electrolyte}$ values. This points toward a form of liquid saturation, as the contribution relating to the ionic liquid does not increase further.

When looking at cell 5 with a BASE particle size of 35.6 nm instead of 67.4 nm, we can see a relatively higher resistance. This is to be expected, as a smaller particle results in higher surface area, thus more point contacts. For the same liquid addition, $R_{electrolyte}$ is four times greater for a particle roughly twice as small. This could be an indication of a surface area correlation; for a particle twice the size, the contribution is squared (2^2).

We can also observe that the pellet series shows a similar resistance at double the liquid addition.

For the high frequency and medium frequency, the time constants are respectively attributed to SEI for high frequency, and charge transfer resistance and double layer capacitance for medium frequency. These parameters are not dependent on the thickness of the electrolyte. Therefore, they shall only be plotted versus the modelled data for R1 and C1.

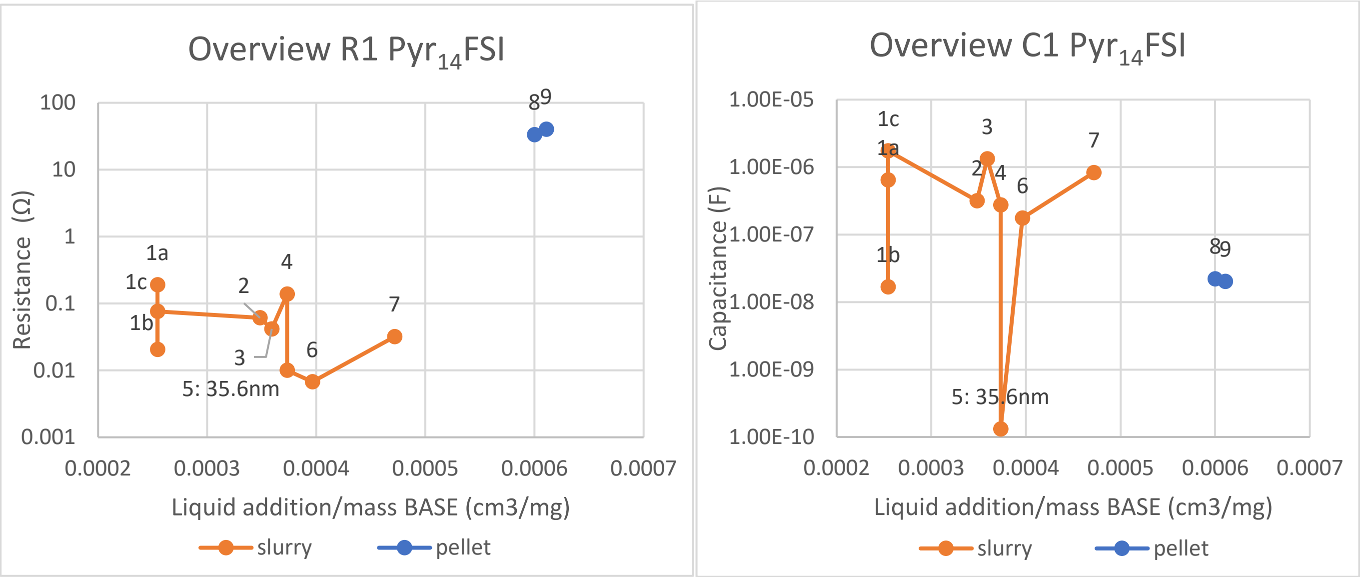

Figure 26. Overview of the Resistance R1 and capacitance C1 for the pellet and slurry series done with the ionic liquid $Pyr_{14}FSI$ without added salt. The numbers indicate the ranking in liquid addition per mass of solid electrolyte. A higher number means a larger liquid addition.

The high frequency values measured here (R1 and C1) are generally attributed to SEI. Ionic liquid addition or electrolyte particle size should not influence this factor.

The resistance plot R1 shows that for the slurry concept, liquid addition slightly improves the resistance for this time constant, while resistance increases for the pellet concept. This is to be expected, as the SEI should only be influenced by electrode-electrolyte interphase parameters. If the resistance values were to change as a function of liquid addition, it would be evidence of a side-reaction provoked by the ionic liquid.
The pellet concept shows a resistance almost a thousand-fold compared to the slurry. This brings into evidence the electrode-electrolyte interphase contact issue relating to solid-state batteries, which is highlighted here when comparing slurry and pellet.

A clear statement regarding the influence of particle size cannot be made for this parameter. However, the dry BASE slurry shows a somewhat lower resistance at the interphase, which could be related to the absence of corrosion in the cell.

The capacitance plot highlights the particle size variation. The slurry presents a steady higher capacitance compared to the pellet concept, except for the dry BASE cell 1b and the smaller particle cell 5. This can also be attributed to the interface difference between both concepts. The excess capacitance shown by the cells could be related to the moisture contamination. The very low capacitance C1 for cell 5 can be related to the concept of reactive power. Indeed, if a system (in our case the BASE particles) requires a certain amount of reactive power to function, smaller particles would require less reactive power to function. Similarly, a more performant particle (dry BASE) would also require less reactive power to fulfil its conducting purpose.

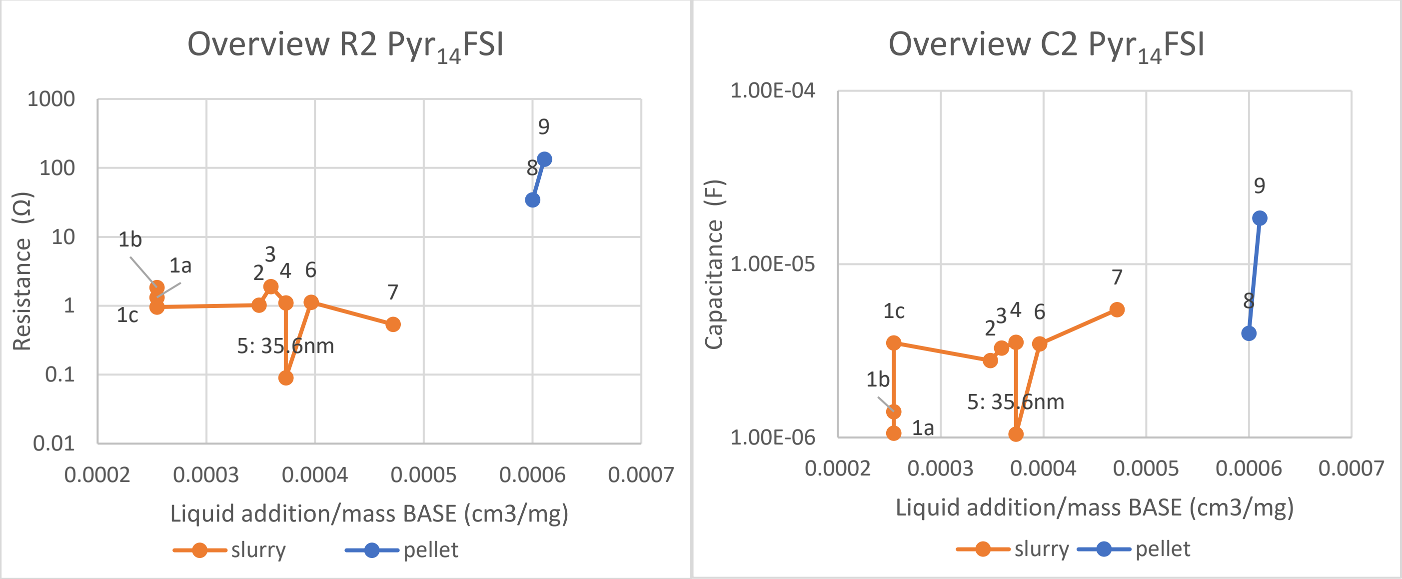

Figure 27. Overview of the Resistance R2 and Capacitance C2 for the pellet and slurry series done with the ionic liquid $Pyr_{14}FSI$ without added salt. The numbers indicate the ranking in liquid addition per mass of solid electrolyte. A higher number means a larger liquid addition.

The mid-frequency range resistance R2 in Figure 27 shows that liquid addition barely influences the resistance. This coincides with the attribution of this time constant to charge transfer capabilities. The charge transfer resistance should be influenced solely by particle size of the electrode material, which relates to electron transfer from the electrode to the current collector.
It should be noted that the pellet concept reports a higher resistance despite having the same charge transfer competences as the slurry concept. This could be explained by overlapping phenomena. Seeing as the pellet concept has proven to have higher resistances, it is possible that the reported resistance R2 is actually an overlapping phenomenon. This could be due to an overlapping higher mass transport resistance. This would be more prominent for the pellet concept (relating to the slurry concept) due to the intrinsic properties of the mechanically pressed concept.

We should also address the lower resistance R2 of the smaller particle size of cell 5. Seeing as charge transfer is not related to the electrolyte particle size, the reported resistance could also be related to an overlapping impedance contribution. Even though it is challenging to pinpoint why the resistance is lower for cell 5, it does indicate that smaller BASE particles would perform better than bigger ones.

Capacitance plot C2 indicates that a similar capacitance is reached for the pellet compared to the slurry, by adding almost twice the volume of ionic liquid. Yet for a same BASE particle size, the slurry once again proves to be more performant.
A difference can be noted however. The capacitance C2 is 10 times smaller post-cycling for the bigger particle cells (Appendix), while the capacitance for the smaller particles remained constant. This points toward a higher stability for the double layer capacitance around the smaller particles. The charges in the double layer for the bigger particles could have been neutralized by other charges present in the bigger particle outer layers, while all the charges have been fully extracted from the smaller particles.

When comparing particle sizes and a potential correlation with a space-charge layer, a smaller particle size should have a higher ionic liquid effect, so potentially more space charge effect than a bigger particle. This logic does not seem to apply here, as the smaller particle cell 5 shows the opposite. The lower capacitance for C2 is similar to the behaviour for C1, as are the patterns for both figures, pointing towards an overlap in the phenomena for C1 and C2. Thus, the overview for C2 indicates the same phenomenon as for C1, that a smaller particle would require less reactive power to fulfil its ionic conductivity function.

Even though the C2 overview does not support the potential correlation between space charge and particle size, it does highlight the flaws relating to EIS. It also illustrates why one should not attribute the modelled electrical components to electrochemical phenomena light-heartedly, without previously accurately proving its existence.

A concept should be formulated, where all cells have the same liquid to solid ratio. A clear conclusion could be derived from such a concept.

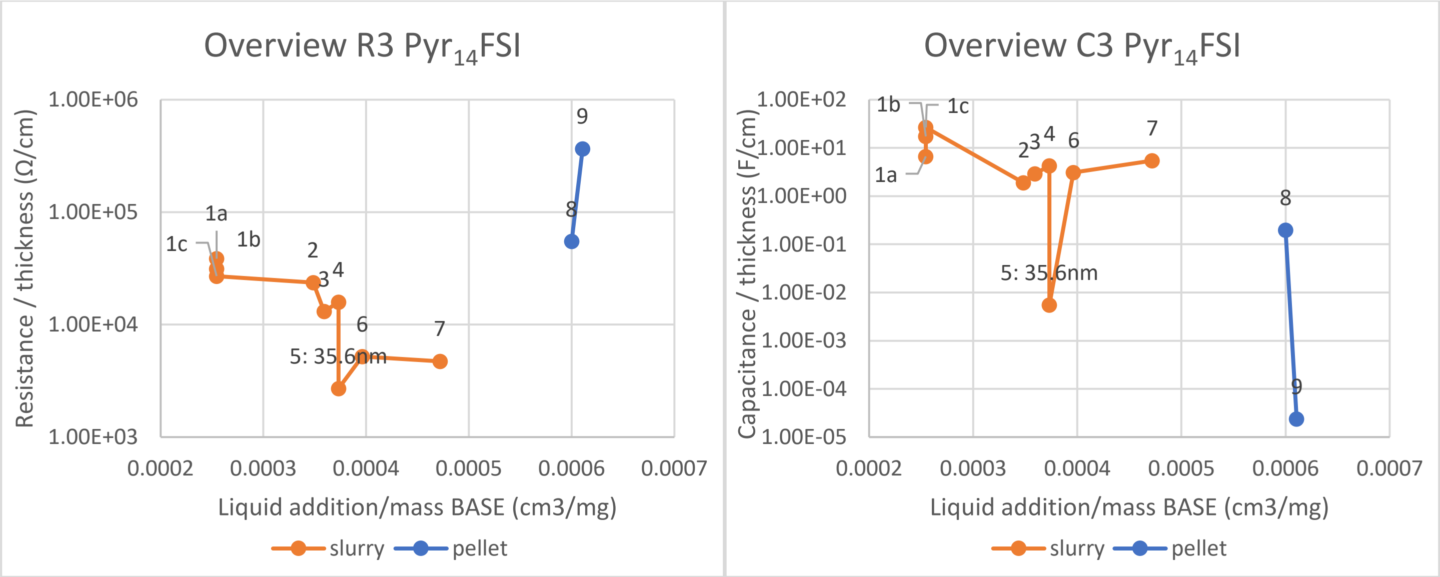

Figure 28. Overview of the Resistance R3 and capacitance C3 for the three series done series done with the ionic liquid $Pyr_{14}FSI$ without added salt.

For the $Pyr_{14}FSI$ ionic liquid series, the low frequency part of the Nyquist plots (high time constant) presents a few interesting points. First of all, resistance R3 indicates a clear correlation between ionic liquid addition to resistance for the slurry concept, while the pellet concept just shows the same pattern previously observed: a higher impedance than the slurry concept. For the slurry concept, the higher the liquid addition, the more it decreases the resistance. This points toward a promotion of mass transport for increasing IL addition. The smaller particle also shows a lower resistance, which can be explained by the larger ionic liquid contribution in relation with the surface area. This would indicate that ionic transport is promoted by increasing the surface area of the BASE particles, thus increasing the interaction that $Pyr_{14}FSI$ has with the solid electrolyte.

The general pattern for the resistance concurs with the rest of the resistance measurements, showing that the pellet series has a higher resistance than the slurry resistance. This is to be expected. However, the Capacitance C3 presents the same pattern as for C2 and C1. It shows a similar capacitance for all the cells, in spite of additional ionic liquid. Yet, cell 5 still reports a smaller capacitance, explained for the previous figures.

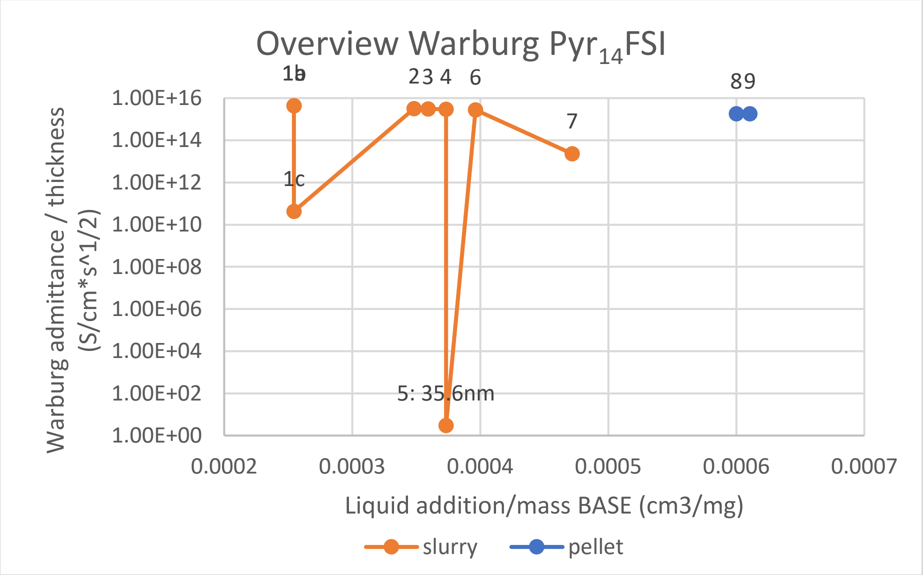

Figure 29. Low frequency equivalent element Warburg for ionic liquid $Pyr_{14}FSI$ series; pertaining to ionic diffusion through the cells.

The pellet concept indicates an inverse correlation between resistance and capacitance. The higher the capacitance, the lower the resistance, yet almost equal Warburg impedances. This concurs with the behaviour in the organic electrolyte series, but not the TES-TFSI series. This inconclusive behaviour can be attributed to the circuit modelling. The low frequency part of the spectrum is always more challenging to simulate and fit, therefore the resulting values are not as accurate as for the high and medium frequency part of the spectrum. A clear conclusion cannot be drawn regarding this correlation for the pellet concept. The pellet cells both failed during cycling, meaning the values drawn from these EIS measurements should be taken lightly.

From the Warburg admittance in Figure 29, we can derive one clear piece of information. The smaller particle presents a much lower ionic diffusion. This is unlike what we expected, yet it concurs with the previous TES-TFSI series. Indeed, the intrinsic diffusion constant is scale dependent and significantly reduced at large particle size. A smaller particle presents a smaller diffusion path and nanosizing should therefore improve ionic transport. Yet the contrary is observed. This is certainly related to the particle size reduction, yet the cause is unclear. It could be in relation to point defects in the solid electrolyte, or the promotion of side-reactions for particles with a smaller surface area. In smaller particles, one defect could have a much larger impact than for bigger particles, where the ions can still diffuse through side-channels. The effect of a side-reaction has an equally large impact, as a similar impeding reaction would impede the smaller particle more.

5.2 Cycling electrochemical cells at 0.1 C-rate

After analysing the dynamics inside the electrochemical cells, they were put through a sequence of charge-discharge cycles. This was done in order to evaluate whether the reported impedance parameters were in line with reality. If this would be the case, the batteries with higher reported conductivities, better charge transfers and better ionic diffusion would result in the better performing batteries. This procedure also allows us to assess the effect of electrolyte thickness on the aging of the battery. Charging and discharging results in volume change within the battery, giving rise to fatigue and aging, ultimately resulting in a less performant battery.

Coulombic efficiency is literally accounting for the amount of charges available in the cells, as a ratio of the amount of charges after discharge divided by the amount of charges of the previous charging (see paragraph 2.1.2)

Faradaic losses in electrochemical cells are due to charged particles participating in (unwanted) side-reactions, producing compounds that could either be beneficial or detrimental to the efficiency of the battery. These charges, which should be accessible as the battery capacity, are now unusable, effectively reducing the battery capacity.

Faradaic losses are not the only form of energy loss, overpotential also reduces the overall efficiency of batteries. Where coulombic efficiency accounts for number of charges, overpotential assesses the additional voltage (potential) necessary to extract the charges

Energy efficiency is also extremely relevant when assessing energy storage in batteries. Energy loss is related to internal resistances and thus overpotential, which is a more apt description of the efficiency of a battery than coulombic efficiency, which only accounts for charge transport. Energy efficiency is consequently typically lower than coulombic efficiency. Yet both of these values can be misleading, as they do not account for the overall amount of energy stored in the battery, merely the ratio of discharge versus charge. So even a poorly performing battery that charges and discharges poorly can have a high coulombic and energy efficiency, seeing as the difference between the two is minimal. Showing percentage would not quantify the amount of energy transferred or initially lost. By plotting the energy difference and the actual amount of energy stored, one can more accurately assess the battery performance.

The C-rate is set at C/10 for all charging-discharging cycles. This is done in order to study the electrolyte efficiency and possible side-reactions (also relating to the particle size variation) rather than a high C-rate which would put the accent on the insertion mechanism in the electrode active material NNM.

For the sake of the reader, the assessment of battery efficiency will only take into account the highest stored energy battery, as well as the battery with the smallest difference between charge and discharge energy. This will also provide more clarity than a complete assessment of all the cells. The remaining cells can still be viewed at the end of this Thesis, in the Appendix.

5.2.1 Adding ECPC with 1M $NaClO_4$ – 63.3 nm BASE particle size

The most important characteristic of an electrolyte is its capability to vehicle ions from one electrode to the other (while impeding electrons). The aim of these series of tests is to evaluate whether the solid electrolyte can facilitate this function alone, seeing as it is not a dense pellet but merely a series of particles loosely in contact with each other. For Sodium cells, $NaClO_4$: ECPC is reported to be an excellent organic electrolyte due to the formation of a conducting passivation layer, and will therefore be the starting point of our study.

For these electrochemical cells, the mass of active material present in the cathode is 1.125mg. For a reported capacity of 80mAh/g when cycling between 2.5-4.1V, this yields a maximal capacity of 1×10^{-4} mAh/cell.

87μm - 3drops of added $NaClO_4$: ECPC liquid solution

The first battery presented is the one with the highest concentration of added organic electrolyte (5th in Table 3). It should show the highest cyclability because it has the highest addition of liquid per mass of BASE. Anyhow, the organic electrolyte is sufficient to vehicle Na^+ ions back and forth, without requiring interactions with BASE.

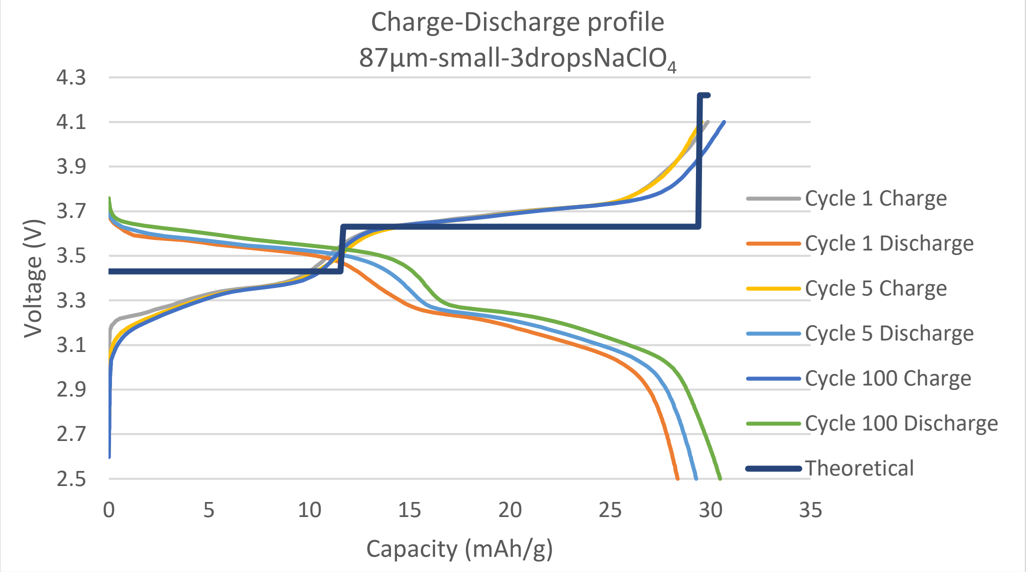

Figure 30. Charge-discharge voltage profile for the battery with 87μm tape casted BASE and 3drops of added $NaClO_4$: ECPC liquid solution, as well as the theoretical phase changes of the cathode material during charging.

Theoretical plateaus for phase shift within the cathode material occur at 3.43V, 3.63V and 4.22V, illustrated in Figure 30. A separate study could be made regarding the effect of liquid addition on the degree of overpotential observed. Naturally, charging the cells at a lower rate would reduce the overpotential. Yet in order to study the quality of the charge-discharge curve, a set C-rate must be defined. In our case, the C-rate is set at C/10.

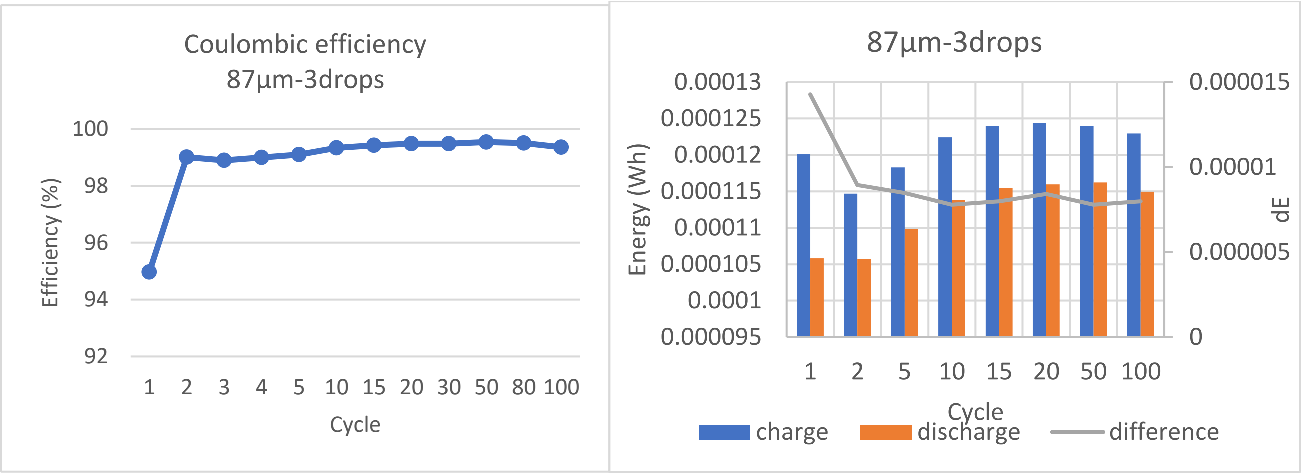

Figure 31. The coulombic efficiency (left) and Energy difference (right) for the 87µm - 3drops of added $NaClO_4$: ECPC liquid battery.

Even though the Coulombic efficiency reaches 99% after the first cycle (Figure 31), the energy efficiency indicates that the stored energy reaches a maximum after 15 cycles, with a constant margin between charging energy and discharging energy of 7.9 x 10^{-6} Wh. Furthermore, the stored energy and relating capacity remain constant over the course of the 100 first cycles. This validates the extremely high reported cyclability. Unfortunately, this cell shows a capacity reaching 30 mAh/g active material, 37.5% of the theoretical capacity

55µm - 1 drop of added $NaClO_4$: ECPC liquid solution

This electrochemical cell is labelled 2nd in the liquid to mass ratio in Table 3, while the cell previously shown is ranked 5th. Having a lower organic liquid addition, this cell is expected to perform less efficiently than the previous one.

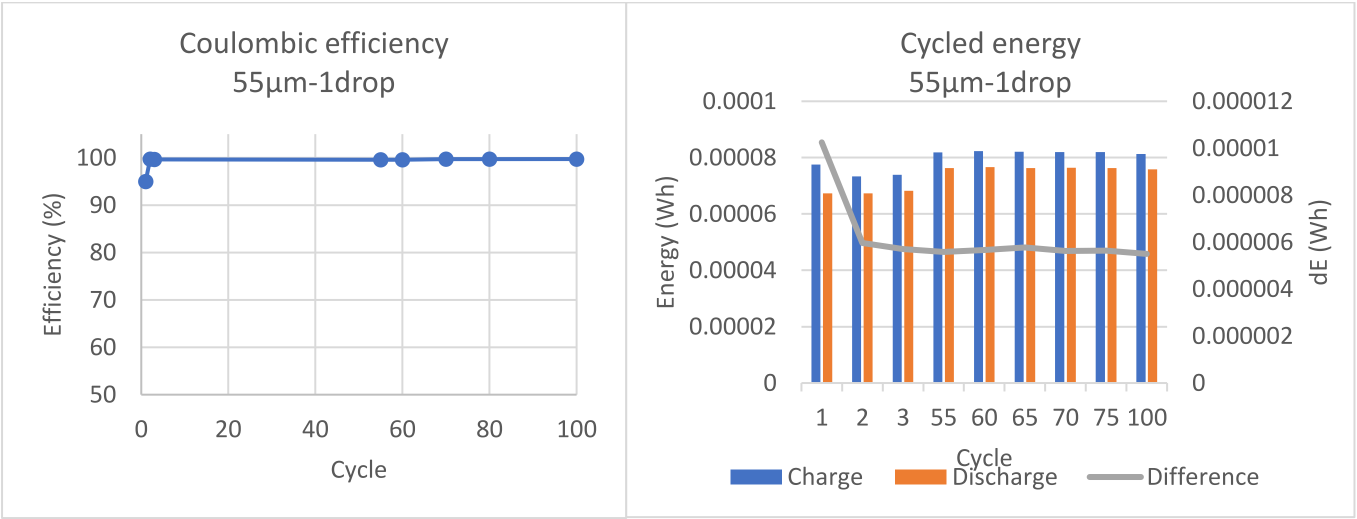

Figure 32. The coulombic efficiency (left) and Energy difference (right) for the 55µm - 1drops of added $NaClO_4$: ECPC liquid battery.

Using this approach, it is now more evident that the energy stored by the 87µm-3drops cell is highest (1,2 x 10^{-4} Wh), while the 55 µm-1drop shows the highest efficiency with the lowest charge discharge energy difference (6 x 10^{-6} Wh), displayed in Figure 32. The only difference between these cells can be observed for the low frequency values of R3 and C3, in Figure 15. The cell ranked 2nd (lower volume/mass addition), 55µm, presents a higher resistance and capacitance at low frequency, indicating lower mass transport characteristics. This could explain that less ions have been transported. The higher efficiency of the 55µm cell could be explained by the difference in thickness, shorter ionic transport relating to a higher efficiency for cycling.

5.2.2 Adding 1M $NaClO_4$: ECPC with 67.4 nm BASE particle size

The following cells are ranked 4th and 1st in the relating Table 4, meaning the highest and lowest volume of added liquid/mass of BASE respectively. The only difference between both cells is the thickness of the tape casted electrolyte, 75 µm and 200µm respectively.

75µm - 1drop of added $NaClO_4$: ECPC liquid solution

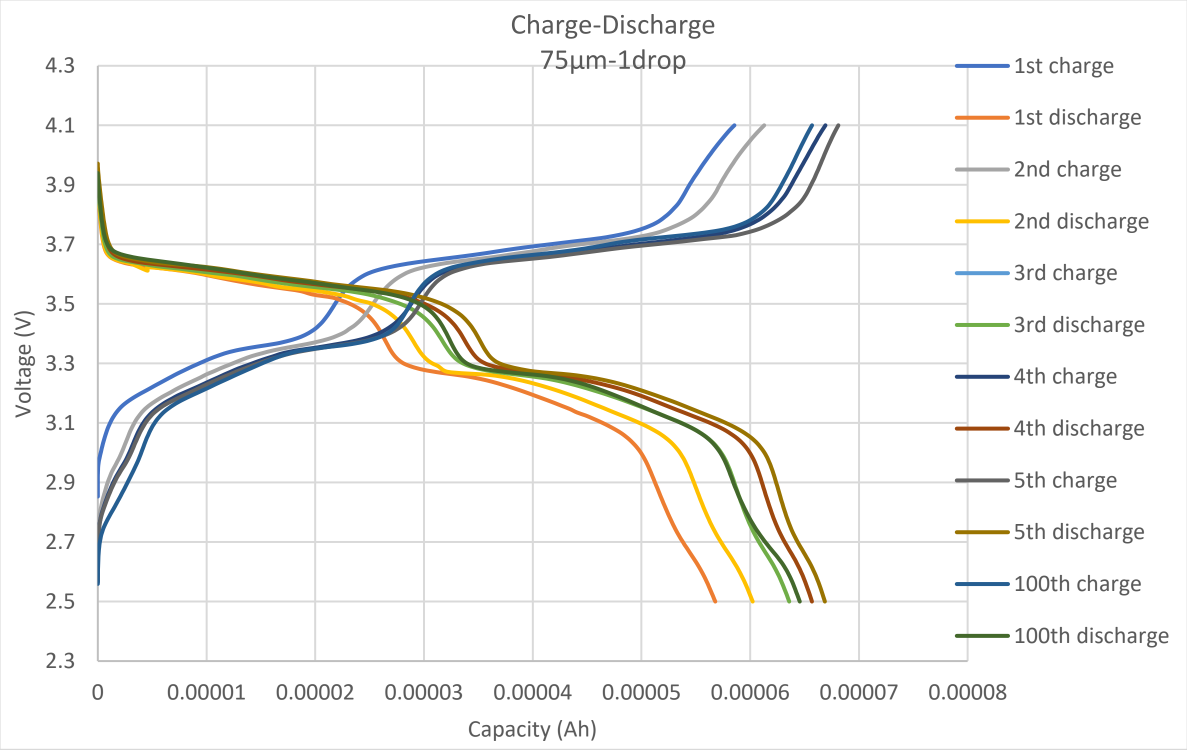

Figure 33. Charge-discharge voltage profile for the battery with 75µm tape casted BASE and 1drop of added $NaClO_4$: ECPC liquid solution.

Figure 33 shows the Charge-Discharge curve for the 75µm-1dropcell, the cell with 67.4nm BASE particles and the highest relative volume of additives. It gives an appreciation for the lack of capacity loss, even after 100 cycles. This highlights the performance of 1 M of $NaClO_4$: ECPC as an organic electrolyte. It also reaches 6.7 x10^{-5} mAh/cell, 67% of theoretical capacity. The cathode thin film was measured to be thinner for the 67.4 nm series, with the same thin film weight of 1.125 mg of active material. Yet it presents a higher capacity. This could indicate that the active material loads more efficiently for thinner films, but more likely a slight variation in the preparation and tape casting method, resulting in a slightly smaller active material particle size and associated better ionic diffusion in the active material.

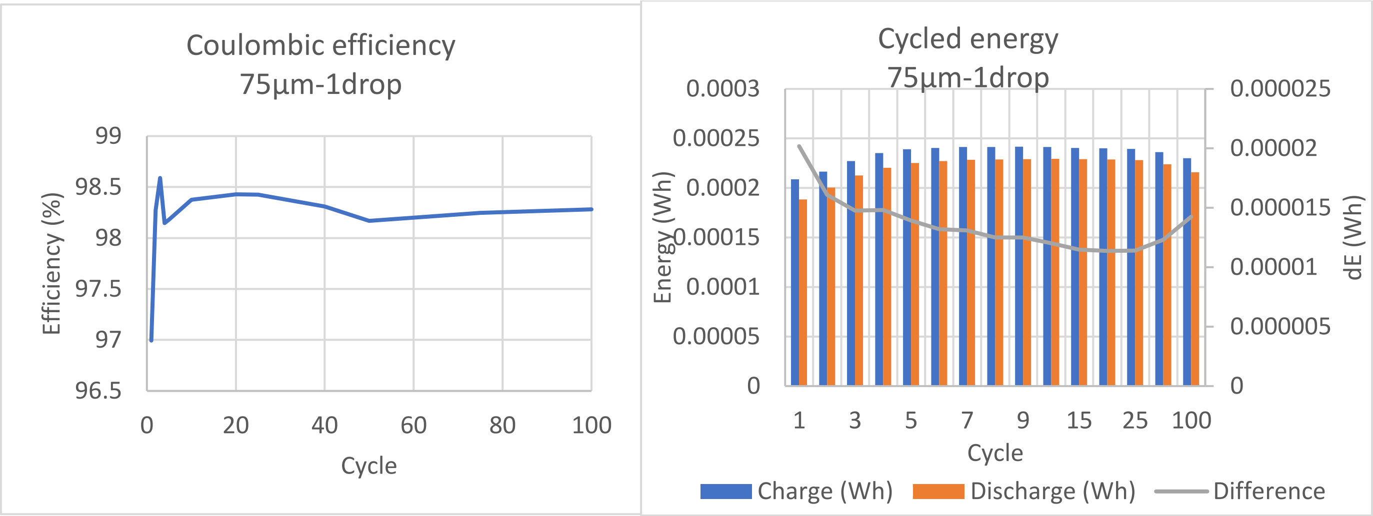

Figure 34. The coulombic efficiency (left) and Energy difference (right) for the 75μm - 1drops of added $NaClO_4$: ECPC liquid battery.

Figure 34 indicates that the 75μm-1drop has its lowest charge discharge energy difference (1.14×10^{-5} Wh) at 25 cycles, even though the Coulombic efficiency does not increase past 98.5%. The energy storage quickly rises to 2.25×10^{-4} Wh and remains constant during the 100 cycles.

200μm tape casted BASE with particle size of 67.4 nm and 1 drop of $NaClO_4$: ECPC solution

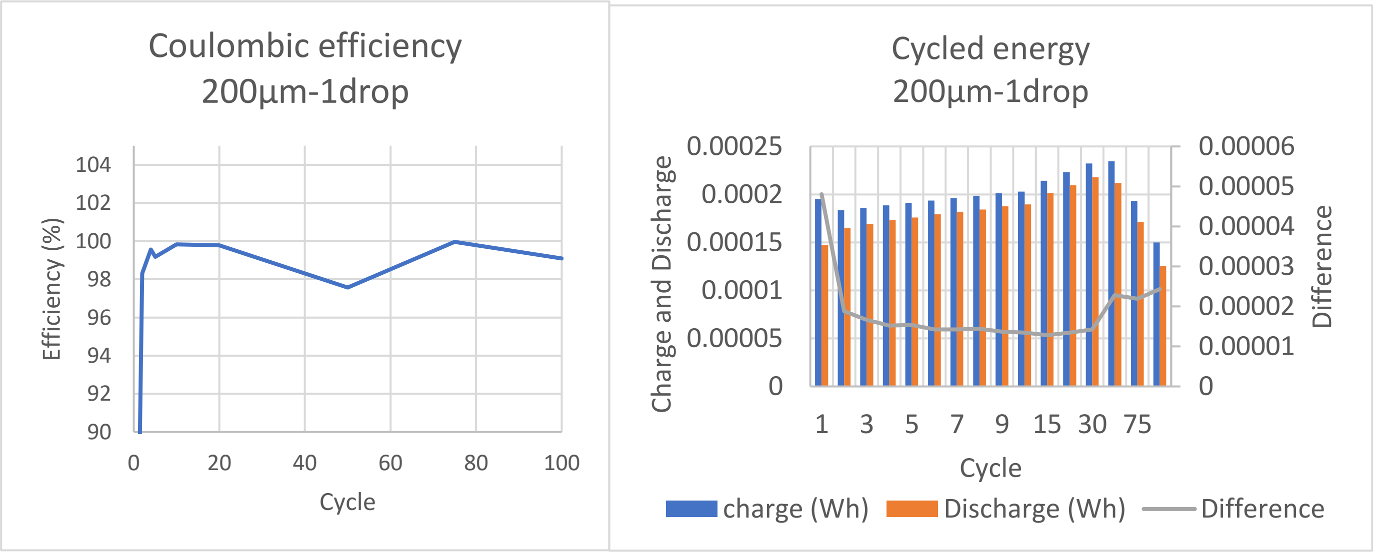

Figure 35. Coulombic efficiency (left) and energy figure (right) for an electrochemical cell with 200 μm tape casted BASE coating, with $NaClO_4$: ECPC addition.

In Figure 35, the energy stored by the 200µm-1drop cell is highest at 2.2 x 10^{-4} Wh, with a Coulombic efficiency close to 100% after 10 cycles and an energy difference of 1.35 x10^{-5} Wh; while the 75µm-1drop shows an equally high stored energy, but with higher consistency and the highest energy efficiency with the lowest charge discharge energy difference (1.1 x 10^{-5} Wh) at 25 cycles.

These are interesting findings, as they indicate that the batteries with smaller BASE particle size (63.3nm) present a relatively higher energy efficiency compared to the batteries with bigger BASE particle size (67.4nm). One could present the argument that this is the case due to the smaller BASE series storing less energy.
Yet one must not forget the liquid addition to BASE mass ratio. When comparing the addition for both these cells, the ratio is 9.43 x 10^{-3} for the 75µm cell (bigger BASE series), and 1.29 x 10^{-2} for the 55µm cell (smaller BASE series). And finally, the effective addition of salt for the 55µm cell was 3 drops of liquid, while only 1drop was added to the 75µm cell.
In theory, the smaller particles should have lower conductivity due more point contacts relating to a higher resistance. Despite having smaller particles, the 55µm battery produced a higher relative energy efficiency. Also, the resistance R_e/thickness indicates similar values regarding both batteries (with electrolyte resistance increasing linearly with thickness), which would indicate that their electrolytic contributions in the system are the same per thickness. The low frequency resistance actually indicates that the smaller particle systems have a higher resistance/thickness, which should result in a lower efficiency than the bigger particles. This leads us to the conclusion that for the $NaClO_4$: ECPC series, liquid addition is dominating regardless of the BASE particle size.

5.2.3 ECPC – No additional dissolved $NaClO_4$ salt.

By introducing the organic solvent without additional salt, we can see whether the Na-beta”-alumina particles are sufficient to vehicle the Na^+ ions through the electrochemical cells.

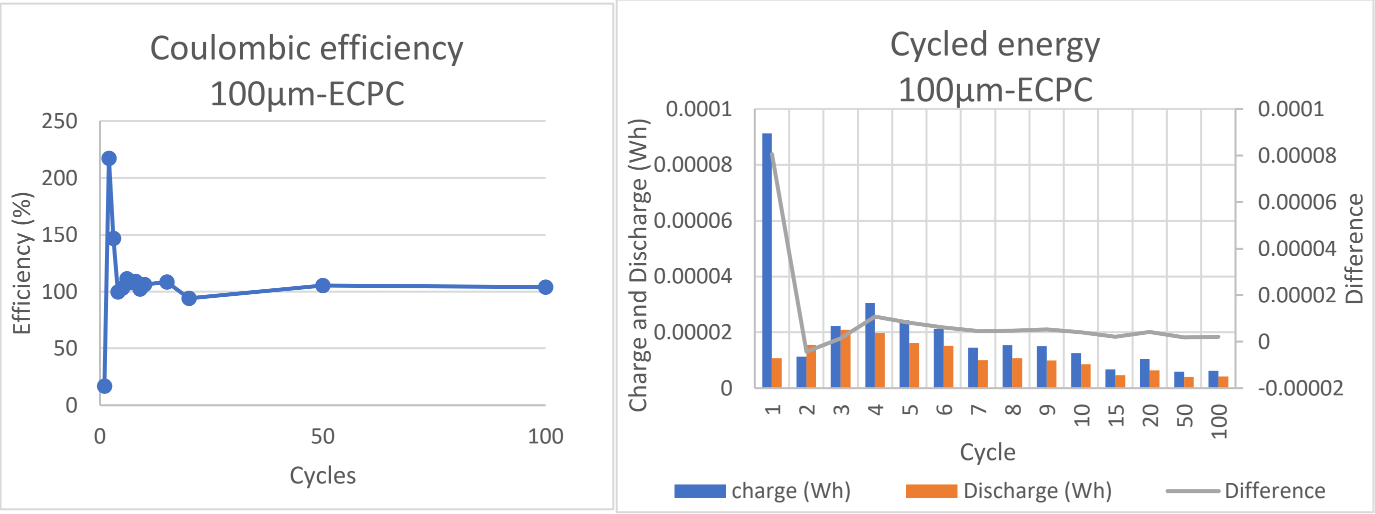

Figure 36. Coulombic efficiency (left) and energy figure for an electrochemical cell with 100 µm tape casted BASE coating, with only ECPC as liquid addition (right).

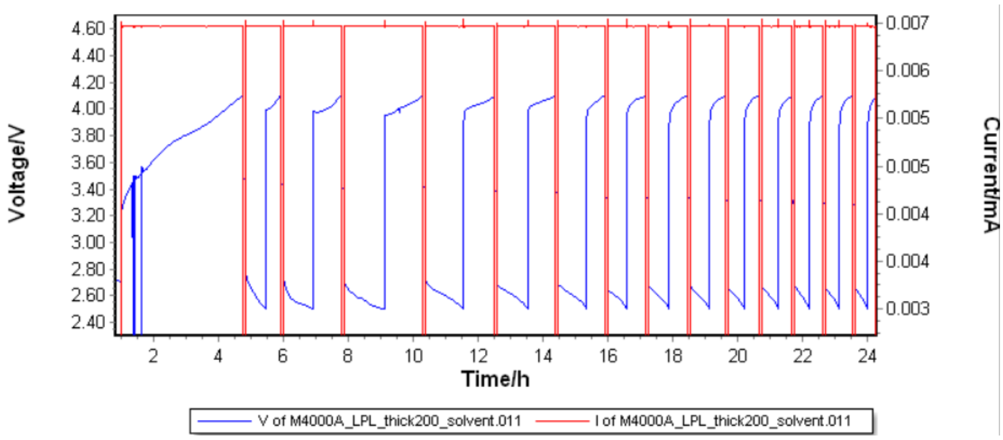

Figure 37. Charge-discharge pattern of the best performing ECPC battery assembled, without additional $NaClO_4$ salt.

In Figure 37, the charge-discharge pattern of this 100µm-ECPC cell with tape casted Na-beta”-alumina-ECPC shows a high polarization, an indication that the battery requires a lot of additional energy to put Na^+ ions into the host material. This is in line with theory, as the organic solution ECPC does not have dissolved Sodium salt. This makes it very challenging for the solution to vehicle Na^+ ions through the system. The Na-beta”-alumina itself should have the capability to fulfil that function by itself, yet the BASE particles are only in contact through point contacts, surrounded by an organic solvent that requires a lot more energetical input to extract the Sodium ions.

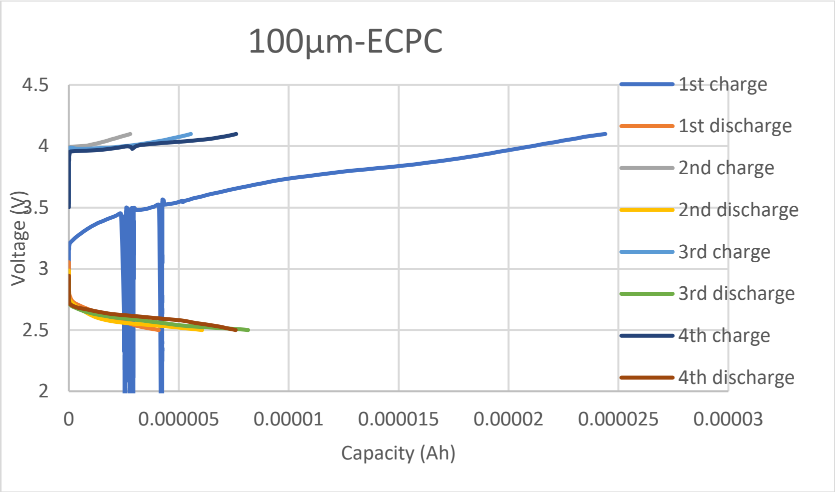

Figure 38. Charge and discharge curves for the first cycles of 100µm-ECPC.

This is a good example where energy efficiency or coulombic efficiency can be misleading factors. Even though the battery is clearly performing poorly, it still reaches high efficiency percentage

The Charge-discharge curve in Figure 38 indicates that even for the first charge, the stored capacity was $2.5x10^{-5}$ Ah, while the following cycles only managed to store $1/5^{th}$ of this. The first charge is already exceeding expectations, as the maximum it could reach was $1\ x10^{-4}$ mAh/cell. The coulombic efficiency in Figure 36 indicates an efficiency superior to 100%, which in this case can only mean a side-reaction. Electrons resulting from an electrolyte decomposition participated in a side-reaction, therefore providing additional electrons and increasing the number of electrons available. According to the charge-discharge curve and supported by the Coulombic efficiency for the first cycles, the electrolyte decomposition could be the reason for the sudden decrease in capacity. The decomposition could be explained by the sudden overpotential. Seeing as the energy necessary to extract the Na^+ ions was much greater than for previous cells, it would have shown new phenomena in the battery, not previously observed. This is akin to separation processes in chemical engineering, or boiling water. When no water is present in the pan, temperature will rise in order to heat up the compounds in the pan with higher evaporation temperatures.

These findings indicate that the dissolved salt $NaClO_4$ is essential to the high cyclability of these batteries, and that the sole contribution of the BASE tape casted particles in combination with ECPC results in an extremely high overpotential and possibly electrolyte decomposition. The conclusion regarding the $NaClO_4$: ECPC series holds, liquid addition is dominating regardless of the BASE particle size.

5.2.3 Adding TES-TFSI ionic liquid for slurry electrolyte

For both the ionic liquid series, the pellet and slurry version have been attempted. This was done in order to determine which of the concepts would perform better. We have now uncovered that the slurry version presents better electrical properties when analysing the EIS data, but it would be interesting to see whether it performs better regarding the cycling behaviour.

The pellet concept is an attempt to make a mechanically pressed pellet, adding a few drops of ionic liquid to facilitate the ionic network within the electrolytic circuit

BASE pellet with Na-beta”-alumina particle size of 67nm and 0.3 cm^3 TES-TFSI additive

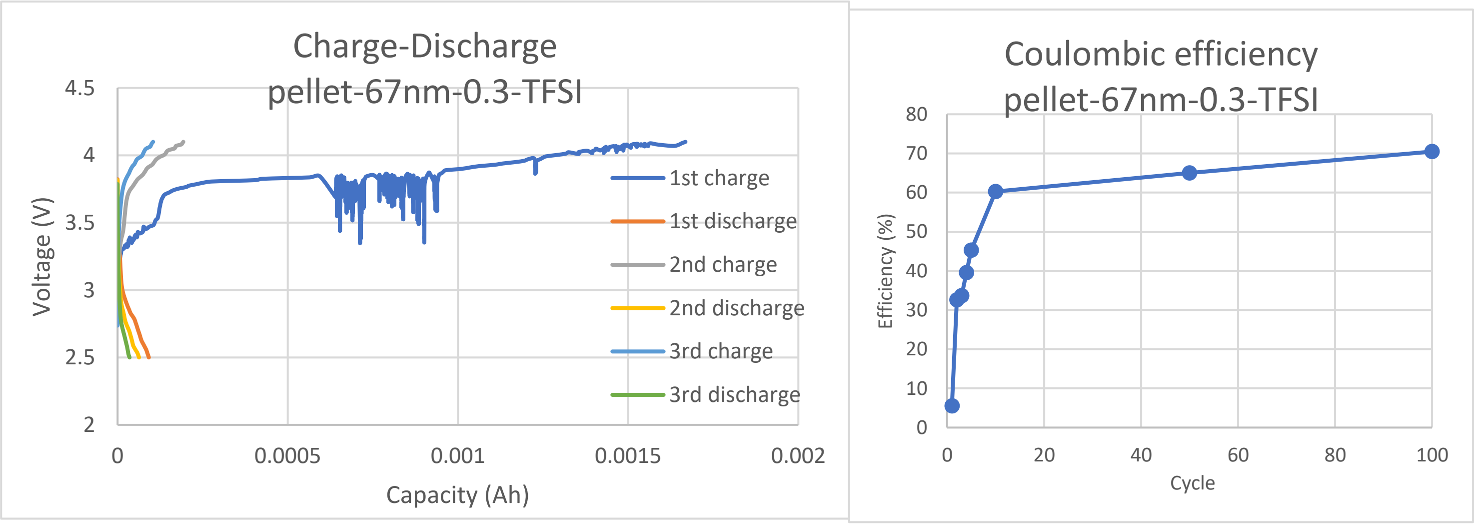

Figure 39. Charge-discharge voltage pattern (left) of the battery containing a slurry of 0.3cm^3 of TES-TFSI and BASE with particle size of 67 nm and (right) relating Coulombic efficiency.

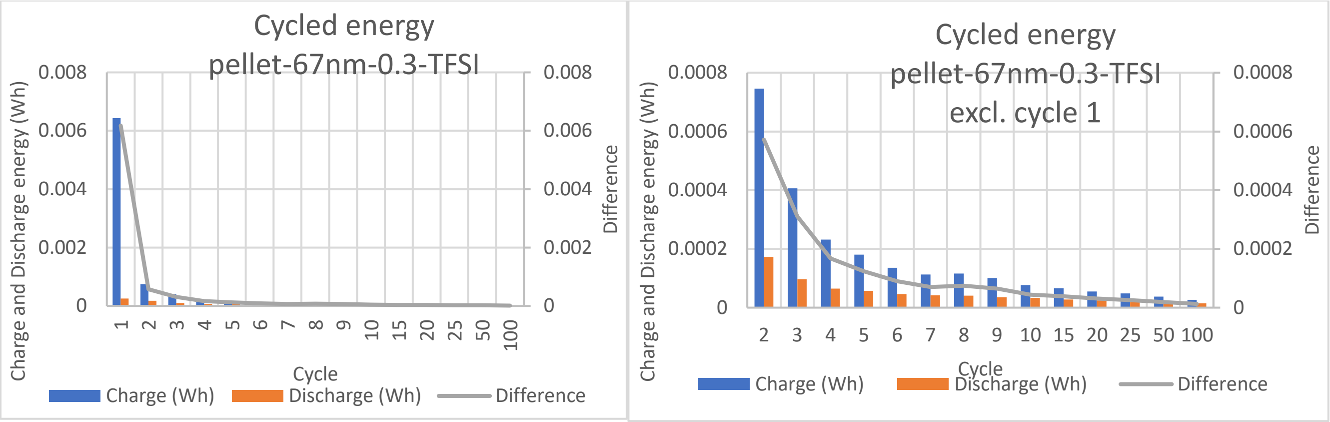

Figure 40. Energy plots for the BASE pellet concept with addition of 0.3cm³ of TES-TFSI. The right plot contains the same information as the left one, excluding the first cycle.

A long voltage pattern is observed regarding the pellet with 0.3mL of TES-TFSI addition (Figure 39). In our experience, this is a behaviour that occurs often when attempting to cycle this battery concept. This particular cell also comprises a contact issue during the second phase charging of the first cycle. This could be the result of volume expansion, which is challenging to compensate due to the rigid structure of pellets. Yet it can naturally be remedied using a slurry, which is a middleground between solid pellet and liquid electrolyte.

Excluding the first charging pattern, we can observe that both the charge and discharge energy steadily decrease (Figure 40). This could be an indication of a gradual decomposition of one of the components. We suppose it is the result of either water content in the system, impurities in the ionic liquid, corrosion at the interphases, or merely active material losing its structural integrity. Further research can be done regarding this phenomenon.

<u>TES-TFSI slurry with Na-beta”-alumina particle size of 67nm</u>

Aside from the pellet concept, a similar experiment was executed using a slurry electrolyte. This would solve the contact issue at the electrode-electrolyte interphase, but no additional steps have been undertaken to prevent the previously observed side-reaction. This evidently led to an unsurprising first charge taking almost 24hours instead of 10h (at a C/10 rate).

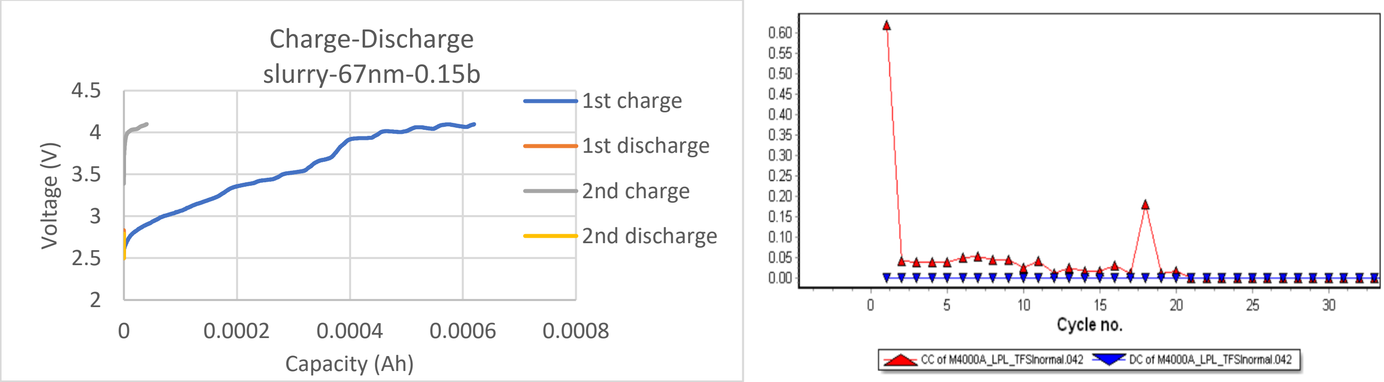

Figure 41. Charge-discharge voltage pattern (left) of the battery containing a slurry of 0.15mL of TES-TFSI and BASE with particle size of 67 nm and (right) relating capacity of the first 35 cycles.

Capacity per cycle in Figure 41 shows that the first charge is large, while the next ones are stable at 0.05mAh, until even charge capacity goes to 0 after 20 cycles.

The discharge capacity remains 0 throughout the process. This can be due to self-discharge during the 5-minute resting phase after the charging process, as well as the potential evidence for an insulating layer formation at the Na metal anode side impeding discharge. When water comes in contact with Na metal, a layer of insulating NaOH can form at the surface, which would impede ionic transport through the layer, resulting in the absence of recombination of the ions with electrons on the Na metal side. This water could be present in the glovebox in which the cells were assembled, as well as potential water content in the ionic liquid. Yet water content in the ionic liquid would show evidence in all the assembled cells, not just a few. The ionic liquid was also rigorously dried previous to introduction into the glovebox in order to minimize external impeding factors. The lack of discharge cannot be attributed to the cathode material deterioration, as the next cycle shows evidence of charging again.

TES-TFSI ionic liquid with separator

An idea to investigate which of the components could be the cause for the previously shown cycling behaviour, was to exclude the solid Na-beta"-alumina electrolyte from the system. By simply adding TES-TFSI to a glass fiber separator, one could shed light upon this behaviour. Theoretically, the ionic liquid does not contain Na^+ ions, so should be unable to vehicle these ions back and forth during cycling. The experiment showed quite the opposite result, as can be observed in Figure 42.

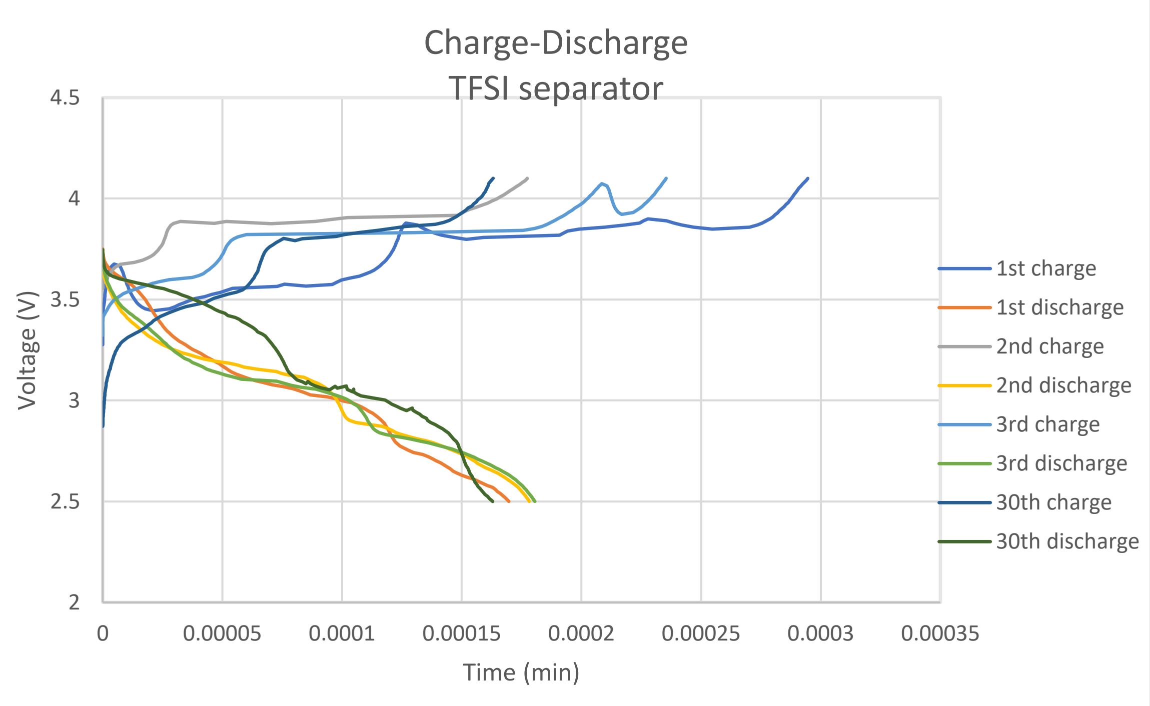

Figure 42. Charge-discharge voltage pattern of the battery containing TES-TFSI and a separator, excluding BASE.

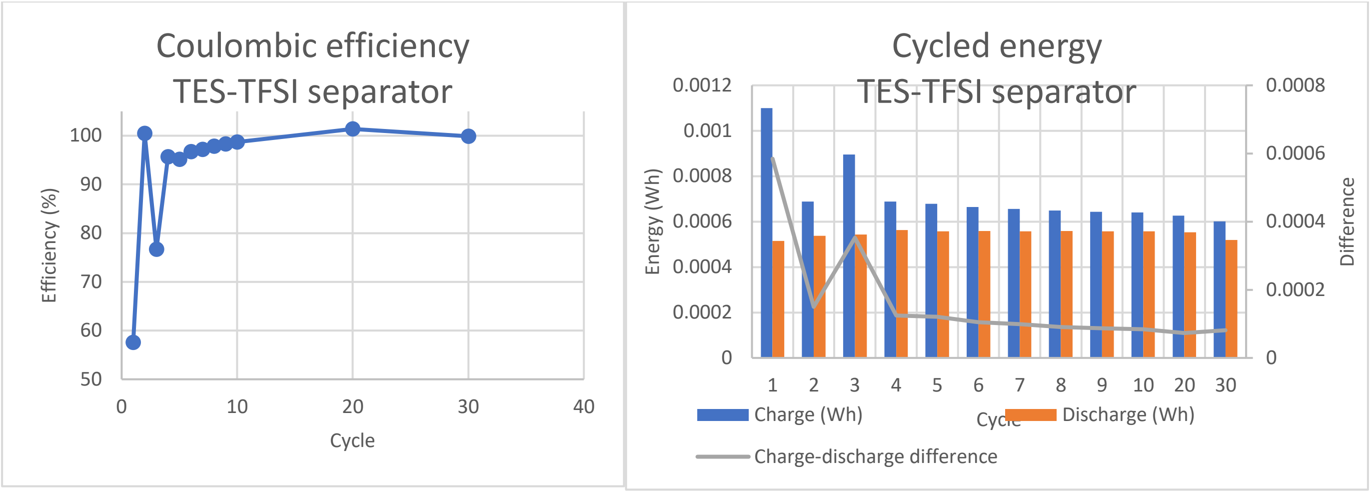

Figure 43. Coulombic efficiency (left) and energy figure (right) for an electrochemical cell with glass fiber separator with ionic liquid TES-TFSI addition.

This experiment presented a few interesting findings. Firstly, it managed to vehicle Na^+ ions continuously, and much more efficiently than the cells previously made. This poses the question of how the ionic liquid was able to procure the ions. NaTFSI could have formed, explaining the varying Coulombic efficiency in the first few cycles in Figure 43. Secondly, the charge-discharge curves in Figure 42 indicated a slightly different pattern than expected. This can be an indication that the active material was also affected by the ionic liquid. The overpotential peaks at higher voltage for the first few cycles are indication of an internal resistance, probably due to a side-product formation. This could very well be an indication for NaTFSI formation The internal resistance increase was also illustrated by the potential increase during charging. It jumped from 2.5V to 3.5V at 1st charge, yet from 2.5V to 3.2V when starting the 4th charge and finally 2.5 to 2.8V when starting the 30th charge, indicative of a completed side-reaction. With a significant observed performance, it would even lead us to believe that this concept resulted in a decent passivation layer. This is supported by the initially low Coulombic efficiency, which reached 99% within the first 4 cycles.

What this tells us, is that even though the Na-beta”-alumina was part of the cause, the ionic liquid could have reacted with the active material (or an impurity contained in the viscous IL). After formation of a side-product in the first 3 cycles, the battery presented excellent cycling capabilities. This was supported by a low energy difference as well as a high Coulombic efficiency.

In conclusion, we have not been able to assemble a highly performing cell using TES-TFSI as ionic liquid, whether for the pellet or slurry concept. This inconclusive result only highlights the challenge that is assembling efficient batteries in an experimental environment. The purity of the components is of high importance, and a slight degree of impurity can cause malfunctions, as well as dramatic decreases in performance. If anything, the slurry concept still proves to have a better electrode-electrolyte interphase contact, being able to retain mechanical integrity throughout the cycling process and associated volume expansion.

5.2.4 Adding Pyr_{14}-FSI ionic liquid for slurry electrolyte

As previously observed in the TES-TFSI series, anomalies often happen in the 4V range, after which the following charging cycles have absent (or too fast) phase transitions. Excluding the 4V range decreases the capacity and energy potentially stored in the cells, yet a lower cut-off could have the benefit of mitigating the deterioration. Unfortunately, it did not seem to previously negate the deterioration. Consequently, the following step is excluding components to see the resulting effect. The Na-beta”-alumina component was excluded in the following $Pyr_{14}FSI$ cell in order to ascertain the origin of this deterioration behaviour. The overpotential behaviour observed in the TES-TFSI series is observed again here in Figure 44, shown clearly in the first charging voltage.

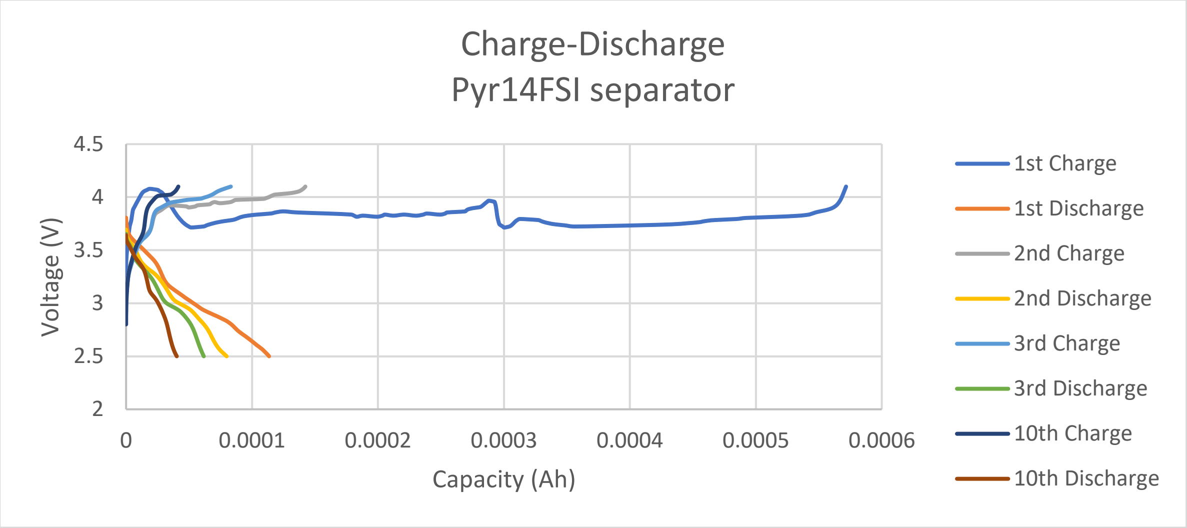

Figure 44. Charge-discharge voltage pattern of the battery containing $Pyr_{14}FSI$ and a separator, excluding BASE.

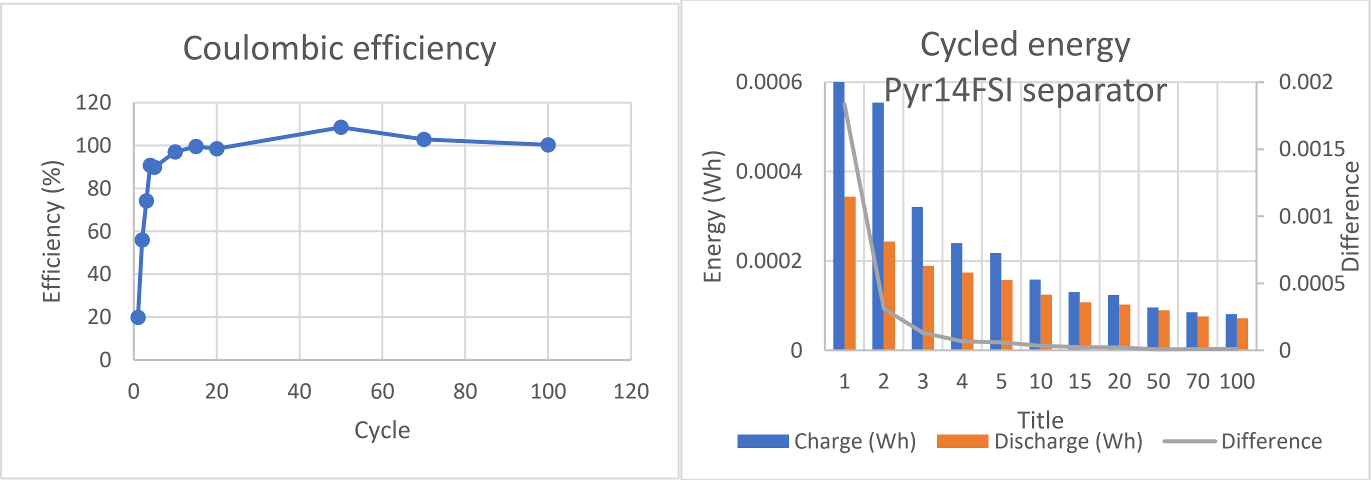

Figure 45. Coulombic efficiency (left) and energy figure (right) for an electrochemical cell with glas fiber separator with ionic liquid $Pyr_{14}FSI$ addition.

The battery shows a decent behaviour in Figure 44, yet the cycling capacity becomes 5 times smaller after the first cycle, even though the Coulombic efficiency reaches 100% within 20 cycles in Figure 45. It was previously mentioned that this could be due to contamination of the ionic liquid, passivation layer formation as well as water content present in the system. By thoroughly drying the ionic liquid $Pyr_{14}FSI$ in vacuum at 80°C, as well as drying the Na-beta”-alumina powder in an oven for 6 hours at 600 °C, the water content potentially present in the cell was taken out. The resulting cell is presented hereafter.

<u>Slurry of $Pyr_{14}FSI$ and dried Na-beta”-alumina with particle size of 67.4 nm</u>

Even though this cell does not show a highly efficient battery as previously shown for the $NaClO_4$ series, it was the most successful cell containing ionic liquid in combination with Na-beta”-alumina. This success was attributed to the thorough drying process of the components. Not only the electrolyte particles, ionic liquid, but also the cathode thin film. Even though NNM is not reactive to water itself, the surface can still contain water particles, thus had to undergo the same drying process as the ionic liquid in order to avoid any water content.

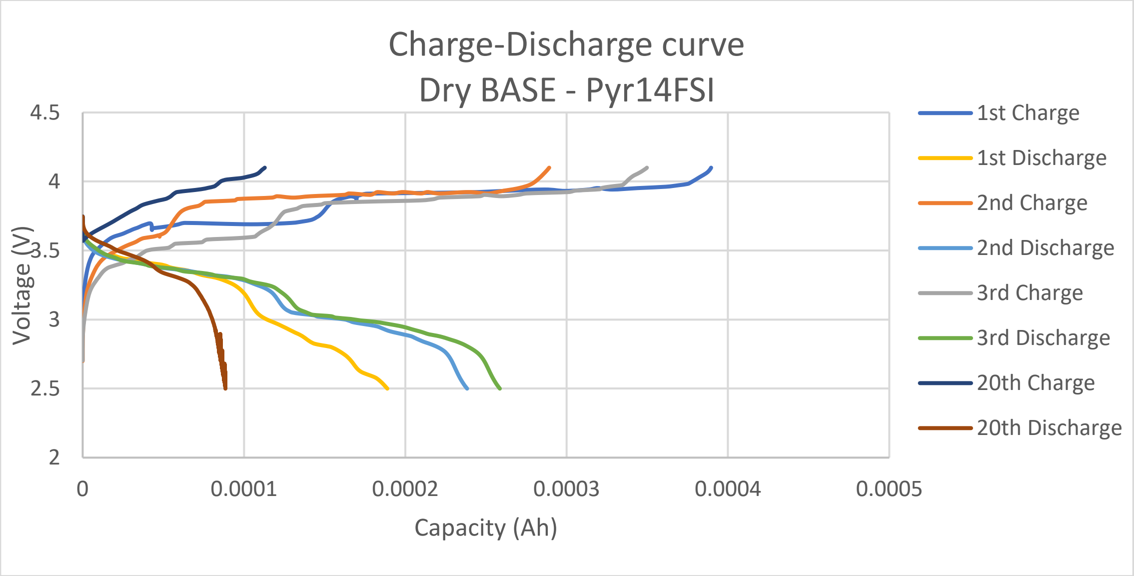

Figure 46. Charge-discharge voltage pattern of a battery containing a slurry electrolyte of $Pyr_{14}FSI$ and Na-beta”-alumina.

First charge takes 23hours instead of 10, while the first discharge takes 10hours. This pattern remains the same until the 10th cycle, where discharge takes 8hours, and charging takes 10hours. The capacity mirrors this effect in Figure 45, indicating a correlation between capacity and charging time.

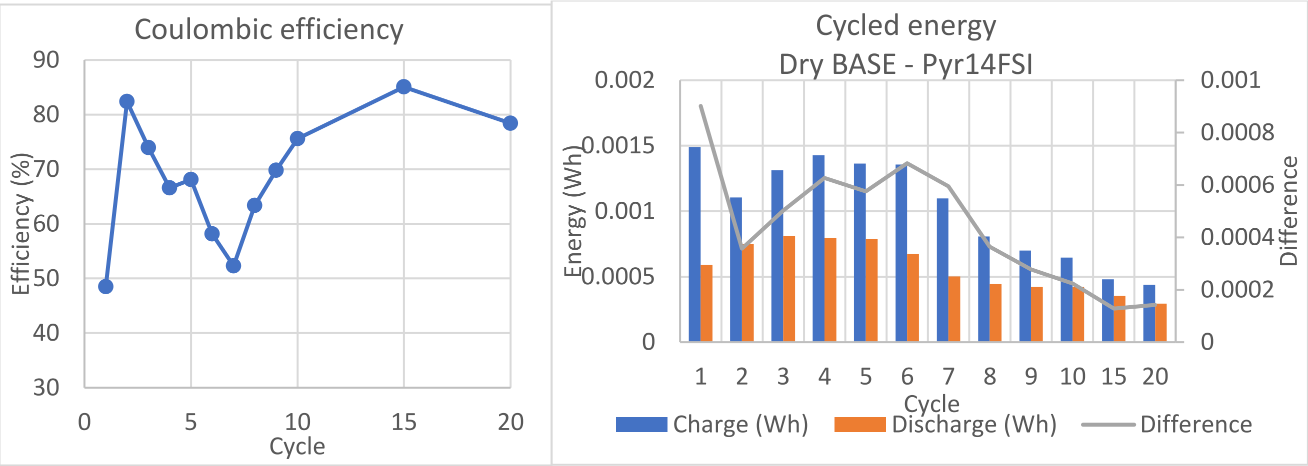

Figure 47. Coulombic efficiency (left) and energy figure (right) for an electrochemical cell with a slurry electrolyte of $Pyr_{14}FSI$ and Na-beta”-alumina.

The cell shows a decent reversibility shown in the energy for Figure 47, yet the first charging pattern still shows a form of side-reaction or surface passivation. We can say with high assurance that the water content is minimal in this system. Meaning that the observed behaviour can be attributed to either an SEI formation reported for the $Pyr_{14}FSI$ ionic liquid [**152**], or the presence of impurities in the system.

In order to relate back to the subject of this thesis and the role of Na-beta”-alumina particle size, cells with smaller particle BASE have been introduced in the slurry. These were previously done without success, and only one cell presented acceptable results. It should be noted that the reproducibility of these results is questionable, as it took us 4 attempts to get a working battery with limited side-reactions for smaller particle size.

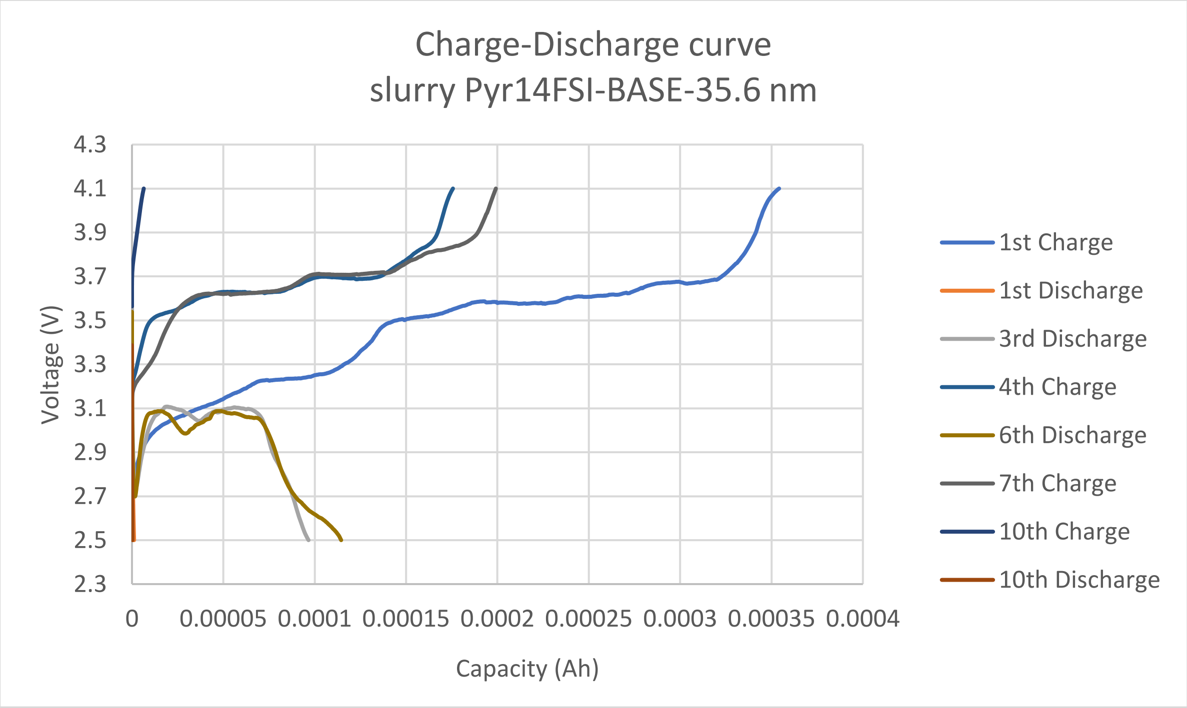

Figure 48. Voltage curves for charge and discharge of the battery containing a slurry of $Pyr_{14}FSI$ and Na-beta”-alumina small particles of 35.6 nm, as opposed to the regular size of 67.4 nm.

As can be seen in Figure 48, the Charge-discharge curve shows very nice charging phase transition, while discharge remains an issue. 14h charging instead of 10 is indicative of a side-reaction. This could be caused by impurities in the ionic liquid or at the surface of the tape casted thin film. The charging capacity of the 1st charge is relatable to the previous Dry BASE battery, yet still manages to store less than 50% of the theoretical capacity of the cathode thin film.

Smaller particle size of Na-Beta"-alumina in this battery can also enhance the reactivity in the battery. With smaller particle size comes higher relative surface area and lower activation energy. This can be a contributing factor to interactions within the cells, yet it also indicates that the presence of impurities would be affirmed faster, with a battery more prone to side-reactions, ultimately leading to lower performance. In an ideal battery with no impurities, smaller particles could be beneficial, yet experience has shown that experimental assembly of the batteries usually comes with unwanted impurities which strongly affect the resulting outcome.

Even though measures regarding the elimination of impurities and water content were put into action, the ideal battery has yet to be reported. Water content definitely played a role in the low performance previously shown, yet it does not seem to be the only factor impeding the efficiency of the electrochemical cells.

To conclude, the objective to correlate impedance data to cycling behaviour was unfruitful for the ionic liquid series, and was found to be a lot more challenging than previously anticipated. Only few batteries showed presentable results, while the others were strongly affected by external parameters. These can be found in the Appendix. The presentable batteries did not show a high enough performance to accurately correlate to the EIS data. Even though definite correlations can be made regarding ionic liquid and various particle sizes for Na-beta"-alumina, these do not transpose to cycling behaviour in our case. This highlights the necessity for extremely pure components and thorough drying before assembly, as well as further study.

5.4 Experimental issues

Water content is an important factor when considering Na-beta"-alumina, which is an extremely strong desiccant. Water also strongly reacts with Sodium metal, which is our anode material. It would form an insulating layer preventing further ionic migration through the electrolyte/anode interface.

Even when taking extreme care during assembly, a few water particles in the surrounding Argon atmosphere of the glovebox can be detrimental to the performance of the battery. This is evident from Picture 2.

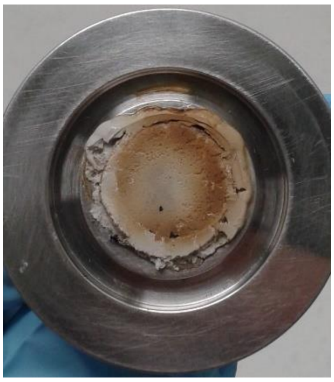

Picture 2. Evidence of water contamination on the electrode-electrolyte interphase, resulting in battery failure.

For this reason, it was an interesting aspect to study the effect of water content on the EIS measurements. Water and contaminants affect the performance of the battery during charging and discharging, so we expected to unravel similar characteristics in impedance spectroscopy. A higher impedance was anticipated, seeing as when coming in contact with water, Na-beta”-alumina replaces the Na^+ ions in the interlayers by protons H^+ from water. These are then extremely hard to remove.

Plots regarding the various resistances, capacitances and diffusion parameters for the various cells relating to water contamination can be found in the Appendix, as well as attempts to unravel the proton location in XRD measurements, without success. Only a slight shift of the whole spectrum was observed, as well as corroding battery interfaces which were only discovered during disassembly, illustrated in Picture 2.

The ionic liquids were dried at 80 °C in a vacuum antechamber, which had to be flushed multiple times during the drying time, as the water content was not effectively evacuated. The solid-state electrolyte has to be heated for a prolonged time at 600 °C to get rid of the water content. Unfortunately, this process can lead to a reported volume expansion, potentially damaging for the structural integrity of the Na-beta”-alumina framework. This phenomenon was observed for during drying of the mechanically pressed pellets (Picture 3). For powder, it leads to particle agglomeration. Particles can then be separated again through ball-milling at low revolution velocity, but this will bring the particles in contact with water once more.

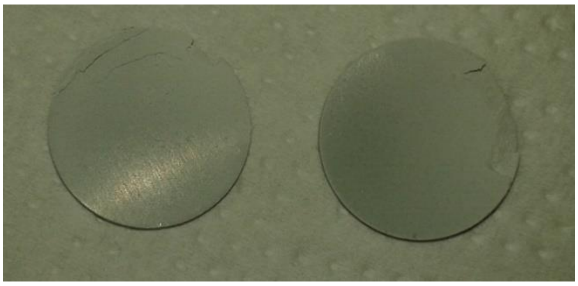

Picture 3. Challenges relating to mechanically pressing a BASE pellet. Cracking occurs, resulting in compromised structural integrity.

Making a mechanically pressed pellet that could keep a structural integrity was also challenging. Even though this sounds straightforward, simply pressing a pellet together at high pressure of 550 MPa did not suffice. The pressure release had to be done overtime and gradually. Only by releasing the pressure progressively over 10 minutes time would the resulting pellet present no cracks, and remain so until after the heat treatment at 600°C for water removal.

Discussion

The underlying framework of this thesis, is that results are transferable to other electrochemical cell experiments, as long as the ambient conditions remain the same. Considering a changing environment (temperature) or charging conditions (C-rate as well as depth of discharge), the resulting aging behaviour during cycling may differ. This would lead to different current densities, enhancing different characteristics of the electrochemical cells. The relationship between the deterioration mechanisms and electrochemical properties may also differ.

Correlating EIS data with BASE particle size and liquid addition was interesting from a fundamental point of view.

When comparing particle sizes and a potential correlation with a space-charge layer, a smaller particle size should have a higher resistance due to higher concentration of point contacts, and also a higher ionic liquid effect relating to a higher surface area, so more double layer and potentially more space charge effect than a bigger particle. Effectively, if smaller particles work better, it means the dielectric layer is the dominating mechanism (but gives no indication about Na-beta"-alumina conductivity) AND/OR the liquid addition is dominating (more ionically conducting liquid electrolyte coverage). Yet if bigger particles work better, then Na-beta"-alumina ionic conductivity is the dominating mechanism. Present work points toward the latter for ionic liquid addition.

In order to generate a clear conclusion regarding this subject, the particle shape should be determined, where the surface area can be derived accurate. A concept should be formulated, where all cells have the same liquid volume to solid surface area ratio. A clearer and definitive conclusion could be derived from such a concept.

Even though Electrochemical Spectroscopy is a very attractive tool, the signification attributed to the measured data (correlation between the EIS measurements, electrical circuit elements and electrochemical properties of batteries) should be supported by other techniques. A major flaw of this technique is that different mechanisms can occur in a similar range, making them hard to differentiate. This can result in erroneous conclusions, even if the result is reproductible. One should always be careful when drawing conclusions based on interactions within a battery system, as the electrochemical processes may overlap. As such, one should take extreme care in isolating the phenomena in order to make an accurate assessment.

6. Conclusions

Electrochemical Impedance has allowed great insight into the dynamics of batteries due to being non-disruptive. Various factors impeding efficient battery operation can be studied and interpreted, often in line with theory. The value of EIS is especially important when considering interfacial effects in electrochemical systems, which is increasingly important when considering solid state electrochemistry. Yet EIS can be misleading if conclusions are drawn too hastily. Probing effects such as charge transfer, ionic diffusion or SEI growth can provide insight, but requires support for proper quantification of the effects. Also, a debate still remains on which time constant relates to which electrochemical parameter.

A few technical matters also need to be considered for a critical assessment. Above all the preparation of the components is paramount, as well as the composition of the electrolytic system, particle size and thickness, electrode composition and potential decomposition products or side-reactions. Any of these factors can affect the recorded impedance data, and consequently the recorded effects in the system. As such, only optimal conditions allow for a solid conclusion.

Regarding our EIS conclusions, we can affirm that the mechanically pressed BASE electrolyte pellet concept performs worse than the slurry electrolyte concept. This is related to the improved slurry contact, as well as the increased point contacts for the pellet in combination with a suspected lower ionic liquid coverage.
We can also conclude that the electrolyte resistance is lowered with organic electrolyte or ionic liquid addition.
The evidence space-charge of has yet to be demonstrated for our components, as smaller particles resulted in lower conductivity and capacitance, regardless of the various series and concepts experimented with.
Finally, the Na^+ diffusion was better for bigger particles for all three liquid additions.

Although we managed to relate the cycling capabilities of the organic electrolyte series with EIS, the same can unfortunately not be said for the ionic liquid series. We were unable to correlate EIS data and cycling performances of the ionic liquid concepts with particle size variation of Na-beta”-alumina. Poor performance of the batteries can be related to pre-assembly treatments such as water removal and liquid addition impurities. Another reason could be the charge transfer limitations at room temperature. Charge transfer is the main limiting factor related to temperature, and designing a performant battery for room temperature applications remains a challenge due to its fundamental temperature limitation.

Large scale production of a safe solid-state battery comprising Na-beta”-alumina may be costly and problematic. Within such a concept, water and oxygen need to be utterly absent, which is especially challenging for large scale production. Even if tape-casting is a great tool for producing thin film batteries, the process needs to be optimized to reduce porosity as well as surface imperfections at the interfaces. Temperature treatments are mostly likely necessary to increase density without damaging the integrity of the various chemical structures and electrochemical properties.

Luckily, the tools necessary to investigate the hurdles are available. The key is to deliver reliable and reproductible results, as well as a critical eye to interpret them.

Above all, the challenge is to devise a solid correlation between impedance behaviour and other experiments to make EIS more convincing.

Recommendations for future work

The issue reported most in this Thesis, is the potential impurity relating to the liquid additions in the electrochemical cells. In order to increase the performance of the cells, liquid compounds should be ordered more regularly, and in lower volumes. We extracted our ionic liquids from large containers, consequently dried them out in vacuum antechambers. Yet this does not solve the potential previous contaminations in the liquid relating to our inability to filter out impurities, as well as our inability to test the purity of the compounds. Electrochemical cells require compounds that are 99.99% pure, especially when striving to report accurate results. Anything less can severely hamper findings and lead to inconclusive results.

As mentioned in the Discussion, determining the shape of the Na-beta”-alumina particles is also highly relevant to make an accurate assessment for the surface area. Only by determining the shape can the surface area be determined and a more accurate correlation be made. This can be done using SEM for example.

Isolating the properties of Na-beta”-alumina and the effects of liquid addition may be more viable using a well-defined symmetric cell. Corrosion has been reported when using Na symmetric cells, so maybe the cathode material P2-NNM can be used. Further research should be done on the subject of symmetric cells, as well as the consideration of which material to choose.

Material decomposition can be investigated further through operando in situ XRD. This can provide insight into the phase change and/or rate of decomposition throughout the cycling process.

A more accurate quantification of the compounds present in the system can be done using Energy Dispersive X-ray Spectrometry (EDS). This can provide elemental mapping to identify potential growing phases

To gain fundamental understanding of the Sodium-ion mobility in Na-beta”-alumina, the material needs to be isolated and characterized using solid-state nuclear magnetic resonance (NMR) spectroscopy.

References

[1] Rohde, R. A., & Muller, R. A. (2015). Air pollution in China: mapping of concentrations and sources. *PloS one*, *10*(8), e0135749.

[2] Ritchie, H., & Roser, M. (2014). Energy production & changing energy sources. *Our World in data*.
[3] World Energy Outlook 2017. Technical report, International Energy Agency, 2017

[4] Seinfeld, J. H., & Pandis, S. N. (2016). *Atmospheric chemistry and physics: from air pollution to climate change*. John Wiley & Sons.

[5] Speirs, J., McGlade, C., & Slade, R. (2015). Uncertainty in the availability of natural resources: Fossil fuels, critical metals and biomass. *Energy Policy*, *87*, 654-664.

[6] [Scarlat, N., Dallemand, J. F., Monforti-Ferrario, F., Banja, M., & Motola, V. (2015). Renewable energy policy framework and bioenergy contribution in the European Union–An overview from National Renewable Energy Action Plans and Progress Reports. *Renewable and Sustainable Energy Reviews*, *51*, 969-985.

[7] Schleicher-Tappeser, R. (2012). How renewables will change electricity markets in the next five years. *Energy policy*, *48*, 64-75.

[8] Park, J. K. (Ed.). (2012). *Principles and applications of lithium secondary batteries*. John Wiley & Sons.

[9] David, W. I. (2011). Effective hydrogen storage: a strategic chemistry challenge. *Faraday Discussions*, *151*, 399-414.

[10] [Lee, D. Y., Elgowainy, A., Kotz, A., Vijayagopal, R., & Marcinkoski, J. (2018). Life-cycle implications of hydrogen fuel cell electric vehicle technology for medium-and heavy-duty trucks. *Journal of Power Sources*, *393*, 217-229.

[11] [Notter, D. A., Gauch, M., Widmer, R., Wager, P., Stamp, A., Zah, R., & Althaus, H. J. (2010). Contribution of Li-ion batteries to the environmental impact of electric vehicles.

[12] Quartarone, E., Mustarelli, P., & Magistris, A. (1998). PEO-based composite polymer electrolytes. *Solid State Ionics*, *110*(1-2), 1-14.

[13] Hwang, J. Y., Myung, S. T., & Sun, Y. K. (2017). Sodium-ion batteries: present and future. *Chemical Society Reviews*, *46*(12), 3529-3614.

[14] Bard, A. J., Faulkner, L. R., Leddy, J., & Zoski, C. G. (1980). *Electrochemical methods: fundamentals and applications* (Vol. 2). New York: wiley.

[15] Nazri, G. A., & Pistoia, G. (Eds.). (2008). *Lithium batteries: science and technology*. Springer Science & Business Media.

[16] Megahed, S., & Scrosati, B. (1994). Lithium-ion rechargeable batteries. *Journal of Power Sources*, *51*(1-2), 79-104.

[17] Nishi, Y. (2001). The development of lithium ion secondary batteries. *The Chemical Record*, *1*(5), 406-413.

[18] Yaksic, A., & Tilton, J. E. (2009). Using the cumulative availability curve to assess the threat of mineral depletion: The case of lithium. *Resources Policy*, *34*(4), 185-194.

[19] Zu, C. X., & Li, H. (2011). Thermodynamic analysis on energy densities of batteries. *Energy & Environmental Science*, *4*(8), 2614-2624.

[20] Pan, H., Hu, Y. S., & Chen, L. (2013). Room-temperature stationary sodium-ion batteries for large-scale electric energy storage. *Energy & Environmental Science*, *6*(8), 2338-2360.

[21] De La Llave, E., Borgel, V., Park, K. J., Hwang, J. Y., Sun, Y. K., Hartmann, P., ... & Aurbach, D. (2016). Comparison between Na-Ion and Li-Ion cells: understanding the critical role of the cathodes stability and the anodes pretreatment on the cells behavior. *ACS applied materials & interfaces*, *8*(3), 1867-1875.

[22] Hong, S. Y., Kim, Y., Park, Y., Choi, A., Choi, N. S., & Lee, K. T. (2013). Charge carriers in rechargeable batteries: Na ions vs. Li ions. *Energy & Environmental Science*, *6*(7), 2067-2081.

[23] U.S. Geological Survey, 2017, Mineral commodity summaries 2017: U.S. Geological Survey, 202 p.

[24] Slater, M. D., Kim, D., Lee, E., & Johnson, C. S. (2013). Sodium-ion batteries. *Advanced Functional Materials*, *23*(8), 947-958.

[25] Luo, W., & Hu, L. (2015). Na metal anode:"holy grail" for room-temperature Na-ion batteries?.

[26] Kundu, D., Talaie, E., Duffort, V., & Nazar, L. F. (2015). The emerging chemistry of sodium ion batteries for electrochemical energy storage. *Angewandte Chemie International Edition*, *54*(11), 3431-3448.

[27] Zhao, J., Zhao, L., Chihara, K., Okada, S., Yamaki, J. I., Matsumoto, S., ... & Nakane, K. (2013). Electrochemical and thermal properties of hard carbon-type anodes for Na-ion batteries. *Journal of Power Sources*, *244*, 752-757.

[28] Ong, S. P., Chevrier, V. L., Hautier, G., Jain, A., Moore, C., Kim, S., ... & Ceder, G. (2011). Voltage, stability and diffusion barrier differences between sodium-ion and lithium-ion intercalation materials. *Energy & Environmental Science*, *4*(9), 3680-3688.

[29] Ellis, B. L., & Nazar, L. F. (2012). Sodium and sodium-ion energy storage batteries. *Current Opinion in Solid State and Materials Science*, *16*(4), 168-177.

[30] An, S. J., Li, J., Daniel, C., Mohanty, D., Nagpure, S., & Wood III, D. L. (2016). The state of understanding of the lithium-ion-battery graphite solid electrolyte interphase (SEI) and its relationship to formation cycling. *Carbon*, *105*, 52-76.

[31] Xu, K. (2004). Nonaqueous liquid electrolytes for lithium-based rechargeable batteries. *Chemical reviews*, *104*(10), 4303-4418.

[32] Fong, R., Von Sacken, U., & Dahn, J. R. (1990). Studies of lithium intercalation into carbons using nonaqueous electrochemical cells. *Journal of The Electrochemical Society*, *137*(7), 2009-2013.

[33] Liu, Y., Merinov, B. V., & Goddard, W. A. (2016). Origin of low sodium capacity in graphite and generally weak substrate binding of Na and Mg among alkali and alkaline earth metals. *Proceedings of the National Academy of Sciences*, *113*(14), 3735-3739.

[34] Stevens, D. A., & Dahn, J. R. (2000). An In Situ Small-Angle X-Ray Scattering Study of Sodium Insertion into a Nanoporous Carbon Anode Material within an Operating Electrochemical Cell. *Journal of The Electrochemical Society*, *147*(12), 4428-4431.

[35] Stevens, D. A., & Dahn, J. R. (2000). High capacity anode materials for rechargeable sodium-ion batteries. *Journal of the Electrochemical Society*, *147*(4), 1271-1273.

[36] Ponrouch, A., Goñi, A. R., & Palacín, M. R. (2013). High capacity hard carbon anodes for sodium ion batteries in additive free electrolyte. *Electrochemistry communications*, *27*, 85-88.

[37] Stevens, D. A., & Dahn, J. R. (2001). The mechanisms of lithium and sodium insertion in carbon materials. *Journal of The Electrochemical Society*, *148*(8), A803-A811.

[38] Thomas, P., & Billaud, D. (2002). Electrochemical insertion of sodium into hard carbons. *Electrochimica Acta*, *47*(20), 3303-3307.

[39] Alcántara, R., Jiménez-Mateos, J. M., Lavela, P., & Tirado, J. L. (2001). Carbon black: a promising electrode material for sodium-ion batteries. *Electrochemistry Communications*, *3*(11), 639-642.

[40] Beaulieu, L. Y., Hatchard, T. D., Bonakdarpour, A., Fleischauer, M. D., & Dahn, J. R. (2003). Reaction of Li with alloy thin films studied by in situ AFM. *Journal of The Electrochemical Society*, *150*(11), A1457-A1464.

[41] Liu, W. R., Yang, M. H., Wu, H. C., Chiao, S. M., & Wu, N. L. (2005). Enhanced cycle life of Si anode for Li-ion batteries by using modified elastomeric binder. *Electrochemical and Solid-State Letters*, *8*(2), A100-A103.

[42] Li, J., Lewis, R. B., & Dahn, J. R. (2007). Sodium carboxymethyl cellulose a potential binder for Si negative electrodes for Li-ion batteries. *Electrochemical and Solid-State Letters*, *10*(2), A17-A20.

[43] Slater, M. D., Kim, D., Lee, E., & Johnson, C. S. (2013). Sodium-ion batteries. *Advanced Functional Materials*, *23*(8), 947-958.

[44] Kim, S. W., Seo, D. H., Ma, X., Ceder, G., & Kang, K. (2012). Electrode materials for rechargeable sodium-ion batteries: potential alternatives to current lithium-ion batteries. *Advanced Energy Materials*, *2*(7), 710-721.

[45] Wang, L. P., Yu, L., Wang, X., Srinivasan, M., & Xu, Z. J. (2015). Recent developments in electrode materials for sodium-ion batteries. *Journal of Materials Chemistry A*, *3*(18), 9353-9378.

[46] Shibata, A., & Sato, K. (1999). Development of vanadium redox flow battery for electricity storage. *Power Engineering Journal*, *13*(3), 130-135.

[47] Okamoto, Y. (2013). Density functional theory calculations of alkali metal (Li, Na, and K) graphite intercalation compounds. *The Journal of Physical Chemistry C*, *118*(1), 16-19.

[48] Ong, S. P., Chevrier, V. L., Hautier, G., Jain, A., Moore, C., Kim, S., ... & Ceder, G. (2011). Voltage, stability and diffusion barrier differences between sodium-ion and lithium-ion intercalation materials. *Energy & Environmental Science*, *4*(9), 3680-3688. [49] C. Delmas, C. Fouassier, P. Hagenmuller, Physica B & C, 99 (1980) 81-85

[50] Yabuuchi, N., Kajiyama, M., Iwatate, J., Nishikawa, H., Hitomi, S., Okuyama, R., ... & Komaba, S. (2012). P2-type Na x [Fe 1/2 Mn 1/2] O 2 made from earth-abundant elements for rechargeable Na batteries. *Nature materials*, *11*(6), 512. [51] D. Kim, E. Lee, M. Slater, W.Q. Lu, S. Rood, C.S. Johnson, Electrochem Commun, 18 (2012) 66-69.

[52] Lu, Z., & Dahn, J. R. (2001). In Situ X-Ray Diffraction Study of P 2 Na2/3 [Ni1/3Mn2/3] O 2. *Journal of The Electrochemical Society*, *148*(11), A1225-A1229.

[53] Hemalatha, K., Jayakumar, M., Bera, P., & Prakash, A. S. (2015). Improved electrochemical performance of Na 0.67 MnO 2 through Ni and Mg substitution. *Journal of Materials Chemistry A*, *3*(42), 20908-20912.

[54] Lee, D. H., Xu, J., & Meng, Y. S. (2013). An advanced cathode for Na-ion batteries with high rate and excellent structural stability. *Physical Chemistry Chemical Physics*, *15*(9), 3304-3312.

[55] Van der Ven, A., & Ceder, G. (2000). Lithium diffusion in layered Li x CoO2. *Electrochemical and Solid-State Letters*, *3*(7), 301-304.

[56] Singh, G., Tapia-Ruiz, N., Lopez Del Amo, J. M., Maitra, U., Somerville, J. W., Armstrong, A. R., ... & Bruce, P. G. (2016). High Voltage Mg-Doped Na0. 67Ni0. 3–x Mg x Mn0. 7O2 (x= 0.05, 0.1) Na-Ion Cathodes with Enhanced Stability and Rate Capability. *Chemistry of Materials*, *28*(14), 5087-5094.

[57] Buchholz, D., Vaalma, C., Chagas, L. G., & Passerini, S. (2015). Mg-doping for improved long-term cyclability of layered Na-ion cathode materials–The example of P2-type NaxMg0. 11Mn0. 89O2. *Journal of Power Sources*, *282*, 581-585.

[58] Wu, X., Xu, G. L., Zhong, G., Gong, Z., McDonald, M. J., Zheng, S., ... & Yang, Y. (2016). Insights into the effects of zinc doping on structural phase transition of P2-type sodium nickel manganese oxide cathodes for high-energy sodium ion batteries. *ACS applied materials & interfaces*, *8*(34), 22227-22237.

[59] Masquelier, C., & Croguennec, L. (2013). Polyanionic (phosphates, silicates, sulfates) frameworks as electrode materials for rechargeable Li (or Na) batteries. *Chemical Reviews*, *113*(8), 6552-6591.

[60] Masquelier, C., & Croguennec, L. (2013). Polyanionic (phosphates, silicates, sulfates) frameworks as electrode materials for rechargeable Li (or Na) batteries. *Chemical Reviews*, *113*(8), 6552-6591.

[61] Oh, S. M., Myung, S. T., Yoon, C. S., Lu, J., Hassoun, J., Scrosati, B., ... & Sun, Y. K. (2014). Advanced Na [Ni0. 25Fe0. 5Mn0. 25] O2/C–Fe3O4 sodium-ion batteries using EMS electrolyte for energy storage. *Nano letters*, *14*(3), 1620-1626.

[62] Monti, D. (2016). *Innovative Electrolytes for Safer Sodium-Ion Batteries*. Chalmers University of Technology.

[63] Hong, H. P. (1976). Crystal structures and crystal chemistry in the system Na1+ xZr2SixP3– xO12. *Materials Research Bulletin*, *11*(2), 173-182.

[64] Goodenough, J. B., Hong, H. P., & Kafalas, J. A. (1976). Fast Na+-ion transport in skeleton structures. *Materials Research Bulletin*, *11*(2), 203-220.

[65] Chen, S., Wu, C., Shen, L., Zhu, C., Huang, Y., Xi, K., ... & Yu, Y. (2017). Challenges and Perspectives for NASICON-Type Electrode Materials for Advanced Sodium-Ion Batteries. *Advanced Materials*, *29*(48), 1700431.

[66] Francisco, B. E., Stoldt, C. R., & M'Peko, J. C. (2015). Energetics of ion transport in NASICON-type electrolytes. *The Journal of Physical Chemistry C*, *119*(29), 16432-16442.

[67] Aurbach, D., Talyosef, Y., Markovsky, B., Markevich, E., Zinigrad, E., Asraf, L., ... & Kim, H. J. (2004). Design of electrolyte solutions for Li and Li-ion batteries: a review. *Electrochimica Acta*, *50*(2-3), 247-254.

[68] Xu, K. (2014). Electrolytes and interphases in Li-ion batteries and beyond. *Chemical reviews*, *114*(23), 11503-11618.

[69] Ponrouch, A., Marchante, E., Courty, M., Tarascon, J. M., & Palacin, M. R. (2012). In search of an optimized electrolyte for Na-ion batteries. *Energy & Environmental Science*, *5*(9), 8572-8583.

[70] Hwang, J. Y., Myung, S. T., Yoon, C. S., Kim, S. S., Aurbach, D., & Sun, Y. K. (2016). Novel Cathode Materials for Na-Ion Batteries Composed of Spoke-Like Nanorods of Na [Nio. 61Coo. 12Mno. 27] O2 Assembled in Spherical Secondary Particles. *Advanced Functional Materials*, *26*(44), 8083-8093.

[71] Yabuuchi, N., Kubota, K., Dahbi, M., & Komaba, S. (2014). Research development on sodium-ion batteries. *Chemical reviews*, *114*(23), 11636-11682.

[72] Croce, F., Appetecchi, G. B., Persi, L., & Scrosati, B. (1998). Nanocomposite polymer electrolytes for lithium batteries. *Nature*, *394*(6692), 456.

[73] Croce, F., Settimi, L., Scrosati, B., Zane, D., Gallegos, A. A., Martinez, S. S., & Reyes, J. L. R. (2006). Nanocomposite, PEO-LiBOB polymer electrolytes for low temperature, lithium rechargeable batteries. *Journal of New Materials for Electrochemical Systems*, *9*(1), 3.

[74] Salomon, M. (1998). Solubility problems relating to lithium battery electrolytes. *Pure and applied chemistry*, *70*(10), 1905-1912.

[75] Barthel, J. M. G., Gores, H. J., Neueder, R., & Schmid, A. (1999). Electrolyte solutions for technology-new aspects and approaches. *Pure and Applied Chemistry*, *71*(9), 1705-1715.

[76] Yoshio, M., Brodd, R. J., & Kozawa, A. (2009). *Lithium-ion batteries* (Vol. 1). New York: Springer.

[77] Zhang, S. S. (2006). A review on electrolyte additives for lithium-ion batteries. *Journal of Power Sources*, *162*(2), 1379-1394.

[78] Verma, P., Maire, P., & Novák, P. (2010). A review of the features and analyses of the solid electrolyte interphase in Li-ion batteries. *Electrochimica Acta*, *55*(22), 6332-6341.

[79] Scrosati, B., & Garche, J. (2010). Lithium batteries: Status, prospects and future. *Journal of power sources*, *195*(9), 2419-2430.

[80] Schaefer, J. L., Lu, Y., Moganty, S. S., Agarwal, P., Jayaprakash, N., & Archer, L. A. (2012). Electrolytes for high-energy lithium batteries. *Applied Nanoscience*, *2*(2), 91-109.

[81] Fong, R., Von Sacken, U., & Dahn, J. R. (1990). Studies of lithium intercalation into carbons using nonaqueous electrochemical cells. *Journal of The Electrochemical Society*, *137*(7), 2009-2013.

[82] Zhao, J., Zhao, L., Dimov, N., Okada, S., & Nishida, T. (2013). Electrochemical and thermal properties of α-NaFeO2 cathode for Na-ion batteries. *Journal of The Electrochemical Society*, *160*(5), A3077-A3081.

[83] Xia, X., & Dahn, J. R. (2012). A study of the reactivity of de-intercalated P2-NaxCoO2 with non-aqueous solvent and electrolyte by accelerating rate calorimetry. *Journal of the Electrochemical Society*, *159*(5), A647-A650.

[84] Komaba, S., Murata, W., Ishikawa, T., Yabuuchi, N., Ozeki, T., Nakayama, T., ... & Fujiwara, K. (2011). Electrochemical Na insertion and solid electrolyte interphase for hard-carbon electrodes and application to Na-Ion batteries. *Advanced Functional Materials*, *21*(20), 3859-3867.

[85] Yu, C., Ganapathy, S., Van Eck, E. R., Wang, H., Basak, S., Li, Z., & Wagemaker, M. (2017). Accessing the bottleneck in all-solid state batteries, lithium-ion transport over the solid-electrolyte-electrode interface. *Nature communications*, *8*(1), 1086.

[86] Tel'nova, G. B., & Solntsev, K. A. (2015). Structure and ionic conductivity of a beta-alumina-based solid electrolyte prepared from sodium polyaluminate nanopowders. *Inorganic Materials*, *51*(3), 257-266.

[87] Wang, Y., & Zhong, W. H. (2015). Development of Electrolytes towards Achieving Safe and High-Performance Energy-Storage Devices: A Review. *ChemElectroChem*, *2*(1), 22-36.

[88] Lotsch, B. V., & Maier, J. (2017). Relevance of solid electrolytes for lithium-based batteries: A realistic view. *Journal of Electroceramics*, *38*(2-4), 128-141.

[89] Kazemiabnavi, S., Zhang, Z., Thornton, K., & Banerjee, S. (2016). Electrochemical stability window of imidazolium-based ionic liquids as electrolytes for lithium batteries. *The Journal of Physical Chemistry B*, *120*(25), 5691-5702.

[90] Kummer, J. T. (1972). β-alumina electrolytes. *Progress in solid state chemistry*, *7*, 141-175.

[91] Goodenough, J. B., Hong, H. P., & Kafalas, J. A. (1976). Fast Na+-ion transport in skeleton structures. *Materials Research Bulletin*, *11*(2), 203-220.

[92] Tel'nova, G. B., & Solntsev, K. A. (2015). Structure and ionic conductivity of a beta-alumina-based solid electrolyte prepared from sodium polyaluminate nanopowders. *Inorganic Materials*, *51*(3), 257-266.

[93] Fergus, J. W. (2012). Ion transport in sodium ion conducting solid electrolytes. *Solid State Ionics*, *227*, 102-112.

[94] Noguchi, Y., Kobayashi, E., Plashnitsa, L. S., Okada, S., & Yamaki, J. I. (2013). Fabrication and performances of all solid-state symmetric sodium battery based on NASICON-related compounds. *Electrochimica Acta*, *101*, 59-65.

[95] Lee, S. T., Kim, S. G., Jang, M. H., Hwang, S. H., Haw, J. R., & Lim, S. K. (2010). The phase relationship of Na-beta-aluminas synthesized by a sol-gel process in the ternary system Na2O-Al2O3-Li2O. *Journal of Ceramic Processing Research*, *11*(1), 86-91.

[96] Yao, Y. F. Y., & Kummer, J. T. (1967). Ion exchange properties of and rates of ionic diffusion in beta-alumina. *Journal of Inorganic and Nuclear Chemistry*, *29*(9), 2453-2475.

[97] Dunn, B., Schwarz, B. B., Thomas, J. O., & Morgan, P. E. D. (1988). Preparation and structure of Li-Stabilized Na+ β ″-Alumina single crystals. *Solid State Ionics*, *28*, 301-305.

[98] Chen, G., Lu, J., Li, L., Chen, L., & Jiang, X. (2016). Microstructure control and properties of β ″-Al2O3 solid electrolyte. *Journal of Alloys and Compounds*, *673*, 295-301.

[99] Chi, C., Katsui, H., & Goto, T. (2017). Effect of Li addition on the formation of Na-β/β″-alumina film by laser chemical vapor deposition. *Ceramics International*, *43*(1), 1278-1283.

[100] Santhanagopalan, D., Qian, D., McGilvray, T., Wang, Z., Wang, F., Camino, F., ... & Meng, Y. S. (2013). Interface limited lithium transport in solid-state batteries. *The journal of physical chemistry letters*, *5*(2), 298-303.

[101] Liu, L., Qi, X., Ma, Q., Rong, X., Hu, Y. S., Zhou, Z., ... & Chen, L. (2016). Toothpaste-like electrode: a novel approach to optimize the interface for solid-state sodium-ion batteries with ultralong cycle life. *ACS applied materials & interfaces*, *8*(48), 32631-32636.

[102] J.H. Kennedy, In Solid electrolytes, Vol. 21, ed. By S. Geller (Springer, Berlin, 1977), p.105

[103] Hueso, K. B., Armand, M., & Rojo, T. (2013). High temperature sodium batteries: status, challenges and future trends. *Energy & Environmental Science*, *6*(3), 734-749.

[104] Olivier-Bourbigou, H., & Magna, L. (2002). Ionic liquids: perspectives for organic and catalytic reactions. *Journal of Molecular Catalysis A: Chemical*, *182*, 419-437.

[105] Armand, M., Endres, F., MacFarlane, D. R., Ohno, H., & Scrosati, B. (2011). Ionic-liquid materials for the electrochemical challenges of the future. In *Materials For Sustainable Energy: A Collection of Peer-Reviewed Research and Review Articles from Nature Publishing Group* (pp. 129-137).

[106] Hallett, J. P., & Welton, T. (2011). Room-temperature ionic liquids: solvents for synthesis and catalysis. 2. *Chemical reviews*, *111*(5), 3508-3576.

[107] Zhang, S., Sun, N., He, X., Lu, X., & Zhang, X. (2006). Physical properties of ionic liquids: database and evaluation. *Journal of physical and chemical reference data*, *35*(4), 1475-1517.

[108] Welton, T. (1999). Room-temperature ionic liquids. Solvents for synthesis and catalysis. *Chemical reviews*, *99*(8), 2071-2084.

[109] Ma, X., Chen, H., & Ceder, G. (2011). Electrochemical properties of monoclinic NaMnO2. *Journal of The Electrochemical Society*, *158*(12), A1307-A1312.

[110] Ponrouch, A., Monti, D., Boschin, A., Steen, B., Johansson, P., & Palacin, M. R. (2015). Non-aqueous electrolytes for sodium-ion batteries. *Journal of Materials Chemistry A*, *3*(1), 22-42.

[111] Jessop, P. G. (2011). Searching for green solvents. *Green Chemistry*, *13*(6), 1391-1398.

[112] https://www.sigmaaldrich.com/technical-documents/articles/chemfiles/ionic-liquids-electrochemical.html

[113] Ding, C., Nohira, T., Kuroda, K., Hagiwara, R., Fukunaga, A., Sakai, S., ... & Inazawa, S. (2013). NaFSA–C1C3pyrFSA ionic liquids for sodium secondary battery operating over a wide temperature range. *Journal of Power Sources*, *238*, 296-300.

[114] Fukunaga, A., Nohira, T., Kozawa, Y., Hagiwara, R., Sakai, S., Nitta, K., & Inazawa, S. (2012). Intermediate-temperature ionic liquid NaFSA-KFSA and its application to sodium secondary batteries. *Journal of Power Sources*, *209*, 52-56.

[115] Yamamoto, T., Nohira, T., Hagiwara, R., Fukunaga, A., Sakai, S., Nitta, K., & Inazawa, S. (2012). Charge–discharge behavior of tin negative electrode for a sodium secondary battery using intermediate temperature ionic liquid sodium bis (fluorosulfonyl) amide–potassium bis (fluorosulfonyl) amide. *Journal of Power Sources*, *217*, 479-484.

[116] Chagas, L. G., Buchholz, D., Wu, L., Vortmann, B., & Passerini, S. (2014). Unexpected performance of layered sodium-ion cathode material ináionic liquid-based electrolyte. *Journal of Power Sources*, *247*, 377-383.

[117] Matsumoto, K., Hosokawa, T., Nohira, T., Hagiwara, R., Fukunaga, A., Numata, K., ... & Inazawa, S. (2014). The Na [FSA]–[C2C1im][FSA](C2C1im+: 1-ethyl-3-methylimidazolium and

FSA–: bis (fluorosulfonyl) amide) ionic liquid electrolytes for sodium secondary batteries. *Journal of Power Sources*, *265*, 36-39.

[118] Zhang, Z., Chen, S., Yang, J., Wang, J., Yao, L., Yao, X., ... & Xu, X. (2018). Interface re-engineering of Li10GeP2S12 electrolyte and lithium anode for all-solid-state lithium batteries with ultralong cycle life. *ACS applied materials & interfaces*, *10*(3), 2556-2565.

[119] Zhang, Z., Chen, S., Yang, J., Wang, J., Yao, L., Yao, X., ... & Xu, X. (2018). Interface re-engineering of Li10GeP2S12 electrolyte and lithium anode for all-solid-state lithium batteries with ultralong cycle life. *ACS applied materials & interfaces*, *10*(3), 2556-2565.

[120] Takada, K., Ohno, T., Ohta, N., Ohnishi, T., & Tanaka, Y. (2017). Positive and negative aspects of interfaces in solid-state batteries. *ACS Energy Letters*, *3*(1), 98-103.

[121] Tian, H. K., & Qi, Y. (2017). Simulation of the effect of contact area loss in all-solid-state Li-Ion batteries. *Journal of The Electrochemical Society*, *164*(11), E3512-E3521.

[122] Takada, K., Ohta, N., Zhang, L., Xu, X., Hang, B. T., Ohnishi, T., ... & Sasaki, T. (2012). Interfacial phenomena in solid-state lithium battery with sulfide solid electrolyte. *Solid State Ionics*, *225*, 594-597.

[123] Yamamoto, K., Iriyama, Y., Asaka, T., Hirayama, T., Fujita, H., Fisher, C. A., ... & Ogumi, Z. (2010). Dynamic visualization of the electric potential in an all-solid-state rechargeable lithium battery. *Angewandte Chemie International Edition*, *49*(26), 4414-4417.

[124] Peled, E., & Yamin, H. (1979). Solid Electrolyte Interphase (SEI) Electrodes. Part 1. The Kinetics of Lithium in LiAlCl4-SOCl2. *Israel Journal of Chemistry*, *18*(1-2), 131-135.

[125] Verma, P., Maire, P., & Novák, P. (2010). A review of the features and analyses of the solid electrolyte interphase in Li-ion batteries. *Electrochimica Acta*, *55*(22), 6332-6341.

[126] Muñoz-Márquez, M. A., Zarrabeitia, M., Castillo-Martínez, E., Eguía-Barrio, A., Rojo, T., & Casas-Cabanas, M. (2015). Composition and evolution of the solid-electrolyte interphase in Na2Ti3O7 electrodes for Na-ion batteries: XPS and Auger parameter analysis. *ACS applied materials & interfaces*, *7*(14), 7801-7808.

[127] Muñoz-Márquez, M. A., Zarrabeitia, M., Castillo-Martínez, E., Eguía-Barrio, A., Rojo, T., & Casas-Cabanas, M. (2015). Composition and evolution of the solid-electrolyte interphase in Na2Ti3O7 electrodes for Na-ion batteries: XPS and Auger parameter analysis. *ACS applied materials & interfaces*, *7*(14), 7801-7808.

[128] Wenzel, S., Hara, T., Janek, J., & Adelhelm, P. (2011). Room-temperature sodium-ion batteries: improving the rate capability of carbon anode materials by templating strategies. *Energy & Environmental Science*, *4*(9), 3342-3345.

[129] Komaba, S., Murata, W., Ishikawa, T., Yabuuchi, N., Ozeki, T., Nakayama, T., ... & Fujiwara, K. (2011). Electrochemical Na insertion and solid electrolyte interphase for hard-carbon electrodes and application to Na-Ion batteries. *Advanced Functional Materials*, *21*(20), 3859-3867.

[130] Moshkovich, M., Gofer, Y., & Aurbach, D. (2001). Investigation of the electrochemical windows of aprotic alkali metal (Li, Na, K) salt solutions. *Journal of The Electrochemical Society*, *148*(4), E155-E167.

[131] Wu, B., Wang, S., Evans IV, W. J., Deng, D. Z., Yang, J., & Xiao, J. (2016). Interfacial behaviours between lithium ion conductors and electrode materials in various battery systems. *Journal of Materials Chemistry A*, *4*(40), 15266-15280.

[132] Maier, J. (1987). Defect chemistry and conductivity effects in heterogeneous solid electrolytes. *Journal of The Electrochemical Society*, *134*(6), 1524-1535.

[133] Braun, S., Yada, C., & Latz, A. (2015). Thermodynamically consistent model for space-charge-layer formation in a solid electrolyte. *The Journal of Physical Chemistry C*, *119*(39), 22281-22288.

[134] Guo, X., & Chen, C. (2016). Space charge layer effect in solid state ion conductors and lithium batteries: principle and perspective. *Acta Chimica Slovenica*, *63*(3), 489-495.

[135] Haruta, M., Shiraki, S., Suzuki, T., Kumatani, A., Ohsawa, T., Takagi, Y., ... & Hitosugi, T. (2015). Negligible "negative space-charge layer effects" at oxide-electrolyte/electrode interfaces of thin-film batteries. *Nano letters*, *15*(3), 1498-1502.

[136] Yamada, H., Suzuki, K., Nishio, K., Takemoto, K., Isomichi, G., & Moriguchi, I. (2014). Interfacial phenomena between lithium ion conductors and cathodes. *Solid State Ionics*, *262*, 879-882.

[137] Haruyama, J., Sodeyama, K., Han, L., Takada, K., & Tateyama, Y. (2014). Space–charge layer effect at interface between oxide cathode and sulfide electrolyte in all-solid-state lithium-ion battery. *Chemistry of Materials*, *26*(14), 4248-4255.

[138] Yamada, H., Tsunoe, D., Shiraishi, S., & Isomichi, G. (2015). Reduced grain boundary resistance by surface modification. *The Journal of Physical Chemistry C*, *119*(10), 5412-5419.

[139] Kumar, P. P., & Yashonath, S. (2006). Ionic conduction in the solid state. *Journal of Chemical Sciences*, *118*(1), 135-154.

[140] Processing and Application of Ceramics*, Volume* 10*, Number* 2*,* 2016*, pp.* 67-72*(6)*

[141] Butee, S. P., Kambale, K. R., & Firodiya, M. (2016). Electrical properties of sodium beta-alumina ceramics synthesized by citrate sol-gel route using glycerine. *magnesium*, *3*, 9H2O.

[142] Whittingham, M. S., & Huggins, R. A. (1971). Measurement of sodium ion transport in beta alumina using reversible solid electrodes. *The Journal of Chemical Physics*, *54*(1), 414-416.

[143] Bragg, W. H., & Bragg, W. L. (1913). The reflection of X-rays by crystals. *Proceedings of the Royal Society of London. Series A, Containing Papers of a Mathematical and Physical Character*, *88*(605), 428-438.

[144] Larson, A. C., & Von Dreele, R. B. (1994). Gsas. *Report lAUR*, 86-748.

[145] Macdonald, J. R., & Barsoukov, E. (2005). Impedance spectroscopy: theory, experiment, and applications. *History*, *1*(8), 1-13.

[146] Pyun, S. I., Shin, H. C., Lee, J. W., & Go, J. Y. (2012). *Electrochemistry of insertion materials for hydrogen and lithium*. Springer Science & Business Media.

[147] Zhang, S. S., Xu, K., & Jow, T. R. (2004). Electrochemical impedance study on the low temperature of Li-ion batteries. *Electrochimica acta*, *49*(7), 1057-1061.

[148] Keil, P., & Jossen, A. (2012). Aufbau und parametrierung von batteriemodellen. In *19. DESIGN&ELEKTRONIK-Entwicklerforum Batterien & Ladekonzepte*.

[149] http://www.consultrsr.net/resources/eis/zarc.htm#ref1 – Accessed September 2018

[150]
https://www.researchgate.net/post/How_can_I_get_capacitance_value_from_EIS_Impedance_spectra_- accessed January 2019

[151] Abraham, D. P., Poppen, S. D., Jansen, A. N., Liu, J., & Dees, D. W. (2004). Application of a lithium–tin reference electrode to determine electrode contributions to impedance rise in high-power lithium-ion cells. *Electrochimica Acta*, *49*(26), 4763-4775.

[152] Shkrob, I. A., Marin, T. W., Zhu, Y., & Abraham, D. P. (2014). Why bis (fluorosulfonyl) imide is a “magic anion” for electrochemistry. *The Journal of Physical Chemistry C*, *118*(34), 19661-19671.

Appendix

All the EIS measurements could not be included in this report, at there are close to 300 measured cells, including pre/post cycling measurements, Na-beta”-alumina pellets as well as EIS measurements isolating certain components such as organic electrolyte ECPC, ionic liquids TES-TFSI and $Pyr_{14}FSI$.

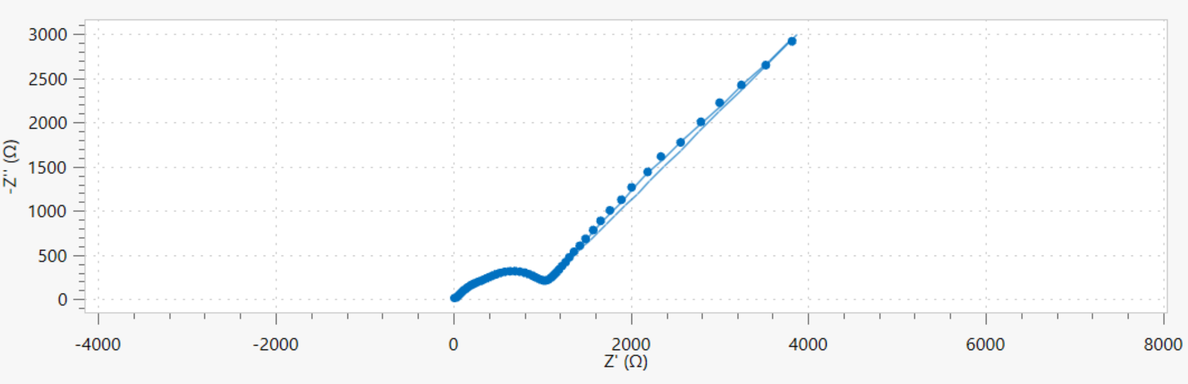

Figure. EIS measurement of battery with 87µm tape casted BASE and 3drops of $NaClO_4$: ECPC

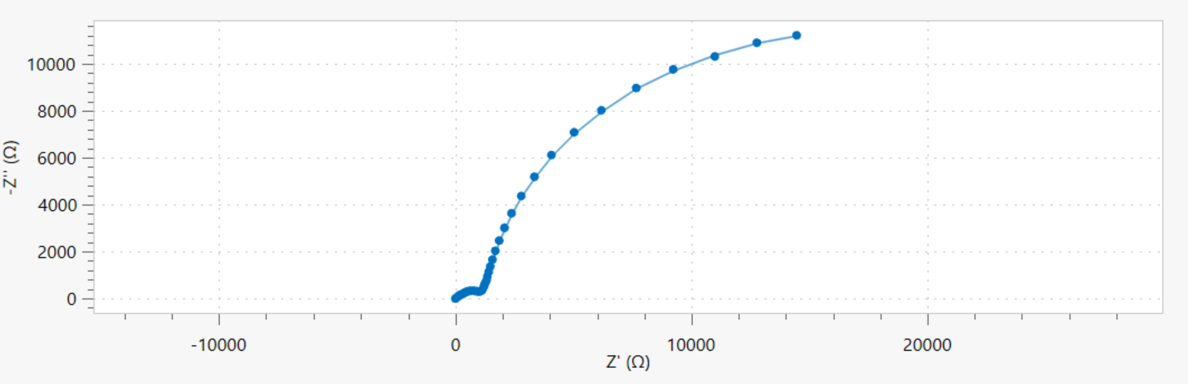

Figure. EIS measurement of battery with 55µm tape casted BASE and 1 drop of $NaClO_4$: ECPC

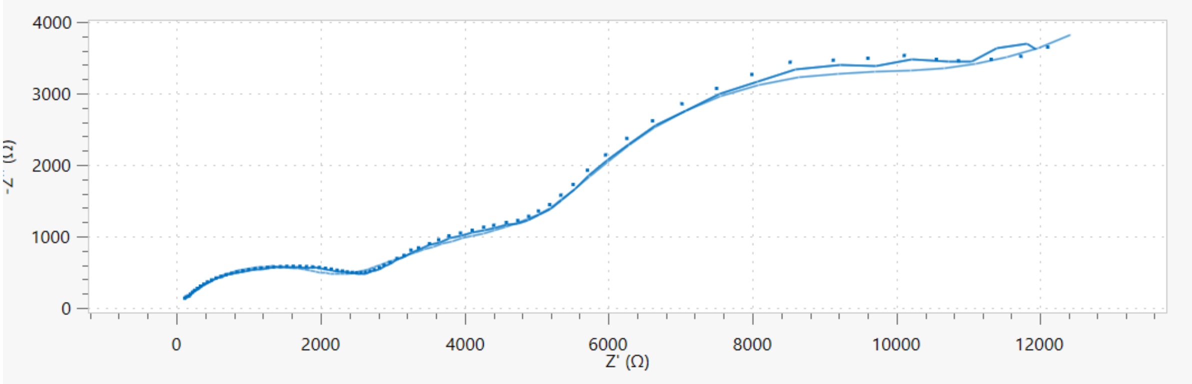

Figure. EIS measurement of battery with 75µm tape casted BASE and 1 drop of $NaClO_4$: ECPC pre-cycling

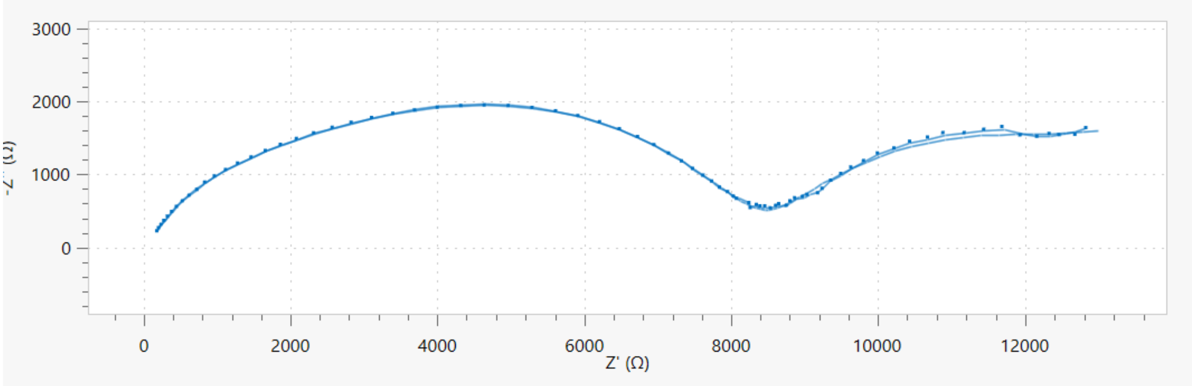

Figure. Battery with 75μm tapecasted BASE and 1 drop of $NaClO_4$: ECPC - post-cycling

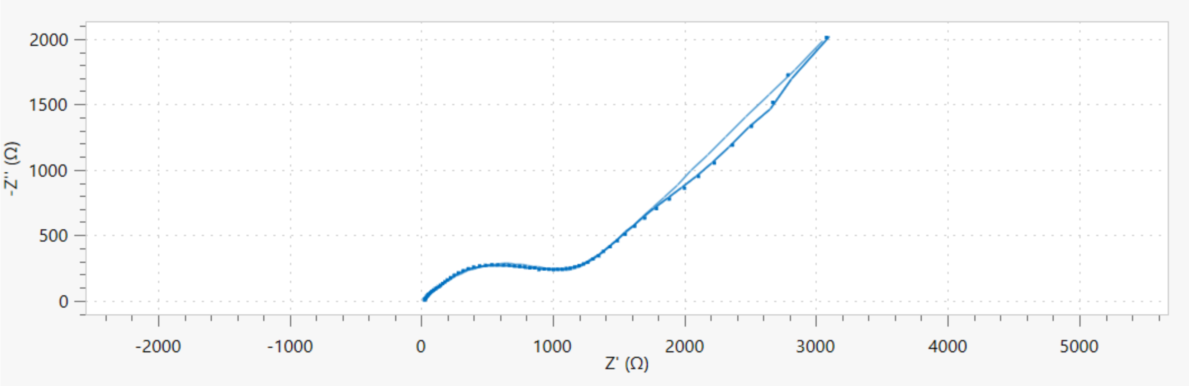

Figure. Battery with Pyr14FSI slurry with small BASE particles

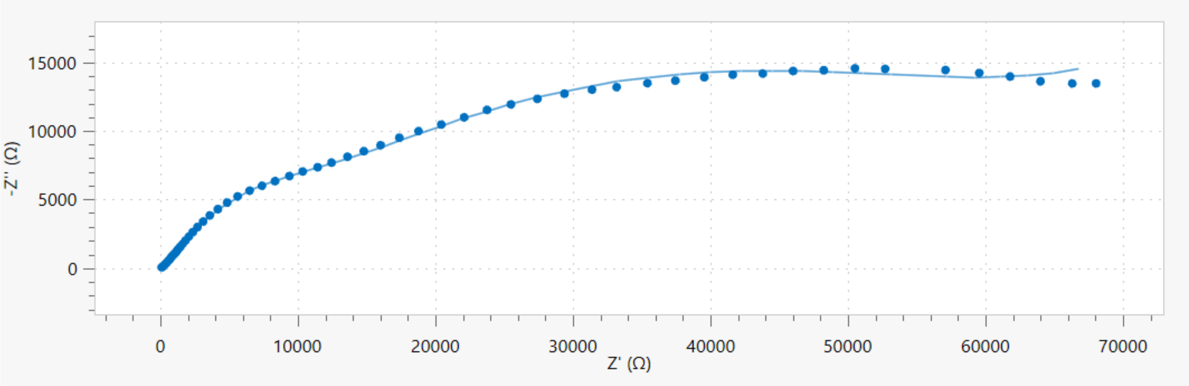

Figure. Battery with Pyr14FSI slurry with small BASE particles-postcycling

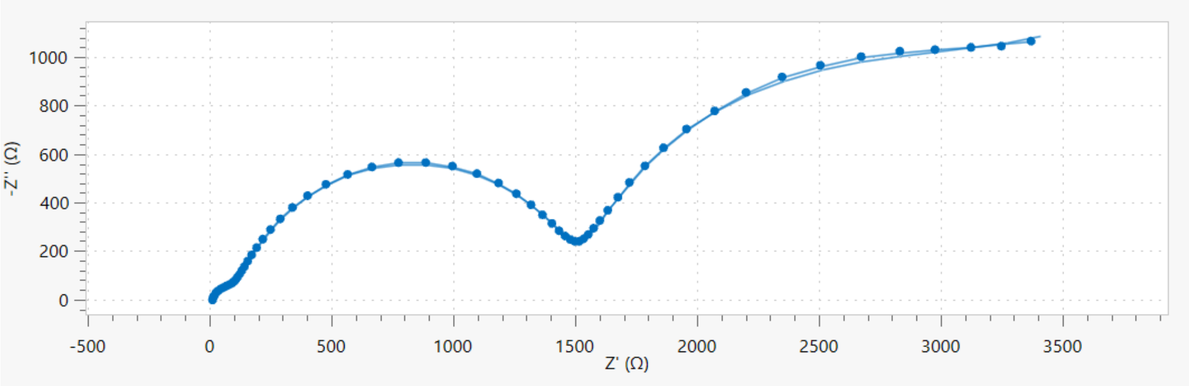

Figure. Battery with Pyr14FSI with separator

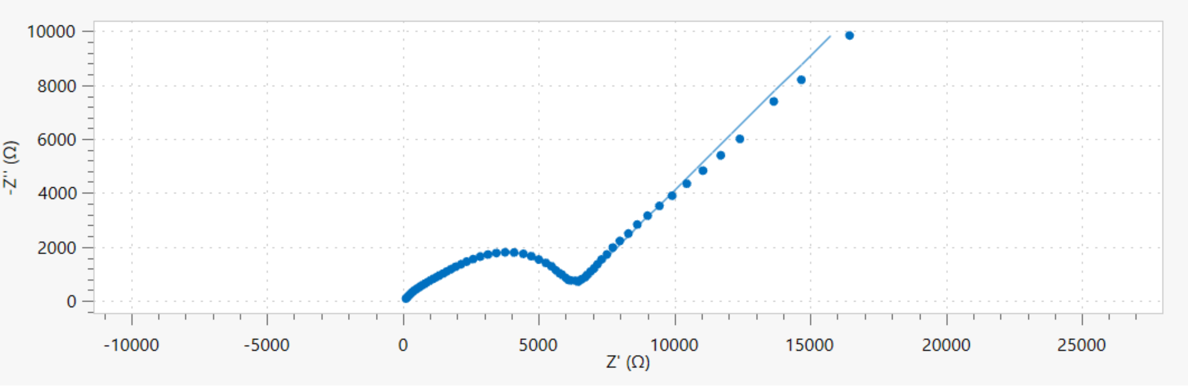

Figure. Battery with TES-TFSI slurry with small BASE particles-precycling

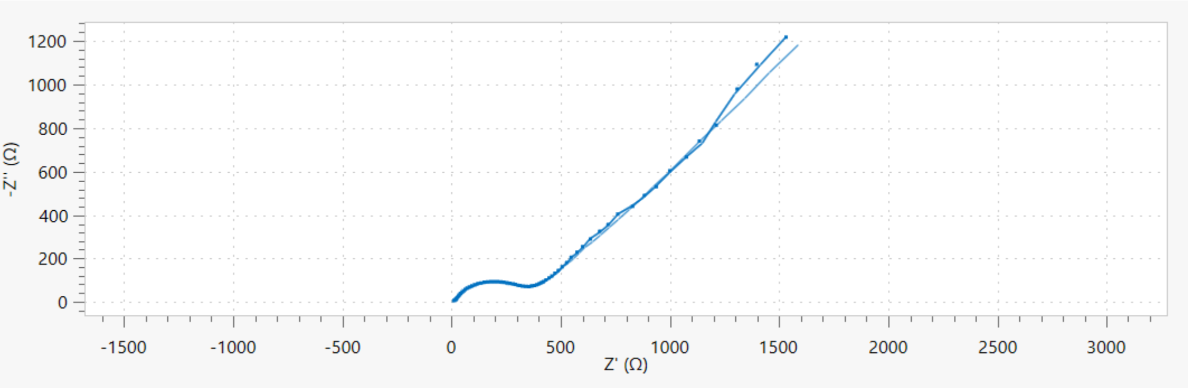

Figure. Battery with TES-TFSI slurry with small BASE particles-postcycling

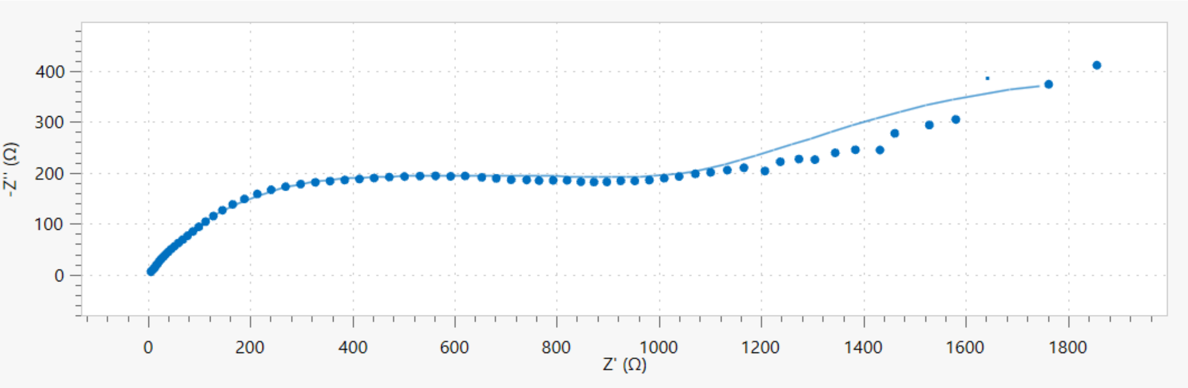

Figure. Battery with TES-TFSI slurry with big BASE particles-precycling

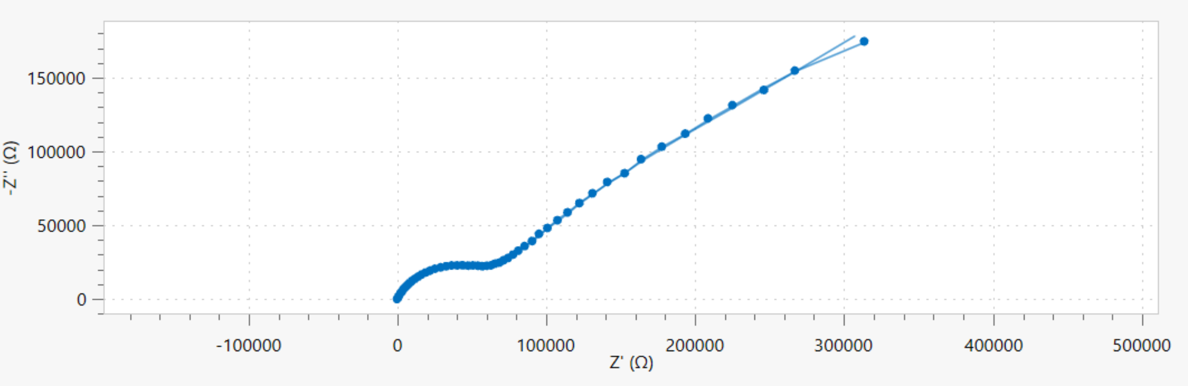

Figure. Battery with TES-TFSI slurry with big BASE particles-postcycling

Table. Overview of all the electrochemical cells, OCP before and after cycling as well as the fitting errors for the EIS measurements

		OCP		fitting error	
		pre	post	pre	post
4h milling					
140 µm		2.86	3.29	2.5	4
55 µm		2.78		5.1	
87 µm-2drops		2.78		7	
30 µm		2.81		5	
87 µm-3drops		3.05		2.3	
2h milling					
200 µm		2.81	3.22	1	0.7
24 µm-170 µm		2.83	3.31	3	1
100 µm		2.9	2.81	0.5	1
75 µm		2.85	2.77	6.4	0.4
ECPC					
12.5-75 µm		2.4		3.3	
7.5-100 µm		3.13		8	
12.5-100 µm		2.75		1.4	
24-170 µm		2.29		3.5	
TES-TFSI					
Ilslurry	**1a**	2.44		3	
TFSInormal	**1b**	2.51	2.08	3	1.1
TFSIslurry	**4**	1.7	1.11	7	2.5
TFSIsmall	**6: 35.6nm**	2.4	2.89	3	4.2
3,5IL	**2**	2.89	2.76	2.6	2.9
4IL	**3**	2.37	2.78	7	10
6IL	**5**	2.84	3.29	9	9
3IL-Small	**7: 35.6nm**	2.9	2.72	3	5.1
3IL-Big	**8: 32.3nm**	1.9	2.87	15	7
IL-sep	sep	2.88	3.2	10	1
PYR14FSI					
EIS-pyr2.5-base7.5-ocp2.67V	**1.a**	2.67	2.28	7	6
EIS-pyr14-betadry(7.5-2.5)(OCP2.86V)	**1.b**	2.86	2.1	5	9
EIS slurry pyr14-base	**1.c**	1.41		8.5	12
pyr14slurry++(2.56VOCP)	**2**	2.56	2.77	10	7.2
slurryPyr14-beta(2.84VOCP)	**3**	2.84	2.29	3.2	9
EIS-PyrnormalSlurry-2.56V	**4**	2.56	0.12	4	6
EIS-PyrsmallSlurry-2.6V	**5: 35.6nm**	2.6	2.35	0.5	2.2
pyr14slurryTHICK(2.59VOCP)	**6**	2.59	2.22	3	12
EIS-NNM-Pyr14FSIslurryBASE-Na	**7**	1.26	3.06	11	5
betapellet-NNMslurry(2.82VOCP)	**8-pellet**	**2.82**		6	6
BASEpellet0.5mm(2.5VOCP)	**9-pellet**	**2.5**	**2.8**	2	12
pyr14fsi-5drops-separator(OCP2.89V)	sep	2.89	3.31	0.5	6

Note that the ratios for battery with 55 µm and 87 µm-2drops are similar, as well as 30 µm and 87 µm-3drops. This allows us to compare them.

For example, 87 µm-2drops is 1,6times thicker than 55 µm, but with double the amount of liquid addittive, the electrolyte resistance should be half of 1.6. According to this reasoning,

$R_{electrolyte}$ of 87 µm-2drops should be 4.4Ω. It was measured at 4.5.
Similarly, 87 µm-3drops is 2.9times thicker than 30 µm (meaning it has 2.9times the resistance), with 3 times the amount of added liquid. Interestingly, the additonal drop of liquid did not improve the resistance as much, indicating that the liquid contribution nears its maximum and points toward saturation.

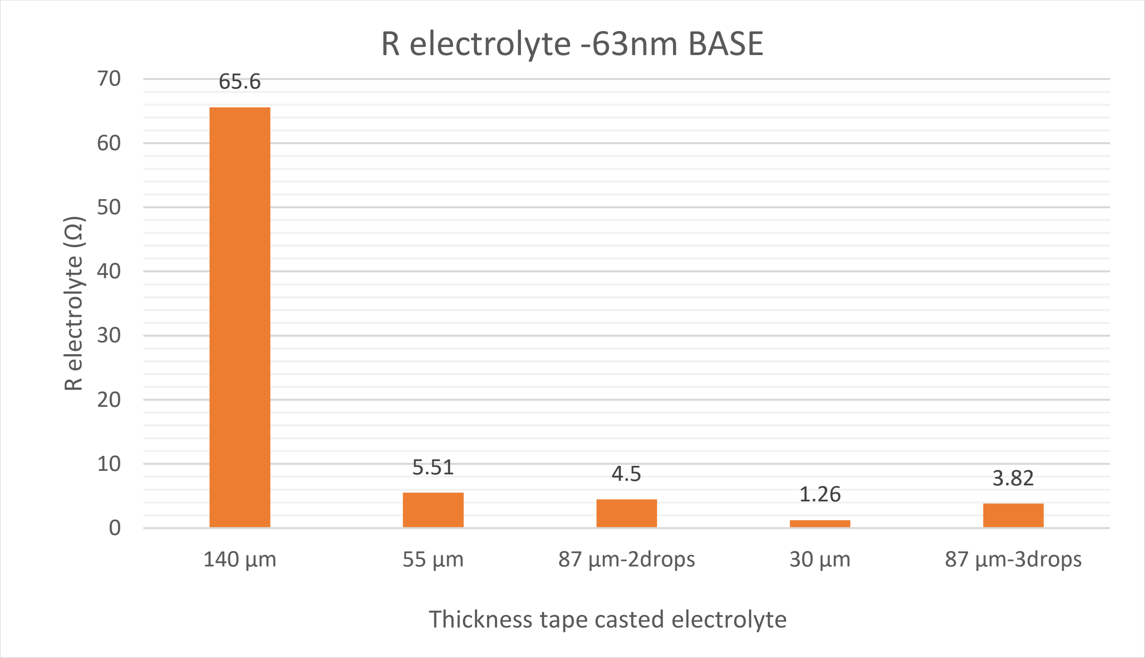

Figure. Electrolyte resistance of the tape casted series with $NaClO_4$ dissolved in ECPC organic electrolyte, with liquid additions varying from 1 to 3drops of added organic electrolyte.

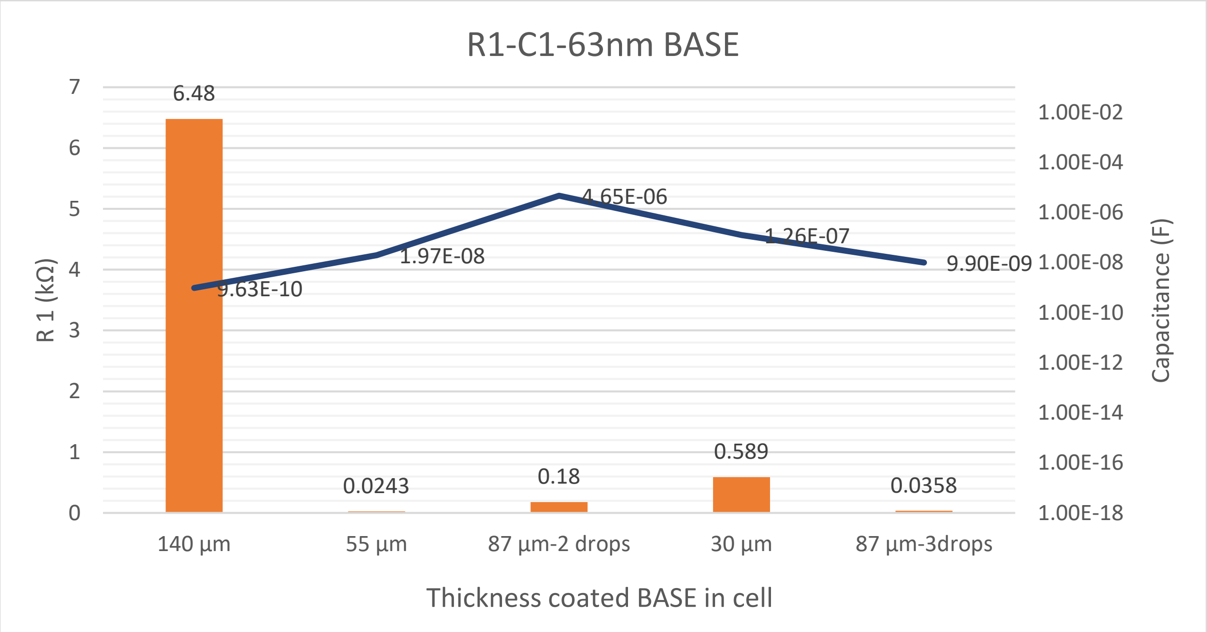

Figure. Equivalent circuit modelling of the first semi-circle of the Nyquist plot, describing the electrochemical interactions at high frequency, typically attributed to the SEI interactions.

R1 and C1 are the parameters usually attributed to the interface between electrode and electrolyte. These factors should only be dependent on the amount of added liquid and different particle sizes of the electrode (not the case here).

We see two trends here: an increasing resistance for the first three batteries, and a decreasing capacitance for the last three batteries. This can be explained by the conceptual flaw of EIS, overlapping phenomena. Since EIS measures a complete system, it is not always possible to isolate the various dynamics in the electrochemical system. If two different types of interactions happen with a similar time constant (here the high frequency), overlapping responses are measured. Only by isolating them can the data be reliable. In our case, the data seems inconclusive.

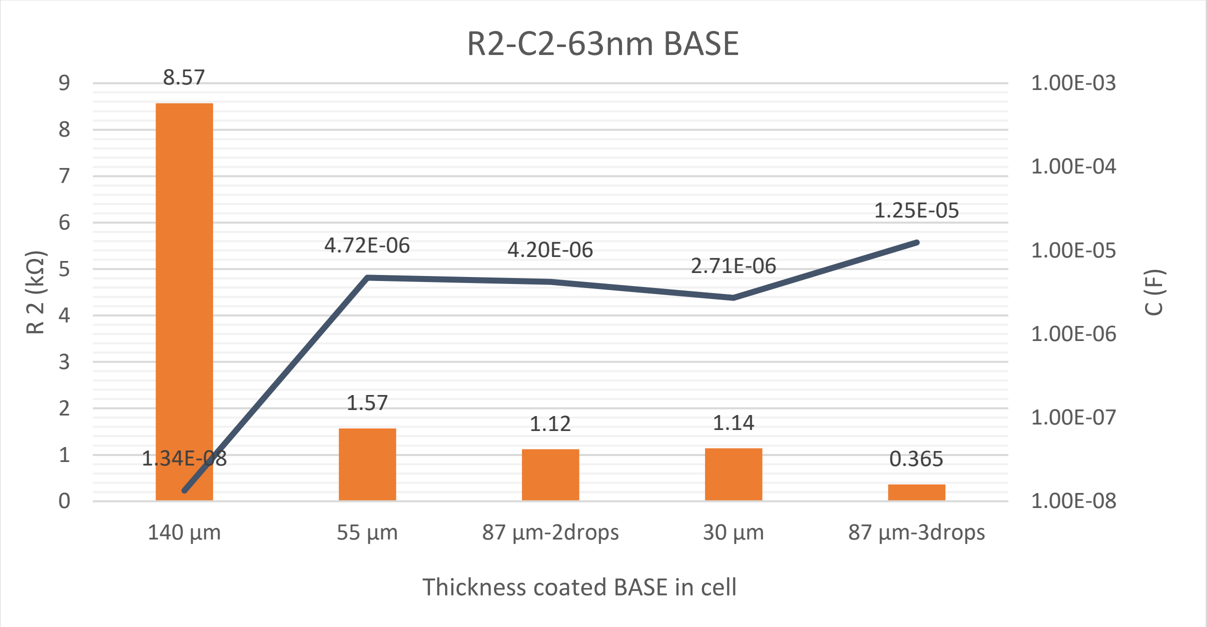

Figure. Equivalent circuit modelling of the second semi-circle of the Nyquist plot, describing the interactions at medium frequency. The resistance R2 is usually attributed to the charge transfer resistance, while the capacitance relates to the Double Layer around the particles.

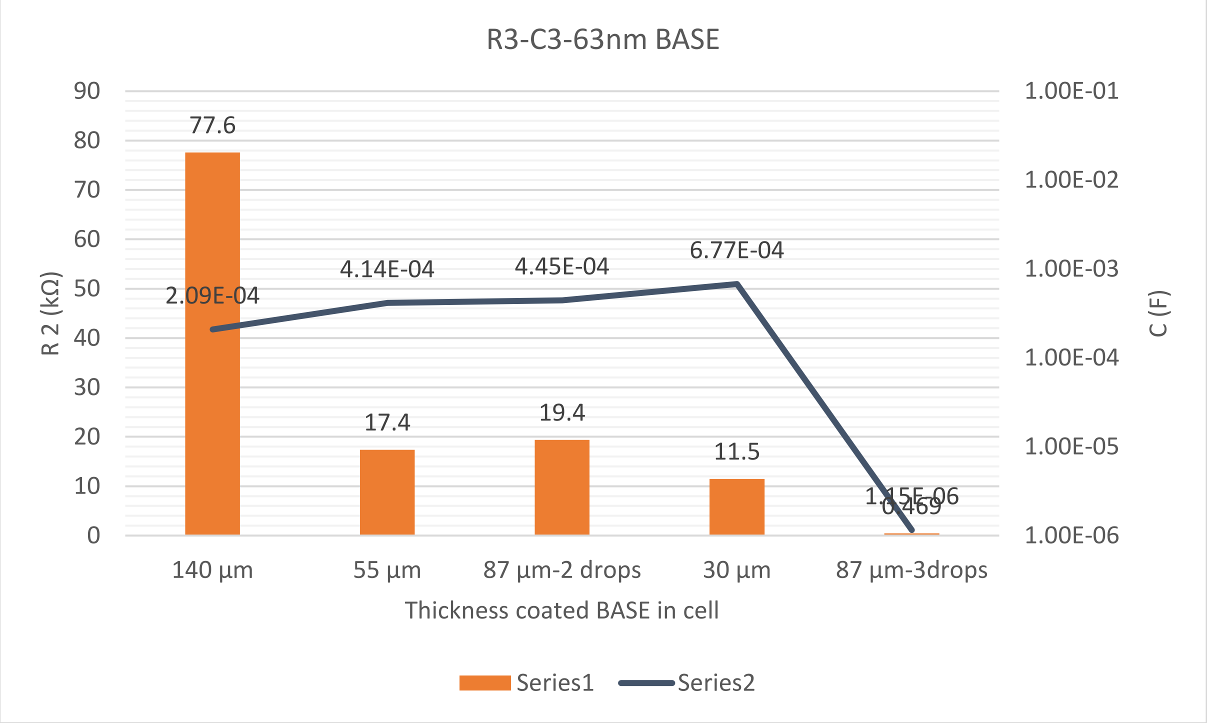

Figure. Equivalent circuit modelling of the third semi-circle of the Nyquist plot, describing the electrochemical interactions at low frequency, typically attributed to the many factors relating to mass transport, also an indication of Na⁺ ionic diffusion.

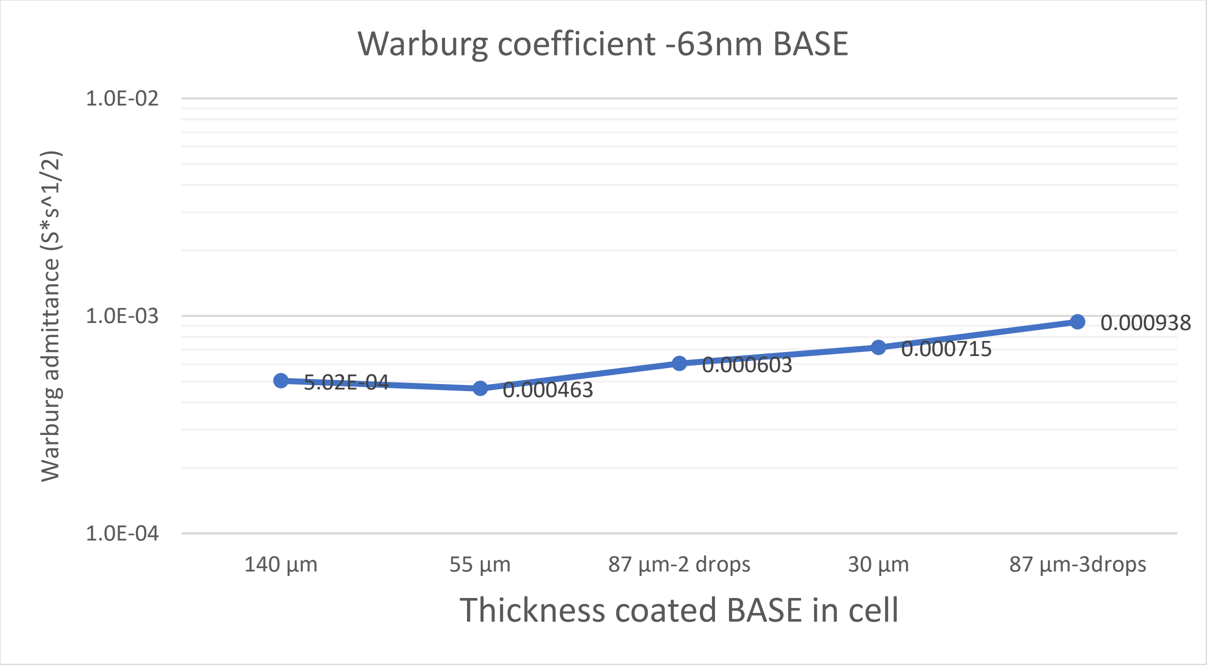

Figure. Diffusion coefficient for the 63nm series

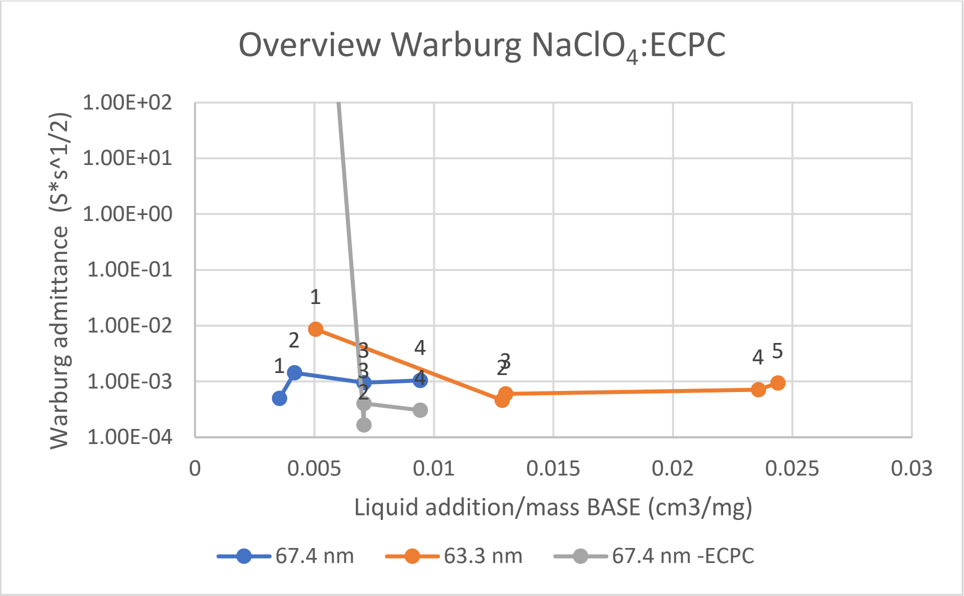

Figure. Overview without correlation to thickness

67nm series

The following plots are cells that have been analysed before and after cycling in order to measure the evolution of the dynamics in the cells. This will also give an indication of the aging and product decomposition in the cells.

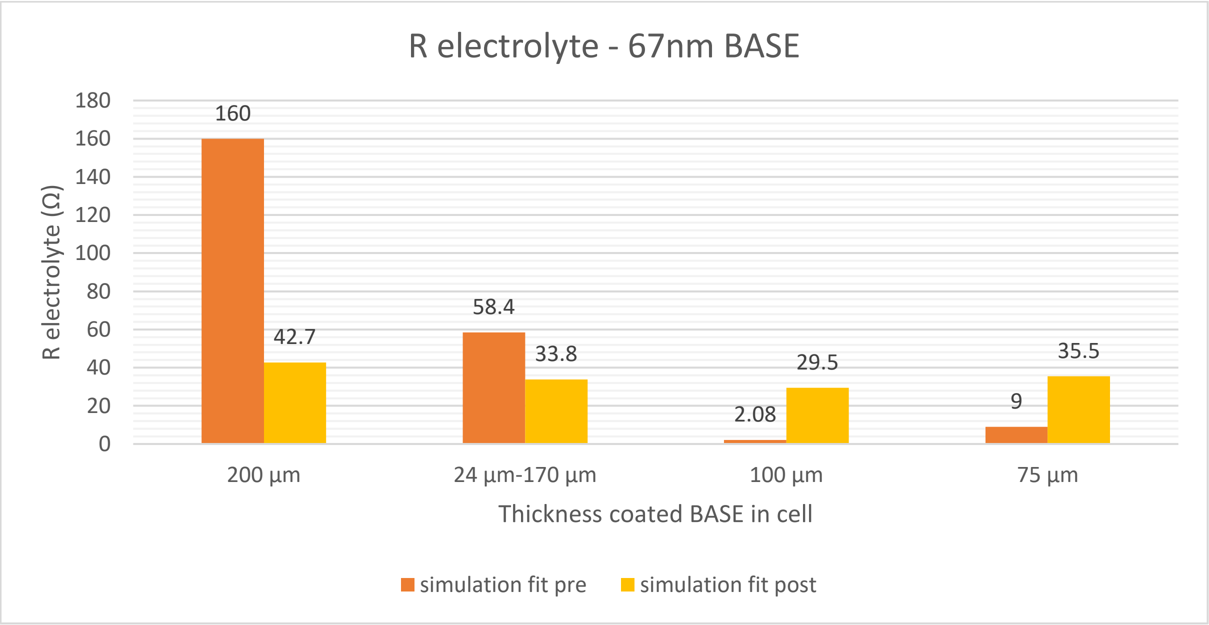

Figure. Electrolyte resistance of the tape casted series with 1 drop of $NaClO_4$ dissolved in ECPC organic electrolyte. The BASE particles are 67nm.

The first two batteries on the left have been casted together, only the second one has a cathode thin film that is double the size of the rest of the series (24 µm-170 µm). We would expect both batteries to have a similar resistance, yet the cell with the cathode twice as thick has a value for $R_{electrolyte}$ almost three times lower. This would suggest that the cathode material plays a role in the overall ionic conductivity of the system, or that the current collectors or connectors of that specific cell possessed a different resistance.

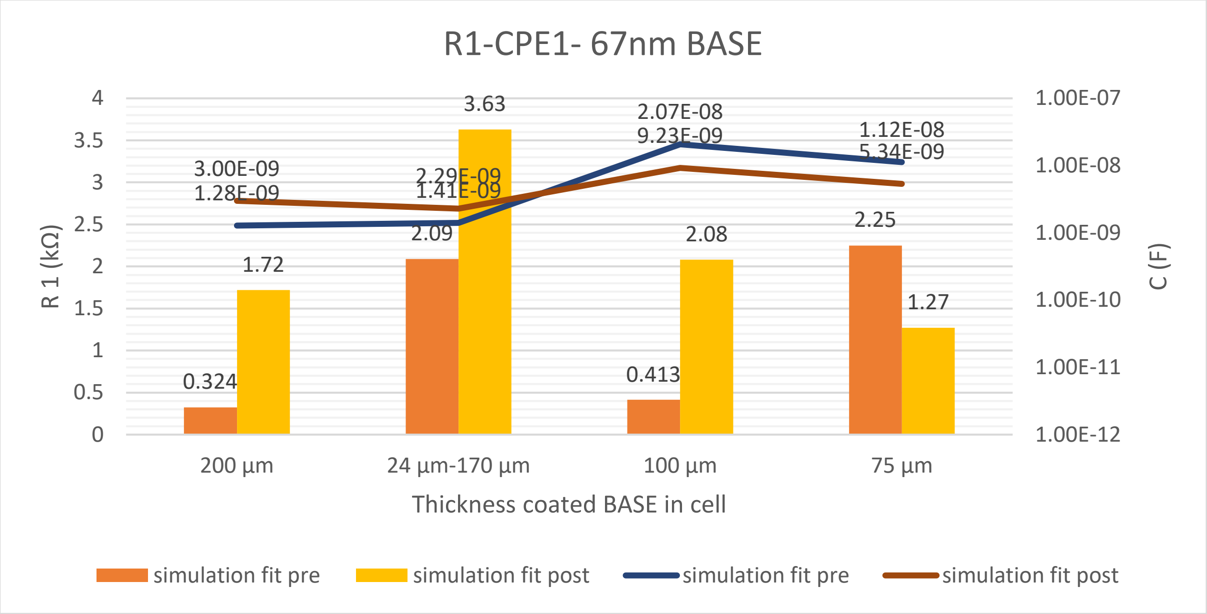

Figure. Resistances and Capacitances relating to the equivalent circuit modelling of the first semi-circle of the Nyquist plot (first parallel RC element). It quantifies the electrochemical interactions at high frequency, typically attributed to the SEI interactions.

We first look at the values before cycling the battery (simulation fit pre). According to the volume of liquid addition to Na-beta”-alumina mass, 200 µm should perform the worst. It has the thickest BASE coating, which should result in the most point contacts, longest diffusion path, highest amount of porosity and highest number of defects. Reading the Figure from right to left shows the increase in liquid contribution.

But according to the EIS data, 200 has the lowest resistance together with 100. 75 and 24-170 are slightly more resistant.

Generally, the resistance increased post-cycling, indicating a growth in the solid electrolyte interphase. Stable SEI formation has been proven using $NaClO_4$ dissolved in ECPC, which made it a viable organic electrolyte for these experiments.

A similar trend appears compared to the previous series of $NaClO_4$ dissolved in ECPC. For the batteries on the left, the resistance increases as the capacitance decreases. But this trend is not visible in the whole data set, which makes it challenging to explain.

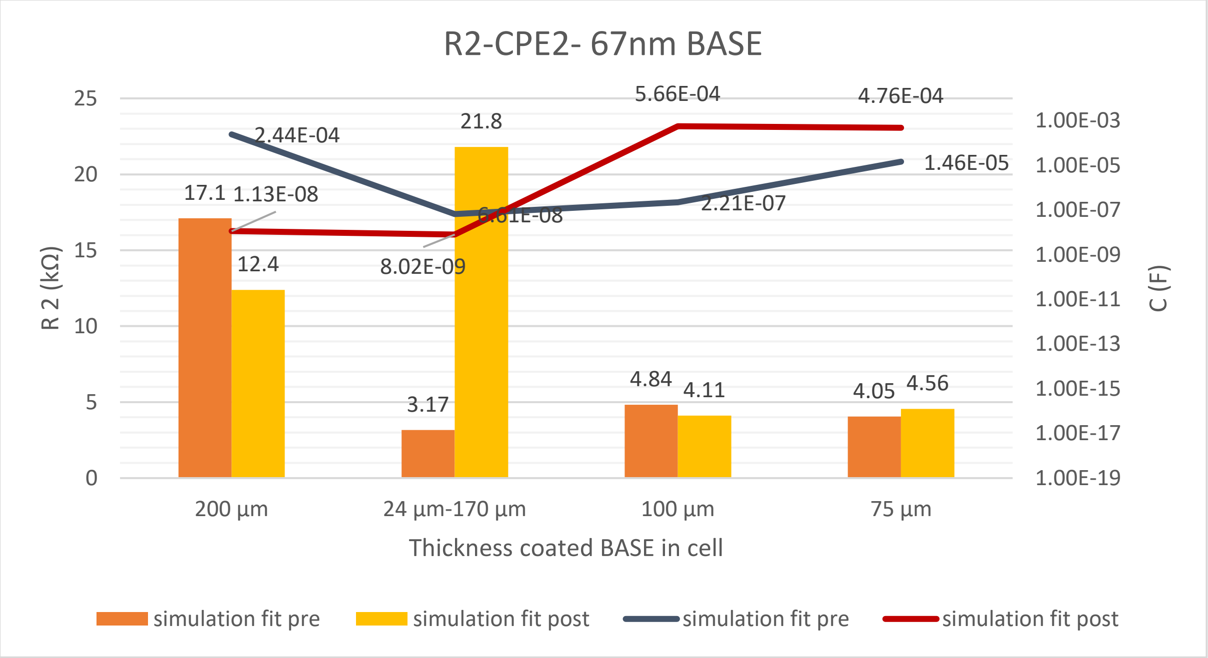

Figure. Equivalent circuit modelling of the second semi-circle of the Nyquist plot, describing the interactions at medium frequency. The resistance R2 is usually attributed to the charge transfer resistance, while the capacitance relates to the Double Layer around the particles.

The resistances for the medium frequency dynamics are proportional to the thickness of the electrolyte. For the thinnest cells (far right), the resistances are low and remain constant post-cycling. This would indicate a good stability regarding the charge transfer capabilities of the cells. The thicker batteries present a more fluctuating mid-frequency resistance, indicating more instability. This figure can also relate to the grain boundary factor relating to solid-solid interactions in the cells. Thicker cells naturally have more grain boundaries, thus showing higher resistances in line with electrolyte thickness.

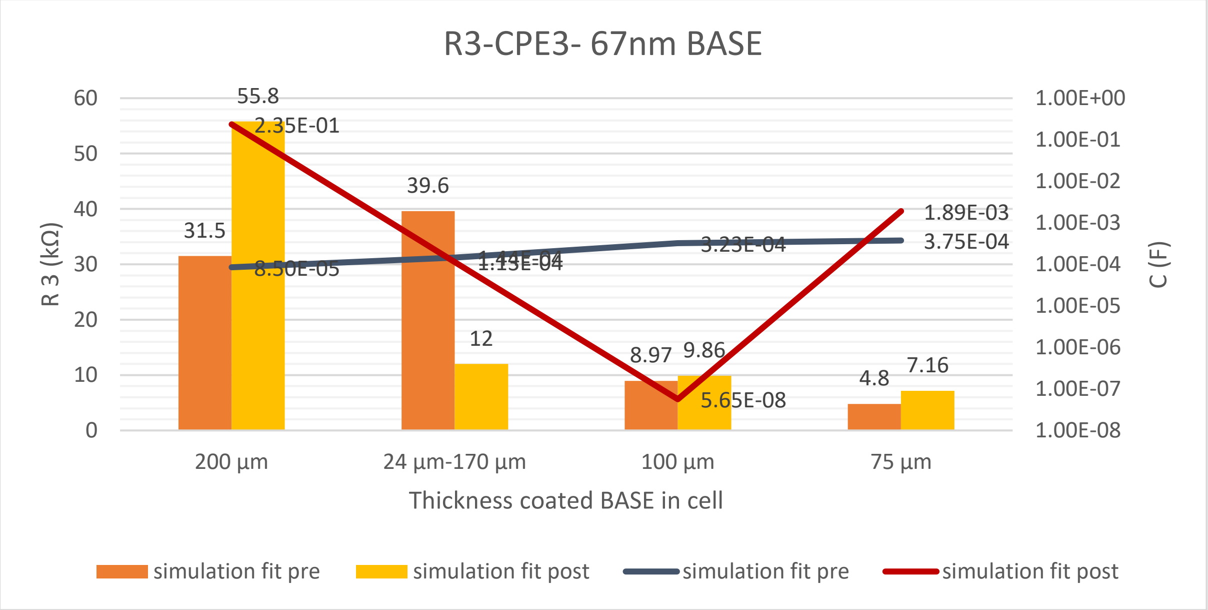

Figure. Equivalent circuit modelling of the third semi-circle of the Nyquist plot, describing the electrochemical interactions at low frequency, typically attributed to the many factors relating to mass transport, also an indication of Na^+ ionic diffusion.

For the third Nyquist semi-circle modelling, a clear post-cycling evolution for resistance is shown, as well as a constant capacitance throughout the series. The decreasing resistance leads us to believe that a good ionic conduction path was formed in each system, promoting cycling capabilities.

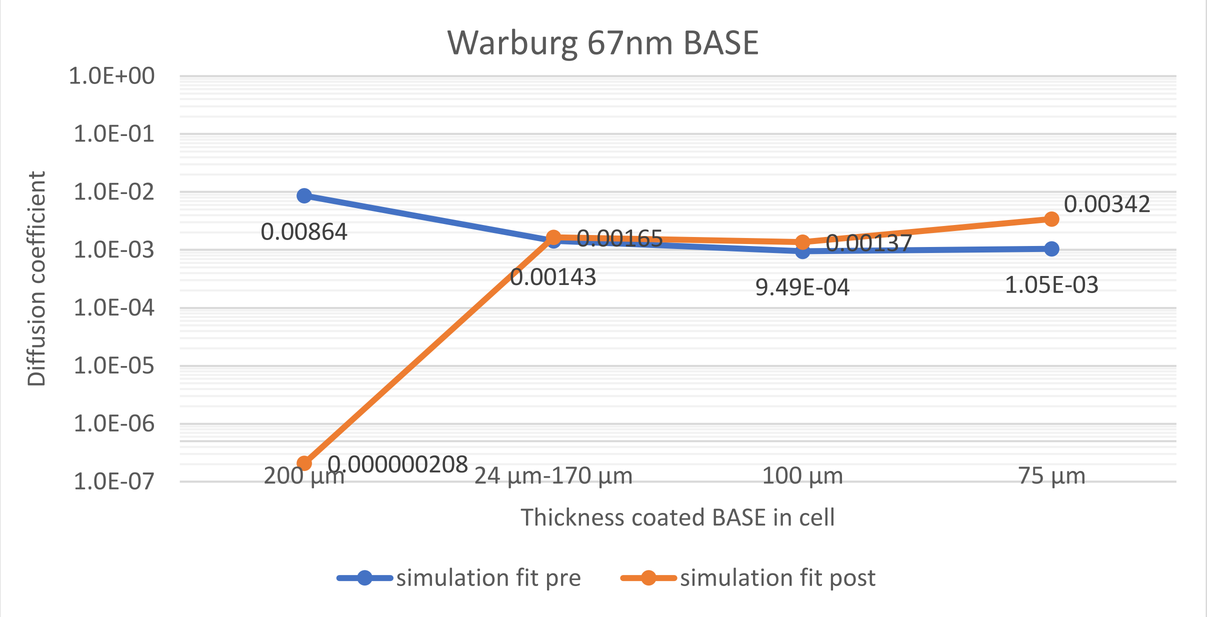

Figure. Diffusion coefficient for Na$^+$ ion through the battery

The diffusion figure coincides with the previous R3-C3 Figure. The 200 µm cell shows a decrease in the diffusion coefficient, which is in line with the previous resitance post-cycling.

ECPC series

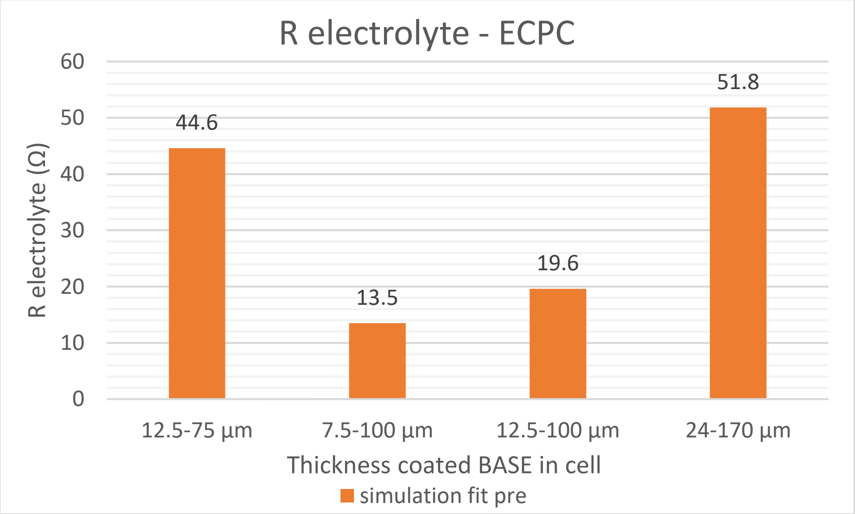

Figure. Electrolyte resistance for the ECPC organic electrolyte series, without added salt.

For the electrolyte resistance, one would expect a proportional increase in resistance as a function of the thickness of the electrolyte. It is true that the thickest pasted electrolyte has the highest resistance (far right), but even though 12.5-75 µm has the highest liquid contribution and the lowest thickness (far left), it does not coincide with the rest of the series. This may be due to a higher contact resistance in the cell, or a faulty current collector.

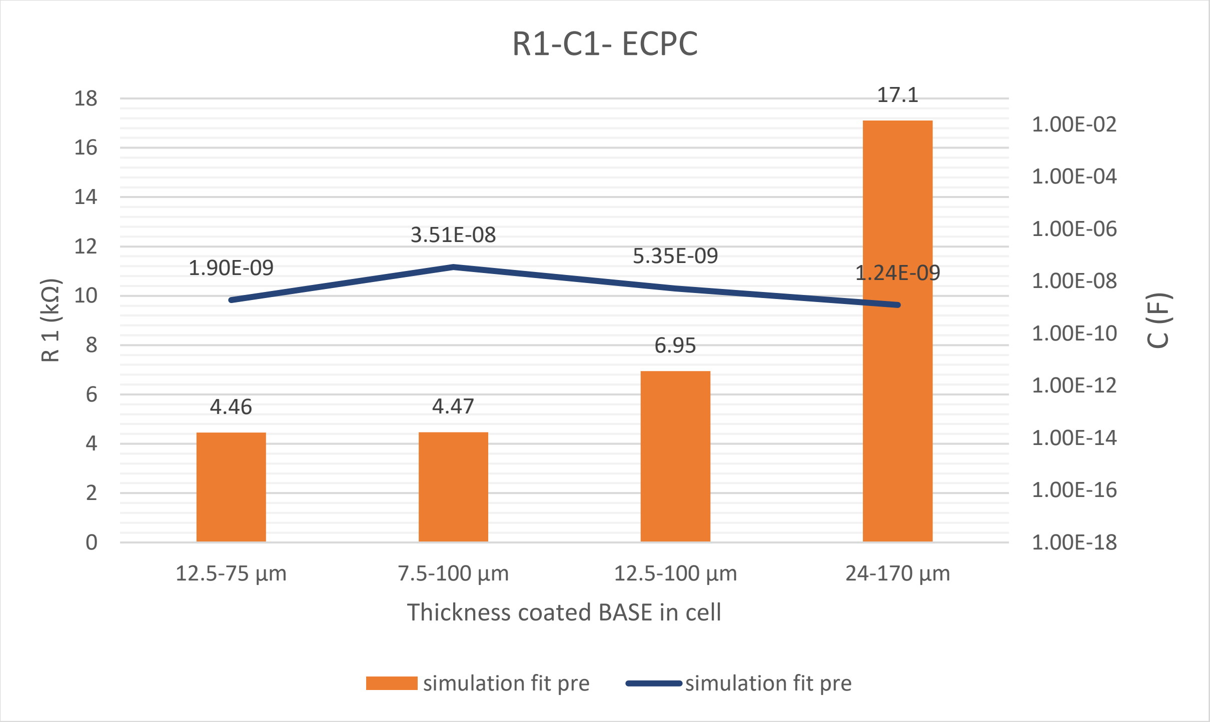

Figure. Resistances and capacitances pertaining to the high frequency interactions of the ECPC series, derived using the equivalent circuit modelling of the first semi-circle of the Nyquist plot (first parallel RC element). These values found at high frequency are typically attributed to the SEI interactions.

The resistance increases with overall thickness of the cell, indicating a correlation with solid electrolyte point contacts. Similarly, the capacitance decreases with increasing thickness. This indicates that a thinner battery is favourable for high frequency interactions.

It can be pointed out that for a thinner cathode material (7.5-100 µm) with equal electrolyte thickness as 12.5-100 µm, resistance also decreases. This should not be the case when assessing SEI resistance, as the interface between electrodes and electrolyte should be independent of electrolyte thickness. The same phenomenon occurs for the thicker cell 24-170 µm. It could be hypothesized that the porosity at the border of the interface also reacted to form SEI. A thicker electrode contains more pores, therefore more possibility to form a side-product.

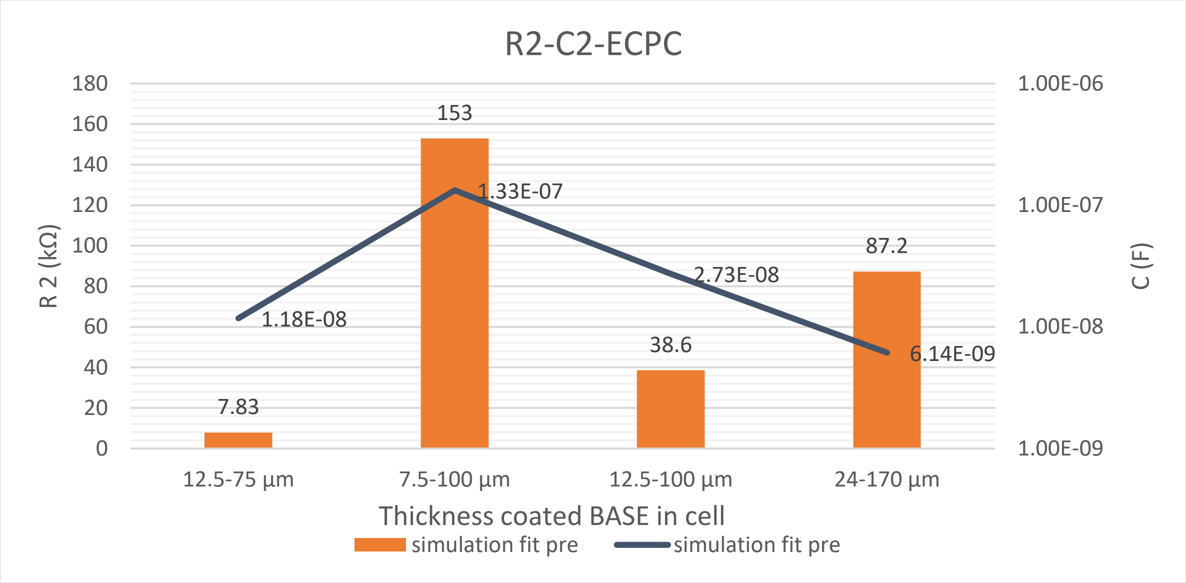

Figure. Equivalent circuit modelling of the second semi-circle of the Nyquist plot, describing the interactions at medium frequency. The resistance R2 is usually attributed to the charge transfer resistance, while the capacitance relates to the Double Layer around the particles.

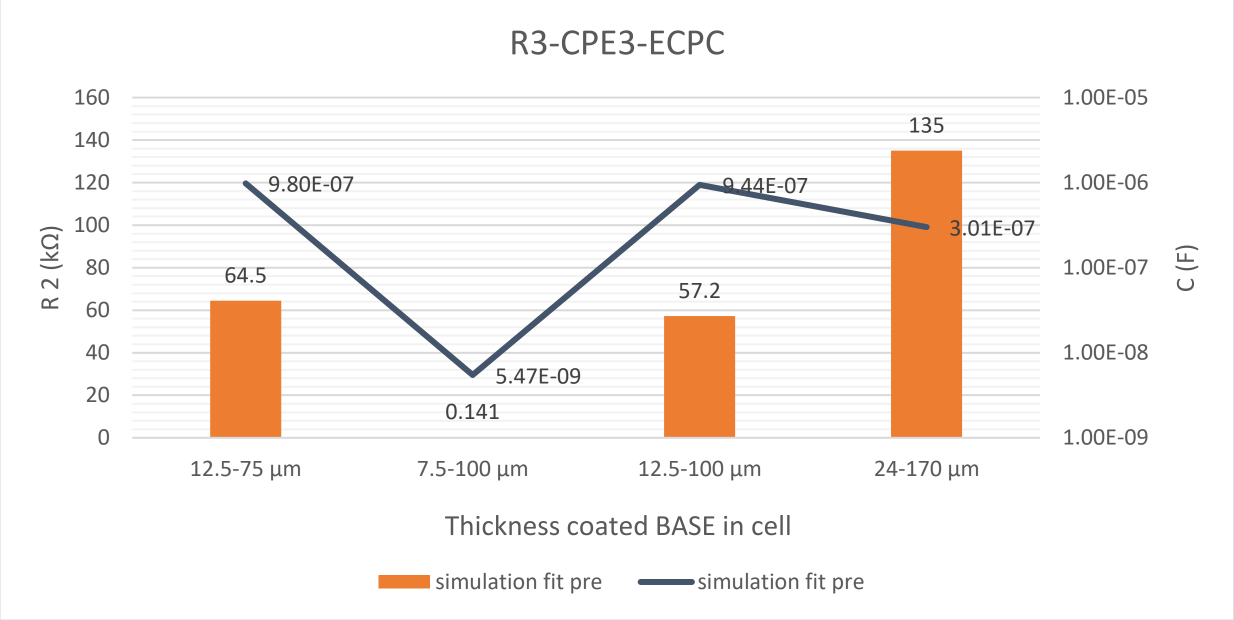

Figure. Equivalent circuit modelling of the third semi-circle of the Nyquist plot, describing the electrochemical interactions at low frequency.

The cells with thickness 75 µm and 100 µm with same cathode thickness show similar electrical properties, while taking a thinner cathode drastically change the electrical properties.

The resistance for the thickest cathode is the highest, as expected, but with a lower capacitance than the other batteries, which is peculiar. **Why? The phase is shifted compared to the other cells in the series. This relates to the amount of reactive power in the system. A low capacitance effectively means that not much reactive power is stored in the system.**

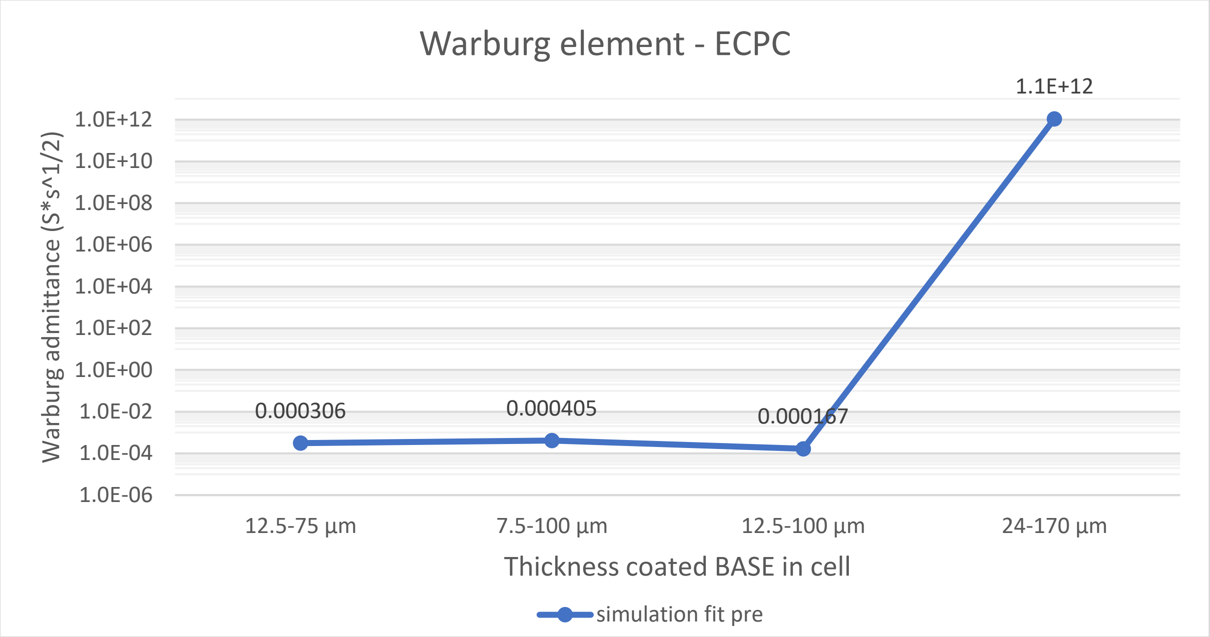

Figure. Diffusion coefficient for the ECPC series.

Here, the diffusion coefficient is dependent on the length of the path that ions need to cross from one electrode to the other. This would theoretically mean that a longer path results in a lower diffusion coefficient. This reasoning holds, except for the thickest battery.

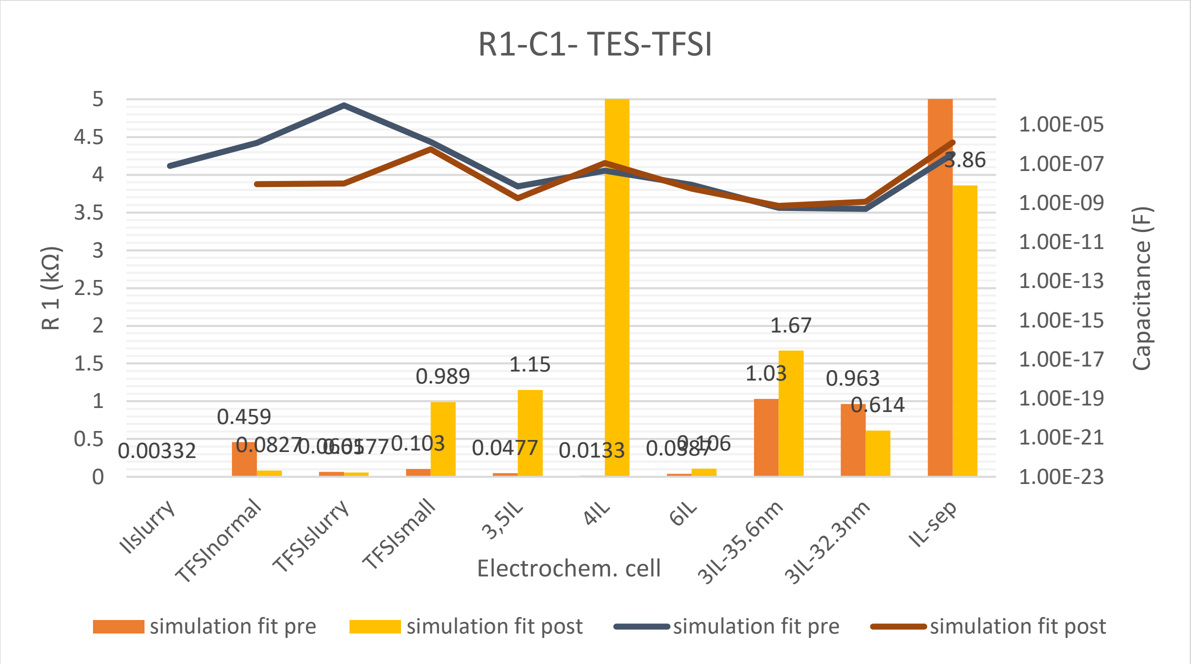

Figure. Resistances and Capacitances relating to the equivalent circuit modelling of the first semi-circle of the Nyquist plot (first parallel RC element). It quantifies the electrochemical interactions at high frequency, typically attributed to the SEI interactions

Similarly to previous series, the R1-C1 plot is challenging to interpret. The resistance values remain constant for some cells, while skyrocket for others. The capacitance remains constant pre/post-cycling throughout the series. It can be pointed out that the cells with particle variation (far right) present a similar pattern compared to their $R_{electrolyte}$ values, and a slight increase in capacitance for the smaller particle cell. The R1-C1 Figure could be an indication for electrode-electrolyte interphase, but further evidence needs to be uncovered to claim this with certainty.

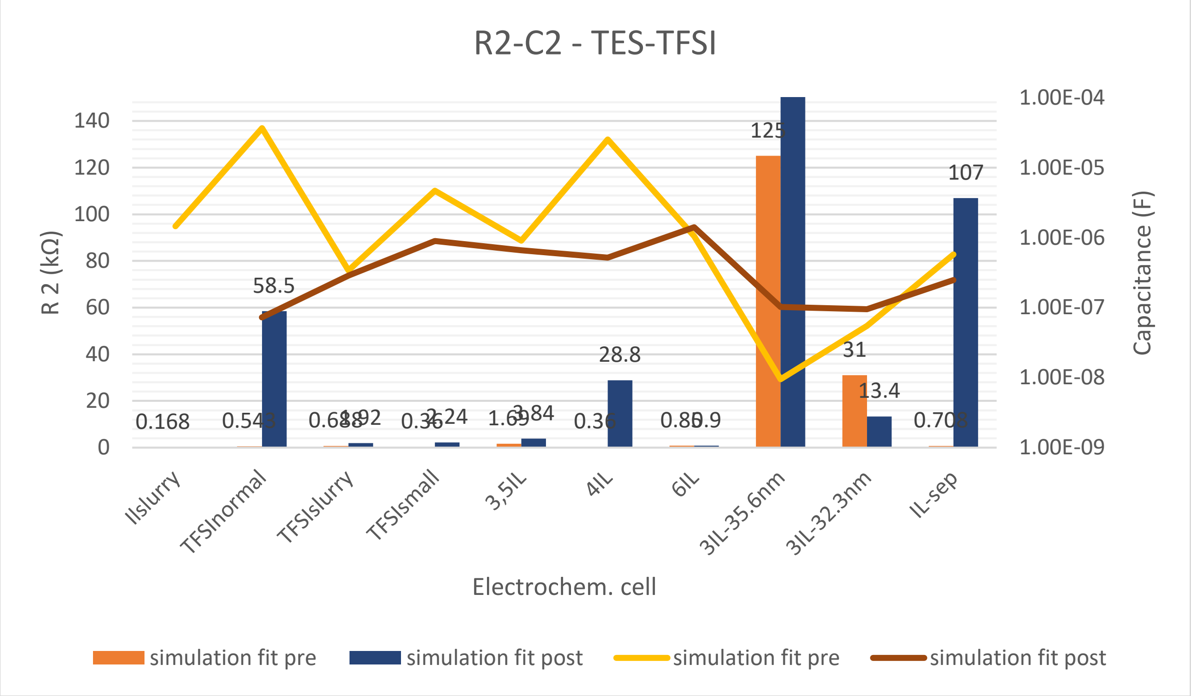

Figure. Equivalent circuit modelling of the second semi-circle of the Nyquist plot, describing the interactions at medium frequency. The resistance R2 is usually attributed to the charge transfer resistance, while the capacitance C2 relates to the Double Layer around the particles.

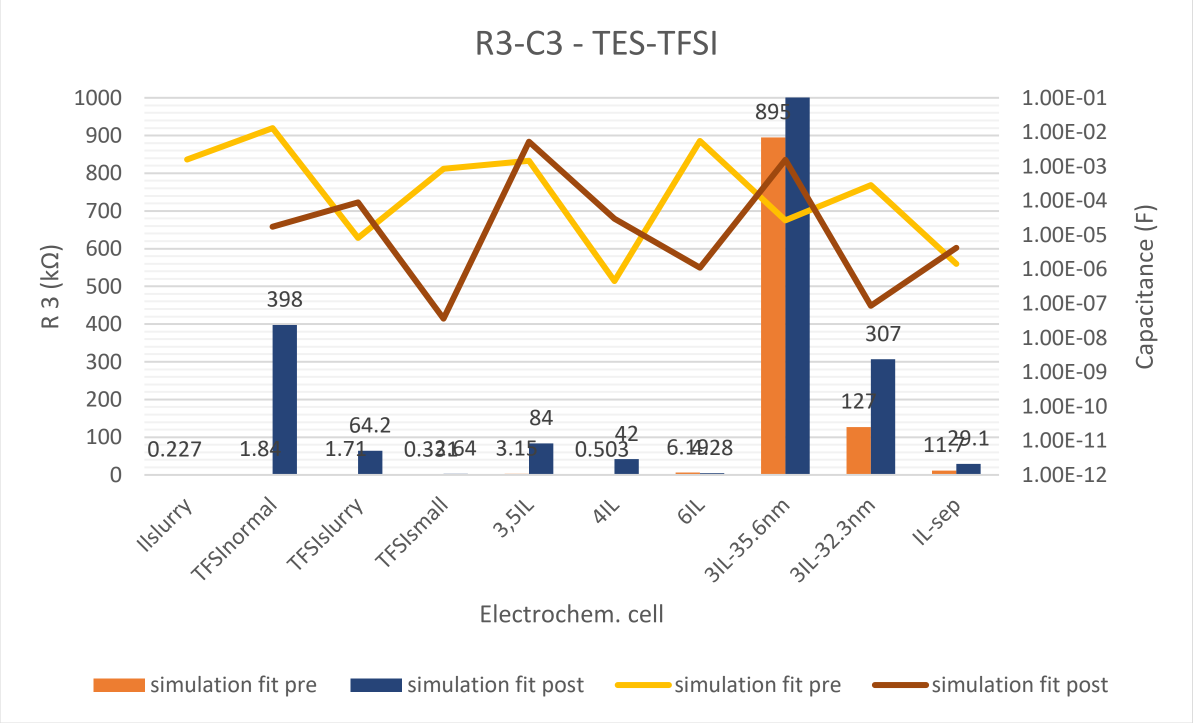

Figure. Equivalent circuit modelling of the third semi-circle of the Nyquist plot, describing the electrochemical interactions at low frequency, typically attributed to the many factors relating to mass transport, also an indication of Na⁺ ionic diffusion.

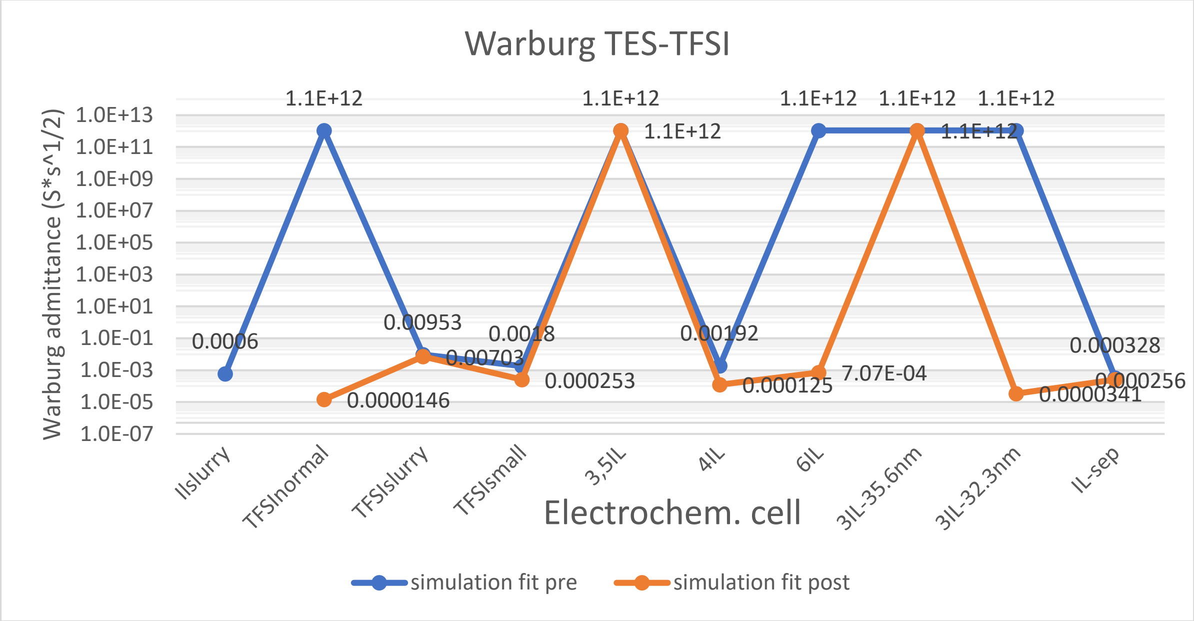

Figure. Diffusion values, quantified by a Warburg impedance element.

A general trend shows that the diffusion decreases post-cycling, which was to be expected.

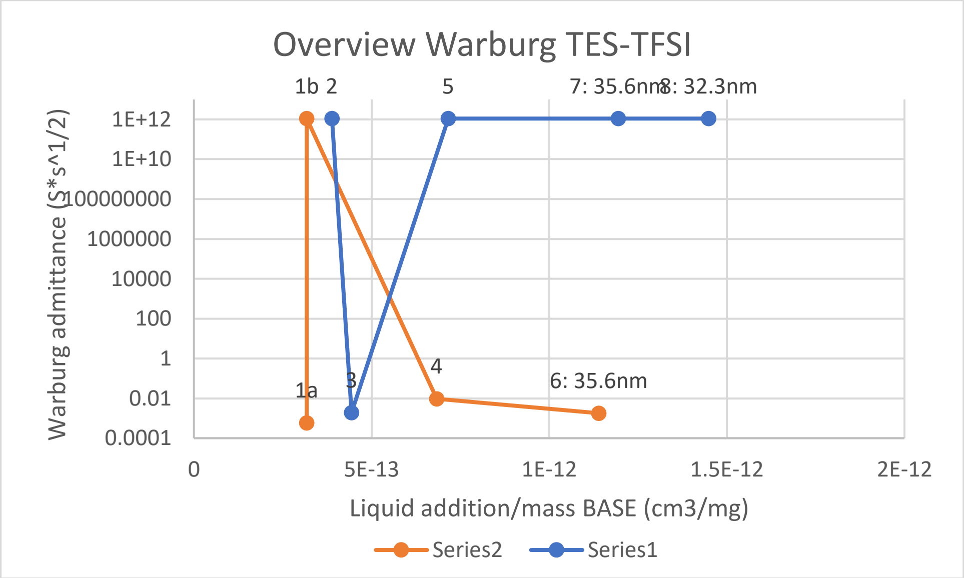

Figure. Overview Warburg TES-TFSI without thickness correlation

Pyr14FSI series

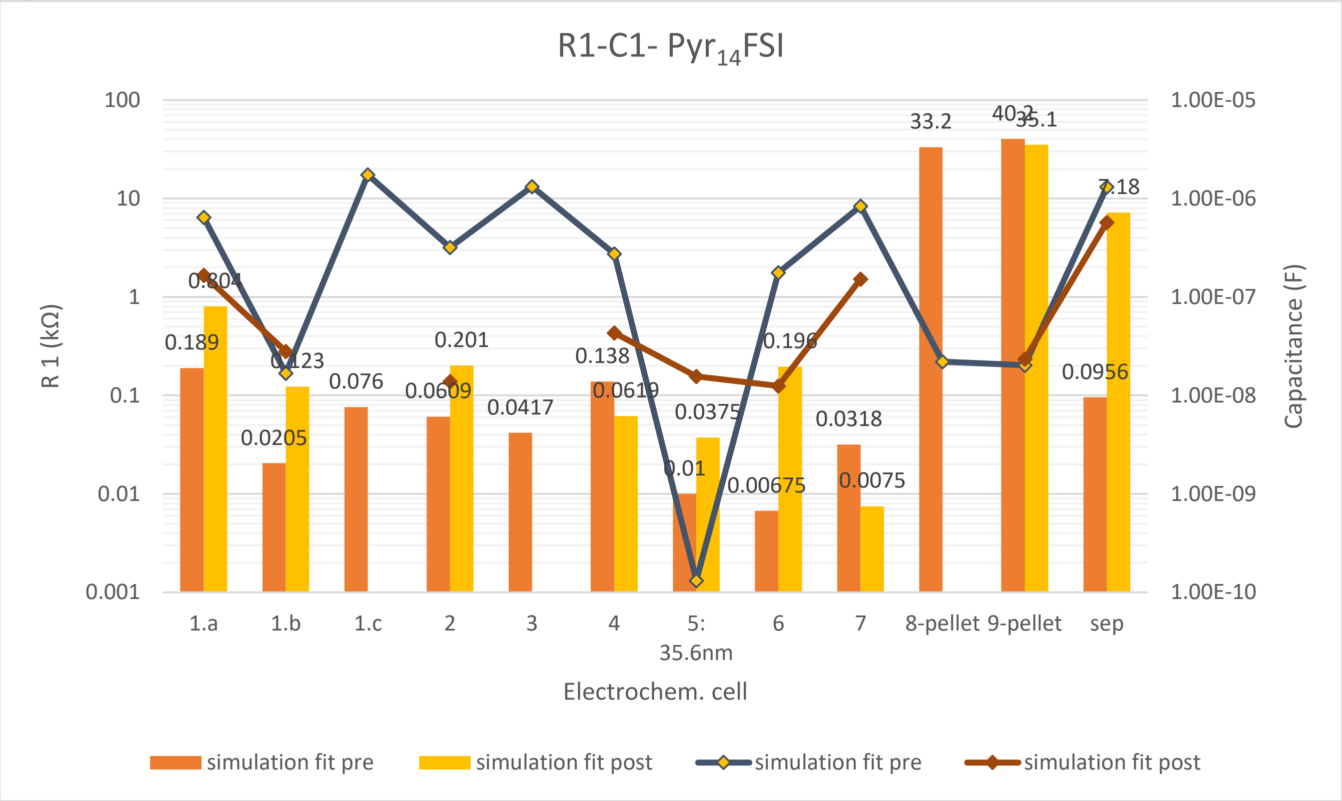

Figure. Resistances R1 and Capacitances C1 relating to the equivalent circuit modelling of the first semi-circle of the Nyquist plot (first parallel RC element) for the Pyr$_{14}$FSI series. It quantifies the electrochemical interactions at high frequency, typically attributed to the SEI interactions

The resistances for the high frequency parameters improve with addition of ionic liquid Pyr$_{14}$FSI, as is shown in **Figure.** The further right, the lower the resistance. Yet this improvement is marginal compared to various other liquid additions. The resistances R1 also remained rather constant post-cycling, indicating little evolution over the course of the charging-discharging process. The same can be said for the capacitance C1.

It can be noted that the cell with smaller BASE particle shows much worse capacitance pre-cycling, yet presents a similar value as the rest of the series post-cycling.

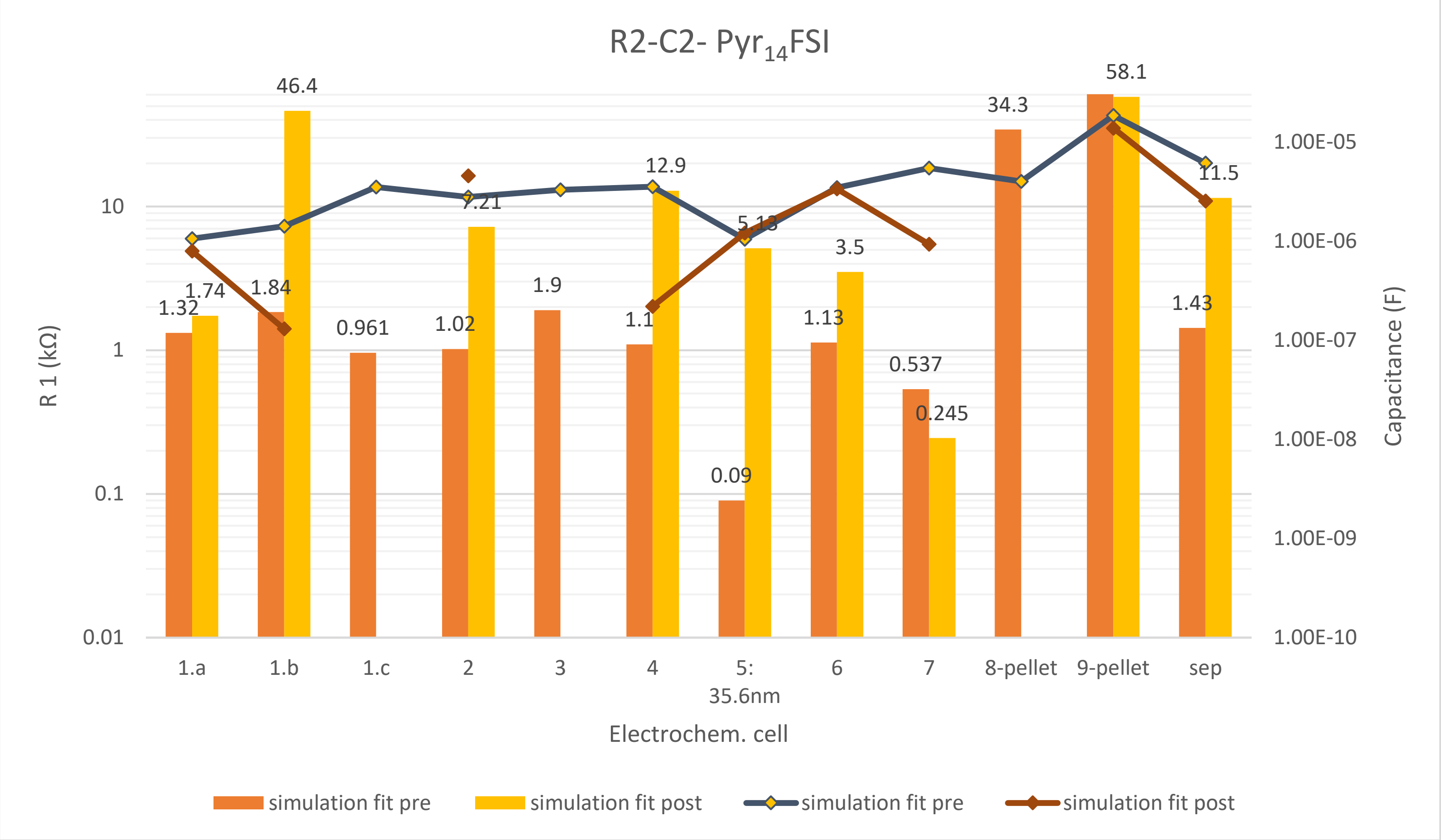

Figure. Resistances R2 and Capacitances C2 relating to the equivalent circuit modelling of the second semi-circle of the Nyquist plot, describing the interactions at medium frequency for the $Pyr_{14}FSI$ series. The resistance R2 is usually attributed to the charge transfer resistance, while the capacitance C2 relates to the Double Layer around the particles.

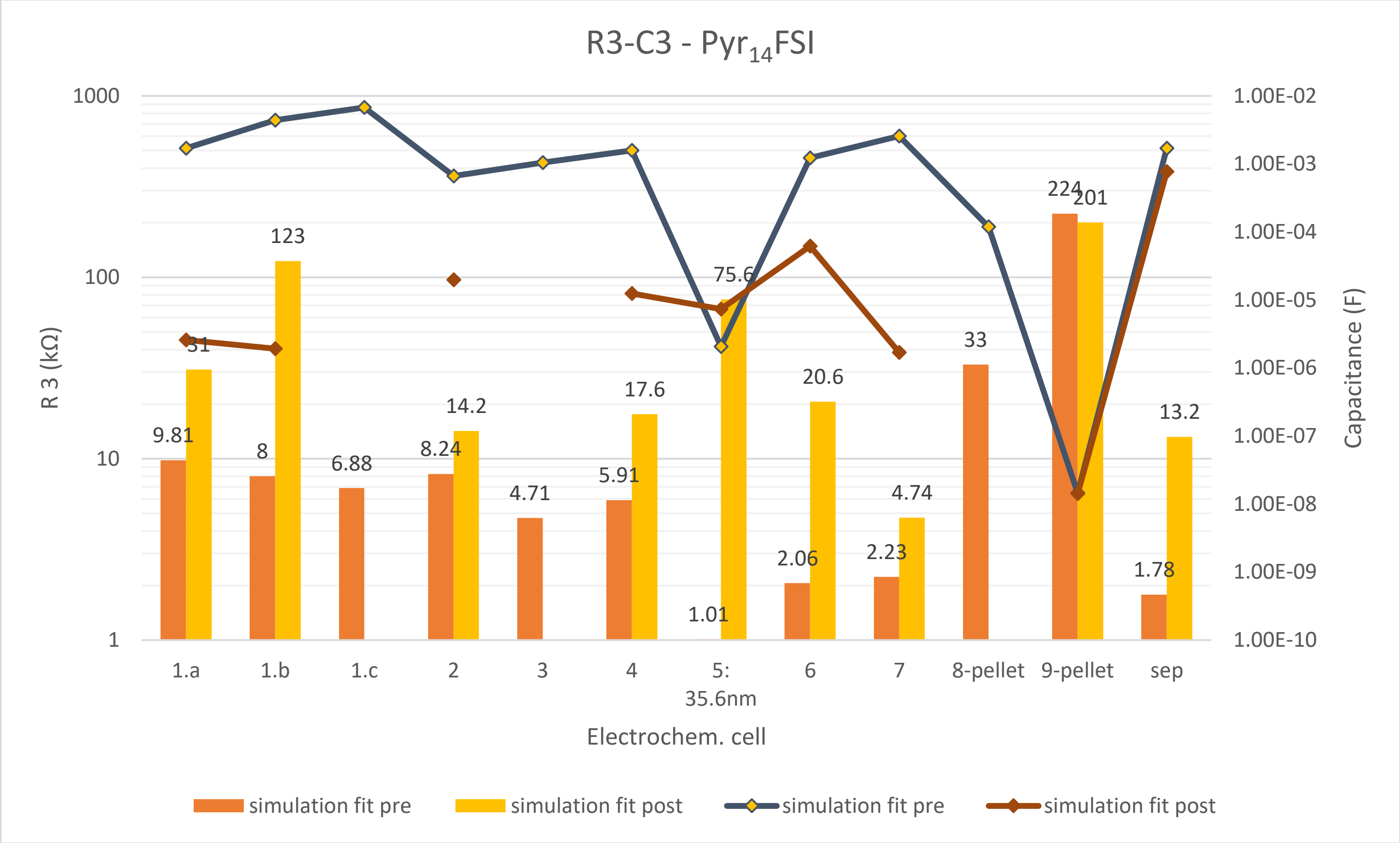

Figure. Equivalent circuit modelling of the third semi-circle of the Nyquist plot, describing the electrochemical interactions at low frequency, typically attributed to the many factors relating to mass transport, also an indication of Na^+ ionic diffusion.

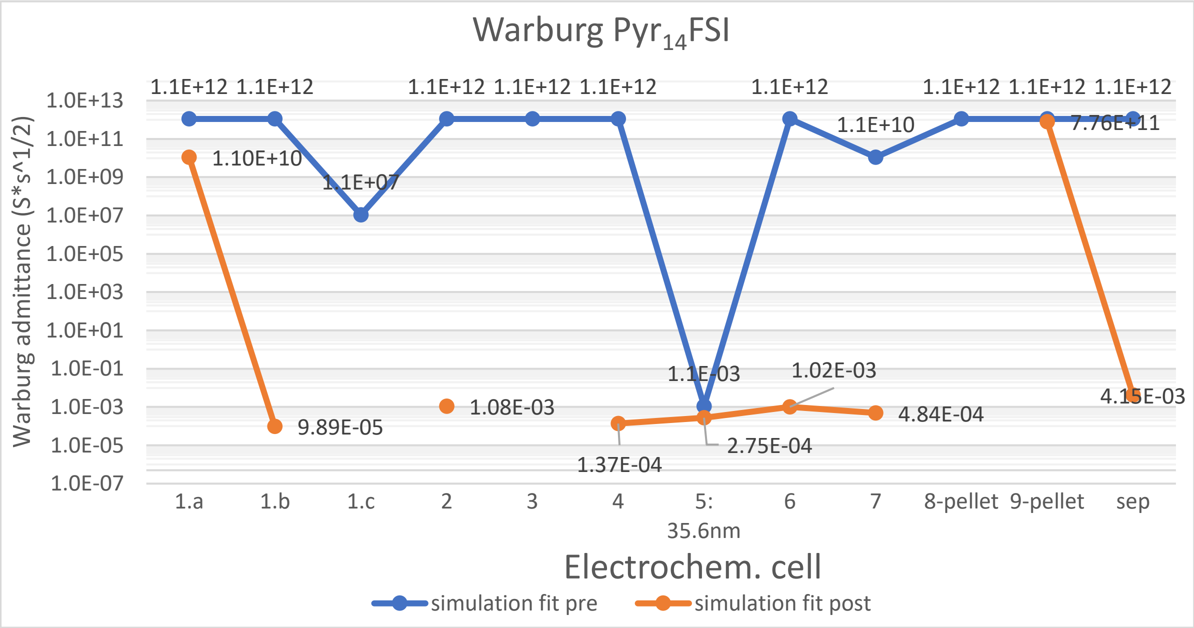

Figure. Diffusion values, quantified by a Warburg impedance.

Ionic transport across the battery is a central subject of our study. The third and final part of the equivalent circuit relates to mass transport.

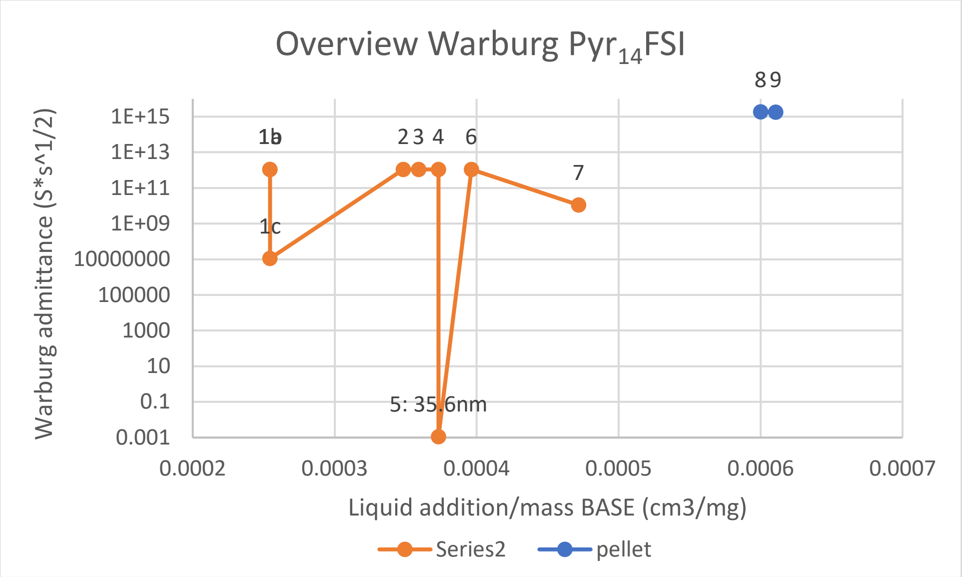

Figure. Overview Warburg Pyr14FSI without thickness correlation

$NaClO_4$ series

Small particle series: 63nm Na-beta"-alumina particle size

30µm - 1 drop of added $NaClO_4$: ECPC liquid

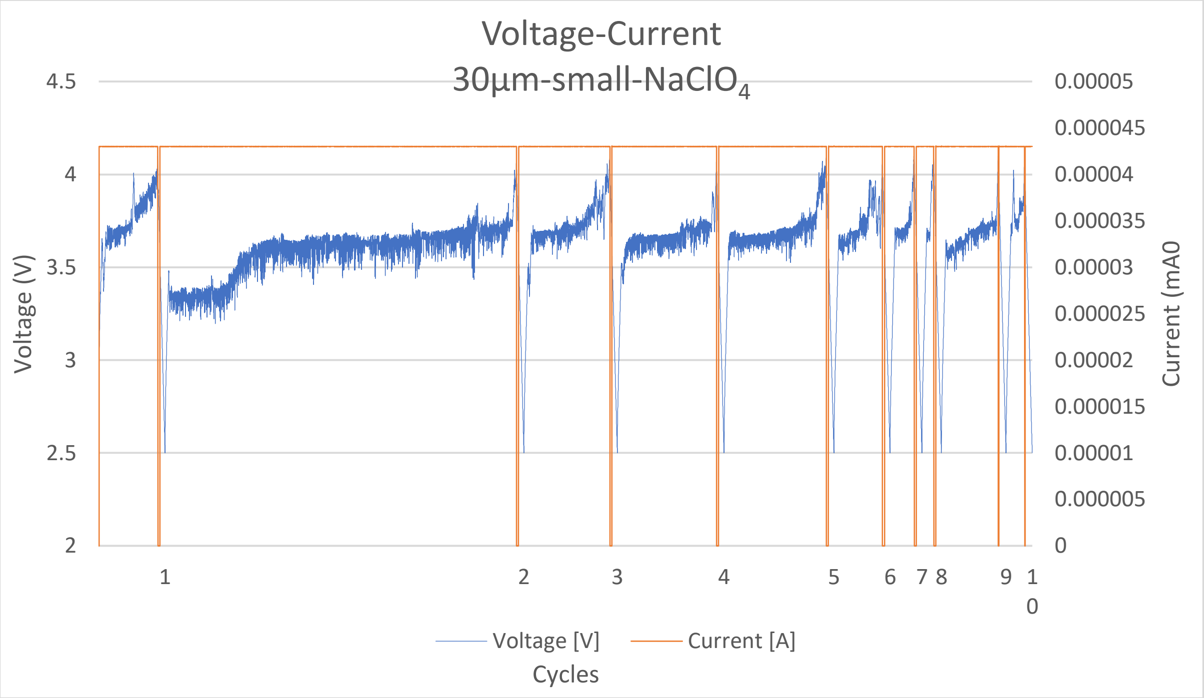

Figure. Charge-Discharge curve for the thinnest tape casted battery for the organic electrolyte serie

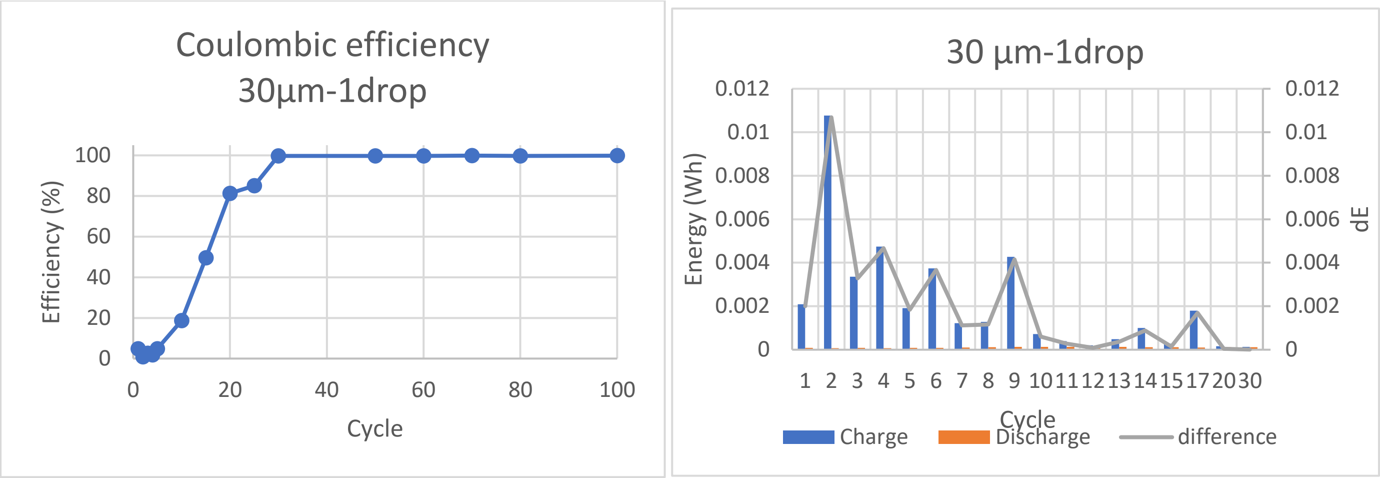

Figure. Coulombic efficiency and energy figure for the 30 µm tape casted cell with $NaClO_4$: ECPC

The 30 µm tape casted electrolyte is illustrative of the contact issue faced when a tape casted film is too thin. The measured potential reflects a lack of contact, yet can be remedied simply by increasing the tape casted thickness. The previously reported cell with electrolyte thickness of 55 µm was sufficient to eliminate this contact issue.

87µm - 2 drops of added $NaClO_4$: ECPC liquid

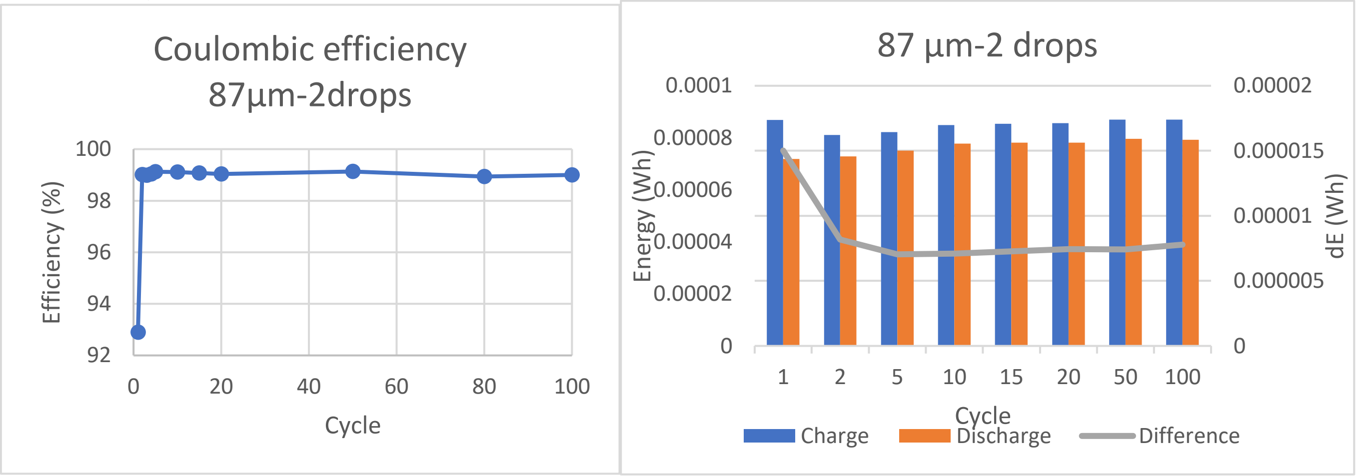

Figure. Coulombic efficiency and energy figure for the 30 µm tape casted cell with $NaClO_4$: ECPC

140μm-1 drops of added $NaClO_4$: ECPC liquid

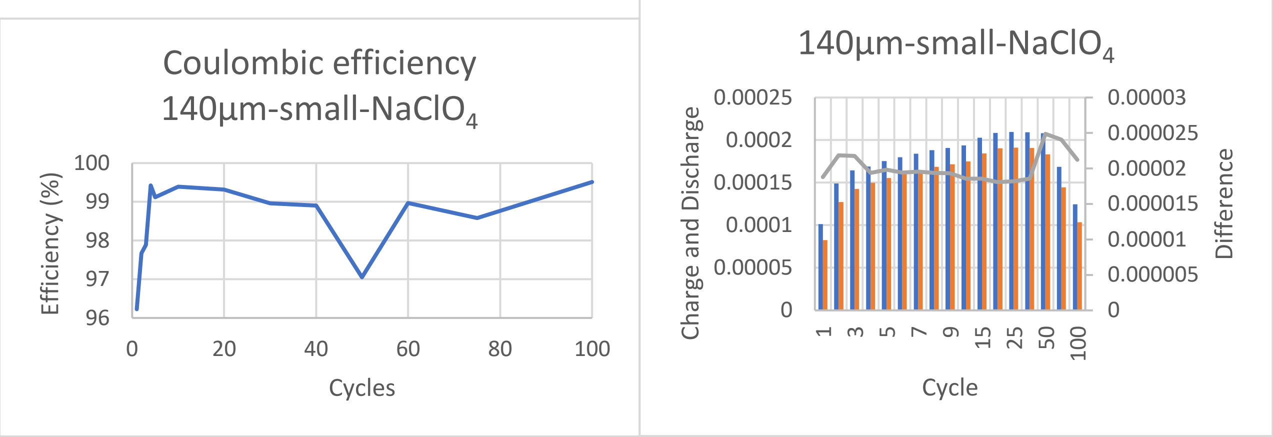

Figure. Coulombic efficiency and energy figure for the 140 μm tape casted cell with $NaClO_4$: ECPC

Thick cathode-170μm-1 drop of added $NaClO_4$: ECPC liquid solution

The reason why we decided to include this cell in the report, is to show the decreasing capacity when making an electrochemical cell too thick. With a cathode thin film twice as thick as the other cells reported, and an electrolyte of 170μm thick, the capacity progressively decreases due to increasing fatigue relating to volume expansion. This is related to the structural integrity of the materials degrading overtime. It was also reported that the inder PVDF shows increased fatigue overtime, and should be replaced by CMC, a less poluent and more performant binder.

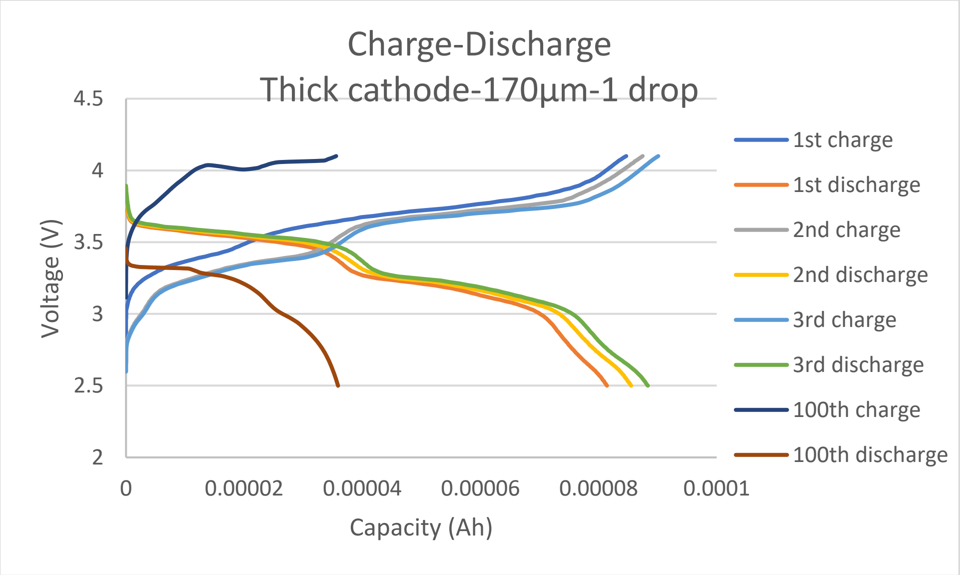

Figure. Charge discharge curve for the cycles of thick cathode-170μm tape casted BASE with 1 drop of added $NaClO_4$: ECPC liquid

Voltage curve at the beginning and end of cycling. The phase change is not the same, and the first phase transition is practically gone, indicating a potential decomposition or deterioration during the first phase transformation of the cathode material.

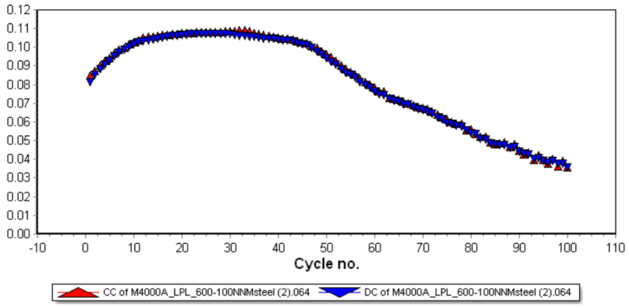

Figure. Decreasing capacity of thick cathode-170µm tape casted BASE with 1 drop of added $NaClO_4$: ECPC liquid after 50 cycles.

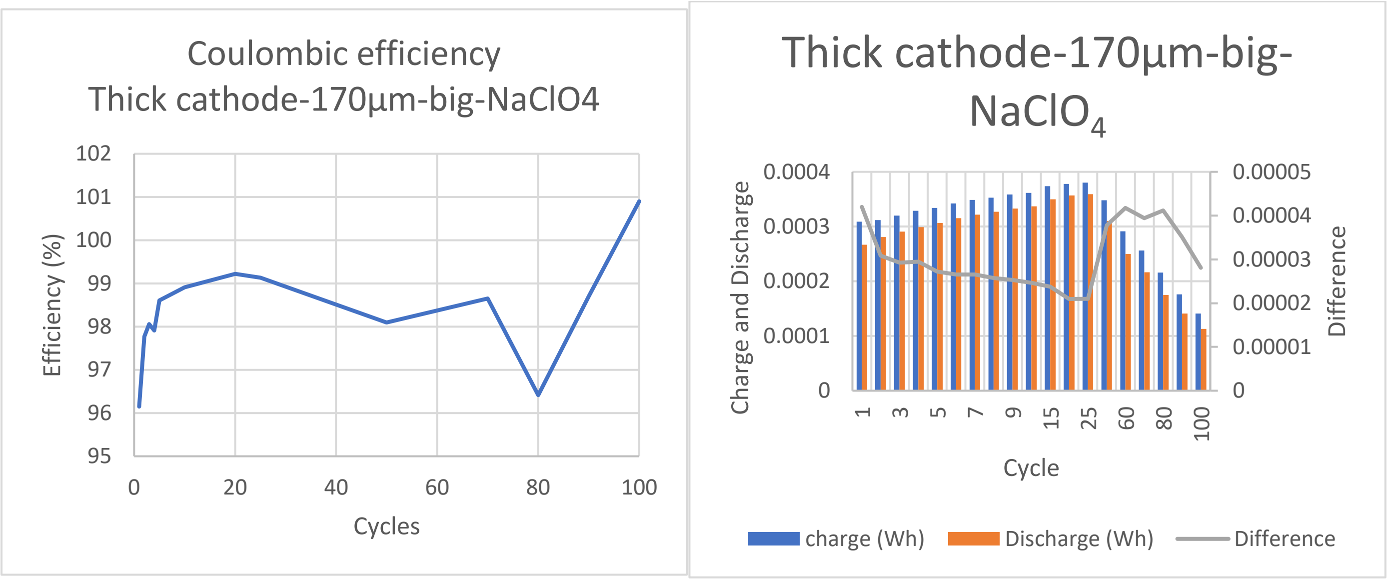

Figure. Coulombic efficiency and energy figure for the 170 µm tape casted cell with $NaClO_4$: ECPC

<u>**400 = 100µm-big-$NaClO_4$**</u>

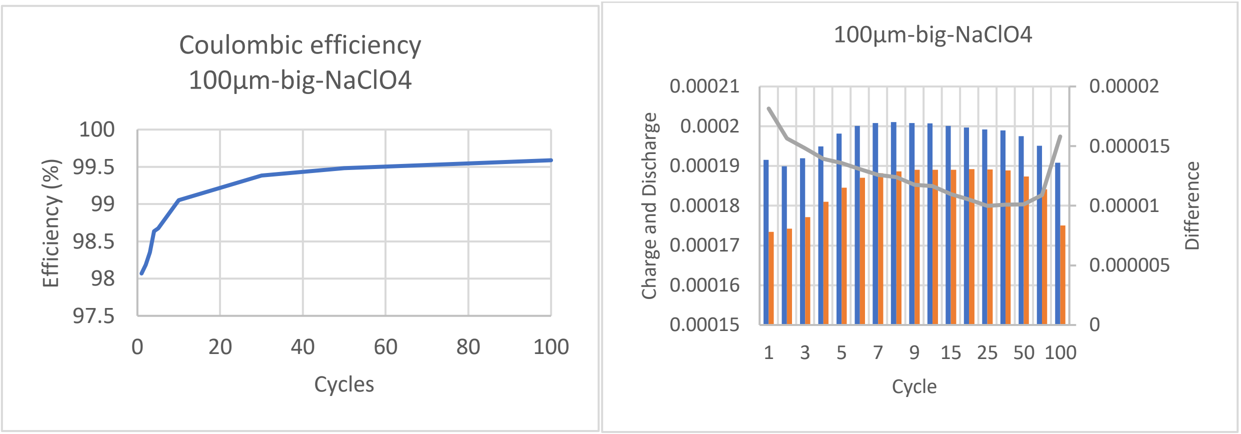

Figure. Coulombic efficiency and energy figure for the 30 µm tape casted cell with $NaClO_4$: ECPC

3ILbig.015

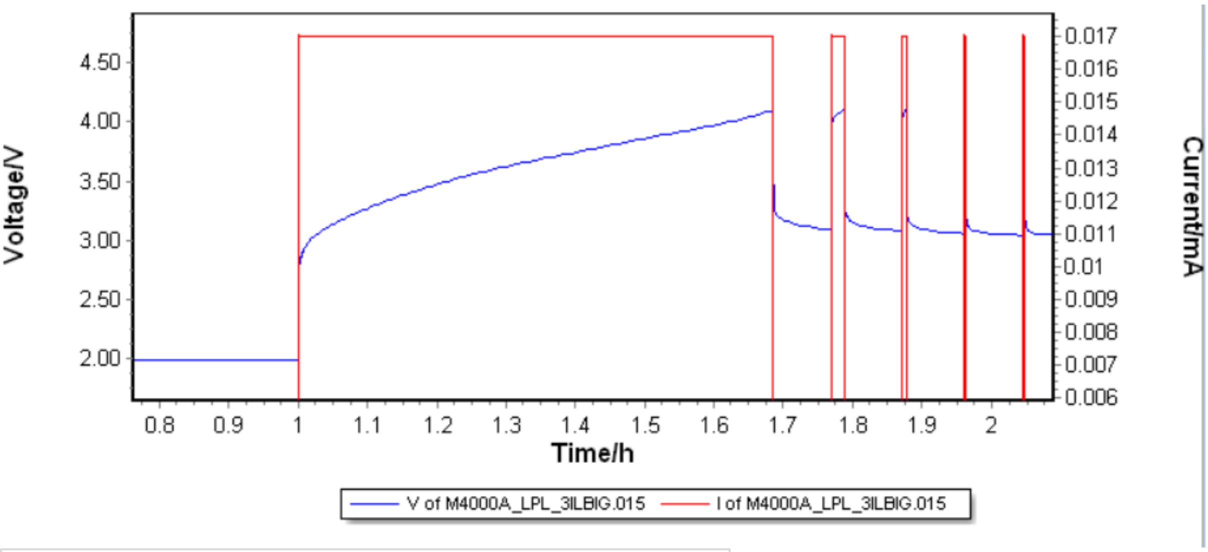

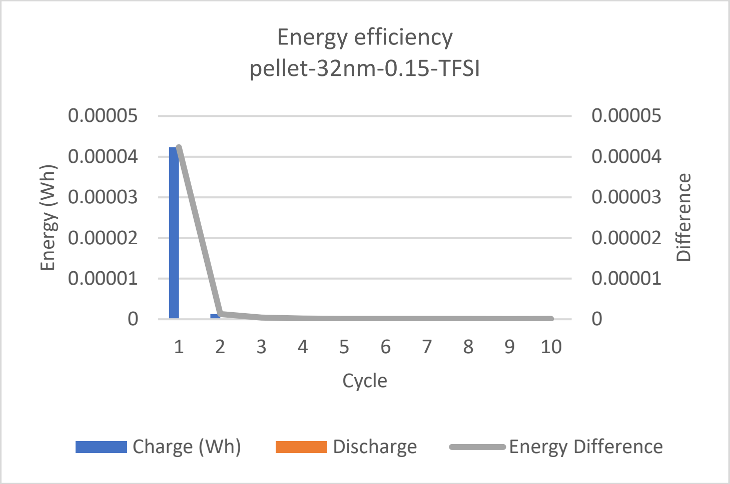

Figure. Voltage Curve (above) and Energy figure (below) for the BASE pellet with big BASE particles and 3drops of TES-TFSI

Discharge goes back to 1.9V after the second cycle, which is under the cathode window of 2.3-4.2V. This indicates that the cathode material has deteriorated during the first charge.

ILslurry – ranked 1a

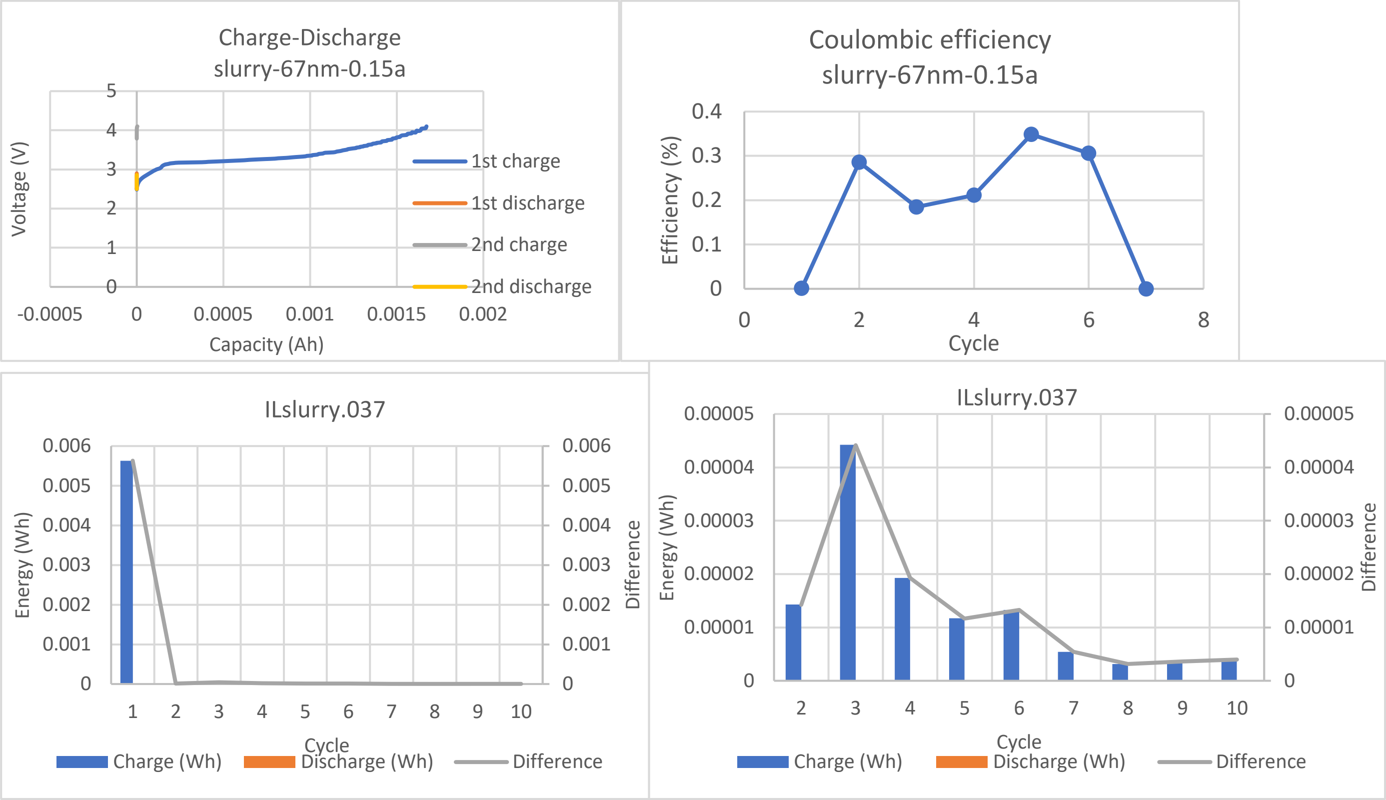

Figure. Charge Discharge curve, Coulombic efficiency and energy curve for ILslurry cell

Jumps from 2.5V to 3.8V when initiating a new charge cycle, indicative of an enormous overpotential?

BASE pellet with particle size of 67nm and 0.175 cm³ of TES-TFSI ionic liquid addition

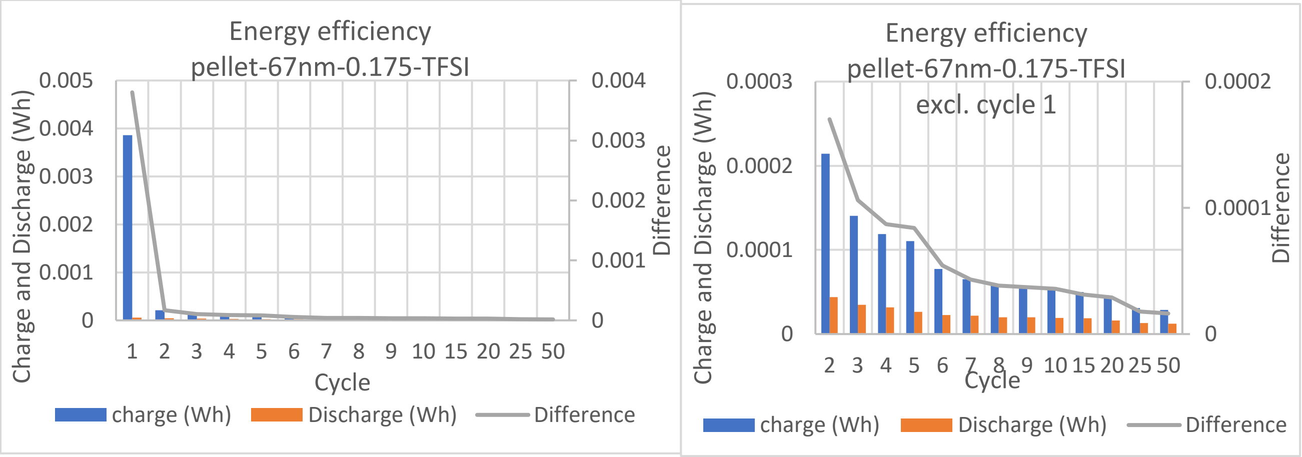

Figure. Energy figure, with the graph on the right excluding the first cycle

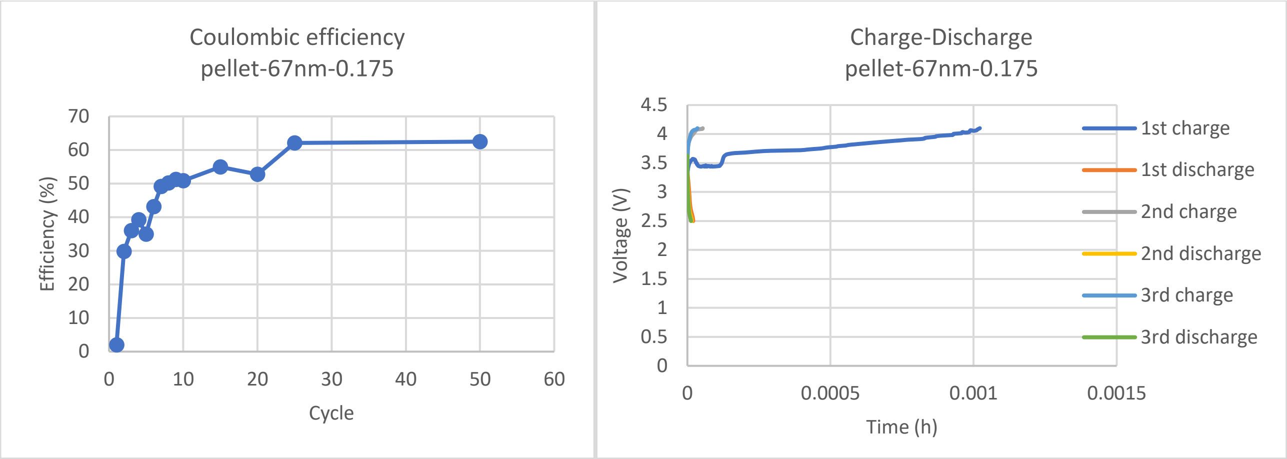

Figure. Coulombic efficiency (left) and Charge-discharge curve (right) for BASE pellet with 0.175cm³ of added TES-TFSI

4 IL

In an attempt to uncover whether the drop in capacity after the first charge is due to active material decomposition, we reduced the voltage window from 2.5-4.2V to 2.5-3.75V, hereby limiting the second phase change which could lead to the decomposition. Unfortunately, this was unfruitful. Yet by excluding this potential factor, we narrowed down the number of potential culprits, which would most likely mean the odd discharge behaviour is related to a side-reaction at the electrode-electrolyte interphase. This could be related to impurities in the ionic liquid, as well as a minimal water content reacting with any of the highly reactive components already present in the batteries.

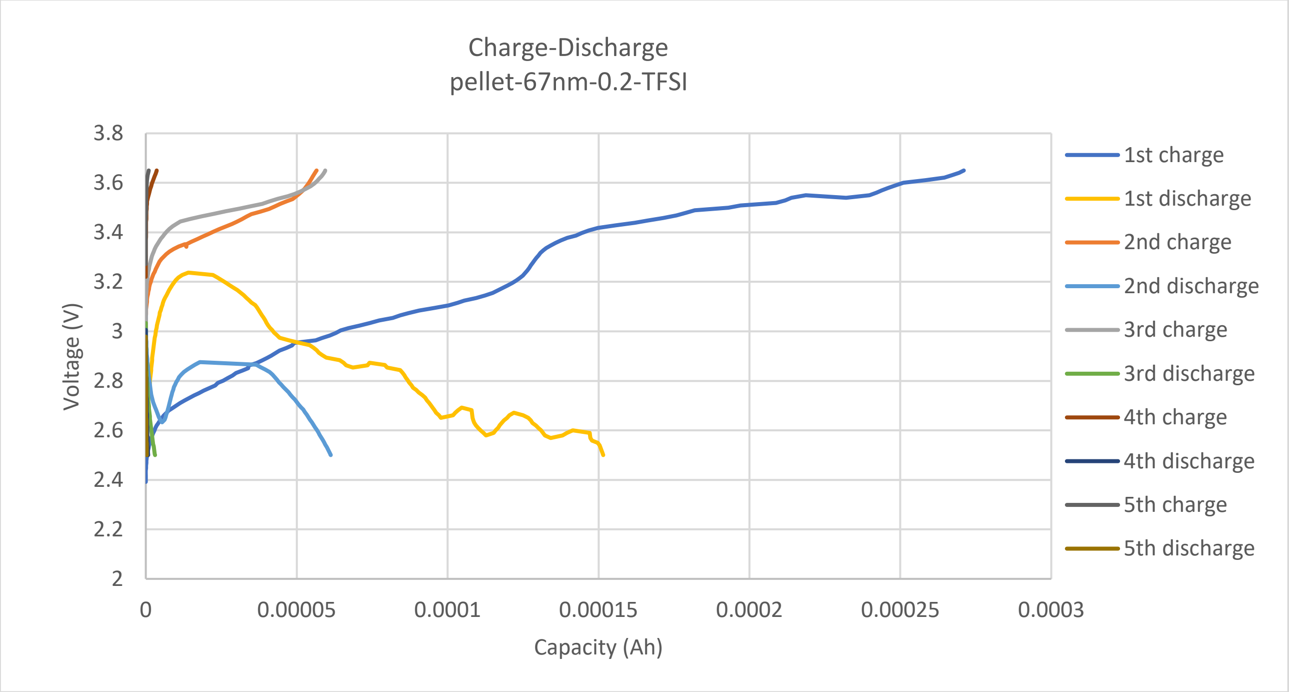

Figure. Charge-Discharge curve BASE pellet with 0.2cm³ of added TES-TFSI

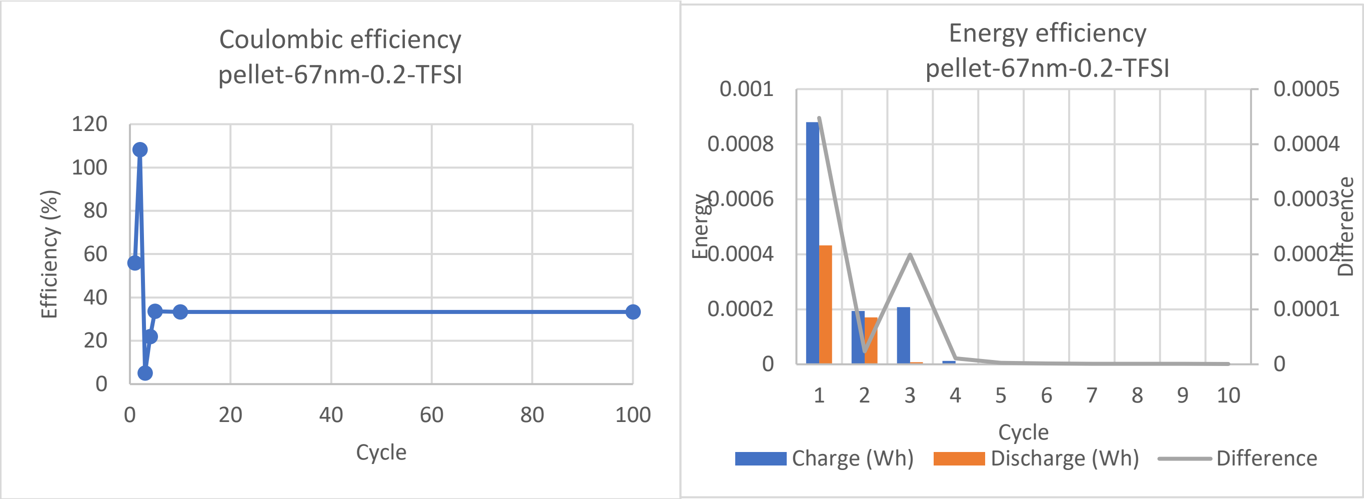

Figure. Coulombic efficiency and energy figure for BASE pellet with $0.2cm^3$ of added TES-TFSI

Larger charge-discharge pattern the slurry Pyr14FSI-BASE-35.6 nm battery, showing odd behaviour. The charging time varies heavily, even though the C-rate remains the same. Furthermore, we can observe that the 4th charging cycle behaves similarly to the first one, while the second and third perform very poorly.

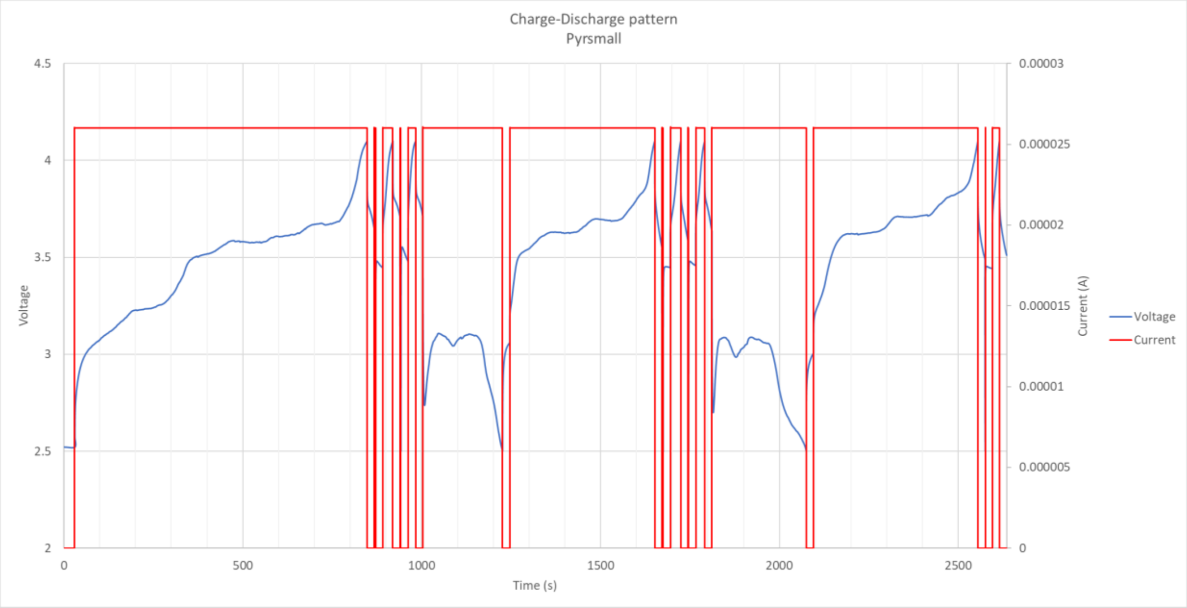

Figure. Charge-Discharge pattern of 7 cycles of the slurry Pyr14FSI-BASE-35.6 nm battery with Voltage on the primary axis and Current on the secondary axis.

Interestingly, the discharge Voltage pattern is the same for the series with TES-TFSI and Pyr14FSI. This leads us to believe the flaw lies within the cathode active material, and not in a contaminant of the ionic liquid.

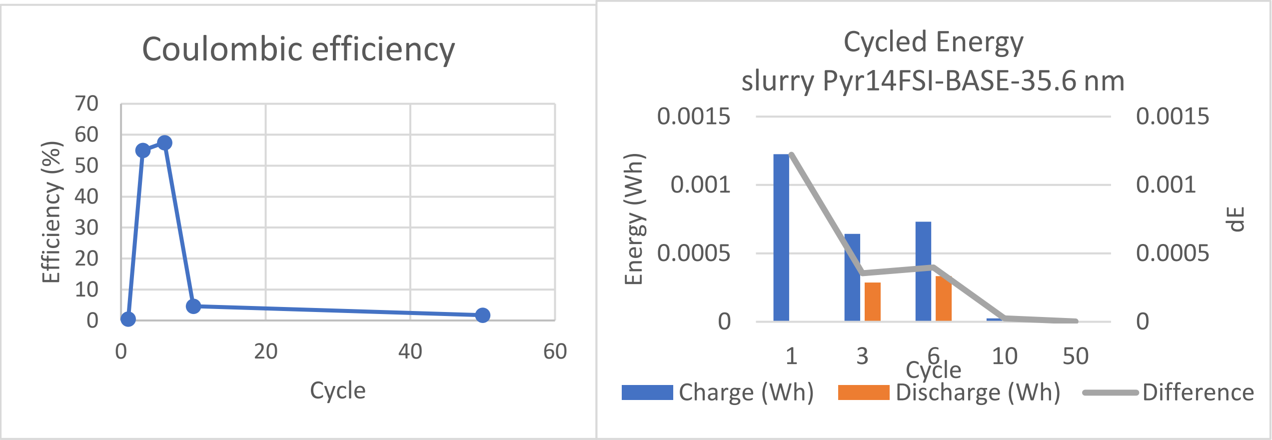

Figure. Coulombic efficiency (left) and Energy figure (right) for the slurry Pyr14FSI-BASE-35.6 nm battery.

EIS-pyr2.5-base7.5-ocp2.67V <u>(pre/post cycling)</u>

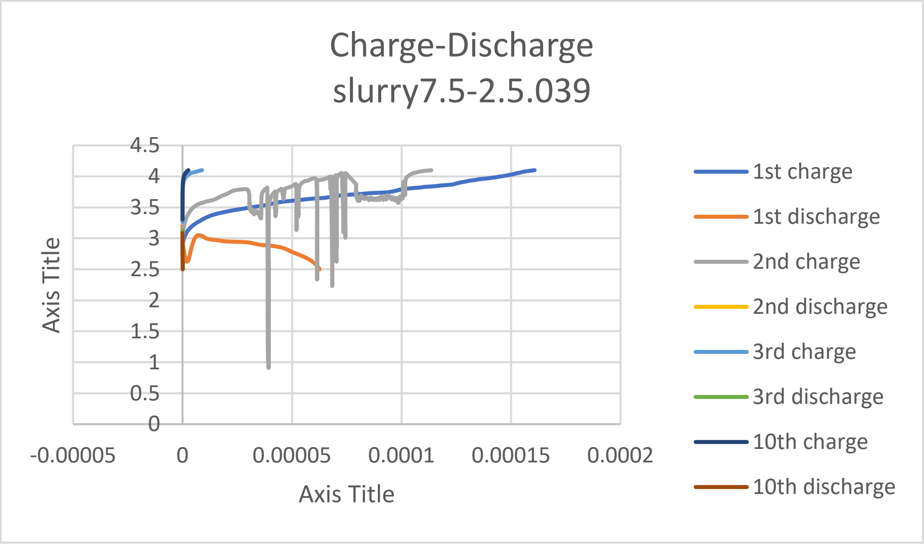

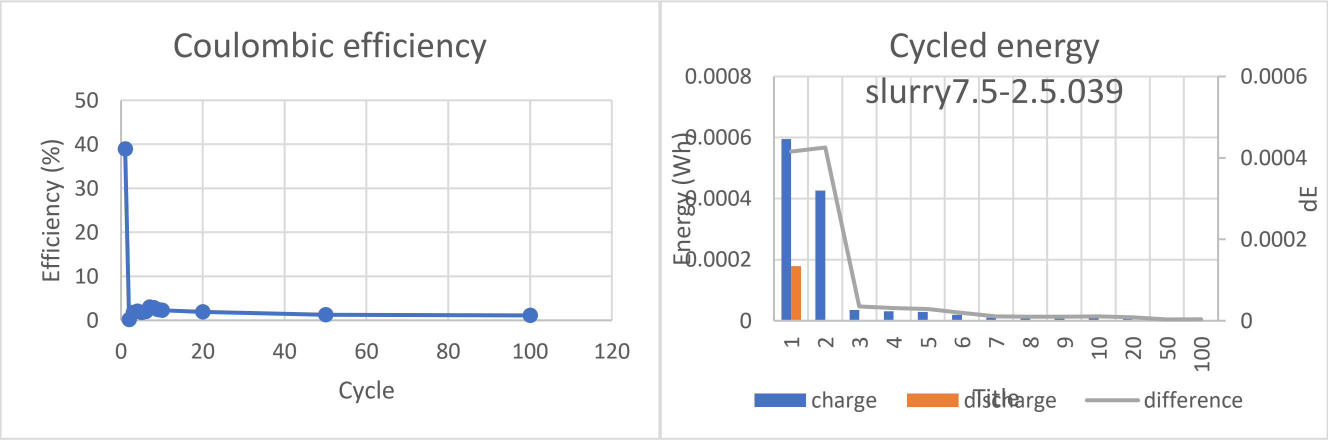

FFigure. Coulombic efficiency (left) and Energy figure (right) for the slurry Pyr14FSI-BASE-67.4 nm battery.

<u>1mmBASE with NNM slurry (toothpaste cathode without pellet sintering)</u>

The toothpaste cathode concept was introduced by [**101**] using a slurry of active material P2-NNM and Pyr14FSI ionic liquid, pasted on a sintered Na-beta”-alumina pellet, reporting high reversible phase-change and cyclability at 70°C. We attempted a similar experiment using a mechanically pressed pellet and the same recipe for the NNM-Pyr14FSI slurry, only at room temperature. This resulted in a similar result as our previous experiments, where the first charging pattern is promising, yet discharge and following charging cycles were almost non-existent. This is indicative of either a side-reaction or cathode material degradation.

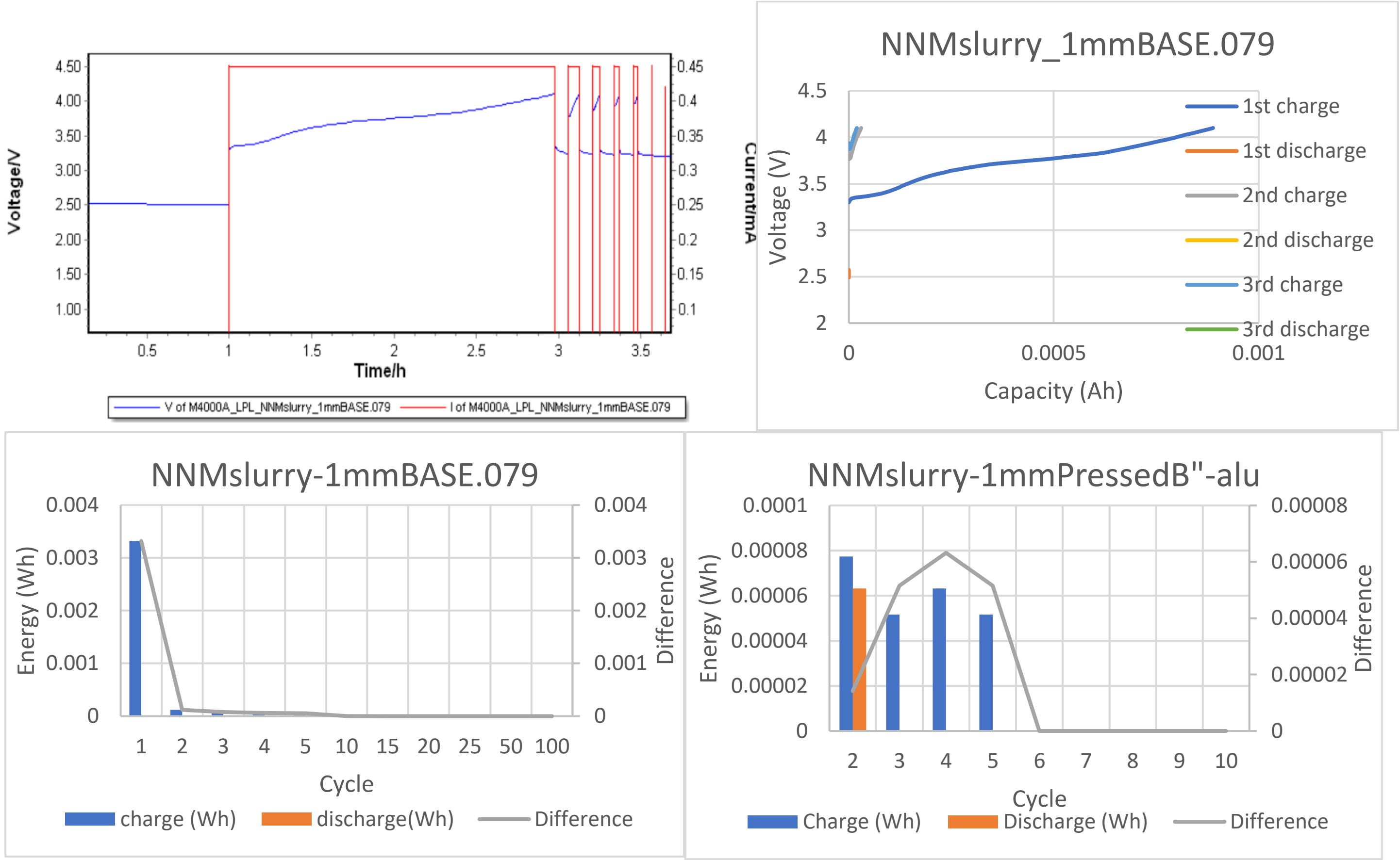

Figure. Battery with 1mm mechanically pressed BASE pellet, with the Voltage curve (top left), Charge-Discharge curve (top right) and energy efficiency curves (bottom)

XRD measurements and their Rietveld refinement

It was found that the Na-beta"-alumina compounds bought from Ionotec contained 5% ZrO_2, a compound that promotes the formation of the beta" phase, as well as increases mechanical integrity.

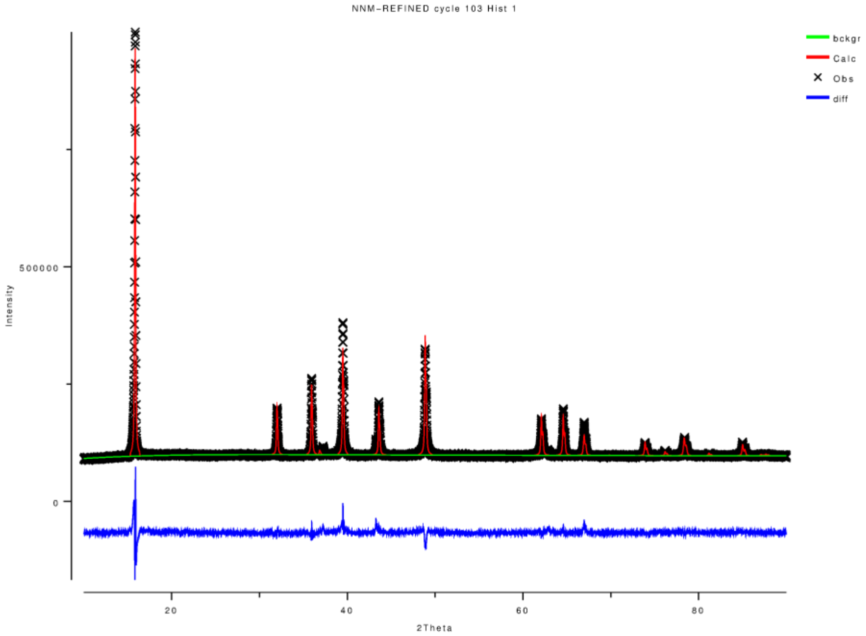

Figure. XRD measurement and Rietveld refinement for P2-NNM, with a reported particle size of 141.18nm.

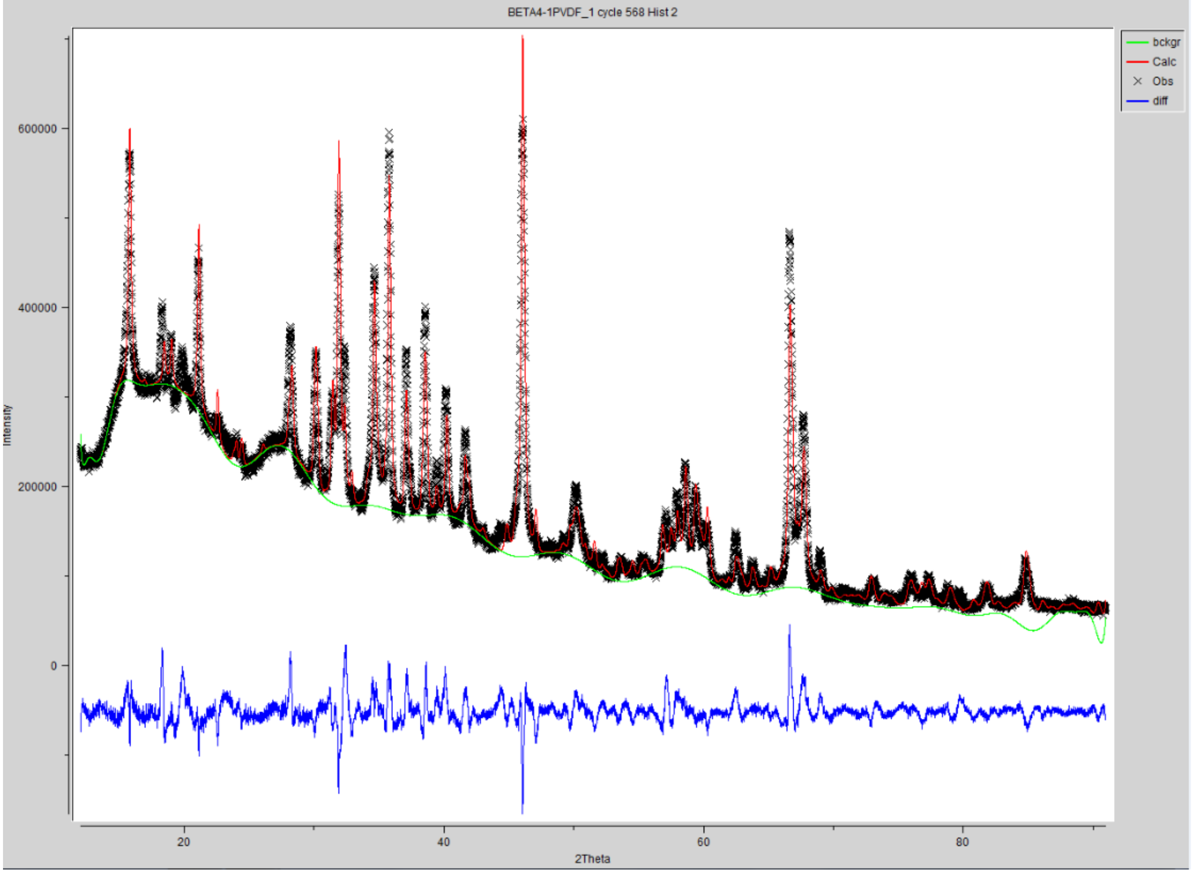

Figure. 4 BASE : 1 PVDF pre cycling, with BASE4-1pvdf-chi-7.2-wRp-6.47%-Rp-4.93%-Lx1=19.25

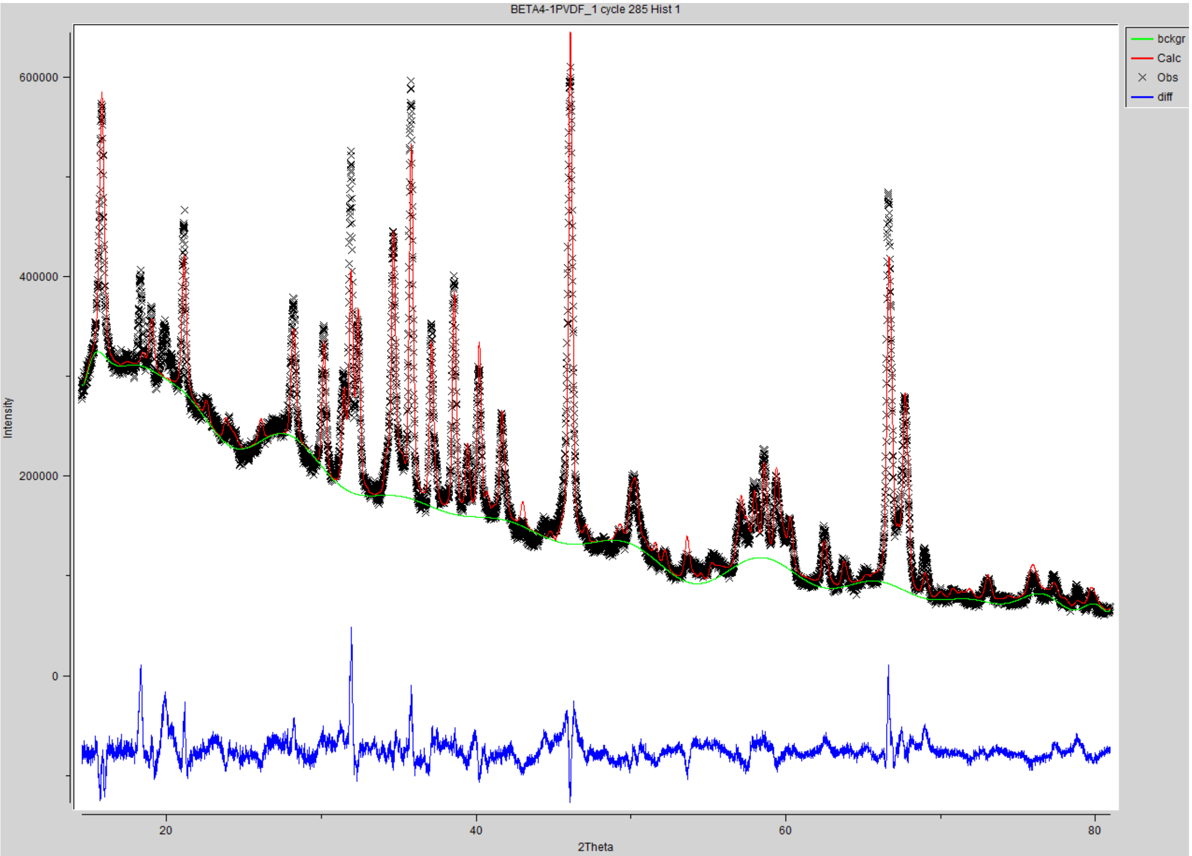

Figure. XRD measurement and Rietveld refinement for BASE4-1PVDF post-cycling, with chi²=6.7 – wRp=6.3% - Rp=4.8% and Lx1=15.3.

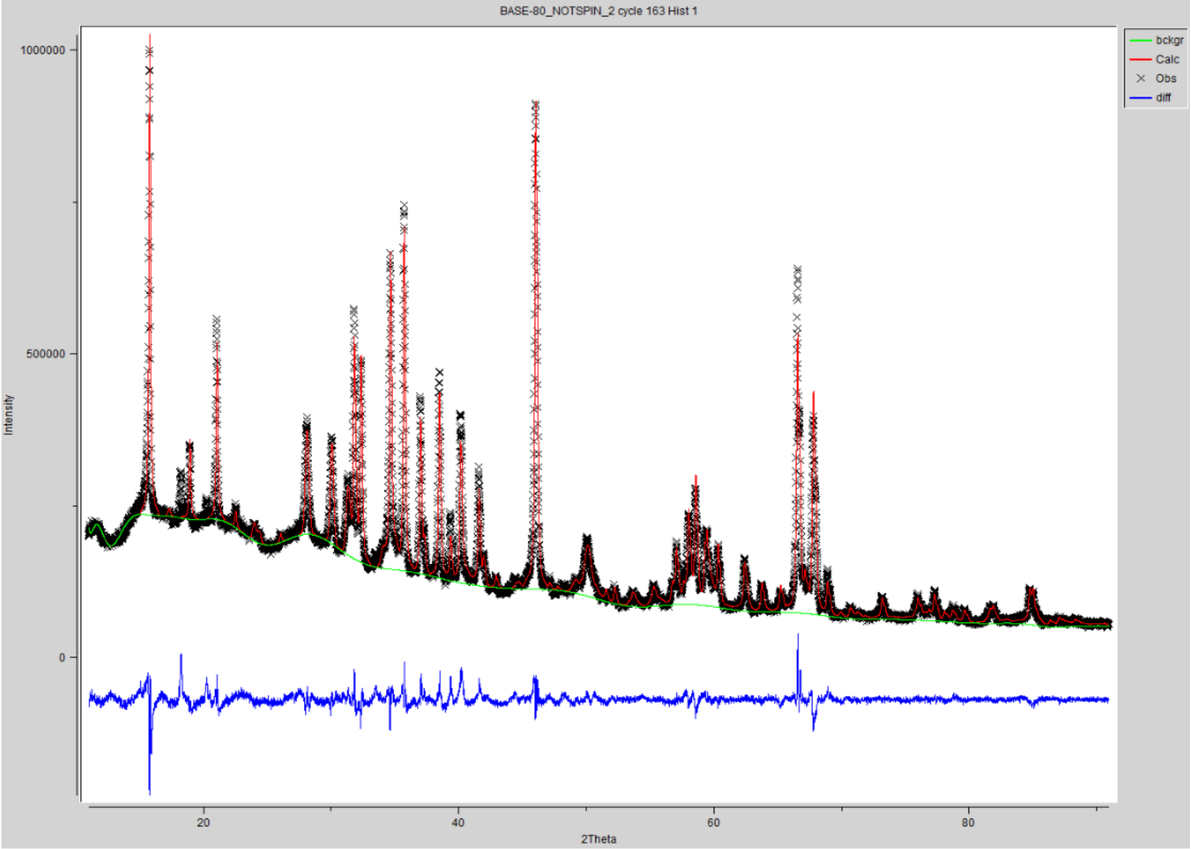

Figure. Attempt at drying BASE at 80 °C in vacuum antechamber for 24hours, XRD measurement under Kapton cover, with wRp4.8% - Rp3.6% -Lx1=12.4

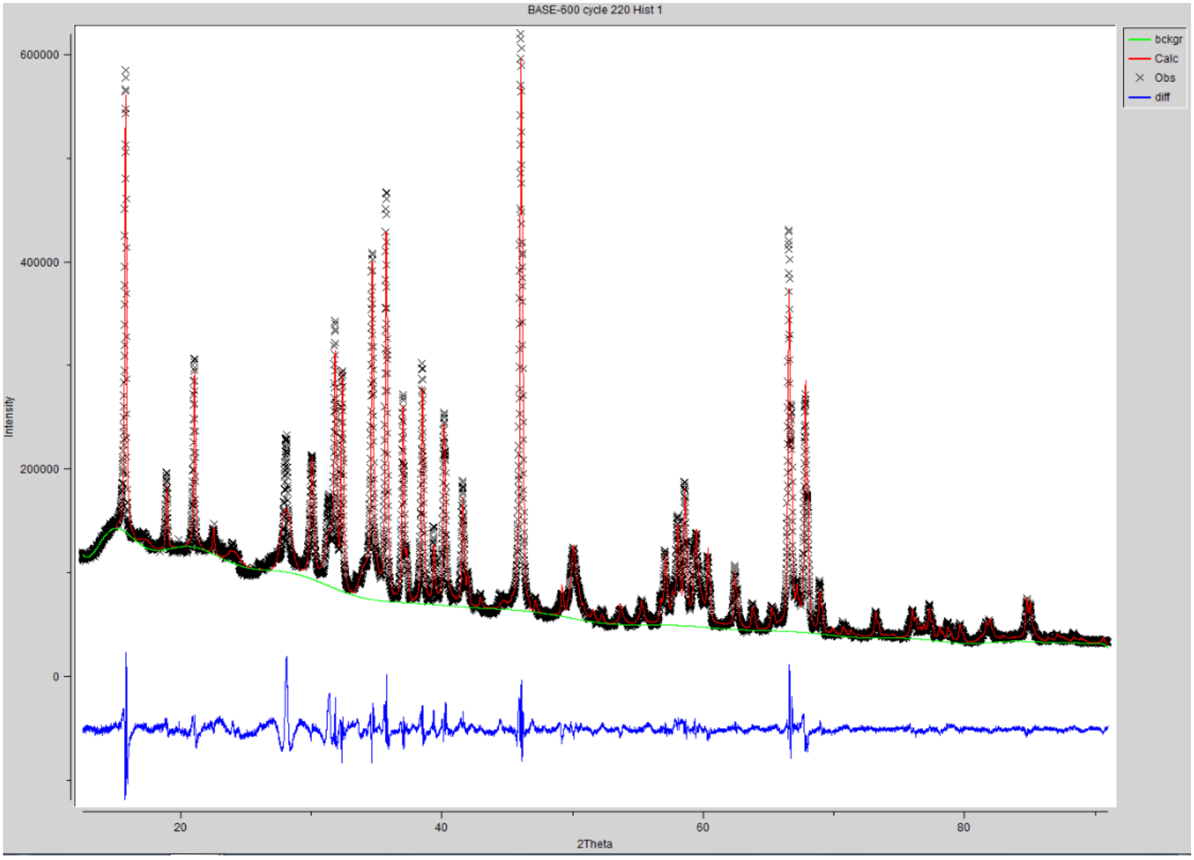

Figure. BASE after thermal treatment at 600 °C to get rid of water content, XRD measurement under Kapton cover, with wRp5.4% - Rp4.0% -L_x1=12.

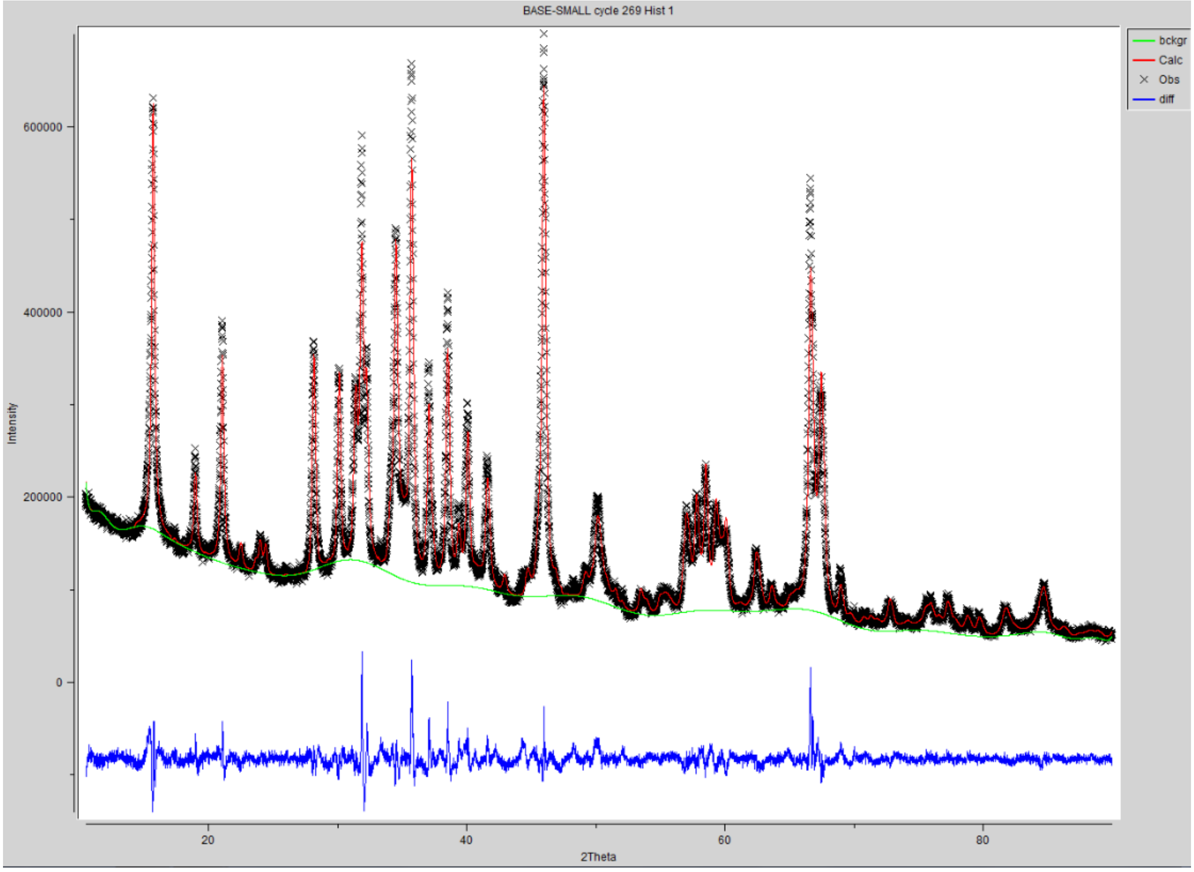

Figure. BASE post ball-milling with small balls, with wRp4.97% - Rp3.8% - Lx1=24.76

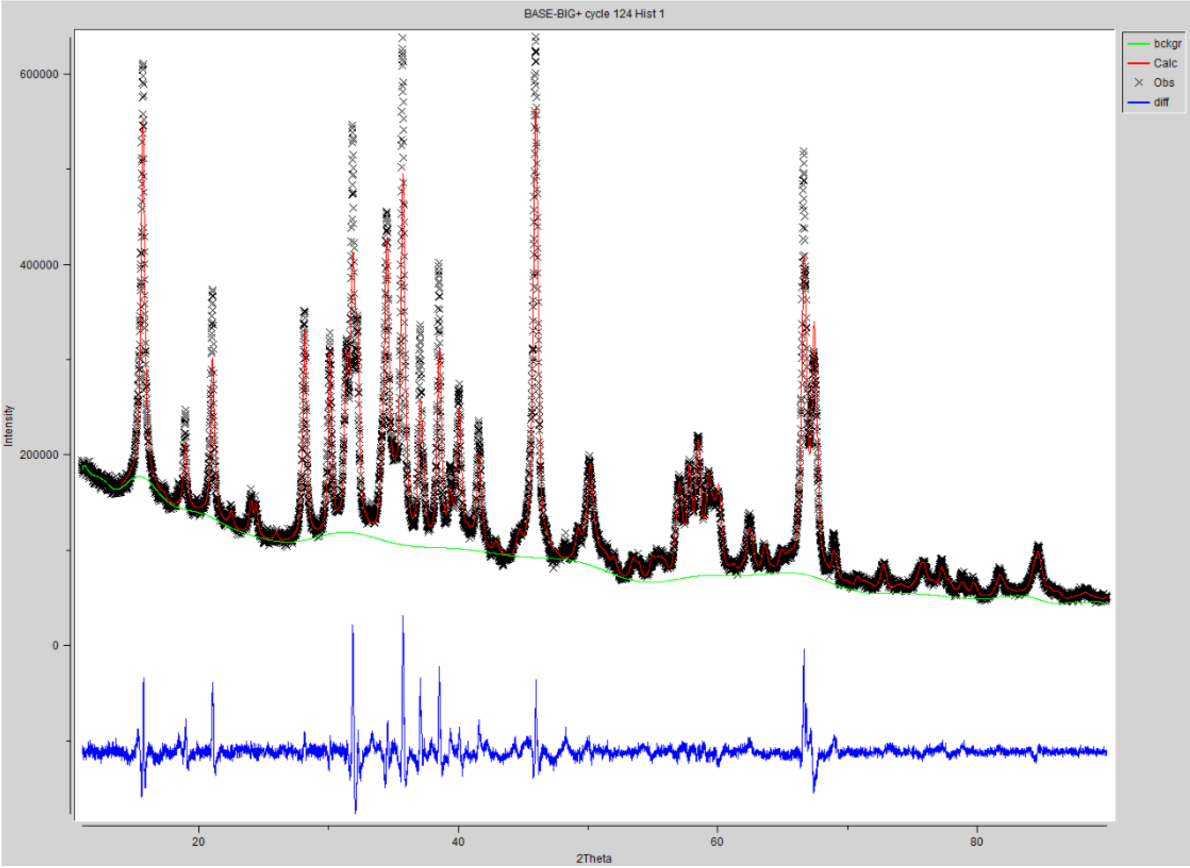

Figure. BASE post ball-milling with big balls, with wRp5.69% - Rp4.19% - chi²=3.67 - Lx1=26.94

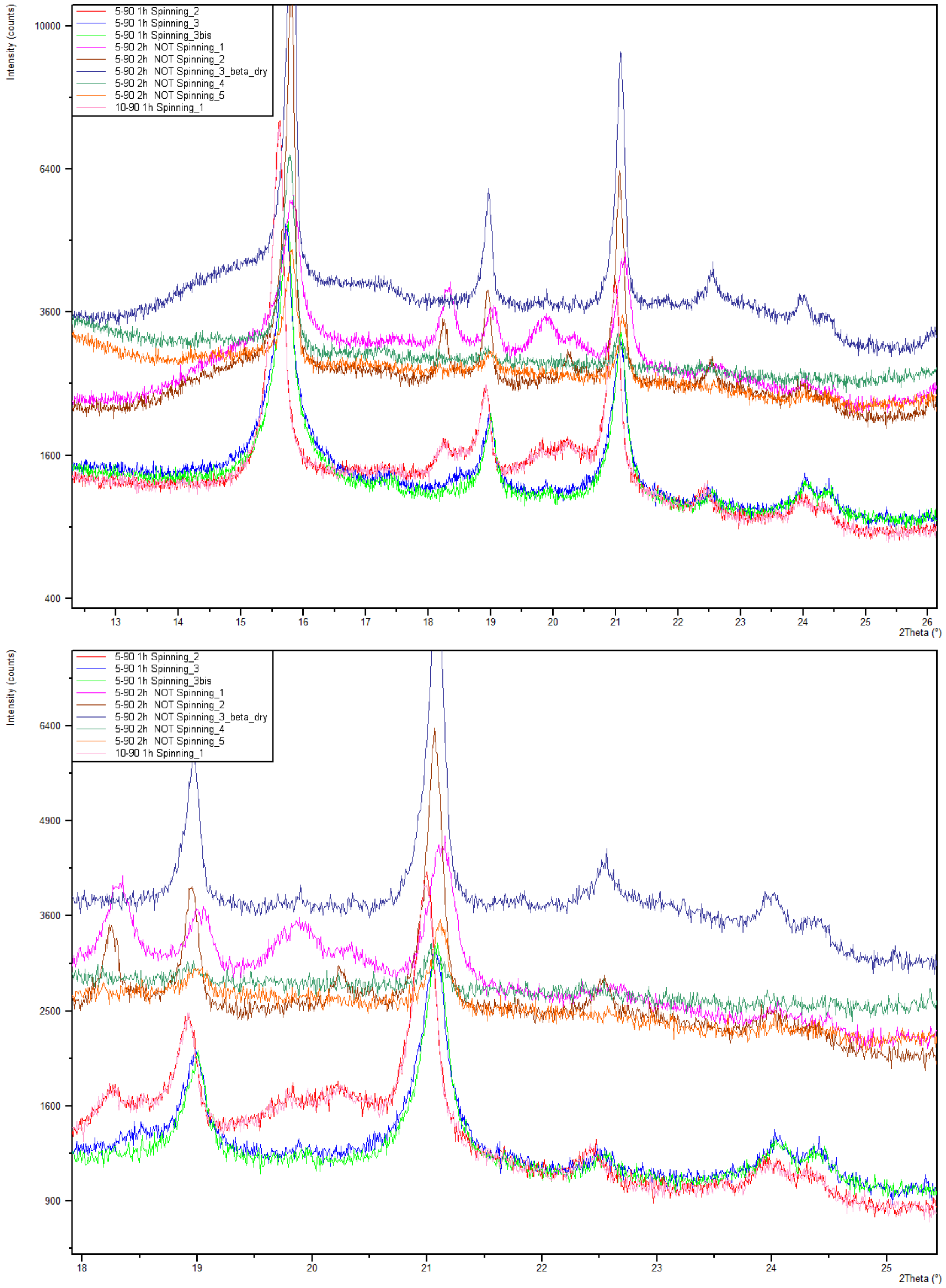

Figure. Superposed XRD measurements, where the highest measurement is dry BASE. A slight shift of the other measurements could be evidence for water absorption in the BASE layers.